Watching Polymer Deformation and Fracture with Atomic Force Microscopy

by

Stephen Jackson

A thesis presented for the degree of

Doctor of Philosophy

Department of Physics and Astronomy

University of Sheffield

Abstract

The deformation and fracture of the semi-crystalline polymers, polyethylene and polypropylene is investigated using AFM in order to observe the processes in situ, on the lamellae scale, for the first time. Samples were stretched on a custom built manual stretching stage under the AFM. Consecutive images were collected of the same area so that the deformation and fracture processes could be watched, from unstretched films to high strains.

For polyethylene, there was observation of many things that have been previously inferred, and some new things. Crazes are seen to start primarily at existing large gaps between edge on lamellae. Their growth appears to be inhibited by branch points of lamellae and they are seen to not all form at once. Meshes of points are fitted to the images in order to help follow the processes and understand why they occur where they do. This analysis revealed the heterogeneous nature of the strain across the sample, and that local shear plays an important part in governing the deformation of individual lamellae. SAXS is also used to compare to what is happening over a larger area of the sample. For polypropylene, the behaviour is even more localised with the strain occurring almost entirely in crazes; there is virtually no deformation in crystalline areas until they break up into individual crystallites. At high strains, crazes where short sections of fibril are arranged in geometric patterns at angles to each other and to the main parallel fibrils are seen, which we refer to as geometric crazes.

The effect of a large scale crack tip in polyethylene is also investigated: A distribution of strain relative to the crack tip is seen, with very high strains close to the edge, and significant shear seen. Similar geometric crazes are also seen here. An attempt was made to use torsional resonance AFM (TRAFM) to monitor the impact of strain on molecular chain orientation. The sensitivity of TRAFM to local organisation of water on the sample surface was confirmed, although no clear

impact of surface hydrophobicity was observed. Unfortunately, it was found that any effect of chain orientation on image contrast was over-shadowed by the effect of scan angle.

Acknowledgements

There are a number of people I would like to thank who've helped me throughout my PhD. Most of all, I'd like to thank my supervisor, Jamie Hobbs, who supplied lots of help, advice and encouragement throughout, even when things weren't going well.

I'd like to thank the following people: Mike Weir who helped with making the polypropylene samples, and taking the SAXS measurements. Paul Chapman, who helped me with various things in chemistry, including making the SAMs. Rebecca Savage who did the earlier work on stretching polymers, and Nic Mullin for various help and expertise around the lab, including developing TR.

I'd also like to thank the members of my office throughout the years: Ross Carter, Richard Bailey, Jacob Albon, Jonny Burns, Lamiaa Alharbe, David Owen, Raveen Tank, Nick Jenkins, Spyros Sovatzoglou, and Laia Pasquina Lemonche. For good company, interesting discussions and help with lots of things. Similar thanks go to lots of other people throughout the physics department, and the members of my CDT for molecular scale engineering.

Contents

Abbreviations

AFM	Atomic Force Microscope
AM-AFM	Amplitude Modulated - Atomic Force Microscope
AUDT	11-Amino undecanethiol
DNA	Deoxyribonucleic acid
EM	Electron microscopy
FM-AFM	Frequency Modulated - Atomic Force Microscope
FWHM	Full Width Half Maxima
GPC	Gel permeation chromatography
HDPE	High Density Polyethylene
IPA	Isopropyl Alcohol
LDPE	Low Density Polyethylene
MUA	11-Mercaptoundecanoic Acid
MUD	11-Mercapto-1-undecanol
ODT	Octadecanethiol
SAM	Self Assembled Monolayer
SANS	Small Angle Neutron Scattering

SAS	Small Angle Scattering
SAXS	Small Angle X-ray Scattering
SEM	Scanning Electron Microscope
SFA	Surface Force Apparatus
ShFM	Shear Force Microscope
SPM	Scanning Probe Microscope
STM	Scanning Tunnelling Microscope
TEM	Transmission Electron Microscope
TM	Tapping Mode
TR	Torsional Resonance
TT	Torsional Tapping
UHV	Ultra High Vacuum

List of figures

Chapter 1 – Overview

Polymers are a class of materials used in a wide range of fields, including construction and food packaging. In particular, the semi-crystalline polymers of polyethylene and polypropylene are the most widely used polymers. Their macro scale material properties depend on the micro scale deformation and fracture processes, so it is important to understand these processes.

Semi-crystalline polymers are made of crystalline regions called lamellae, separated by amorphous regions. As polymers undergo strain, there is a reorganization and breakup of these lamellae and fracture of the amorphous regions leading to void and craze formation.

In this study the samples are cut into dog-bone shapes and stretched under tension. With Atomic Force Microscopy (AFM) these processes can then be observed *in situ* on an individual lamella scale.

There have been many previous studies of these micro-scale processes for semi crystalline polymers; however these have either used techniques which give results averaged over the whole sample such as small angle X-ray scattering (SAXS), or microscopy techniques, which have been used to take snap shots rather than watching the same area as it deforms.

As such, there are a number of unanswered questions in the field. The main questions we attempt to answer are: Firstly where the deformation and fracture processes start and why they might start there? Secondly how heterogeneous these processes are on different length scales, and what influences how the microstructure develops differently in different areas of the sample?

The thesis is laid out as follows: Chapter 2 is an introductory chapter. Part 1 deals with semi-crystalline polymers and their deformation and fracture. Part 2

introduces the techniques used in this project, AFM and SAXS. Chapter 3 explains a number of the methods and materials used in the project.

Chapter 4 explores the deformation and fracture of stretched high density polyethylene (HDPE). Sets of images are taken of the same area to watch the lamellae scale processes in situ over a range of strains. Meshes of points are fitted to the sets to help follow processes.

Chapter 5 explores the deformation and fracture of stretched isotactic polypropylene, which is a more brittle material. Sets of images are again taken of the same area to watch the lamellae scale processes in situ. Previously unseen features, crazes where short sections of fibril are arranged in geometric patterns at angles to each other and the main parallel fibrils are seen. We refer to these as geometric crazes.

Chapter 6 explores how the presence of a large crack cut into the side of the film effects the local deformation and fracture. Sets of images were taken both in different places, to see how the distribution varies around the crack, and in the same place, to allow processes to be watched. Geometric crazes are also seen here.

Chapter 7 uses Torsional Resonance mode (TR) AFM. It is used to measure surface induced molecular water layering on both hydrophobic and hydrophilic surfaces. It is used to image self-assembled monolayers (SAMs) and polyethylene. There was also an attempt to measure molecular chain orientation in polyethylene lamellae.

Chapter 2 – Introduction

2.1: Introduction to polymer films

2.1.1: A brief history of polymer science

Polymers have existed in natural forms for billions of years, and have been used by humans for thousands of years, an example is cellulose. They have been used for many things including clothing, shelter and tool building [1]. However it is not until fairly recently that there were attempts to understand them.

In 1832 Henri Braconnot created the first man-made polymer, developing derivatives of cellulose to produce cellulose acetate, a semi-synthetic polymer. This was the start of many scientists work in this area, and in 1833, the term polymer was coined by Jöns Jakob Berzelius [2]. In 1907 Leo Baekeland invented the first synthetic polymer, Bakelite, which was used widely in household appliances [3].

The polymer industry was now well established, but the understanding of their nature was very limited, with most scientists believing they were aggregates of small molecules. It was not until 1920 that Hermann Staudinger, introduced the concept that polymers were composed of very long molecules of covalently bonded simple units, and coined the word macromolecule to describe them [4].

Since then polymer science has grown significantly, and a large number of synthetic polymers have been produced. Among them polyethylene and polypropylene which are studied here. Polymers have a broad range of properties, are used in many fields, including construction, electronics and food packaging, and are essential to our modern way of life [5].

2.1.2: Basic properties of polymers

Polymers are macromolecules consisting of many repeated subunits known as monomers which are connected together by covalent bonds. These macromolecules

are formed by linking together individual monomers by using chemical reactions, which is known as polymerisation. The simplest polymers are homopolymers, which are comprised of only a single repeated monomer, whereas there are polymers comprised of two or more types of monomer which are known as copolymers. Figure 2.1 shows the chemical formulae for the two polymers studied here, polyethylene and polypropylene, which are both homopolymers.

Polyethylene   Polypropylene
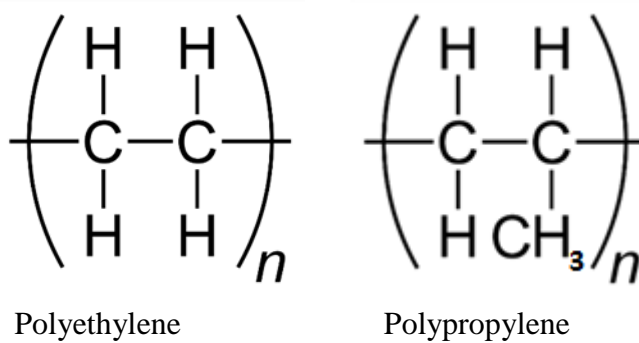
Figure 2.1 – Chemical formulae of polyethylene and polypropylene, the two polymers studied in this work.

The physical properties of polymers vary widely, not just based on the chemical formula but also on the size of the chains. For example with increasing chain length, melting and boiling temperatures increase and strength, toughness, and viscosity tend to increase. This is because longer chains have an increase in entanglements with each other and have larger Van der Waals attractions than short chains. These interactions tend to fix individual chains in position and thus resist deformation. [6]

The size of the molecule can be measured by the number of monomers, N, which is sometimes called degree of polymerisation. This varies drastically between different polymers, from 100 to many thousands.

A more common measure of the size is the molecular weight M_w, which is proportional to N, for homopolymers; it is given by

$$M_w = M_{w0} * N$$

(2.1)

where M_{w0} is the molecular weight of an individual repeat unit.

With only a few exceptions, polymers are made up of macromolecules with a range of molecular weights. This distribution will affect its physical properties. Rather than looking at the full distributions it is convenient to instead refer to molar mass averages. There are two averages used.

The number-average molar mass is the sum of the products of the molar mass of each fraction multiplied by its mole fraction:

$$\bar{M}_n = \sum M_i X_i = \frac{\sum M_i N_i}{\sum N_i}$$

(2.2)

where N_i is the number of molecules in a fraction of molar mass M_i, and X_i is the mole fraction of molecules of molar mass M_i, and is given by the ratio of N_i to the total number of molecules.

The weight-average molar mass is the sum of the products of the molar mass of each fraction multiplied by its weight fraction, it is given by

$$\bar{M}_w = \sum M_i w_i = \frac{\sum M_i^2 N_i}{\sum M_i N_i}$$

(2.3)

where w_i is the weight fraction which is the mass of molecules of molar mass M_i divided the total mass of all molecules present.

The breadth of the molar mass distribution is the polydispersity $Đ_M$, which is given by

$$\eth_M = \frac{\overline{M}_w}{\overline{M}_n}$$

(2.4)

Another property which can affect the physical properties is the degree of branching of the chains. Branching alters the ability of chains to slide past each other, and it can make it more difficult for the chains to stack with each other, thus reducing the intermolecular forces. [5]

An example of this is in the difference between low density polyethylene (LDPE) and high density polyethylene (HDPE). LDPE has highly branched chains compared to HDPE, this leads to lower density as the chains cannot pack well, and a polymer which is softer and more flexible, with a much lower tensile strength.

A further property that can affect material properties is the degree of cross linking. This is only possible in certain polymers, and does not apply to the polymers studied here. Cross linking is a chemical reaction that connects chains together permanently; this leads the polymer to be significantly stronger, harder, more rigid and less elastic.

An important property of many polymers is the glass transition temperature (T_g). Below T_g, these areas transition to a glassy state, which has a very hard and brittle behaviour. This is because the movement of the chains is frozen.

Polymers are usually classified into 3 separate groups; thermoplastics, elastomers, and thermosets. Elastomers are crosslinked rubbery polymers, with a low degree of crosslinking, which form large networks. They do not melt, instead they will pass straight into a gaseous state. They are highly flexible and elastic due to the crosslinks.

Thermosets are polymers with a high degree of cross linking, forming large networks. This greatly reduces chain motion leading to them being very rigid and having high strength. They also do not melt, going straight to a gaseous phase.

Thermoplastics, often just referred to as plastics, are polymers which do not have crosslinks, instead they are held together by intermolecular interactions between neighbouring chains. They melt, allowing them to be moulded and recycled. These are by far the most widely used type of polymers. [7]

Thermoplastics have a wide variety of mechanical properties depending on their structure. They are further subdivided into amorphous and crystalline polymers.

In amorphous structures, polymer chains are not ordered, they from a bundled structure, entangling with neighbouring chains. Below T_g they are very brittle, and above T_g they act as viscoelastic fluids, with the chains sliding past each other, and straightening out or curling up in response to stress.

In crystalline structures, polymer chains are highly ordered and compacted, generally in lamellae structures. The crystal structure does not undergo much elastic deformation before deforming plastically, but has high strength and high melting points.

There are very few completely crystalline polymers, instead they generally exist as semi-crystalline polymers; where both amorphous and crystalline regions are present. This occurs as thermoplastics crystallise slowly from the melt due to the need to untangle and order the highly coiled chains which exist in the liquid state. It is this semi-crystalline state which leads to properties which are very different to other crystalline materials.

The mechanical properties of semi-crystalline polymers depend strongly on the degree of crystallinity, which is the percentage of the polymer which is

crystalline. If the crystallinity is low, it will be highly elastic but have poor strength, whilst if it is high the reverse is true.

Semi-crystalline polymers are divided into crystalline lamellae which are separated by amorphous areas, [8] with amorphous tie chains connect neighbouring lamellae to each other [9][10].

Lamellae are plate like structures and both they and amorphous areas have thicknesses on the order of tens of nanometres. Lamellae consist of ordered folded chains, with the chains perpendicular to the lamellae surface [11][12]. They are not perfectly crystalline but instead have many defects [13], this leads to lower strength than for perfect crystals. They often form spherulites as seen figure 2.2, but this is not always the case.
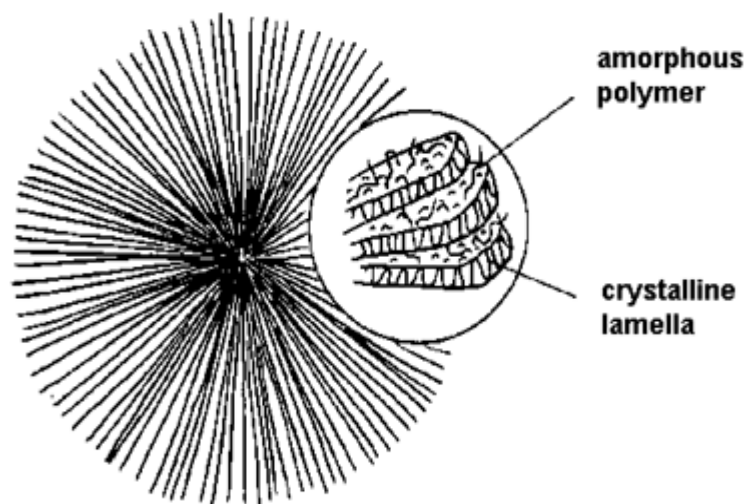
Figure 2.2 – Schematic of a semi-crystalline polymer spherulite structure, with crystalline lamellae separated by amorphous regions. [14]

Another structure formed in semi-crystalline polymers is a shish-kebab structure as seen in figure 2.3. Here the crystalline is split into two regions, the shish, which comprise extended polymer chains and the kebab which comprise folded

polymer chains, with the kebabs occurs in sections radially around the shish. These structure are strain induced, by either flow or shear.

Shish-kebab structures generally are more resistant to deformation than spherulites, leading to different mechanical properties such as higher strength and toughness. Materials with high shish kebab content experience much lower strain before fracture.[15]
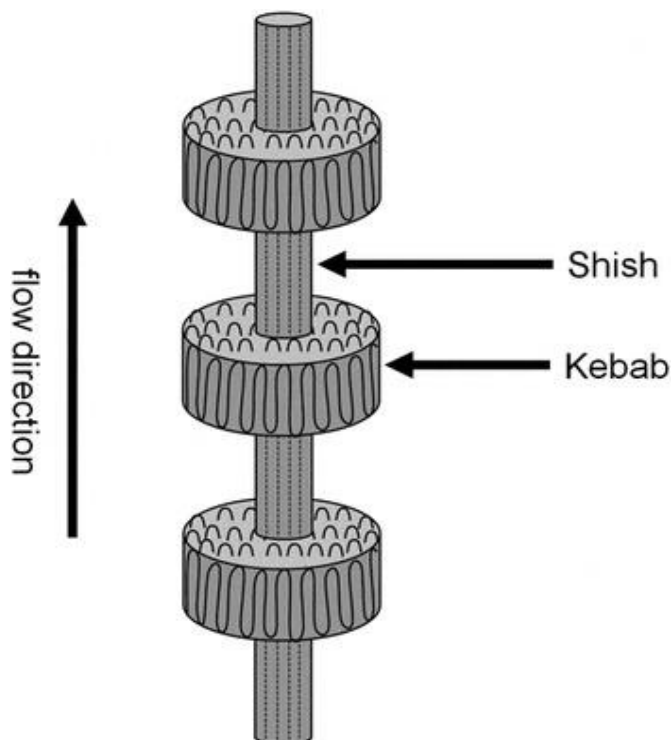
Figure 2.3 - Schematic of a semi-crystalline polymer shish-kebab structure. The shish comprises elongated polymer chains and the kebabs comprise folded polymer chains.[16]

2.1.3: Mechanical properties of semi-crystalline polymers

Two measurements of the deformation of a substance are the stress and the strain. Stress is given by

$$\sigma = \frac{F}{A}$$

(2.5)

where F is the force exerted on a body, and A is the area over which it is exerted.

Strain is given by

$$\varepsilon = \frac{\Delta l}{L}$$

(2.6)

where L is the original length of the substance and Δl is the change in length caused by the applied stress.

An important way of testing the mechanical properties of a substance is by tensile testing, which consists of the material being investigated being cut into a dogbone shape to concentrate the stress and then the sample is pulled apart whilst its stress and strain is measured, this give a stress strain graph.
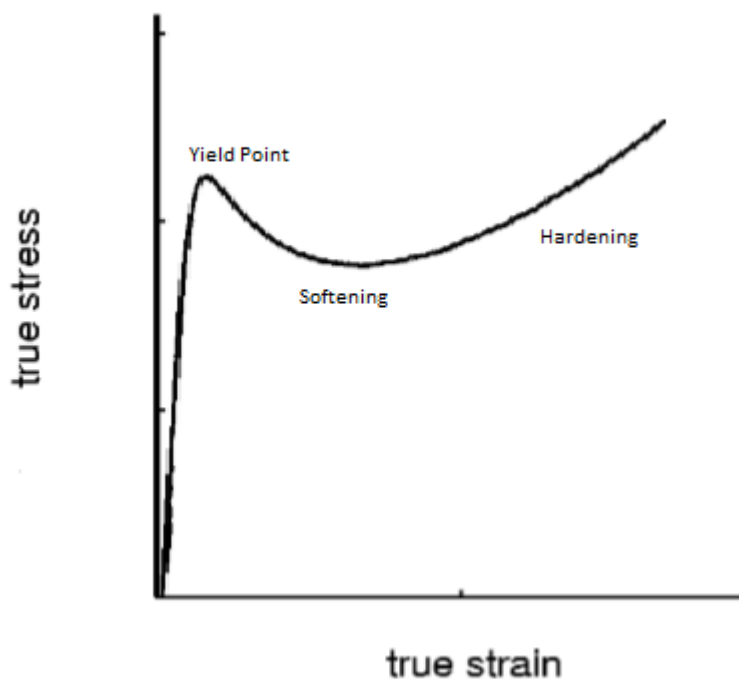
Figure 2.4 – Stress strain curve for a ductile semi-crystalline polymer.

An example of a stress strain graph for a polymer is given in figure 2.4, from it a lot of information can be learned. At the start of the graph, whilst the strain is low the graph is linear. This is elastic behaviour, in agreement with Hooks law, if the stress were removed whilst in this region the sample would return to its original state over time without any deformation. From the gradient of this section it is possible to work out the Young's modulus E, which is also known as the elastic modulus.

If the polymer were brittle it would snap after the elastic region without undergoing any plastic deformation, therefore this polymer must be ductile. The area under the curve gives the energy absorbed by the material, so a ductile material can absorb a lot more before fracturing. This toughness is a very important property for many applications.

After the elastic region the polymer reaches the yield point and plastic deformation begins. After plastic deformation a sample would not return to its original state. The strength at the yield point is called the yield strength.

After yielding there is a decrease in stress caused by necking, here the cross sectional area of the sample starts to decrease quickly, localising a large amount of strain in a small region. The neck then extends in length to areas which were relatively undeformed, which leads to a relatively flat part of the curve. This process is sometimes called cold drawing, and is due to it being easier to deform the new areas than the neck itself. [17]

Later the stress starts to rise again due to strain hardening, which is due to alignment of the polymer chains with the strain direction, before it finally fractures. This is in contrast to many other materials which exhibit strain softening. [18] The stress at the fracture point is called the tensile strength.

Polymers are viscoelastic materials, which are often modelled using the Kelvin-Voigt model. This means that when the stress is removed, it will undergo

relaxation to return to a lower strain. It also means the polymer will undergo creep when subjected to a stress, this is a slow movement or plastic deformation over time, even if the stress is constant. [19]

There is not one stress-strain curve for a material, its behaviour depends on both the temperature and strain rate. With higher temperatures the yield stress drops; and higher strain rates lead to much more brittle behaviour. [20]

2.1.4: Deformation of semi-crystalline polymers

The macro-scale material properties of a system will depend on its microscale properties. So to understand deformation it is important to investigate at the lamellae scale.

Figure 2.5 shows the generally accepted deformation process in a semi-crystalline polymer. [21][22][23] At the start, at A, the sample is undeformed, there are two crystalline lamellae present, which have ordered folded chains, between them is a small amorphous region where the chains are disordered.

By B the lamellae separation has increased significantly, as the amorphous region undergo strain, with the elongation of the amorphous tie chains between lamellae [24][25]. This corresponds to the initial linear section of the stress strain curve seen in figure 2.4, and all deformation is elastic.

By C, the lamellae have begun to tilt and rotate, to align with the stretch direction. Which leads to their kinking and buckling to form chevrons [26][27], and rotation of stacks of lamellae [28][29].

There will be fine crystal slip and some coarse crystal slip. Fine slip consists of displacements of 1 or 2 lattice vectors on every other lattice plane of a crystal. Coarse slip consists of more significant shear displacements of crystal blocks [30]. This is plastic deformation and generally corresponds to the long plateau in

figure 2.4 after the yield point. In tension fine slip predominates at smaller strains [31][32] and coarse slip becomes more important as strain increases [33].

By D the lamellae have broken up into blocky elements, which is called fragmentation, this would have been preceded by coarse crystal slip [34][35]. This is a highly plastic process. Finally in E the chains in the polymer have aligned with the stretch direction, with the former amorphous region now arranged as fibrils, highly orientated with the stretch direction. [36] [37] This corresponds with the rise of stress in the stress strain graph.
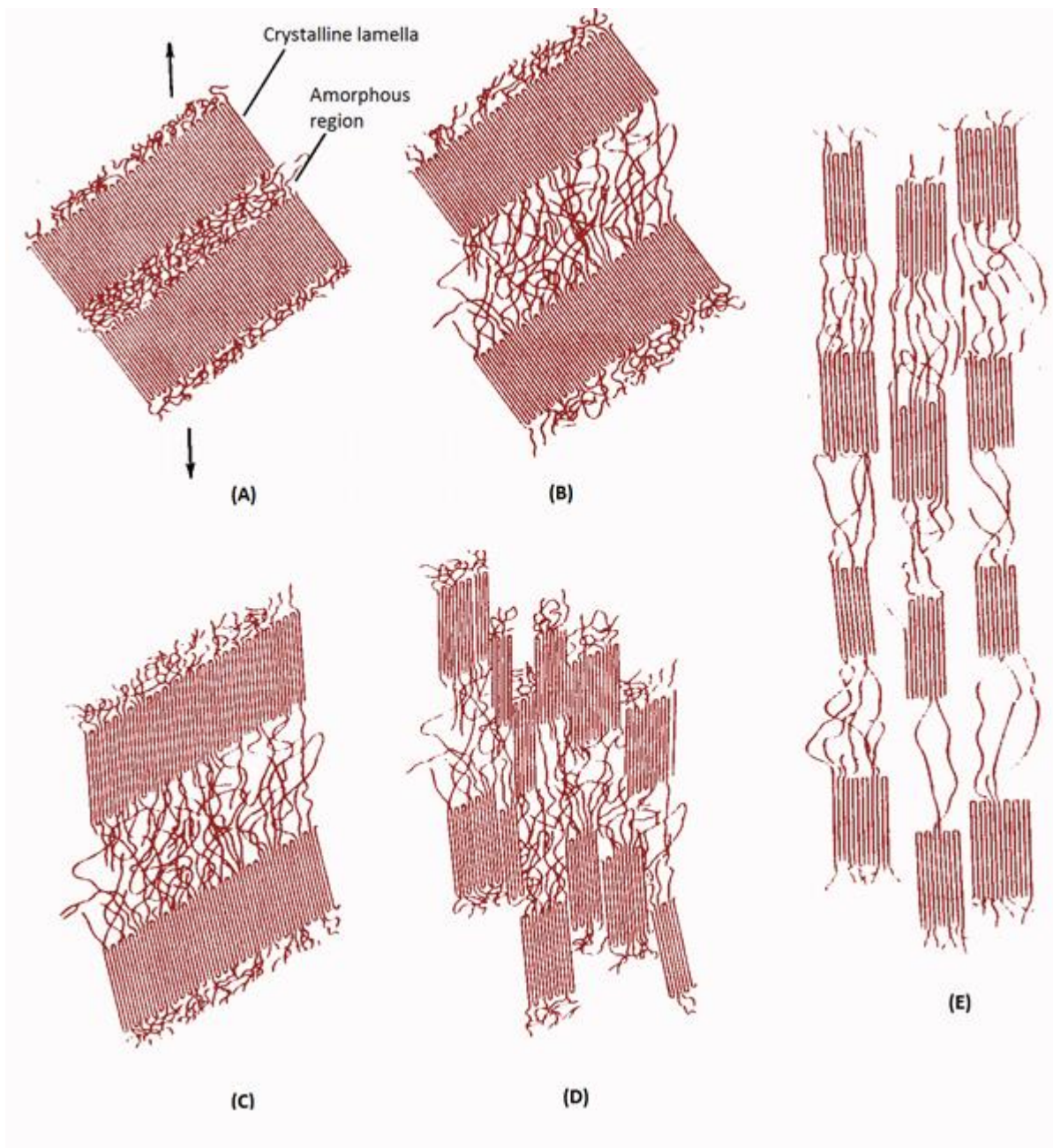
Figure 2.5 –The deformation and reorganisation of semi-crystalline polymers under tension. A – Undeformed, two crystalline lamellae with amorphous material between them. B – Elongation of the amorphous tie chains between lamellae. C – Rotation of lamellae. D – Breakup of lamellae into block segments. E – Orientation with stretching direction. Adapted from [38] by rearranging the image and changing the labels.

Other deformation processes seen are shear banding, which is a narrow zone of intense shearing strain, and large scale wedge formation. [39] More rarely seen possible deformation processes are mechanically induced crystal twinning [40][41], and martensitic transformation [42][43].

2.1.5: Fracture of semi-crystalline polymers

Another major mechanism as polymers undergo stress is local fracture within the amorphous regions between the crystalline lamellae, which leads to cavitation, i.e. crack/void formation, and crazing. These lead to the observed volume increase in deformed materials. [44]

These phenomena are observed only in tension, not in compression or shear, this is due to the need for a 3D local stress state, which is sometimes known as negative pressure [45][46].

It has been thought that the nucleation of voids and crazes was heterogeneous in nature [47] [48], caused by defects in the sample, however Galaskei showed this does not seem to be the case [49] they removed impurities from polypropylene and saw more cavitation rather than less; thus it seems nucleation is homogenous based on local fluctuations in the stress.

In thin films such as those used in this project large scale cavitation cannot usually take place [50] and thus crazing is primarily seen. Crazes are formations of interpenetrating microvoids and fibrils, with approximately 50% of the volume of craze being made of void.

A diagram of what is believed to happen during a craze opening can be seen in figure 2.6. Thermoplastics are held together by a combination of strong covalent bonds within chains and weaker Van der Waals bonds between chains. Crazes start with the formation of a nanovoid caused when the local stress is enough to overcome the Van der Waals bonds [51]. The opening of this nanovoid causes the slack to be taken out of nearby chains which resist further opening due to its covalent bands as these chain are orientated parallel to the stretch direction . This affects the local stress of the surrounding area causing more nanovoids to open and producing fibrils between them, of aligned chains, with the overall craze perpendicular to the stretch direction.

The craze is likely to propagate further, with a higher local stress at the craze tip creating new nanovoids and the craze opening due to the higher stress on the fibrils. A craze will open both by drawing in material from the sides and by thinning of the fibrils. Crazes often turn into cracks as they propagate, as the fibrils elongate they may break, causing the micro and nanovoids to grow and coalesce into a crack.
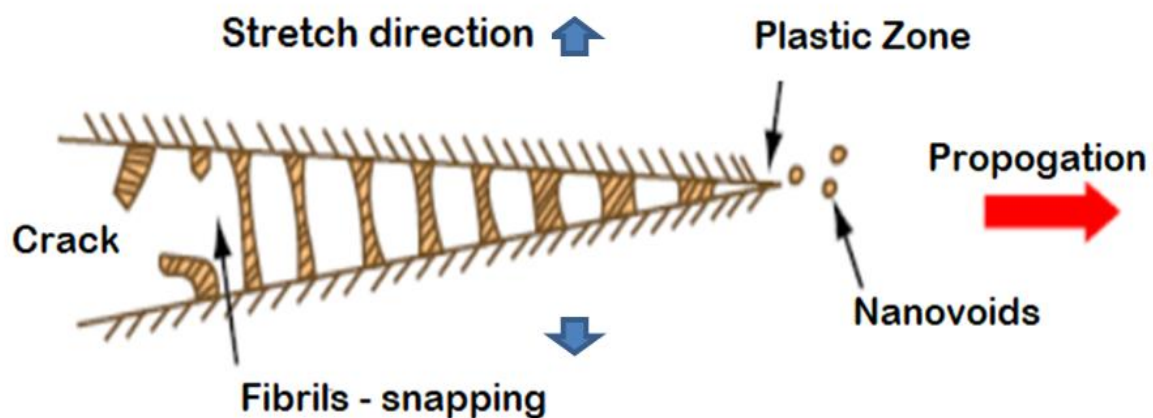
Figure 2.6 – Diagram of craze propagation.

Crazes are ellipsoidal in shape, which is partly determined by the small thickness of the amorphous regions [52], they generally propagate perpendicular to the stretch direction [53], until at high strains they can reorient to align with it. [54] At high strains, the coalescence of crazes and microvoids into larger voids has been seen, as well as the opening of new features. [52] Healing of voids has also been seen at high strains, due to reorientation of chains, via a decrease in film volume [55].

A key mechanical difference between cracks and crazes is that crazes continue to support a load due to their fibrils. They can absorb large amounts of fracture energy and thus increase the fracture toughness of a material.

Usually voids and crazes are detected close to the yield point, suggesting they are related. Some researchers suggested that voiding and yielding occur together

[56], whereas in other studies the voids were detected a little bit earlier or later than at the yield point [57][58].

There is a competition between the two processes, if the crystals are weak, then plastic deformation occurs easily with no cavitation, as the amorphous region is stronger and will not break. However if the crystals are strong with few defects, then cavitation via the breaking of the amorphous region is easier and occurs first.[59]

Morphological factors play a big part in the competition: increased branching is shown to lead to less cavitation [60], higher molar mass leads to less cavitation [56] [61]. Higher cavitation was seen for lower temperatures [62], and higher strain rates [63].

The presence of voids and crazes can be seen by the naked eye, via stress whitening, this is where light is scattered in the visible spectrum, by either microvoids or assemblies of nanovoids, making the sample white.

In a similar way to how the higher stress at the end of a craze causes the creation of nanovoids, a large defect, or notch/crack can have a significant effect on the local deformation and fracture due to its effect on stress concentration. [64] The multi-axial nature of stress is amplified by a notch, even for notches with large radius of curvature. This acts to stimulate a higher generation of cavities. [65] [66] [67] Understanding this is important as slow crack growth is the failure mechanism for many materials including HDPE pipes.

There is a distribution of strain and thus stress, in both strength and orientation in the plastic zone around the crack tip, there is a flow behaviour toward the crack tip assumed from this distribution. Also seen is the development of a craze structure near the crack tip [68]. An example of a distribution of stress caused by a crack is shown in figure 2.7.
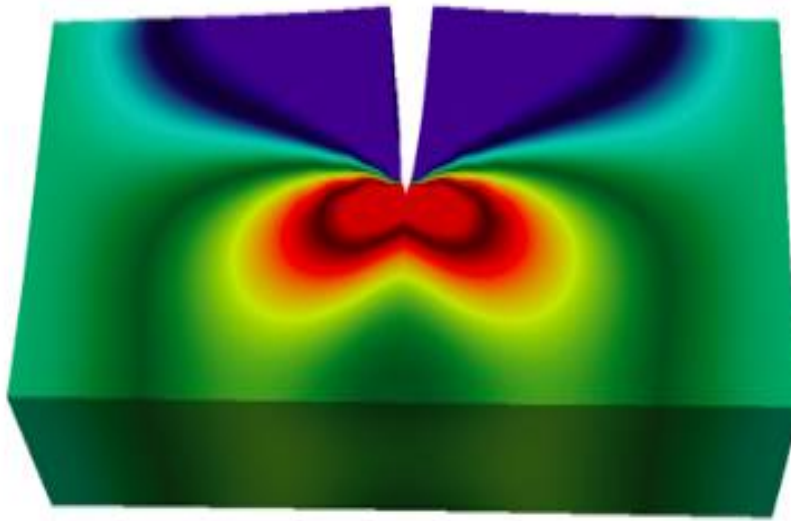
Figure 2.7 - Model of stress distribution around a crack tip [69].

2.1.6: Experimental developments

The fracture and deformation of semi-crystalline polymer on the microscale has been studied extensively for many years. Early studies used small angle X-ray scattering (SAXS) as microscopy techniques did not have high enough resolution. SAXS studies make up the bulk of studies on this topic.

Originally SAXS was undertaken with lab based linear sources, some examples of which include [44] [70][42][71][24][25]. Later, however synchrotron based sources have been used, these are much quicker to collect data, leading to an increase in in-situ studies. [72][56][68][73]. Recently there have been developments in microfocus SAXS, allowing data to be collected on a more local level. [74][68]

The developments of electron microscopy (EM), have allowed it to be used. It has been used indirectly to detect dislocations in polymer crystals, from moiré fringes [75][76][77]. Later it has been used to directly image features; originally with low resolution images of large features [78] [79] but with increasing resolution with time [80][81][82][83] though it still has issues due to surface charging.

In the last couple of decades atomic force microscopy (AFM) has been used to image deformed polymers. Hild was one of the earliest in 1996 imaging polypropylene [84], showing the presence of voids and crazes and an increase in lamellae distance with tensile strain. Misra and Dasari have done a lot of work on polyethylene and polypropylene, and with scratch deformation and the effects of different molecular weights. [83] [85][86]

Seguela has produced significant work on the morphological changes in deformed of poly(1-butene) spherulites at low strain by using AFM [48] [87], taking 25 μm in situ images, and smaller scale images showing crazing. Land and Dual, imaged crack growth in situ with 60 μm images [88]. Roggemann and Williams used an AFM to map surface deformation changes around a crack, however only with 250 μm images [89].

Zhong and He combined universal mechanical testing machine with AFM [90], analysing the relationship between macroscopic mechanical properties and surface nanomorphological changes. Recently Bakeev has taken high resolution images of HDPE crazing in liquid medium have been taken [91], which had delocalized crazing mechanism resulting in the development of a fibrillar-porous structure.

The have been many other experimental techniques applied to the microscale deformation and fracture of semi-crystalline polymers. These include: small-angle neutron scattering (SANS) [92][93] ; incoherent polarized steady-light transport technique (IPLST) [94][95]; infrared spectroscopy and electron paramagnetic resonance (EPR) [96]; and Ultra SAXS (USAXS), which is used to detect features of sizes 300–2000 nm. [97]

There have been a number of tomographic techniques, including x-ray microtomography [98] [66] [65], which allows localised studies of deformation, including around notches, and holotomography [99].

There are also numerous techniques which measure changes in microstructure indirectly. These include: detection of cavitation by acoustic emission [100][101]; densitometry [102] [103]; thermovision to measure increase of surface temperature [104] and differential scanning calorimetry (DSC) [105].

There have been limited theoretical studies due to the complex nature of the system, some include: Bacon and Tharmalingam's simulations of polethylene crytstals and how the dislocations move with deformation [106].

Lee and Rutledge investigated plastic deformation of polethylene via atomistic Monte Carlo and molecular dynamics simulations [107]. They observed that in deformation at constant volume, rotation of the chains within the crystal domains is observed, indicative of crystallographic slip. Whereas in tensile strain deformation with fixed lateral dimensions, plastic flow takes place in concert with melting and recrystallization at the crystal-amorphous interfaces.

Jabbari-Farouji and Barrat used large scale molecular dynamics simulations, to measure the uniaxial tensile response of amorphous and semi crystalline states of a coarse-grained PVA bead-spring model [108]. The found that strain-softening in semi crystalline samples is dominated by deformation of crystalline parts, while strain-hardening involves unfolding and alignment of chains in both amorphous and crystalline parts.

It is not the focus here, but there has also been a great deal of work on the mechanical properties of composites [109][110].

The unique element of this work compared to what has gone before is that we have taken lamellae scale images of the same area as it deforms allowing us to watch the processes as they occur. This allows us to attempt to answer a number of unanswered questions in the field. The main questions we attempt to answer are: Where the deformation and fracture processes start and why they might start there? And how heterogeneous these processes are on different length scales, and what

influences how the microstructure develops differently in different areas of the sample?

2.2: Introduction to primary experimental techniques

2.2.1: Introduction

There are two main techniques used in this work, the primary of which is atomic force microscopy (AFM), which is a microscopy technique that can image on the nanometre scale. The second is small angle X-ray scattering (SAXS) which is a scattering technique.

Microscopy and scattering techniques are useful to use in conjunction as they give complimentary information. Scattering techniques give information averaged over a large area of the sample thus giving a representative picture, and can have very high resolution. Microscopy by contrast, will give information about a small area of the sample, which may not be representative, and on the samples heterogeneity. The trade-off is they may have lower resolution, are often slower and have greater susceptibility to artefacts.

2.2.2: Atomic Force Microscopy

Microscopy is the use of microscopes to view objects too small to be visible to the unaided eye. Historically this was achieved using optical microscopes; however the resolution achievable using optical microscopy is fundamentally diffraction limited and thus depends on the wavelength of light. The resolution d is given by

$$d = \frac{\lambda}{2NA}$$

(2.7)

where λ is the wavelength of light and NA is the numerical aperture of the lens. Because of this far-field optical microscopy is limited to a resolution of approximately 200 nm [111].

To solve this problem new microscopy techniques were developed, the first of these is transmission electron microscopy (TEM) devolved in 1931 by Ruska and Knoll. Here a high energy beam of focused electrons is passed through a thin sample. Electrons have a de Broglie wavelength which depends on their energy and is much smaller than that of light, consequently higher resolutions can be achieved of down to 50 pm [112]. Later scanning electron microscopy (SEM) was developed in 1937 by von Ardenne, here a beam of electrons are focused at a single point on a sample and reflected electrons collected [113]. By scanning the beam across the surface data can be collected for a range of points, these points can be constructed into an image with each point forming a pixel.

In 1981 scanning probe microscopy (SPM) was developed, this is a family of techniques whereby a sharp tip is brought close to the surface of the sample, and interactions between the tip and sample are detected. By scanning the tip across the surface an image can be constructed. Scanning tunnelling microscopy (STM) was the first, created in 1981 by Binnig and Rohrer at IBM; it consists of a sharp conducting metal tip, with a bias voltage applied between tip and surface. When the tip is close enough to the surface electrons tunnel between the two, producing a measurable current. This tunnelling current decays very rapidly with distance and so it is possible to measure the tip-sample distance, and thus the topography of the sample, with a high degree of accuracy [114].

Later atomic force microscopy (AFM) was developed in 1985 by Binnig [115]; this is the main technique used in this project. At its heart it consists of a sharp probe on the end of a cantilever. When the tip is brought close to the sample, tip-surface

interactions will cause the cantilever to deflect, this is measured, giving information about the surface.

AFM has several advantages compared to other microscopy techniques: It can operate in a wide range of conditions, including in ambient and water as well as ultra-high vacuum (UHV), which allows for the study of systems in their natural environment. By contrast SEM and TEM require UHV and highly prepared samples, which can cause significant damage to them, especially if they are biological in nature. UHV is also very inconvenient, if you are using large samples or wish to change something about the sample during the experiment, as is the case here with polymers on a large stretching rig, where the strain is changed multiple times throughout the experiment. AFM can image a wide range of samples, whereas STM and SEM work best on conducting surfaces, and there would problems of charge build up on the polymer surfaces used here [74], so they would have to be metal coated.

AFM and other techniques in the SPM family can give a wealth of information not available in electron microscopy, including surface topography, and properties such as stiffness and viscoelasticity. Possible disadvantages of AFM compared to other techniques are slower scan speeds, which can lead to drift, smaller scan sizes, and the susceptibility to tip artefacts.

The standard setup for an AFM is shown in figure 2.8. It consists of a sharp probe on the end of a flexible cantilever; a laser is reflected off the back of the cantilever onto a photodiode which is segmented into four to allow spatial resolution. When the tip is near a surface, tip-surface interactions act to deflect the cantilever, this causes the reflected laser spot to move on the photodiode. The signal created here then travels to the data capture and feedback electronics. These systems control piezoelectric actuators, which move the tip vertically and allow accurate control of the tip-sample distance.
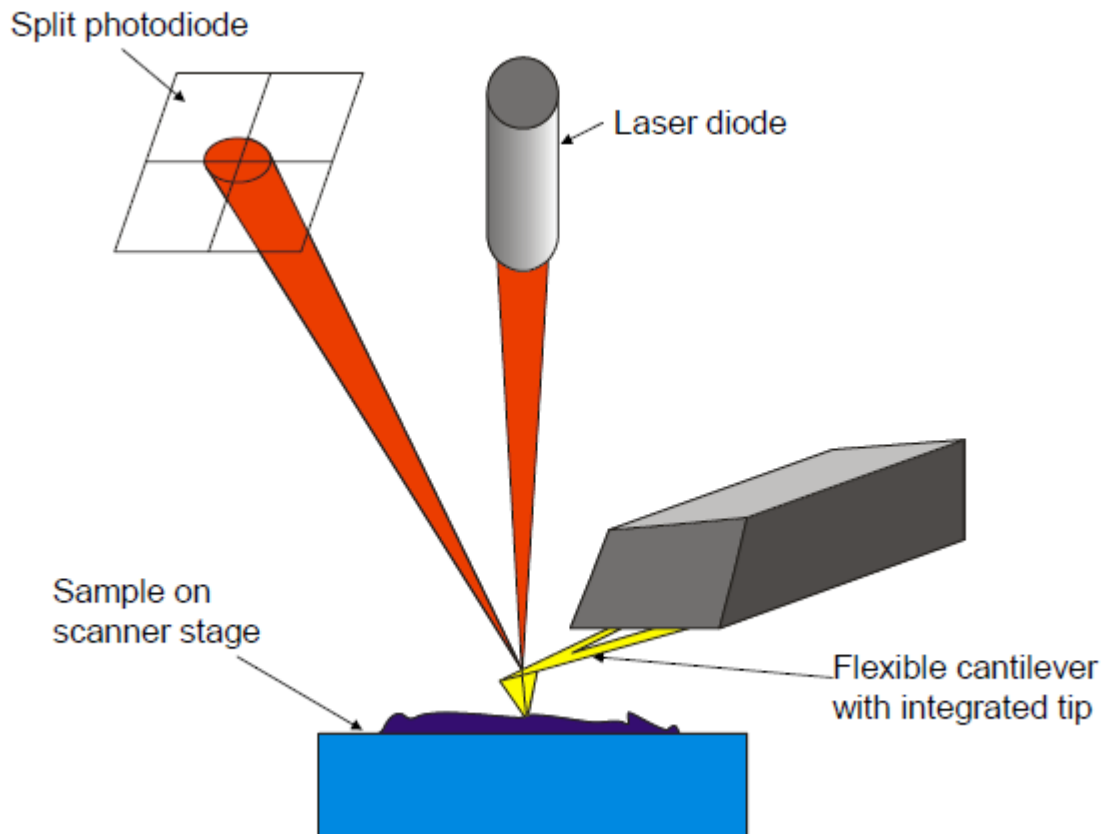
Figure 2.8 - Diagram of a common setup of Atomic Force Microscopy. Reproduced from [116].

For successful operation it is important to have feedback systems in place, here an output of the system is fed back into the system and used to adjust it. A feedback parameter is used, there are many such parameters including; cantilever deflection, oscillation amplitude, and frequency; this is necessary to remain at a stable position relative to the sample [117].

The most common use of AFM is to image a sample. Here the tip is scanned across the sample in a raster pattern where the image is divided into a sequence of horizontal scan lines, with each line broken down into a number of individual pixels. When scanning, the tip sweeps horizontally left-to-right at a steady rate collecting information for each pixel, it then rapidly moves back to the left, where it turns and sweeps out the next line. In this way a series of points on the surface are probed, creating an image.

AFM is not solely used for imaging; it has many uses including nano-manipulation, and nano-fabrication [118]. A major use which is used in this project it to take force curves of a sample, here the cantilever remains stationary in x and y, and is slowly extended to, and retracted from, the surface, as it does so the force is measured, producing a graph of force versus vertical distance from the sample. Force spectroscopy allows us to learn many sample properties, including stiffness, adhesion, chemical binding and viscoelasticity, and also allows measurement of single molecules, including stretching and breaking. Forces down to the order of a few pN have been measured with z resolutions better than 0.1 nm [119].

An AFM can be operated in many different modes, the earliest and simplest of which is contact mode. Here the cantilever does not oscillate and the feedback parameter is the cantilever deflection, which acts to keep the tip-sample interaction force constant.

There are dynamic modes where the cantilever is oscillated. The most common is tapping mode (TM) which is used throughout most of this project. Here the piezoelectric actuators at the base of the cantilever act to cause flexural oscillation, near the first resonance frequency, which causes the tip to oscillate vertically with respect to the sample. As the tip approaches the sample, surface interactions act to shift the resonance frequency and thus reduce the amplitude of oscillation. Good TM operation requires a strong resonance peak, this is measured by the quality factor, which is the ratio of the energy inputted to the energy dissipated for the cantilever per cycle. This can be approximated by the ratio of the wavelength to the FWHM of the resonance.

TM mode gives three different channels of information. The height channel, which is the position of the z-piezo required to keep the amplitude at the setpoint value. The phase difference between the driving force and oscillation of the tip also gives a channel of information known as the phase which is sensitive to surface properties. Finally another channel is the amplitude error, this is the average

difference between the actual amplitude of the cantilever and the setpoint amplitude; it is usually simply referred to as the amplitude. [120]

Throughout this work, all three channels are used. The height channel is often the most useful as it displays the height of the image. The amplitude channel is used throughout as it can have better a dynamic range and possibly better resolution allowing more detail to be seen. The phase channel is not shown as often, it is useful for showing differences in the physical or chemical properties of a sample between areas in an image.

For all dynamic modes both the frequency and amplitude of oscillation can be used as feedback mechanisms, leading to two modes of operation, frequency modulated AFM (FM-AFM) and amplitude modulated AFM (AM-AFM). Generally FM-AFM is used in UHV and AM-AFM is used in liquid and ambient conditions [119].

This is because, AM-AFM is technically easier to achieve in difficult conditions, but in UHV for very sensitive measurements FM-AFM is better as it can make use of higher Q values and thus achieve a lower minimum detectable force gradient. Also, and originally primarily, it was used because the frequency changes as soon as the interaction changes, whereas the amplitude changes at a rate determined by the settle time and therefore Q of the cantilever. In vacuum this is so high, that amplitude modulation takes too long to scan.

Dynamic modes such as TM have several advantages over static modes. The most important of which is to reduce lateral forces between tip and sample; thus reducing the damage done to the surface and the tip, which is useful here as it is necessary to image for a long time at large scan sizes to find the same area after stretching. This allows the imaging of soft and loosely bound samples such as lipid membranes. This also allows the use of sharper tips which lead to higher sensitivity. It is also possible to extract many material properties from the dynamics of the

oscillation; with the phase image able to determine surface properties such as friction, adhesion, and viscoelasticity.

2.2.2.1: Torsional Resonance Atomic Force Microscopy

Another less widely used dynamic AFM mode is used in this project, Torsional Resonance mode (TR). TR is a dynamic AFM mode similar to tapping mode, except instead of being oscillated flexurally the cantilever is oscillated torsionally about its long axis, causing the tip to oscillate parallel to the surface with a small dither motion, as seen in figure 2.9. The first published work on TR mode was from Kawagishi in 2002 [121]. Since then it has seen many advancements including being brought to commercial machines by Veeco with a patent by Su in 2005 [122].

TR has a number of potential advantages compared to tapping mode including higher sensitivity and stability, and a large phase contrast. These advantages can be useful for imaging, force curves and measuring surface properties. It also has the potential to sense in-plane forces and allows us to learn about the environment above the surface of the sample.
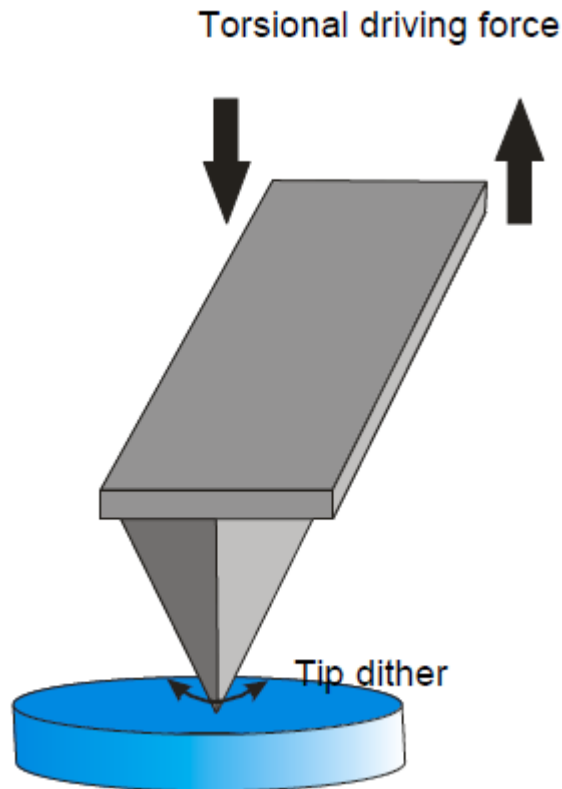
Figure 2.9 – A diagram of the operating principle of TR mode, a torsional driving force producing a small tip dither. Reproduced from [116].

The tip stays close to the surface throughout, with no vertical movement. Horizontally there is little tip movement, less than 1 nm [123], which is necessary to achieve good spatial resolution. The lack of vertical tip movement is important as the tip moves in plane parallel to the surface and thus its motion is not affected by forces normal to the surface.

TR mode has a number of advantages over other AFM modes. The most important is that the dynamics of TR mode are inherently favourable to achieving high force sensitivity, which is useful for both force curves and imaging. This can be seen by considering the minimum detectable force gradient of an oscillating cantilever, which should be minimised to increase force sensitivity. It was shown by Wickramasinghe [124] to be

$$\delta F_{min} = \left(\frac{2k \, k_B T B}{\omega_0 Q \langle z^2_{osc} \rangle} \right)^{\frac{1}{2}}$$

(7.1)

where k is the spring constant of the cantilever, k_B is Boltzmann's constant, T is the absolute temperature in Kelvin, B is the bandwidth of the measurement in Hz, ω_0 is the angular resonant frequency of the cantilever, Q is the quality factor and $\langle z^2_{osc} \rangle$ is the mean square oscillation amplitude in metres. This equation assumes that the cantilever is driven at the optimal frequency for slope detection and that the dominant noise sources are stochastic.

Between TM and TR mode the parameters in the equation differ significantly. In TR mode there are higher resonant frequencies and higher quality factors; which act to reduce δF_{min}. On the other hand, there are higher spring constants which act to increase δF_{min}.

In TR mode the amplitudes of oscillation are smaller and this would appear to increase δF_{min}, however this assumes that the force gradient is constant, linear and independent of the tip-sample force which is not true in AFM. Here the tip-sample force varies significantly, with for example the Lennard-Jones potential having attractive and repulsive regions which vary by $1/r^6$ and $1/r^{12}$ respectively. Also smaller amplitudes are often needed, as in softer systems large amplitudes act to displace the atoms or molecules that make up the system, thus smearing out their position in space. Overall the changes in quality factor and resonant frequency are larger and so TR mode has lower δF_{min} and thus achieves higher force sensitivity.

Another major advantage of TR mode is its greater stability. This is because throughout the oscillation the tip remains in the attractive region of the surface potential, this is in contrast to TM where the tip typically passes through both the attractive and repulsive regions in one oscillation [125]. Another factor increasing the

stability is that the torsional oscillation is perpendicular to long-range normal interactions, and so is not perturbed by them.

There are several other advantages to TR mode: it has the ability to measure forces both parallel and perpendicular to the sample, which is ideal for understanding in-plane surface forces. Also the cantilever dynamics are much simpler, which allows for analytical modelling and thus extraction of the elastic and inelastic components of these in-plane forces. Additionally large phase contrast has been seen, which is suggested to be due to the tip remaining in close proximity to the surface throughout, as well as the higher Q value. This allows TR mode to see some features not visible in TM, potentially including polymer chain orientation.

TR mode also has another advantage for operation in liquid; here a torsionally oscillating cantilever experiences significantly less damping due to a lower volume excited, which leads to higher Q values. This means that a wide range of machines can be used without any need to change the driving mechanism, making the process simpler and easier [126]. A final advantage is in high-speed scanning, here the much higher resonant frequencies seen in TR mode allow for increased scan speeds [127].

It should be noted that a number of these advantages can also be achieved using smaller cantilevers; however these have several issues. Their small size making focusing of the laser spot onto the cantilever very challenging, so specialised machines must be built which is more expensive. TR mode has the benefit of using regular sized cantilever in many commercial machines making it much easier and wider ranging in uses. In the future small cantilevers could also be used in TR mode to maximise the benefits.

2.2.3: Small angle X-ray scattering

Microscopy is not the only way to investigate the structure of materials on the micro and nm scales. One such technique is small angle X-ray scattering (SAXS), as it is a scattering techniques the results it gives are averaged over the whole sample.

Along with small angle neutron scattering (SANS), it forms a family of small-angle scattering (SAS) techniques which are taken at small angles (0.1-10 °). This allows the gathering of structural information of the scale of 1-100 nm. X-ray scattering taken at larger angles is called wide angle X-ray scattering (WAXS), and gives information on the smaller scale, such as crystalline structures.

The principle of diffraction of light has been known for a long time, it was first accurately observed by Francesco Maria Grimaldi in the 1660s [128], and its understanding has been refined over the centuries. X-rays were discovered by Wilhelm Röntgen in 1895 [129], and the diffraction of X-rays was first observed by Max von Laue in 1912 [130]. In 1913 William Lawrence Bragg and his father William Henry Bragg developed Bragg's Law which describes X-ray scattering in ordered structures [131].

The main principles of SAXS were developed in the 1930s by André Guinier [132] and in 1955 he and Gérad Fournet demonstrated that it could be used to determine the structure of disordered and partially ordered systems [133]. Since then SAXS has seen significant further development, and is now used to investigate a wide variety of structures, including polymers, metals [134], and biological systems [135], and can be applied to liquids, particles and solid structures [136].

X-rays are waves and they are scattered by the electrons within molecules. In SAXS they are scattered elastically via Thomson scattering, and as the angle used is small the Thompson equation is significantly simplified. X-rays exhibit interference, if

the two waves are in phase the interference is constructive and if out of phase it is destructive. Thus, if the system is at least partially ordered, then interferences between the waves scattered by the electrons will produce an interference fringe pattern.

Peaks in this pattern occur when the path length difference is an integer number of wavelengths, which leads to Bragg's law:

$$2dsin\theta = \lambda n$$

(2.8)

where λ is the wavelength of light, n is the number of wavelengths, θ is the scattering angle and d is the separation of scatterers. Thus the scattering angle gives you information about the lengths scales in the system.

In SAXS most X-rays go through the sample without interacting, and a minority will scatter. If the sample is isotropic it will produce a series of centric rings, if not the features will be inverted as scattering pattern is the reciprocal of real space.

A simple diagram of a typical set up, is shown in figure 2.10. First a monochromatic X-ray beam is produced, the source can be a synchrotron or a laboratory based linear source. They are than collimated; this can be either point or line collimation changing the shape of the beam, line collimators have shorter collection times but have a problem of smearing the pattern [137]. The beam then hits the sample; most of it passes straight through and is then stopped by a beam stop before hitting the detector. The rest is scattered, missing the beam stop and being detected by the detector.
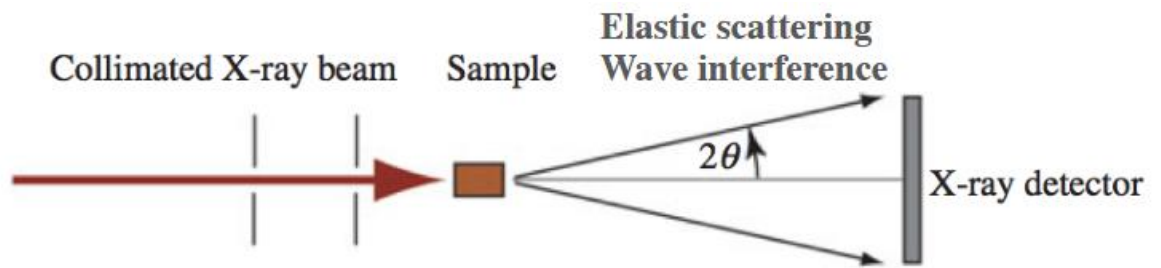
Figure 2.10 – Diagram of a simple SAXS set up.

The position of the scattering is recorded by the scattering angle, but for later analysis this is converted to Q which is the momentum transfer and is known as the scattering vector, it is given by

$$Q = \frac{4\pi sin\theta}{\lambda}$$

(2.3)

From this we can convert to distances in the sample, which is given by

$$d = \frac{2\pi}{Q}$$

(2.4)

Chapter 3 – Experimental Method Development

3.1: Materials

3.1.1: Polyethylene

The polyethylene films used in this study were HDPE (density, 0.97 g/cm^3); they were purchased as sandwich bags from Tesco and were measured using a micrometer to have a thickness 19 µm, which was highly uniform. Gel permeation

chromatography (GPC) was used to measure their molecular weights, giving values of M_w = 142,000 and M_n = 13,900, which leads to a polydispersity of approximately 10.

The samples were cut from the bags, into strips were approximately 20 mm wide. Dog-bone shapes were then cut into the films to create a neck to concentrate the stress and ensure that strain occurred here.

Originally this was done using scissors but this was found to be highly non-uniform in shape between samples. Thus the dog-bone shapes were then formed used a hole-punch with an 8 mm diameter, this did not always cut the shape out completely so a scalpel was used to finish the cutting. This left a neck in the middle of the strip approximately 5 mm wide. An example of a film can be seen in figure 3.1.
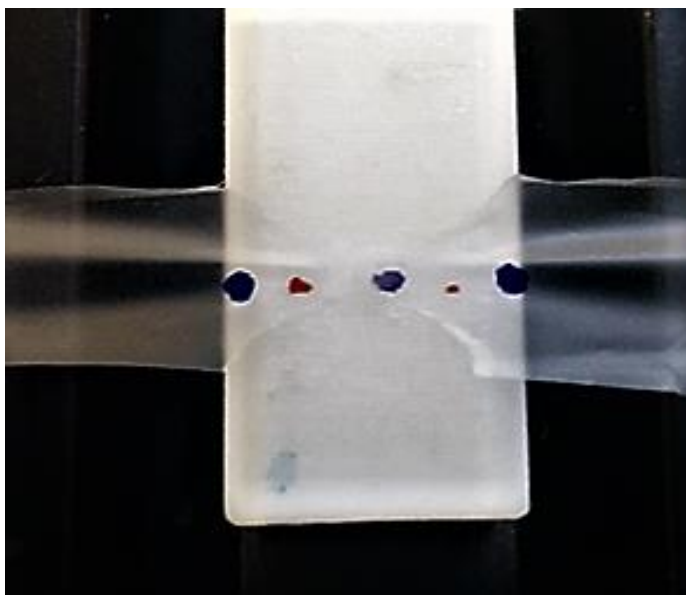
Figure 3.1 - Image of dogbone shape polyethylene film at small strain, with ink dots which are useful both for finding the same area and for measuring strain. It is supported by a white PTFE block.

3.1.2: Polypropylene

Polypropylene films were produced at the Composites Systems Innovation Centre in Sheffield using a hot press; the one used is seen in figure 3.2. A hot press

consists of 2 large metal plates which are heated and pressed together at pressure, this helps to create thin uniform films.

Figure 3.2 – The hot press used to produce polypropylene films, behind a metal safety grid.

Originally the polypropylene used was isotactic polypropylene with a M_w of 12,000, however this had a much too low viscosity when heated and failed to form coherent films. Instead polypropylene with a M_w of 190,000 and M_n of 50,000 was used.

Pellets of the material were placed sandwiched between aluminium foil and two metal plates which had been cleaned with IPA. The hot press was heated to 170 °C and the package was loaded. A pressure of 2.2 MPa (2 tons on a 4" diameter ram) was applied and held for 1 minute before being released, the package was then taken out and the metal plate removed. It was then left to cool in the air and was not quenched. Before use the film was removed from the aluminium sheets.

An example film is seen in figure 3.3, the films were disks with a diameter of approximately 6.5 mm. The thickness was measured in several places per film with a

micrometer, it was found to vary from 60 – 100 μm between films, but only by 10 μm within an individual film.

There were some large scale scratches on the surface of the films which match to features on the plates, this was reduced by using an additional aluminium layer but was not eliminated entirely. The film was cut into dog bone shapes as for polyethylene.

Figure 3.3 – Optical image of one of the polypropylene film disks.

AFM images of one the films can be seen in figure 3.4, this now looks like cross hatched α form polypropylene with some incipient crazes. There are large scale diagonal feature which are due to the grain of the aluminium film. These were judged to not significantly affect the deformation processes.
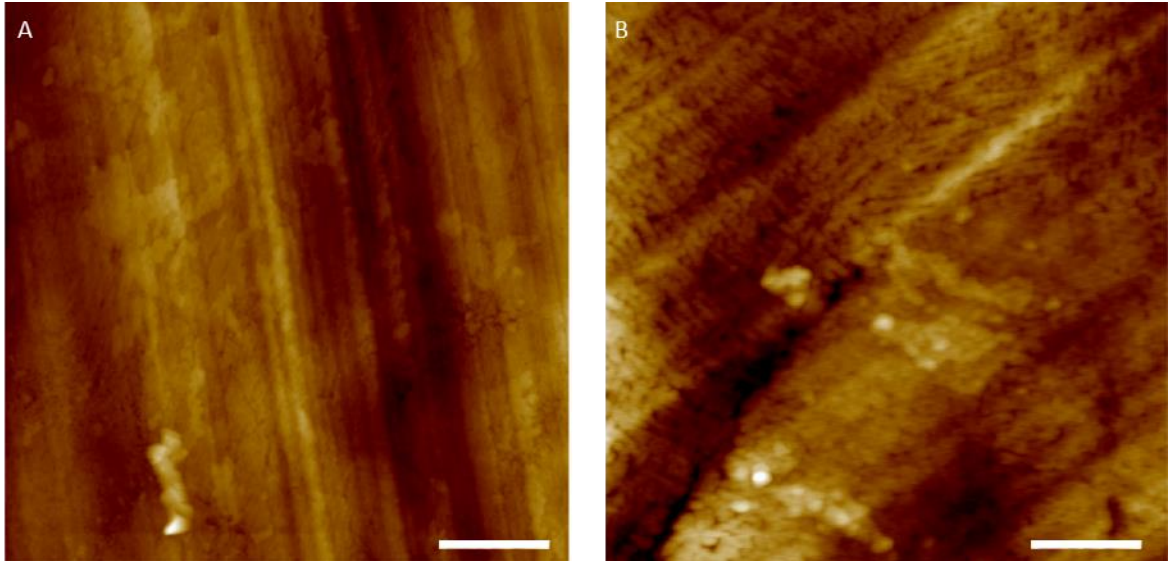
Figure 3.4 – Height images of the produced polypropylene films. A is the larger images showing the diagonal features caused by the aluminium foil. B is a smaller image showing the alpha cross-hatched form. Scale bars A – 1 µm, B – 300 nm. Z scales 120 and 40 nm.

3.2: Methods

3.2.1: Introduction

Other than in chapter 7, the AFM experiments were carried out using a Bruker Dimension 3100 atomic force microscope. Scans were in tapping mode using silicon nitride Tespa-V2 cantilevers at 1 Hz. Images were processed using Nanoscope Analysis software, images were usually flattened, 2nd order, but were occasionally plane fitted. Further processing to clean up the images was not undertaken.

Images which could form part of the sets were generally taken at 512 lines, and were scanned in the same direction, downwards, to eliminate image differences due to scan direction and drift. The experiment was performed in ambient conditions at approximately 20 °C, above the glass transition of the two materials.

3.2.2: Building the stretching stage

This experiment requires the use of a stretching stage to allow the samples to be stretched and imaged without the need to transfer them to a separate piece of equipment. To this end a custom built manual stretching stage was used, which was designed to replace the normal stage in a Dimension.

It can be seen in figure 3.5. It consists of a Thor Labs optical breadboard supporting layer, on which are two Mitutoyo micrometer heads, each of which are attached to a spring and connected to a gripping plate which hold the sample. The film is held between the gripping plates, it is supported by a PTFE supporting block for stability in imaging, this can be more clearly seen in figure 3.1. Turning the micrometer dials causes the film to stretch.

A custom built motorised stage was initially tried but was found to induce vibrations in the images, and was not used further.
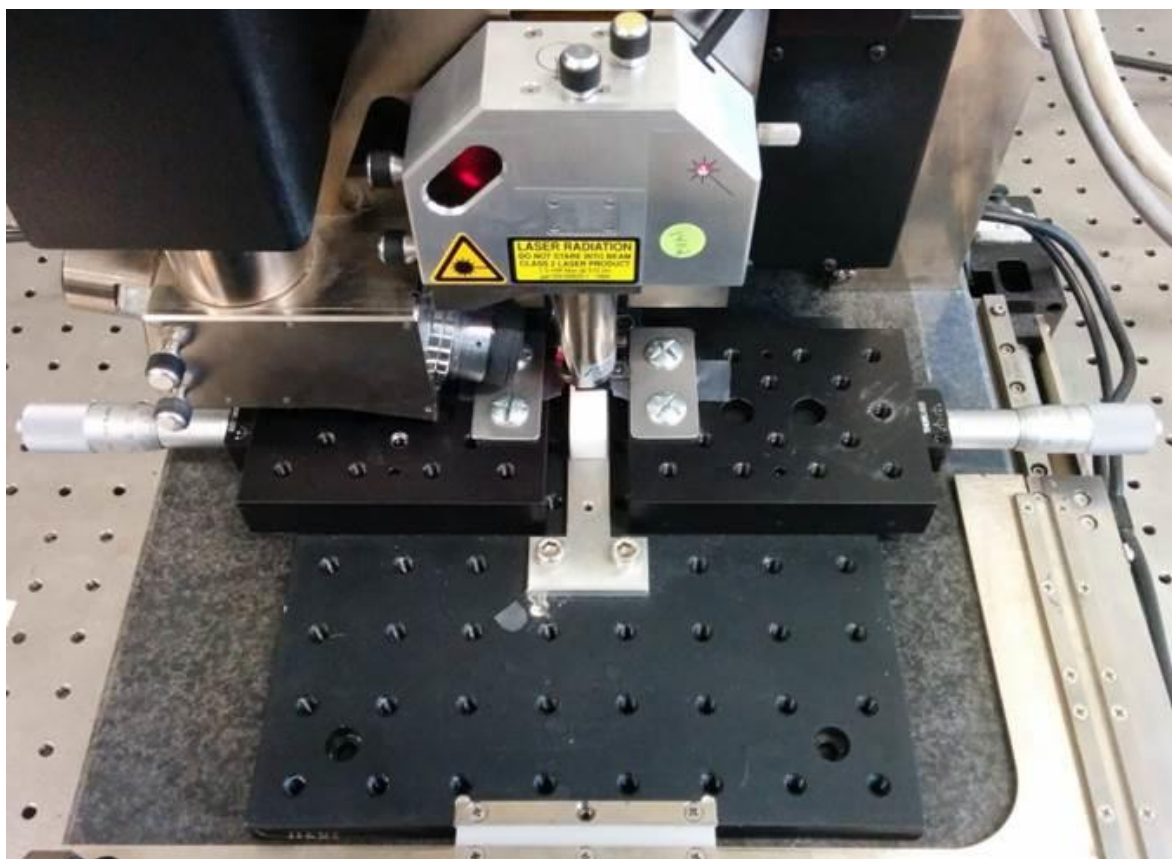
Figure 3.5 - Image of the setup with custom built stretching stage below a Dimension AFM, the film is directly below the AFM tip, supported by a PTFE block from below and held in tension by the gripping plates.

3.2.3: Imaging procedure - Finding the same area

A key challenge in this work is to repeatedly and consistently find the same area after stretching. This was difficult due to the nature of the film, and how it appears in both optical and AFM images; with it possessing a lack of clear features and many areas looking similar. This was compounded by the fact that how an area looks changes upon stretching making it harder to find the same features. Another factor is that it important not to spend too long imaging or use large scale scan sizes (over 20 µm), as this will damage the tip leading to worse imaging quality. It is thus crucial to have a way to reliably locate an area again after stretching. This was done with the aid of two different fiducial marks.

The first is an ink dot placed in the centre of the neck of the film with a felt tip pen, and example of which can be seen in figure 3.6. The investigated region is chosen to be approximately 80 µm, the length of the crosshair, from a clear feature in the ink dot. When the film is stretched the ink dot breaks up as their bond to the film overcomes some internal bonds. The feature on the ink dot will thus stay near the investigated region allowing it to be found with a precision of approximately 50 µm, with a lower precision for higher strains. The breakup ink dot is also used to measure strain. The investigated area was then imaged with larger scans (20 µm) to select an area suitable for investigation, i.e. areas with minimal contamination.
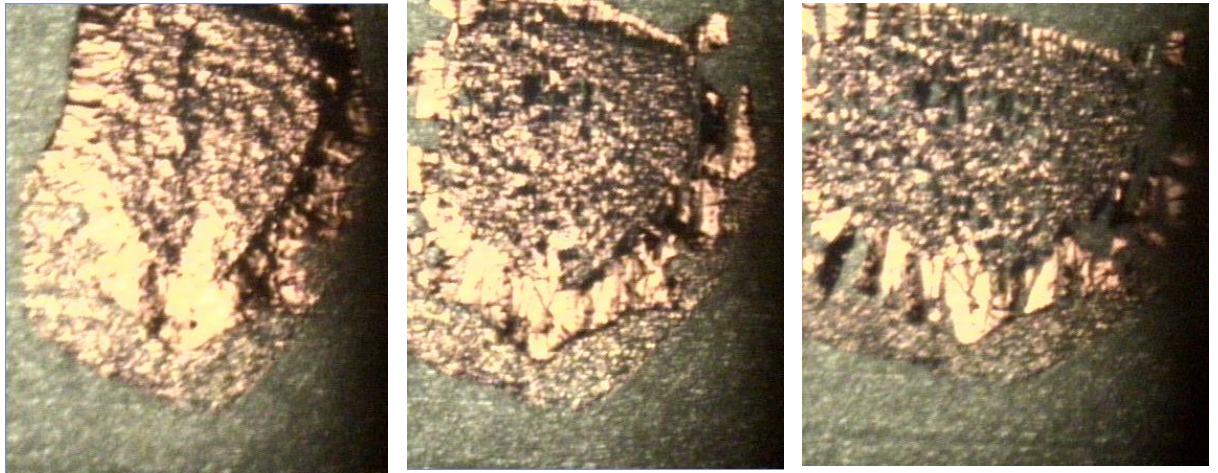
Figure 3.6 - Optical images taken with the AFM optics of the same ink dot as it breaks up under strain. Strains of 0%, 10%, and 42%.

The second fiducial mark works on a smaller scale, after having used the ink dot to get closer. It consists of a diagonal scratch on the surface of the film caused by the AFM tip when imaging at a low setpoint, an example is seen in figures 3.7 and 3.8. A 5 μm scan was chosen, with the angle set to 135° to produce a diagonal scratch. A diagonal mark is easier to pick out then a horizontal or vertical feature due to both lack of similarity to features already present on the film and the limitations of scanning with an AFM. The line was set to the centre of the image and set point was lowered to approximately 0.03 V for 10 seconds, before being raised and imaged at 0°, if the scratch was not clear enough the process would be repeated with a lower setpoint. At first a setpoint of 0 V was used, however this produced a deep gash in the surface because the tip was not under control, and so a controlled scratch was preferred.
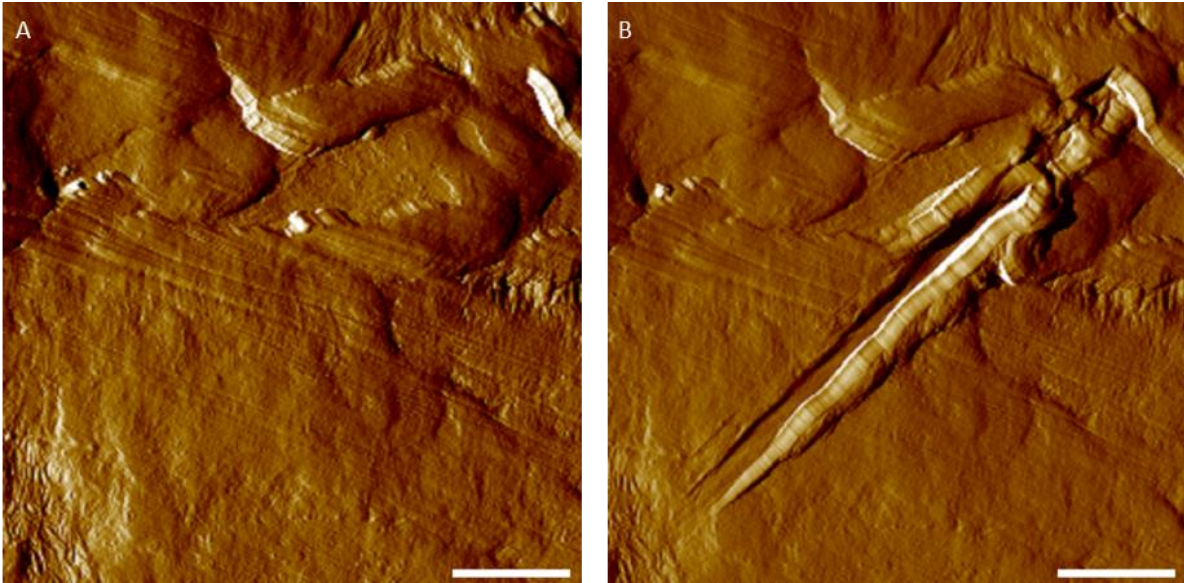
Figure 3.7—Amplitude images of the second fiducial mark, showing the area before (A) and after (B) the scratch. Amplitude images are used as the edges of the scratch show up well due to their steep sides. There is noticeable reduction in image quality between images due to the damage to the tip caused by the scratch. Scale bars 1 μm. Z scale 500 mV.
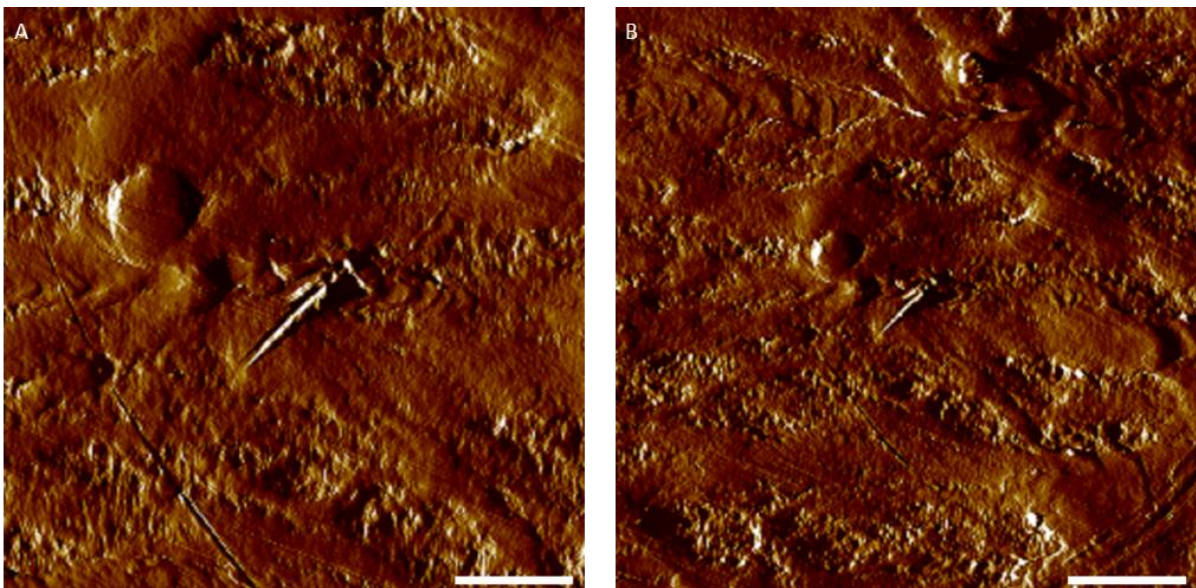
Figure 3.8 –Amplitude images of the scratch at larger scan sizes of 20 μm (A) and 40 μm (B). These images are used to aid in finding the fiducial mark again and show what it looks like when searching for it. The mark is still quite clear compared to its surroundings, though it will become less so when stretched. Scale bars 4 and 8 μm. Z scales 1.1 and 1.5 V.

After the scratch has been made, successively larger images were taken with the now blunted tip to aid in finding the same place again; these were taken at 20, 40

and sometimes 80 μm. The area which is imaged later is chosen to be approximately 5 μm from an end of the scratch; this should be far enough away that the scratch will have limited effect on the processes observed. As the initial lamellae long period is 30 nm there are approximately 170 lamellae to the edge of the scratch so the effect should be minimal. The AFM tip was then replaced with a new tip due to the damage sustained by the old tip in forming the scratch, and the scratch must be found again.

The ink dot is used to position the tip, and then AFM images of 10 or 20 μm were taken to find the scratch. For this image quality is not important and so high gains and high setpoint are used to minimise tip damage. Either above or below the scratch was chosen based on which area looked better and a series of images were taken there, generally 10, 5, 2.5, and 1.5 μm; zooming in each time and adjusting for drift. The end of the scratch is used as fiducial mark included at the edge of all the 10 μm images so they can be easily aligned.

For later images in the set they were aligned to the previous images of the same size, this was done by comparing central features, usually lamellae, and offsetting to get them to line up. When the film becomes highly stretched there is significant reorganisation and so the position of the image can vary depending on which features are kept in a constant position. In a number of cases two offset images are taken at the same size in order to follow more of the features that were present in the original image. Two difficulties in aligning images arose from drift and the use of an open loop scanner.

After being imaged unstretched, the tip was retracted and the film stretched and then left for 30 minutes to reduce creep. The process was then repeated, finding the area, aligning the images and taking a set of images at different length scales. At first the films were stretched by fixed amount on the micrometers (approximately 2 mm) corresponding to fixed amounts in the macro strain. Due to the inhomogeneous nature of the films strain however this provided very uneven stretch intervals

between images. Instead, the breakup of the ink dot was watched when stretching the sample to see the strain and stretching was stopped after an appropriate stretch.

3.2.4: Creep mitigation

A significant issue when imaging stretched polymers with AFM is the problem of creep and the effect this has on images. Creep is the slow movement and plastic deformation over time, even if the stress is constant; it is generally highest immediately after stretching and reduces with time, it generally causes the film to drift in a certain direction relative to the AFM.

Figure 3.9 is a set of images that demonstrate the issue of creep in polyethylene. The images are 512 lines, and the scan rate is 1 Hz, thus it takes 8 minutes 32 seconds for a full image and 4 minutes 16 seconds for a half image.

The start of this image set was taken approximately 1 min after the film was stretched whilst the film was settling, it begins scanning upwards until it reaches the top then the image is saved and the scanning direction reverses and the process repeats.

There are two main effects of creep on the images seen here, firstly features drift to the right, which can be seen by the movement of the blue dot. Secondly this movement causes a slant in the features based on the scanning direction. When scanning up features align towards the top-right/bottom-left diagonal as seen clearly in A, and when scanning down features are aligned top-left/bottom-right diagonal which is clearest at the top in B. Between A and B the black void at the centre top can be seen to change direction. This effect is larger with smaller images

The magnitude of this effect falls quickly with time, A is extremely distorted, B less so, and C and D are not that different meaning that creep is much smaller but still present.

To reduce the effect of creep on imaging the samples were left for 30 minutes for most of the creep to go away, in addition finding the same area and taking large scale images would take approximately another 30 minutes, so the creep should be much smaller than seen here. And all images were taken scanning downwards to make any creep artefacts consistent between images.
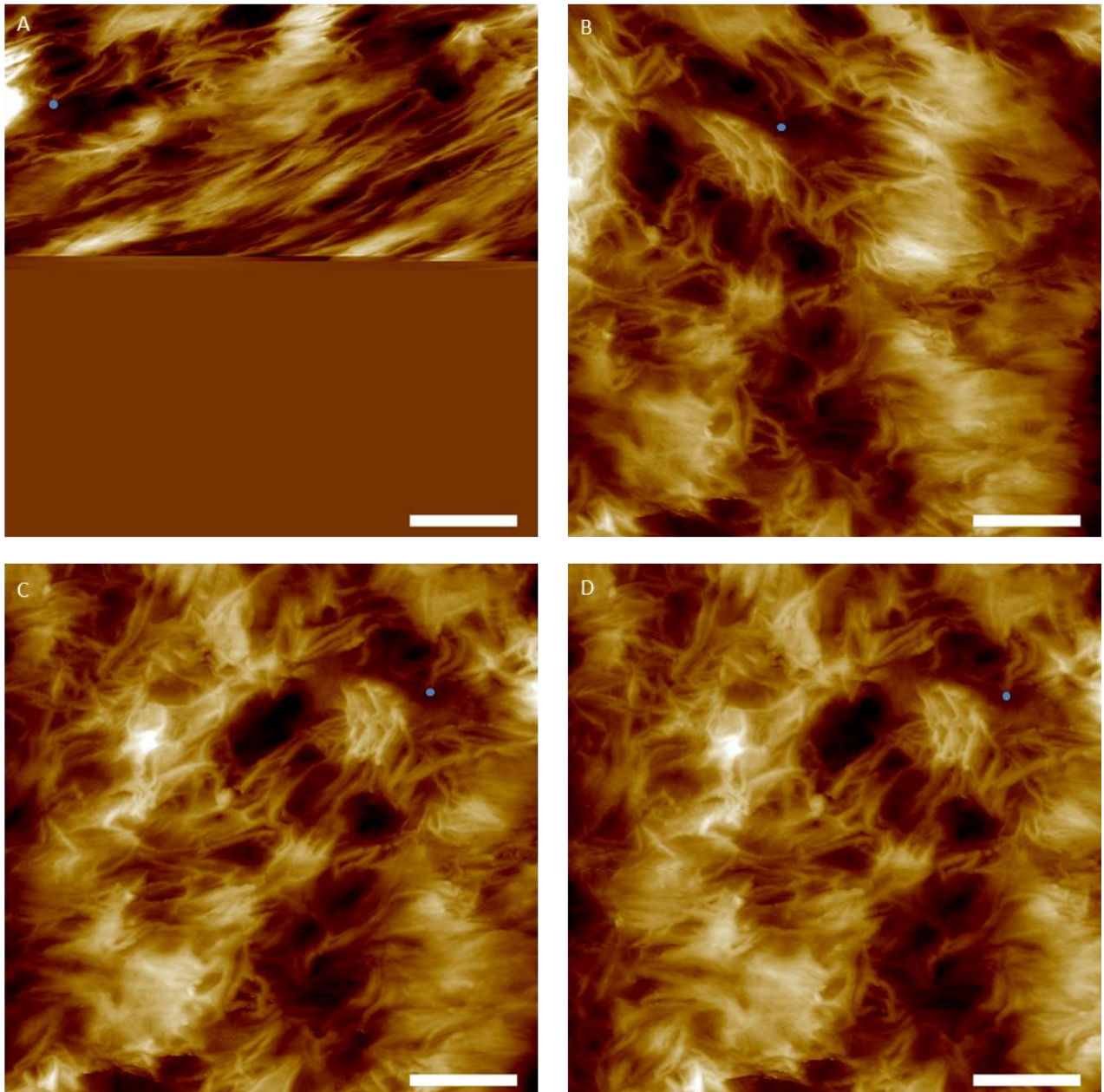
Figure 3.9 –Successive height images of the same area of polyethylene film after it has been left to settle. Scan direction is A up, B down, C up, D down. Blue dots mark the same location on each image to help guide the eye. Scale bars 1 μm. Z scales 250 nm.

The importance of this can be seen in that B would tell you a very different picture of the surface to D. This is especially important when comparing images of the same area at different strains.

3.2.5: Strain measurements

The measurement of strain is vital for this project. The strain for both polyethylene and polypropylene is highly heterogeneous, and so the value for strain for an area will vary drastically depending on the length scale selected. There are three different ways to measure strain used here.

The first measures the macro-scale strain; this measures the strain between the 'bone ends' of the neck of the film, over a length scale of approximately 1mm. This is calculated by measuring the initial size of the neck, and then recording the micrometer dial readings from the sides of the stretching rig to work out the strain; this assumes that all strain occurs in the neck, which appears to be true.

The second method is the optical strain, which measures the strain over length scales of approximately 100 μm. This uses the AFM optics to measure the breakup of the fiducial mark ink-dots on the polymer surface, as can be seen in figure 3.6. It involves features that appear in successive images and measuring how the distance between them changes; several different measurements were taken for each set and averaged. The investigated sample area is directly below the ink dots, and as it is in line with it should undergo similar strain.

The third method is the AFM strain, which measures the strain at length scales of approximately 10 μm. This uses the AFM images at larger scales (usually 10 μm), features within successive images are used, and the distance between features was measured. Once again several different measurements were taken for each set and averaged.

For both optical strain and AFM strain values can change significantly depending on which features are chosen as strain is highly localised, with different areas moving at different rates, features far apart in the images were generally used.

The agreement between the strain values for polyethylene was measured for two different sets of images as can be seen in figure 3.10. Overall the three different methods tend to agree with each other. For set 1, the AFM strain is larger than the optical, which is similar to the macro-scale, whereas for set 2 generally the macro is larger than the optical, which is larger than the AFM; thus showing no pattern in the ratios of strains. Within sets there can be significant differences in value of strain the different methods give, of over 50% in some cases.
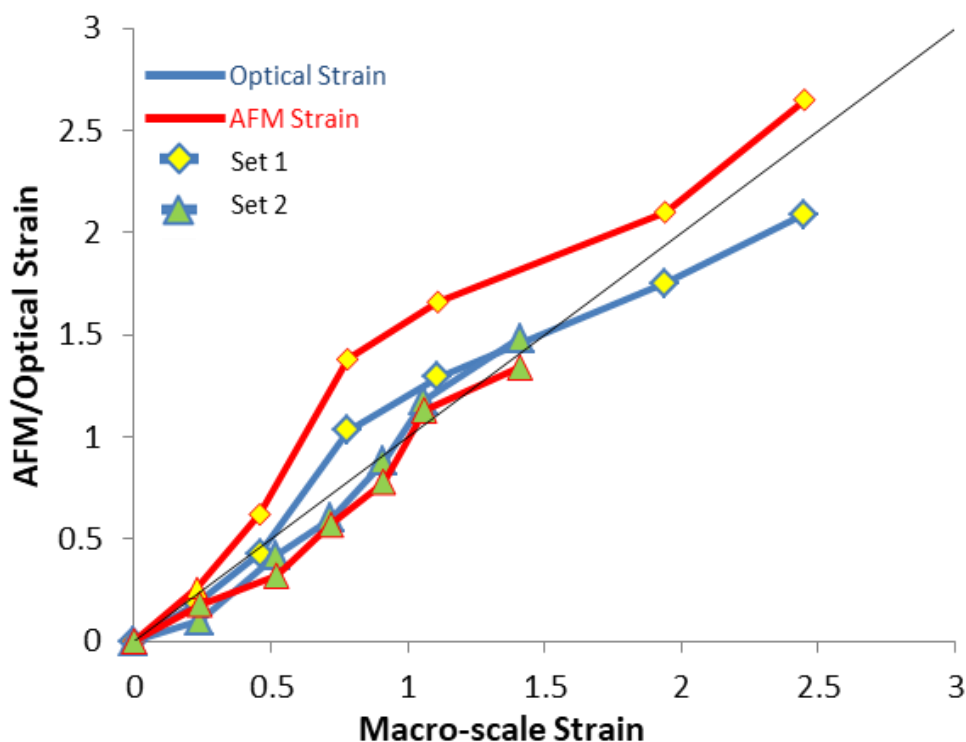
Figure 3.10 – Graph of AFM and optical strain vs. macro-scale strain for two different sets of images of polyethylene. The black line shows a 1:1 ratio.

For the polyethylene samples in chapters 4, optical strain is used to display their strain values. This was chosen because macro-scale strain does not reflect the local area well enough, the AFM strain on the other hand was considered too local and varies significantly depending on what features are chosen. In chapter 6, when a

crack is cut into the polyethylene film, AFM strain is used due to the higher localisation of the strain due to the crack.

For the polypropylene samples in chapter 5, a version of AFM strain is used due to the higher localisation of the strain there. This is explained in that chapter.

Chapter 4 – Stretching Polyethylene

4.1: Introduction

Polyethylene is the world's most widely produced synthetic plastic polymer [138], it is used in many different fields including packaging and construction, and thus understanding its mechanical properties is important.

Polyethylene is a semi-crystalline polymer, consisting of crystalline lamellae and amorphous regions. When subjected to a tensile strain, the polymer will undergo deformation and fracture. The macroscale properties of the system are dependent on the microscale properties of the system.

As previous discussed in Chapter 2 there have been a number of previous studies of the behaviour of polyethylene when stretched under tension. These include SAXS [139][140][72], which has been used to study the processes over time, however it only provides information on changes in structure averaged over the whole sample. Also imaging techniques including AFM [85][141][142] and EM [143] have been used; however they only provide snapshots rather than seeing how an area changes with increasing strain.

In this chapter the same area of a polyethylene film is imaged in successive images, this allows us to watch processes at the lamellae scale as they occur to better understand them. Such in-situ observations of polyethylene deformation have not been carried out previously. Polyethylene is the simplest and most well studied semi-crystalline polymer and so acts as a model system for other polymers.

4.2: Methods

The films used in this chapter were high density polyethylene (HDPE) which had a density of 0.97 g/cm^3, the films were measured to be 19 μm thick and were purchased as sandwich bags from Tesco. Gel permeation chromatography (GPC) was used to measure the molecular weight, with values of M_w = 142,000 and M_n =

13,900, giving a polydispersity of approximately 10. HDPE is highly ductile and so a large amount of both fracture and deformation is seen to occur.

As previously discussed in Chapter 3, strips were cut from the bag and mounted on a custom built stretch rack. The strips were approximately 20 mm wide. Dog-bone shapes were then formed used a hole-punch with an 8mm diameter, leaving a neck in the middle, approximately 5 mm wide, to ensure that strain occurred here. The experiment was performed in ambient conditions at approximately 20 °C, far above the glass transition.

The samples were first imaged unstretched, and then the same area was found again using two different fiducial marks, an ink dot and a scratch produced by the AFM tip. The sample was then imaged again and the process was repeated. Images were taken in TM and all scans which could form part of the sets were taken at 512 lines, and were scanned in the same direction, either up or down, to eliminate image differences due to scan direction and drift.

4.3: Small-angle X-ray Scattering results

Small-angle X-ray Scattering (SAXS) has been used in a number of previous studies on deformation of polyethylene; it is used here to corroborate the later results from AFM. It gives information averaged over the whole sample.

The experiment took place with the aid of Mike Weir, in the Soft Matter Analytical Laboratory (SMALL) using a liquid gallium MetalJet X-ray source, built by Xenocs. A monochromatic X-ray radiation (wavelength $\lambda = 0.134$ nm) and 2D detector (Dectris Pilatus 1M pixel detector) were used in this experiment.

A Q range of $0.045 - 0.287$ Å^{-1} was used, the sample – detector distance was set to 2425 mm, and the detector was calibrated with silver behenate. X-ray

scattering patterns were collected with a beam size of 1 × 1 mm and an acquisition time of 120 seconds. For each strain value 2 offset measurements were taken and line eraser used to reduce the masked areas, by splicing images together.

Data was corrected for the detector's dark current, spatial distortion, and flat field, normalized using sample thickness, exposure time, sample transmission, and the detector normalization coefficient, and integrated using software package Foxtrot. The stretch rig used for AFM images was also used here, the strain values quoted for SAXS are macro-scale strain, from the dials.

The SAXS pattern observed for unstretched polyethylene can be seen in figure 4.1. It has vertical lobes indicating that the lamellae are generally aligned perpendicular to the stretch direction, and what will be vertically in the AFM images. Using linear correlation analysis it was found a lamellar long period of 25 nm, linear stack crystallinity of 85 %, interlamellar distance of 4 nm, and lamellar thickness of 20 nm.

A set of results was taken as the same film was stretched, which can be seen in figure 4.1. First measurements were taken on unstretched polyethylene, then the sample was stretched and measurements taken again, the process was repeated. After 8 measurements the signal dropped dramatically, which was assumed to be due to the beam no longer falling on the neck, these measurements are not shown.

At the start there are large vertical lobes, indicating, fairly well ordered lamellae perpendicular to the stretch direction. With increasing strain the lobes shrink and move inward, indicating less alignment and an increasing lamellae separation. There is also an increase close to the beam centre, due to larger scale features, possible voids and crazes. By the 5th the distribution is now isometric indicating a loss of the original alignment. The distribution then starts to grow horizontally, indicating increasing alignment with the stretch direction.
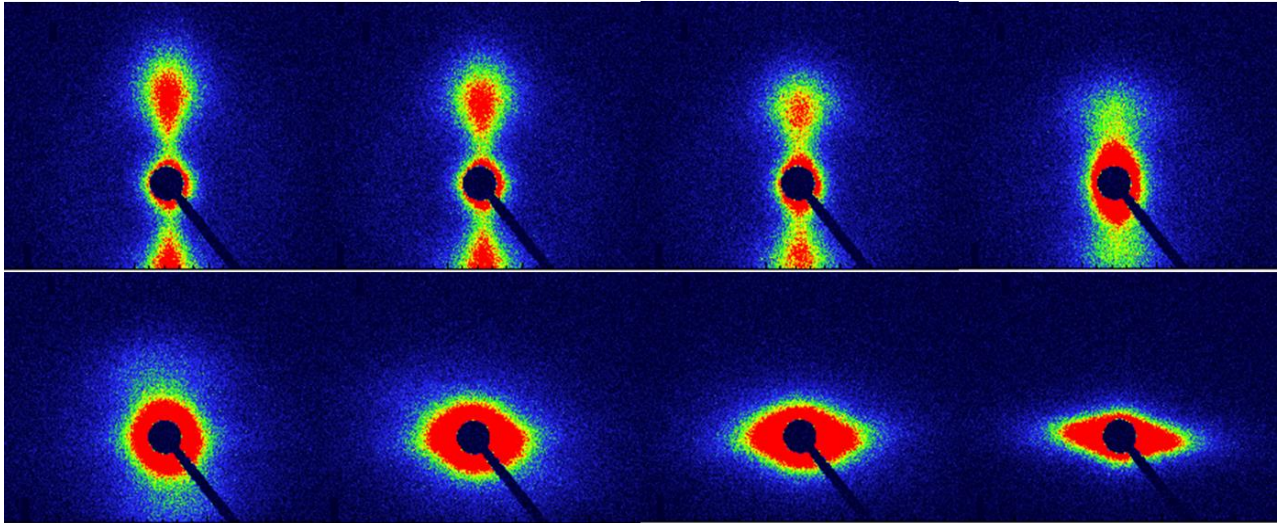
Figure 4.1 - SAXS pattern for polyethylene at a range of strains: Strains, top row: 0%, 22%, 41%, 56%. Bottom row: 75%, 94%, 113%, and 138 %.

In order to extract more information a radial integral was taken, leading to the graph in figure 4.2. In this the data underwent Lorentz correction, whereby the measured intensity is multiplied by Q^2 to account for the fact that scattering is a 2D representation of a 3D system, whereas the lamellae are only ordered in 1D. The line labelled 163% is assumed to be due to the neck falling out of the beam and so shows the background.

In the centre of the graph is the main peak which is attributed to scattering due to lamellae. At the start this peak is at its largest, by 22% it remains approximately as large but has shifted to slightly lower Q. After this the peak begins to decrease in size whilst moving to slightly lower Q, until by 94% it appears to be gone. The change in Q and thus lamellae separation is seen in table 4.1.
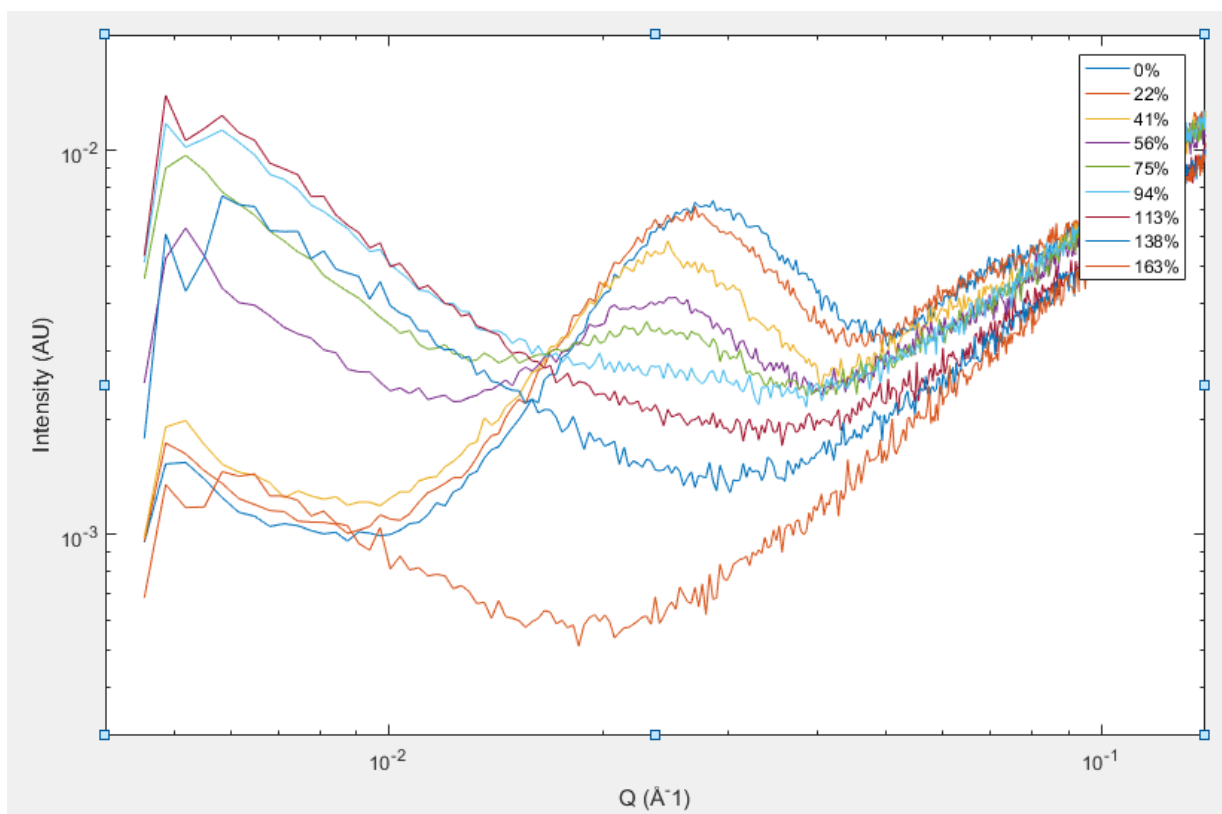
Figure 4.2 – Radial integral plot of Corrected Intensity vs. Q for the SAXS patterns shown in figure 4.1. 163% is assumed to be when the neck was not in the beam and thus gives a background.

Strain (%)	Peak Q ($Å^{-1}$)	Lamellae Separation (nm)
0	0.028	23
22	0.027	24
41	0.025	25
56	0.024	26
74	0.023	27

Table 4.1 – Table of peak position, and lamellae separation vs. strain. Values extracted from figure 4.2.

Meanwhile there are significantly changes seen at lower Q at the start of the graph, the peak here corresponds to approximately 130 nm, and as such the change is likely due to void and craze formation.

From 0 - 41% this stayed relatively constant, after this it rises significantly then stays roughly constant. At 138% it falls again, perhaps due a smaller amount of material leading to lower scattering, or to healing of voids.

The behaviour seen here generally matches what is seen in the AFM data below, where the lamellae are generally initially aligned vertically, as they are stretched there is a long period increase and there is a kinking and rotation of lamellae leading to less alignment and thus weaker scattering. Later on there is alignment of features with the stretch direction.

4.4: Initial PE structure and how it compares to SAXS

The initial structure of the polyethylene film can be seen in figures 4.3 and 4.4. It consists of crystalline lamellae and small amorphous regions between them, also present are some nanovoids. In the AFM images the lamellae appear as bright lines and the amorphous regions as thin dark areas between them.
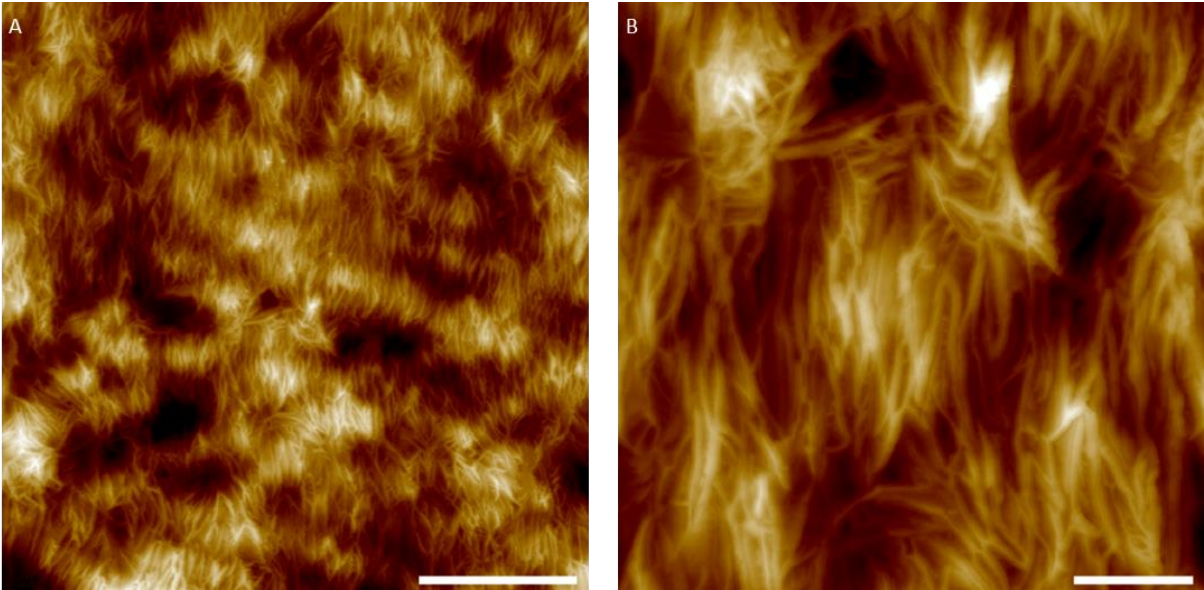
Figure 4.3 - Height images of undeformed polyethylene. B is zoomed in from the centre of the A. At the centre top of A the end of the fiducial mark is present. Scale bar 1.5 μm (A), 500 nm (B). Z scale 280 nm (A), 180 nm (B).
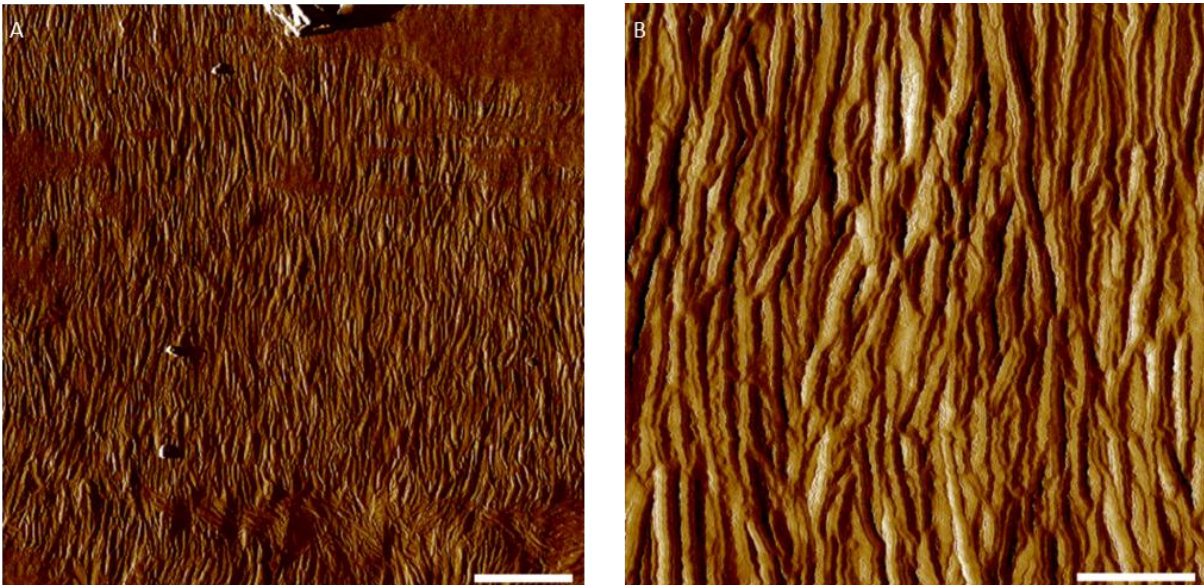
Figure 4.4 - Amplitude images of a different sample of undeformed polyethylene. B zoomed in from A; this is less obvious than in figure 4.3 as there is a lack of clear distinguishing features. This sample is much more uniform than figure 4.3, with lamellae which are more uniformly vertically aligned. In B the lamellae appear more kinked due to noise. Once again there is the end of a fiducial mark at the top centre of the right image. Scale bar 1.2 m (A), 300nm (B). Z scale 830 mV (A), 200 mV (B).

Here the lamellae are largely edge on and thus appear as sharp lines, whereas in some cases, as seen in the top half of figure 4.5, the lamellae are more flat on and they are thus less distinct and will have a larger apparent spacing. Measurements

were taken on several different images using ImageJ software and the measure tool, the values were then averaged. The lamellae were found to have: a long period of 30 nm, inter-lamella spacing of 5 nm and average lamella thickness of 25 nm, with errors of approximately 2 nm, this generally agrees with values measured from SAXS though they is some difference. The images and the values are generally in agreement with previous studies [22].

Initially the lamellae are generally aligned perpendicular to the stretch direction, though with some deviation. In some small regions they start aligned to the stretch direction, this is explored later. They are generally μms in length, and most of them are linear but a large minority are branched. At this stage there is no fragmentation of lamella, nanovoiding or fibrillation present and they are largely straight.

Present in some images are pieces of material which is not PE, these are contamination spots, generally of dust or unknown material. These spots are sometimes much taller than surrounding features in the film and so are generally avoided. Also they do not deform along with the film so they make good fiducial markers in image sets. Very occasionally a new contamination spot with appear in the middle of a set of images due to new contamination.

4.5: Sets of images of polyethylene during film deformation

4.5.1: Early deformation processes

The unique aspect of this work is in the ability to follow the processes of deformation and fracture as they occur. Previous work has imaged semi-crystalline polymer films at different strains; however these were snapshots with images in completely different areas to each other. It is important to take sets of images in the same place in order to gain a better understanding of the processes at work. In all of these images stretch occurs horizontally.

The early sets investigated the deformation and fracture of the films at moderate strains, up to approximately 100%. At higher strains the fiducial mark was too deformed to find the same area again.
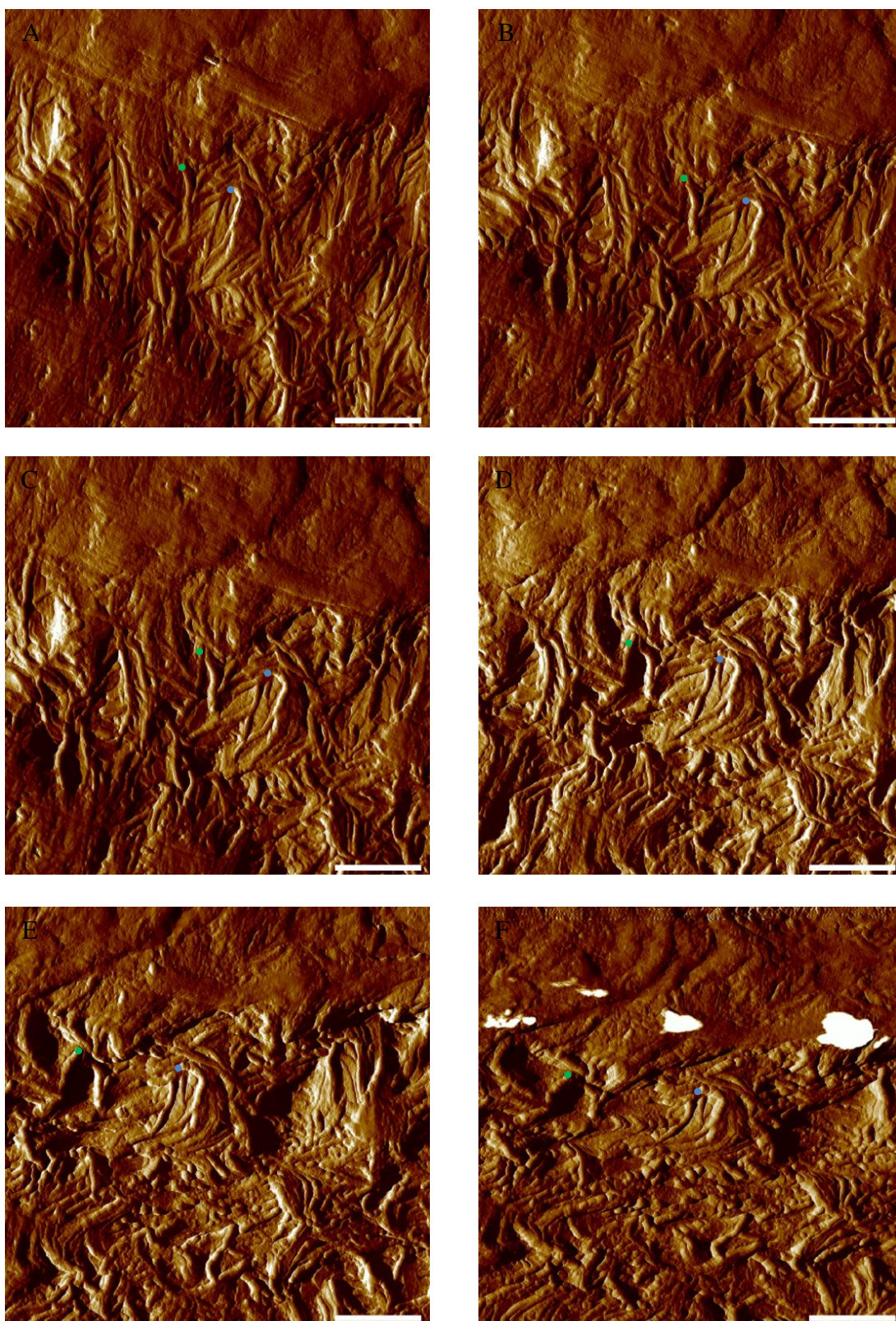
Figure 4.5 - Series amplitude images of PE being stretched. Stretch is in the horizontal direction. With increasing strains from 0%, 13%, 20%, 41%, 60%, 98%. White contamination dots appear on the last image. Large black areas are poor tracking. Scale bars 500 nm. Z scales, 330, 310, 310, 270, 270, 270 mV. Blue and green dots mark the same location on each image to help guide the eye.
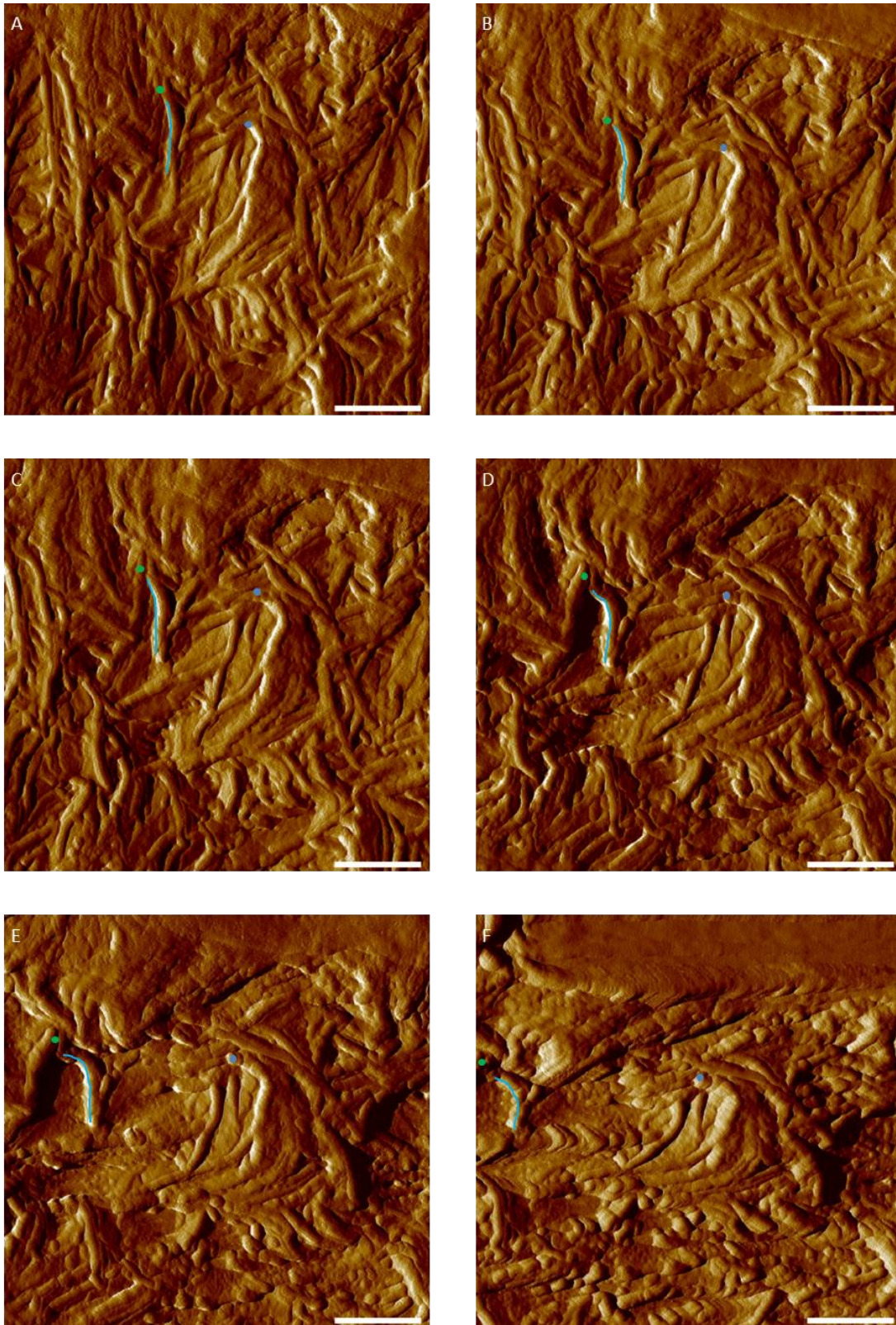
Figure 4.6 - Series of amplitude images of PE being stretched. Stretch is in the horizontal direction. With increasing strains from 0%, 13%, 20%, 41%, 60%, 98%. The top right area which appears is due to flat on lamellae. Scale bars 300nm. Z scales 230, 220, 240, 240, 240, 190 mV. This is the smaller scale corresponding series to figure 4.5, blue and green dots in same place as in figure 4.5. One of the lamellae is marked in blue to aid the eye.

Figures 4.5 and 4.6 are sets of images of the same place on the sample with increasing strain. Those in figure 4.6 are smaller scale images taken zoomed in on the centre of figure 4.5 and thus show more detail.

When subjected to a small uniaxial tensile strain the deformation processes begin. There is the beginning of separation of lamellae due to elongation of amorphous tie chains, increasing the long period. The tie chains are too small to see here.

Also the lamellae start to undergo rotation to align with the stretch direction, which is horizontal in these images; for example, the lamellae which start to the right of the blue dot and end above it. Lamellae largely align with their neighbours, rotating in stacks. In some cases neighbouring lamella go opposite ways, these cases are important as they form nanovoids which will often lead to crazes, an example is at the green dot, where the craze forms below. Lamellae already aligned with the stretch direction largely stay in place before being seen to slip against their neighbours.

As the sample is stretched more these processes continue. The lamellae separation continues to increase. The rotation continues, with lamellae often buckling to form chevron as can be seen from the marked lamellae. Increased nanovoiding is seen and fibrillation begins, with the opening of small crazes 100s of nm in size, perpendicular to the stretch direction, which open between lamellae. An example is seen below the green dot from D onwards, some poor tracking of the surface means some of this craze is black, making it harder to see. The crazes are of roughly ellipsoidal shape though their shape can deviate significantly depending on the neighbouring geometry. Over time crazes are seen to open significantly but undergo very little propagation; also crazes are not seen to coalesce with neighbouring crazes. Many examples of crazes can be seen in figure 4.7.

Fine chain slip is seen from the tilting of lamellae, direct observation of thinning of lamellae is not seen, but it would be hard to see in these images. At the last stages there is the beginning of coarse chain slip causing the lamellae to breakup into blocky elements, which can be seen in many places in the lower half of F in figure 4.6.

These phenomena agree with macroscale observations, including Poisson contraction where the total volume of the film increases whilst there is a contraction perpendicular to the stretch direction. In optical images, stress whitening is seen, which is caused by optical scattering of light by the crazes and nanovoids produced in the film, this gets more prevalent at higher strains.

4.5.2: Regions where lamellae are initially aligned with the stretch direction

The lamellae in these sample are generally initially aligned vertically, perpendicular to the stretch direction, however this will often not be the case and it is important to understand how deformation proceeds if they are aligned with the stretch direction. Regions where this is the case were seen, one such region was imaged in a set as shown in the top half of figure 4.7, which is shown digitally zoomed in in figure 4.8.

When lamellae are aligned with the stretch direction a lot of the processes previously seen are not applicable. Rotation and tilting do not occur significantly as the lamellae are already aligned. Lamellae separation does not increase as the strain is not acting to pull neighbouring lamellae apart. There is limited space for nanovoids and crazes to form. Neighbouring lamellae slipping against each other is the main source of deformation, there is also some thinning of lamellae seen. Later they exhibit coarse chain slip and start to break up into blocky elements.
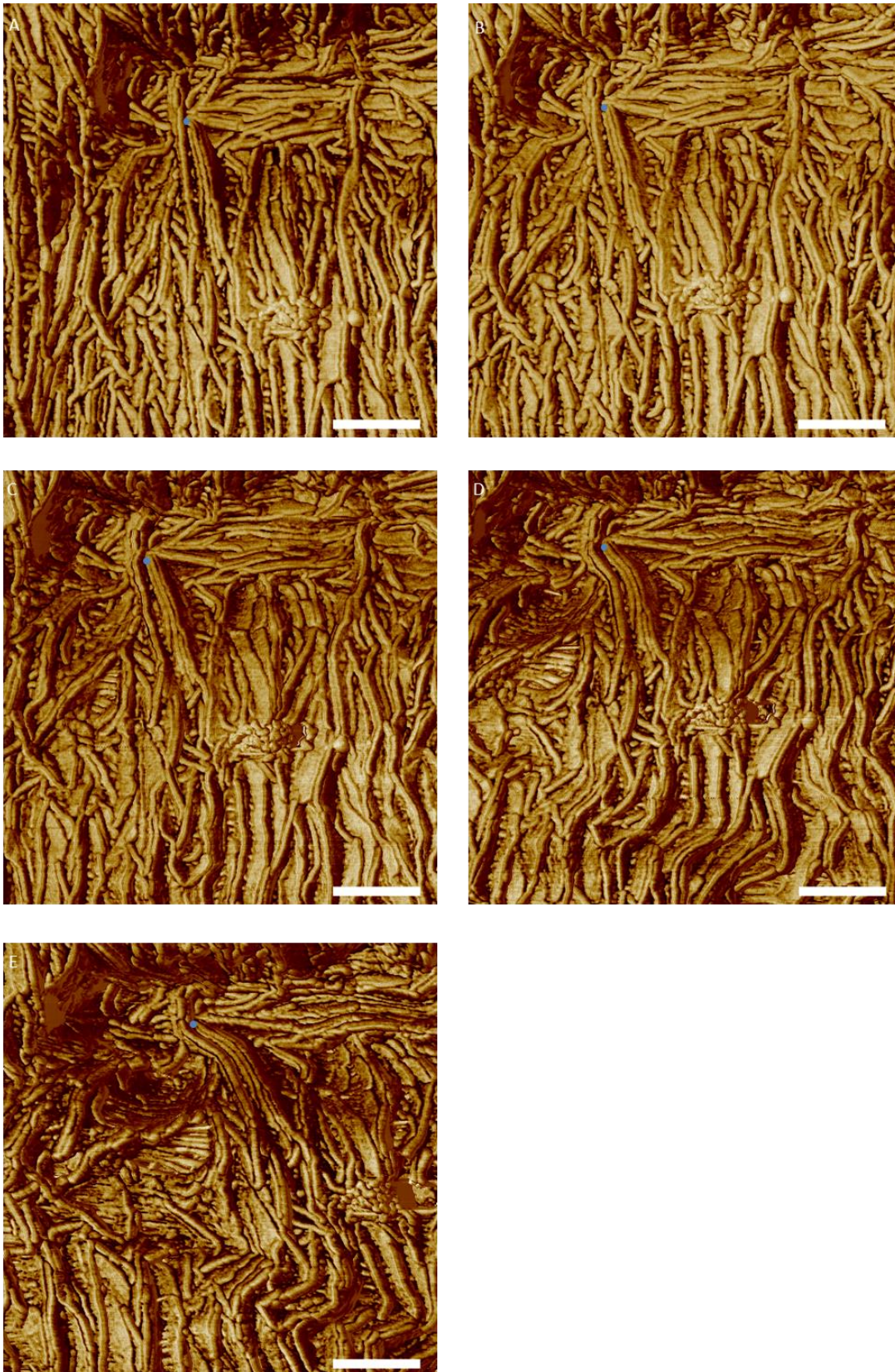
Figure 4.7 - Phase image series of PE images at strains of 0%, 5%, 13%, 22%, 50%. Contains a region at the centre top where the lamellae are aligned with the stretch direction. Scale bars 300 nm. Z scales 72, 72, 63, 62, 62 °.
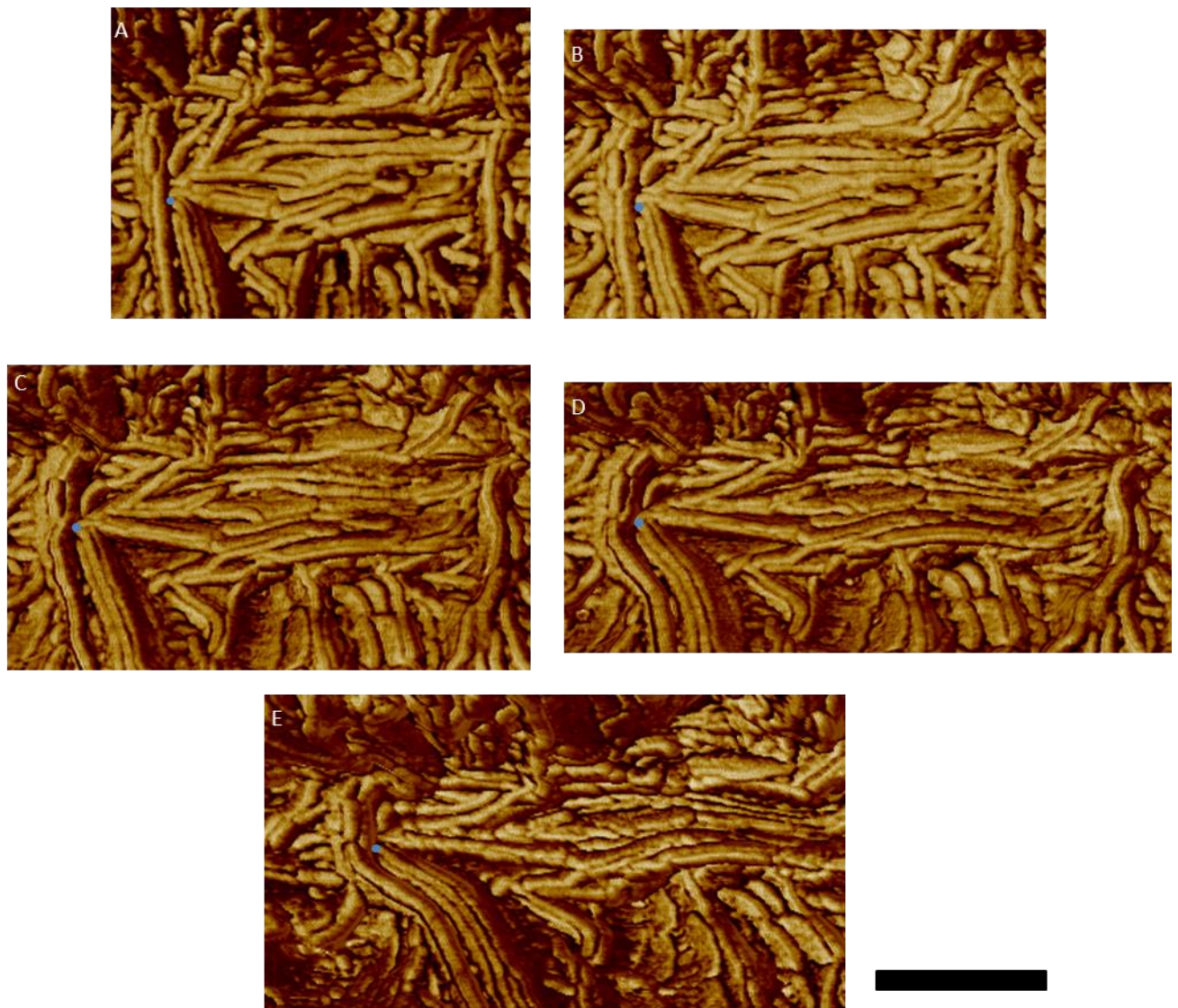
Figure 4.8 – Zoom in on the area towards the top of figure 4.7, showing region with horizontal lamellae. Blue dots in same place as figure 4.7. Phase image series of PE images at strains of 0%, 5%, 13%, 22%, 50%. Scale bars 300 nm. Z scales 72, 72, 63, 62, 62 °.

4.4.3: Late stage processes

The early sets taken only went up to strains of approximately 100%. It is interesting to investigate the late stage behaviour, as it has many differences to early behaviour.

The main difficulty in images at higher strains was the loss of the fiducial mark. As the film is deformed so too is the fiducial mark, and at high strains it

becomes very hard to recognise and find, with it now looking similar to other features present. To solve this, another fiducial mark was used. This was added partway through the series, at approximately 80%. This was once again made by imaging at low setpoint with an AFM tip; it was drawn after imaging the area as part of the larger set, using the same tip. The mark was another 5 µm diagonal line; and it was made away from the imaging area pointing towards the first fiducial mark. The AFM tip was once again changed for a new tip afterwards.

Another difficulty was in the film snapping before higher strains could be reached, which may be due to higher strains occurring elsewhere in the neck, outside the imaging area. It was also observed that often when the strain is high, the area seen in the optical image may undergo very little strain whilst the macroscale strain, set by the dials, increases a lot. It will then increase significantly for a small increase in macroscale strain, often undergoing heavy creep leading to snapping. This is due to strain hardening and necking, where the materials is now harder locally as the lamellae are more aligned with the stretch direction and so it is easy to stretch different material elsewhere.

A narrower neck was used to help concentrate the stress, so that the greatest strain in the film is more likely to occur in the imaged region. Also greater care was taken when stretching samples, with the rate slowed and close attention paid to the optical image for any sign of movement. These approaches were found to be very effective.

Creep is a greater issue at higher strains, firstly that the sample needs to be left longer for the creep to reduce to an acceptable level for imaging, and secondly that the strain can change significantly if left overnight.

Figures 4.9 and 4.10 show two different sets of images, these show all the processes described before occurring. At higher strains rotation continues, though there are still some areas with little deformation. Coarse chain slip occurs and the

lamellae begin to break up into small blocky elements, this is more prevalent in those aligned with the stretch direction. Crazes continue to grow so that an increasing proportion of the surface is now fibrillated, with them now occupying over 50% of the surface. Some new crazes are seen to form late on, long after initial crazes, rather than the crazes all forming at once. An example is in figure 4.9, where the craze below the blue dot has opened by C, but the crazes below the green dot doesn't open until D.
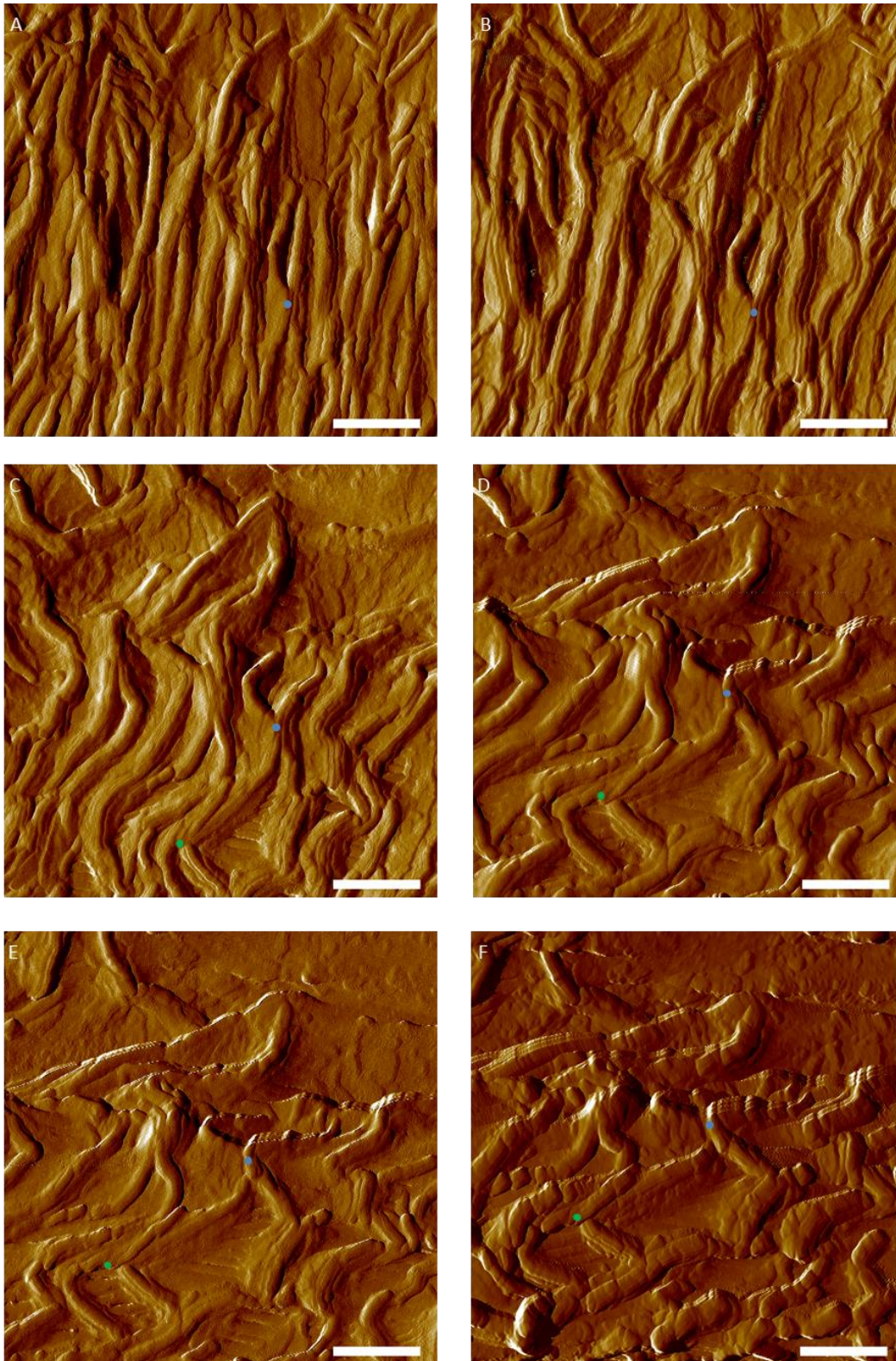
Figure 4.9 - Series of amplitude images of PE being stretched. With increasing strains from 0% 19%, 43%, 103%, 129%, 175% and 209%. The last image in this series has a scratch in the lower left corner which was caused by the AFM tip contacting the surface after a loss of air to the air table. This was judged to not affect the majority of the image and so is still presented. Scale bars 300 nm. Z scales 310, 350, 360, 370, 400, 370 mV.

65
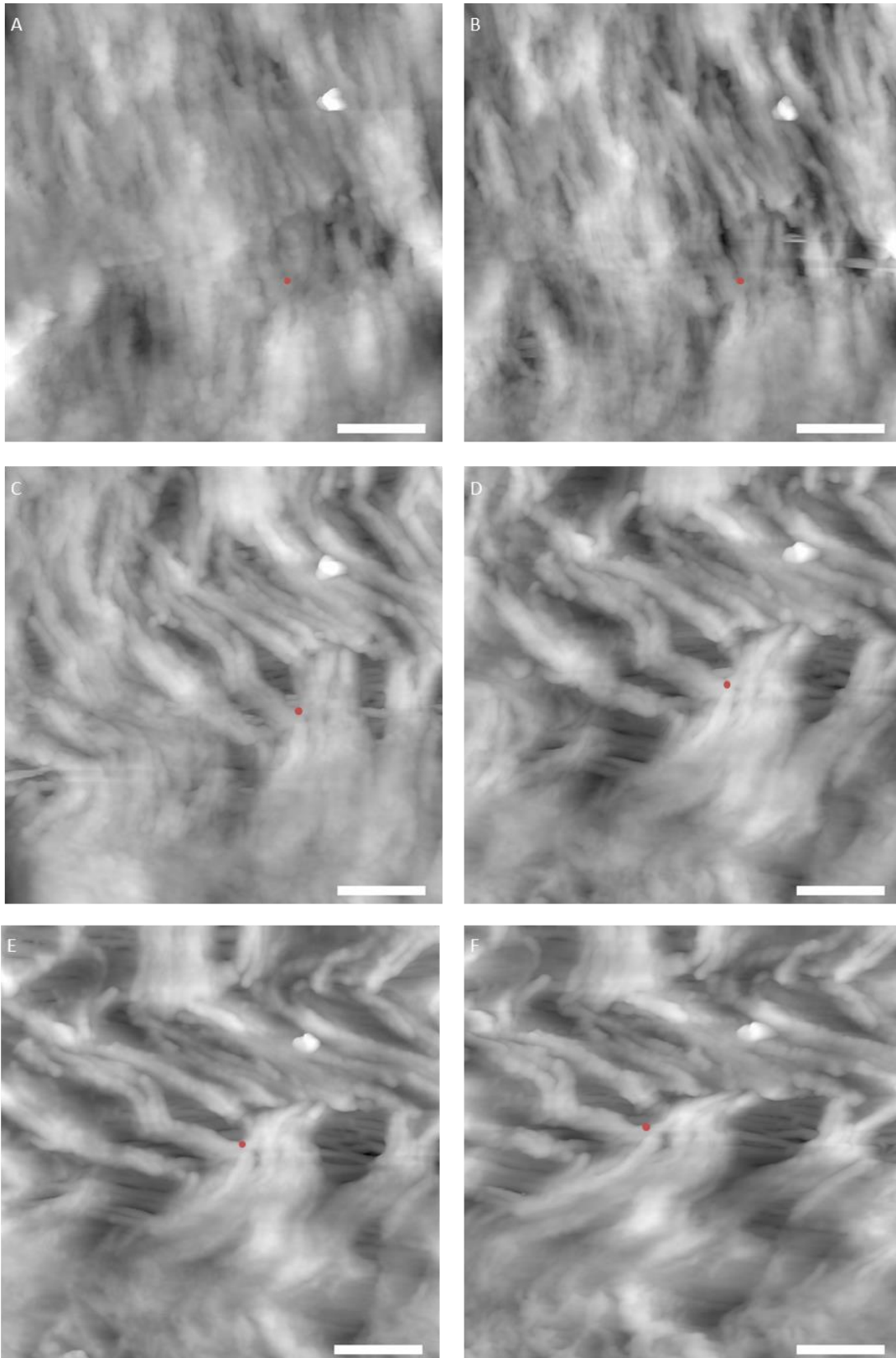
Figure 4.10 –A different series of height images of PE being stretched. Grey scale used to make the crazes easier to see. Increasing strains from 0%, 10%, 42%, 88%, 118% and 148%. The white spot present in all images is a contamination spot, it is useful here as it acts as a fiducial mark. Scale bars 300 nm. Z ranges 81, 76, 108, 116, 112 and 116 nm.

4.5.4: Partial sets

In an effort to better focus on the late stages, partial sets were taken, starting at higher strains. This was done as full sets were very time consuming, and it was possible for a lot of time to be put into a set only for it to fail near the end.

At higher strains creep is now noticeable even after samples are left for a significant time and must be accepted in images. The effect of drift is also important in the need to offset images to image the same area. The impact of this can be seen in figure 4.11. This is the set that appears to reach the furthest stages of deformation.
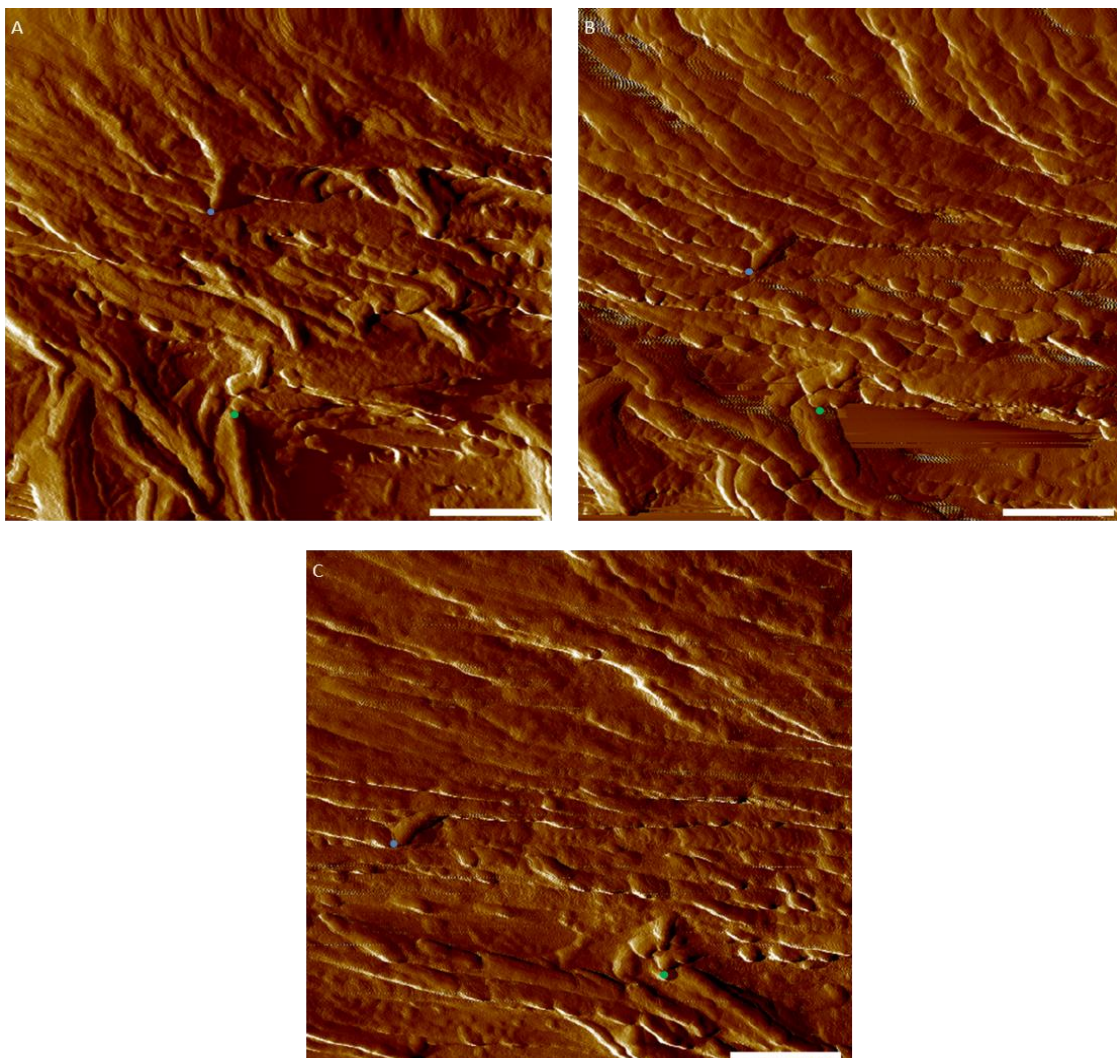
Figure 4.11 – A small series of images of polyethylene being stretched. Starting at high strain, with strains of 58 %, 75%, 91%, based on bone-end strain. There is large scale shear seen, with top of C being areas not seen in A.

The sample is now very stretched and is in a highly fibrillated state with the fibrils taking up the majority of the sample. Lamellae are now well aligned with the stretch direction, and significant breakup into block elements is seen. At this stage there is large scale shear seen with areas that were previously neighbours vertically moving a long way from each other. This can be seen with C sharing lots of area in its bottom half with A, but sharing no area in its top half.

4.4.5: Extremely stretched polyethylene images

The film usually snapped before the final stages of deformation and fracture were reached. This may be due to the imaged region not being the most stretched, with a neighbouring region undergoing a much higher local strain and then snapping. Alternately there may have been flaws in the films that led to them snapping prematurely. On one occasion the film was found to enter a highly stretched state, with a small neck of approximately 40 μm wide without snapping. The neck was seen to possess a rippled structure at the edge which likely aided it in not snapping, the structure in the rippled area was similar though less stretched.
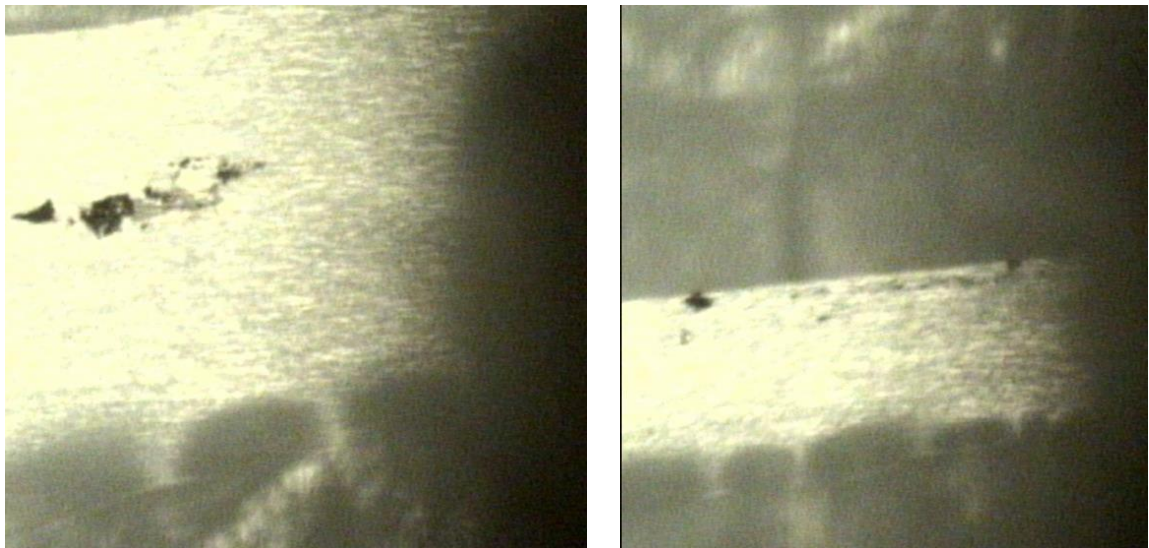
Figure 4.12 – Optical images of the neck of polyethylene film during an experiment. Right is the sample as seen in figure 4.13. Left is the sample during the previous image in the set before it was stretched. Both images show the rippled structure on the lower side of the neck, this was only seen here and may be what allowed the film to reach such high strain without snapping. The Ink dot seen on the right has completely broken up, and possibly

fallen off the film, with only small pieces remaining. This made finding the same area to continue the set impossible.

In this state, the film was seen to continually undergo creep; which was still significant after leaving the sample for 1 hour, and continued until it snapped overnight. This creep has the effect of slanting the image shown here slightly. To help mitigate this all were taken in the downwards scan direction, allowing the overall structure is still seen. The creep also adds a small wobble to the images.

At this level of strain the imaging area is unrecognisable from previous images, as are the fiducial marks, and so this does not form a set with the images taken before.
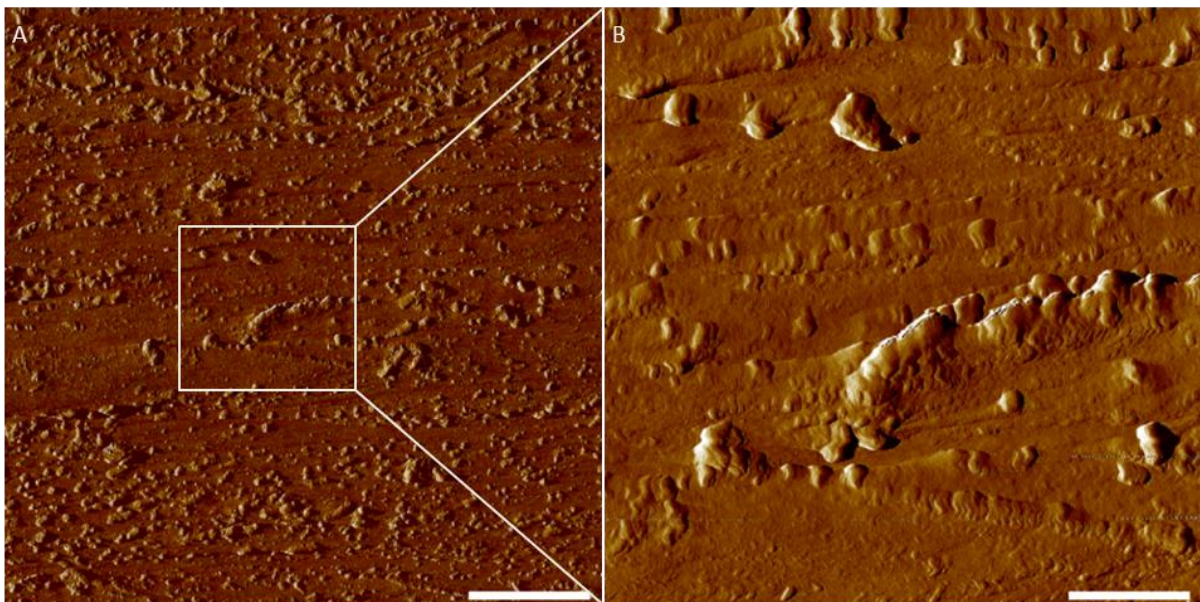
Figure 4.13 – Amplitude image of polyethylene in a highly stretched state. The film is in a highly fibrillated state, with the lamellae nearly entirely broken up into blocky elements. Scale bars 1 µm (left), 300 nm (right). Z values 520 and 220 mV.

The structure can be seen in figure 4.13. Here the polymer reaches an extremely fibrillated state, with over 90% of the surface covered by fibrils. The former lamellae are now all aligned with the stretch direction and their breakup into small blocky elements is nearly total, with a few holdouts such as the central lamella showing signs of the original structure. The blocky elements are approximately 30 nm which corresponds to the initial lamella thickness, though there is a range of

larger and smaller elements. The fibrils have an average thickness of 20 nm and spacing of 40 nm, they are completely aligned with the stretch direction, and linear, with no cross fibrils seen.

4.6: Relaxation set

When a material undergoes strain there are two types of deformation, elastic and plastic. After being stretched then released; in a solely elastic deformation process the material will return to its original position, whereas in a solely plastic deformation the material will remain in its new position.

In order to test the degree of plasticity a small series of images were taken. First the sample was imaged unstretched, and then it was stretched and imaged. Finally the sample was let go by the gripping plates and allowed to relax for approximately 1 hour before being reattached and imaged again. The three images are seen in figure 4.14.
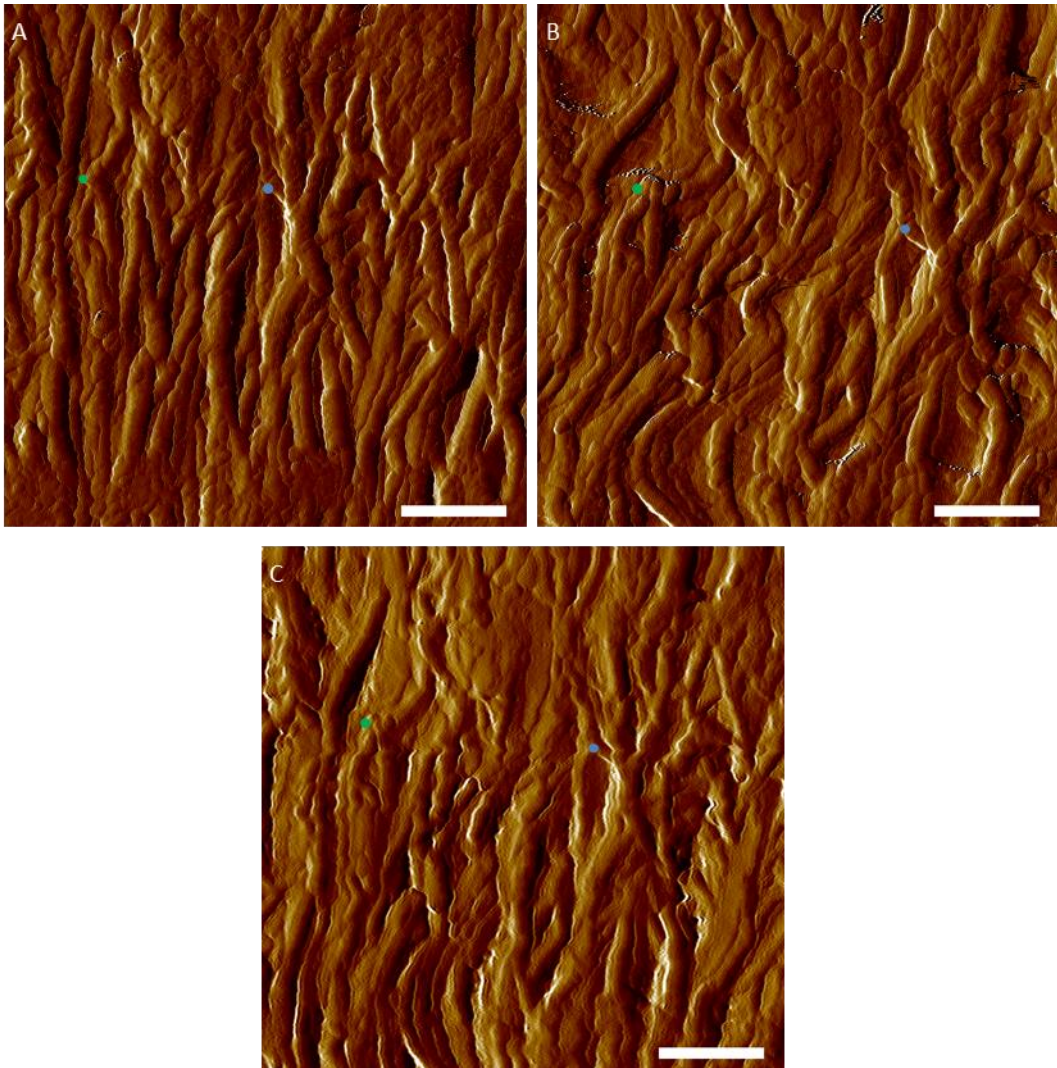
Figure 4.14 – Amplitude images of relaxation set. The images are, unstretched A, 46% strain B, and relaxed with 26% strain C. In the final image the sample has relaxed and so its features and strain are partway between the two previous images. Scale bars 300 nm. Z scales 270, 300 and 650 mV.

A modest strain is exerted between A and B, this produces various deformation processes that have been described earlier. There is separation of lamellae due to elongation of amorphous tie chains, tilting and rotation of lamellae due to fine crystal slip, which leads buckling to form chevrons. Also seen is nanovoiding and some small scale crazing.

Between B and C the sample is allowed to relax, allowing most of the elastic deformation to be undone. The strain of the image reduces roughly half of the stretched value, and the features can be seen to be between the stretched and

unstretched, approximately halfway between the two. The spacing between lamellae is reduced with tie chains appearing to retract elastically. Also the rotation and buckling of lamellae is reduced, and nanovoid width is decreased. The fact that these processes are partly reversed indicates that both plastic and elastic deformations are occurring. In the small number of cases where crazing occurs the fibrils remain, but the crazes contract significantly. Throughout the image there is an apparent wobble, caused by contraction pushing features together.

4.7: Fitting images with a mesh of points

4.7.1: Main sets

To understand what is going on better it is useful to extract more information from these image sets. To do this a mesh of points was fitted to each image allowing the movement of lamellae throughout successive stretches to be followed and mapped. An example of this can be seen in figure 4.15.
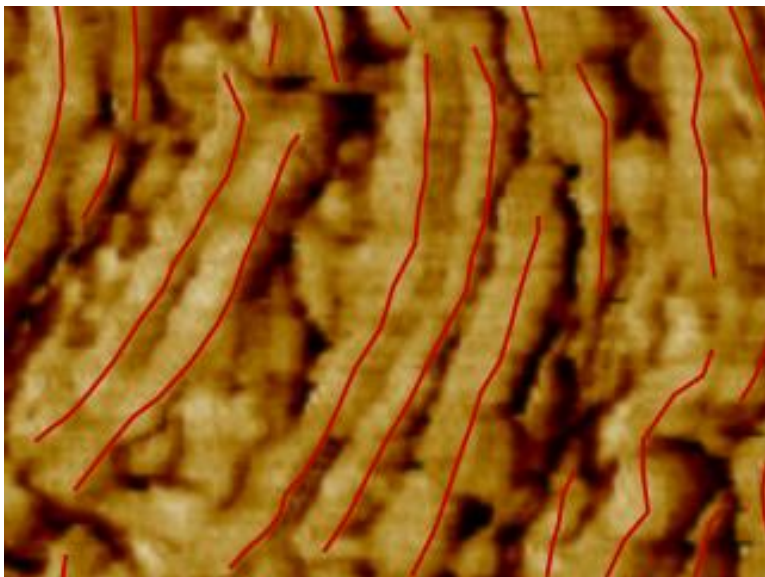
Figure 4.15 – A zoomed in section of an Inkscape file showing lamellae marked as paths in red on top of a height image from one of the sets.

The series of images were uploaded into an Inkscape file. For the first image the positions of the lamellae were marked manually as paths, each path composed of multiple points represents a single lamellae, and these positions were extracted with a custom extension. The first image was swapped with the next in the set, and the paths were adjusted to match the new image and the positions extracted again. This procedure was repeated for all images in the set.

Some lamellae did not appear in later images due to them moving off the sides of the imaging area due to stretch. These were moved out of the way and not measured. This had the effect of making the number of paths and thus points smaller over time, in order to compare the points from an image with the points of an earlier image it was necessary to go back and remove any paths they did not have in common and extract a different set of points.

This fitting procedure was only used on the 1.5 μm images. There were two major problems to fitting larger images. Firstly fitting points to images is time consuming, and this problem is much worse for larger images as it scales with area. Second is the problem of resolution, each image was taken with 512 scan lines, and so for a 1.5 μm image each pixel is 2.93 nm. For larger images they are: 2.5 μm - 4.88 nm; 5 μm - 9.77nm, and 10 μm - 19.53 nm.

As previously stated, when the sample is unreformed the lamellae width is 30 nm and the inter-lamellae spacing is 5 nm, thus for larger images the resolution is not good enough to properly resolve these details.

In this project we focus primarily on lamellae scale processes, rather than those at higher length scales and so information was only collected for the smaller images.

Methods to automate this procedure would have been useful in speeding up the process. A number were investigated including DIC module for Matlab, but were found to not work as successive images were not similar enough to each other due to

the nature of AFM images. This is a problem that likely could have been fixed but was judged to be not worth the time investment needed.

The data for point position was exported to Matlab, the points were converted from pixels to nm, and the y values were inverted to undo a quirk of the Inkscape extension. The point movement between successive images was then calculated. Two different methods for displaying this information were used:
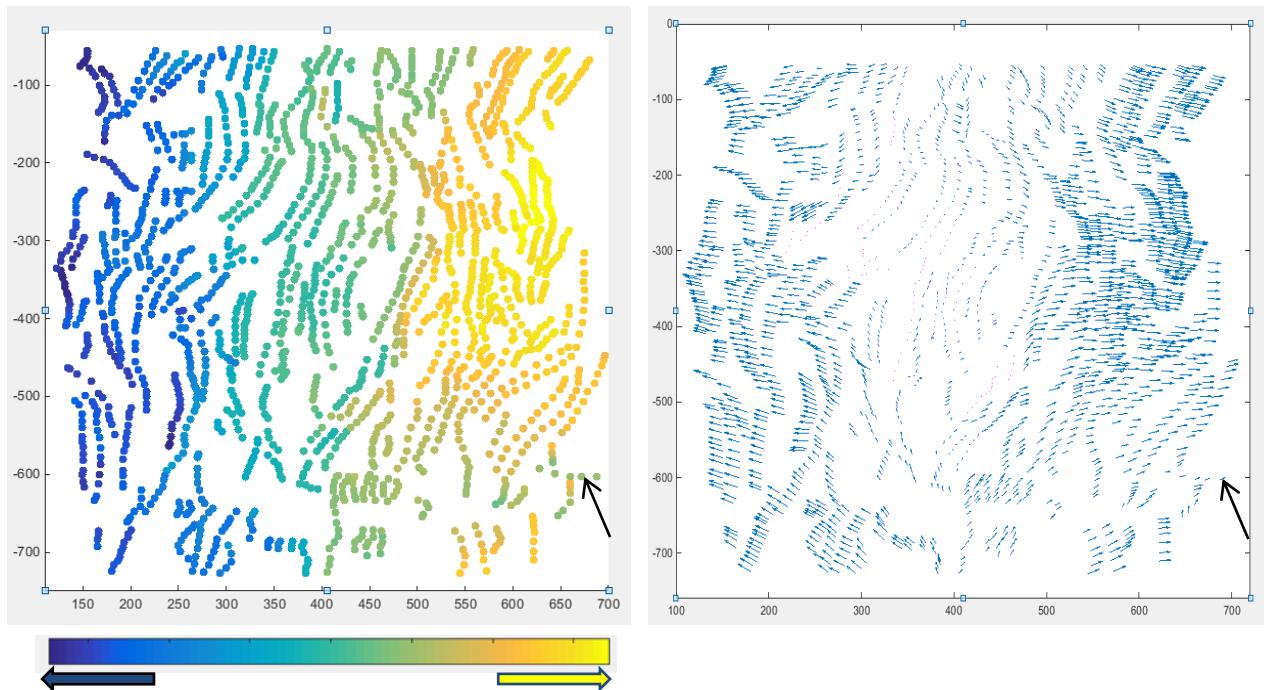
Figure 4.16 – Movement of lamellae between two successive images in a set. Both images show the same data plotted in different ways. (Left) plotted with the scatter function where the colour of a point shows how far it has moved in x. (Right) plotted with quiver where lamellae movement is displayed as arrows. The general behaviour is clearly seen with the lamellae expanding in x and contracting slightly in y. Also seen is some small scale movement often due to craze opening such as the horizontal line in the lower right which does not follow its neighbours, which is marked with a black arrow.

Scatter() which displays the points as small circles with their colour indicating how far they have moved in either x or y. Yellow for right/up and blue for left/down. It can be set up to display x movement as colour and y as size but this looks terrible and is hard to follow, and so was not used. The movement in x is most useful as there is more significant movement occurring. An example is shown on the left in figure

4.16. The base image for the circles' positions is the first image rather than the second.

Quiver() which has arrows which display the movement of points on the lamellae in successive images in both x and y, with the size of arrow showing how much each point has moved. An example is shown on the right in figure 4.16. The scale of arrows is chosen to be clearest, such that there are no overlapping arrows, rather than the true lamellae movement which may be difficult to see clearly. The arrows were later overlaid on the images in order to see movement better.

The two methods have different strengths, with scatter best for seeing large scale movements and quiver best for small scale deviations.
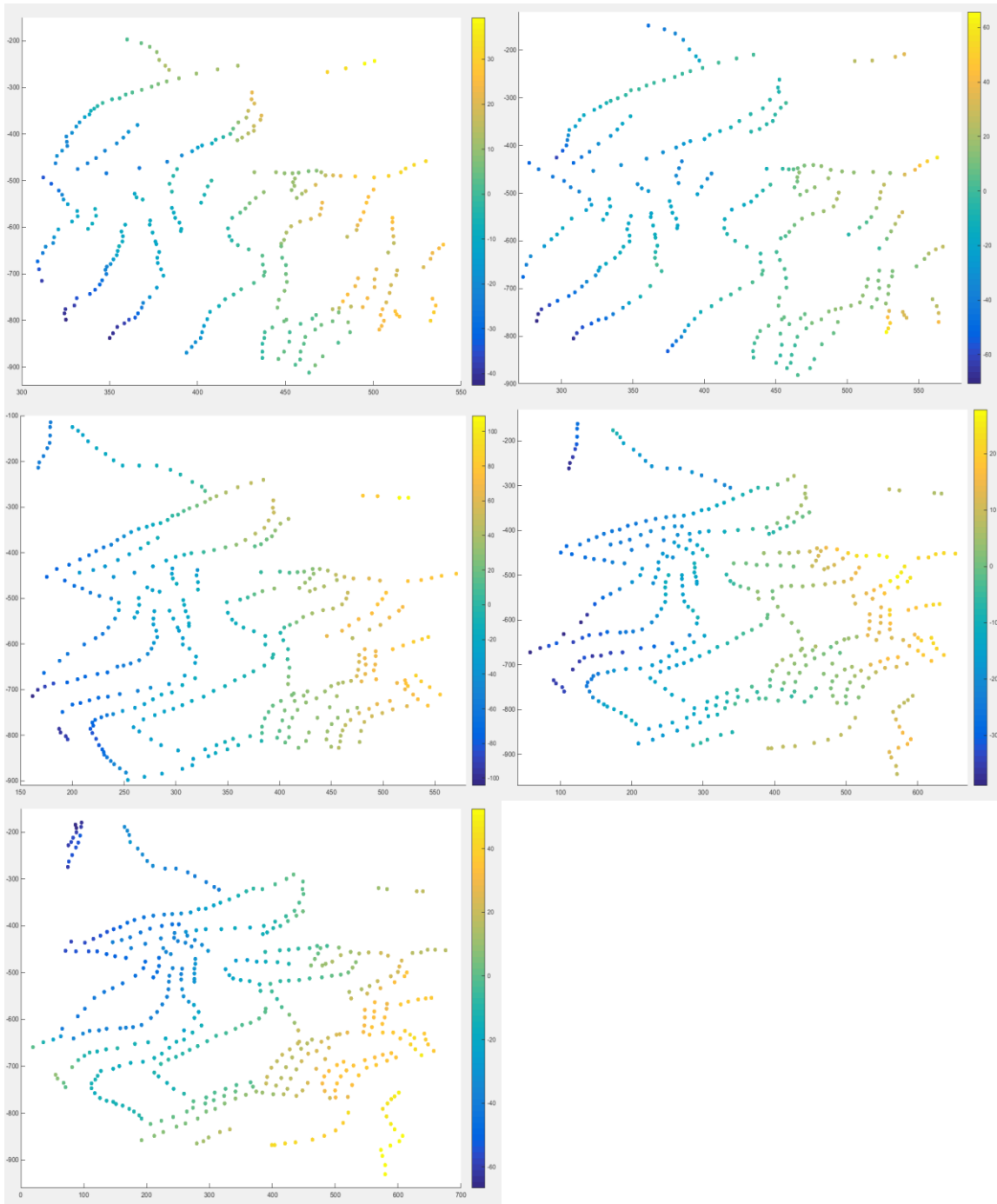
Figure 4.17 - A series of images showing the movement of lamellae between images in x. Here represented as coloured circles. Yellow dots have moved to the right. This corresponds to figures 4.9, 4.18 and 4.19. It has 5 images instead of 6 as it displays the difference between two images. Increasing strains from 0% 19%, 43%, 103%, 129%, 175% and 209%.
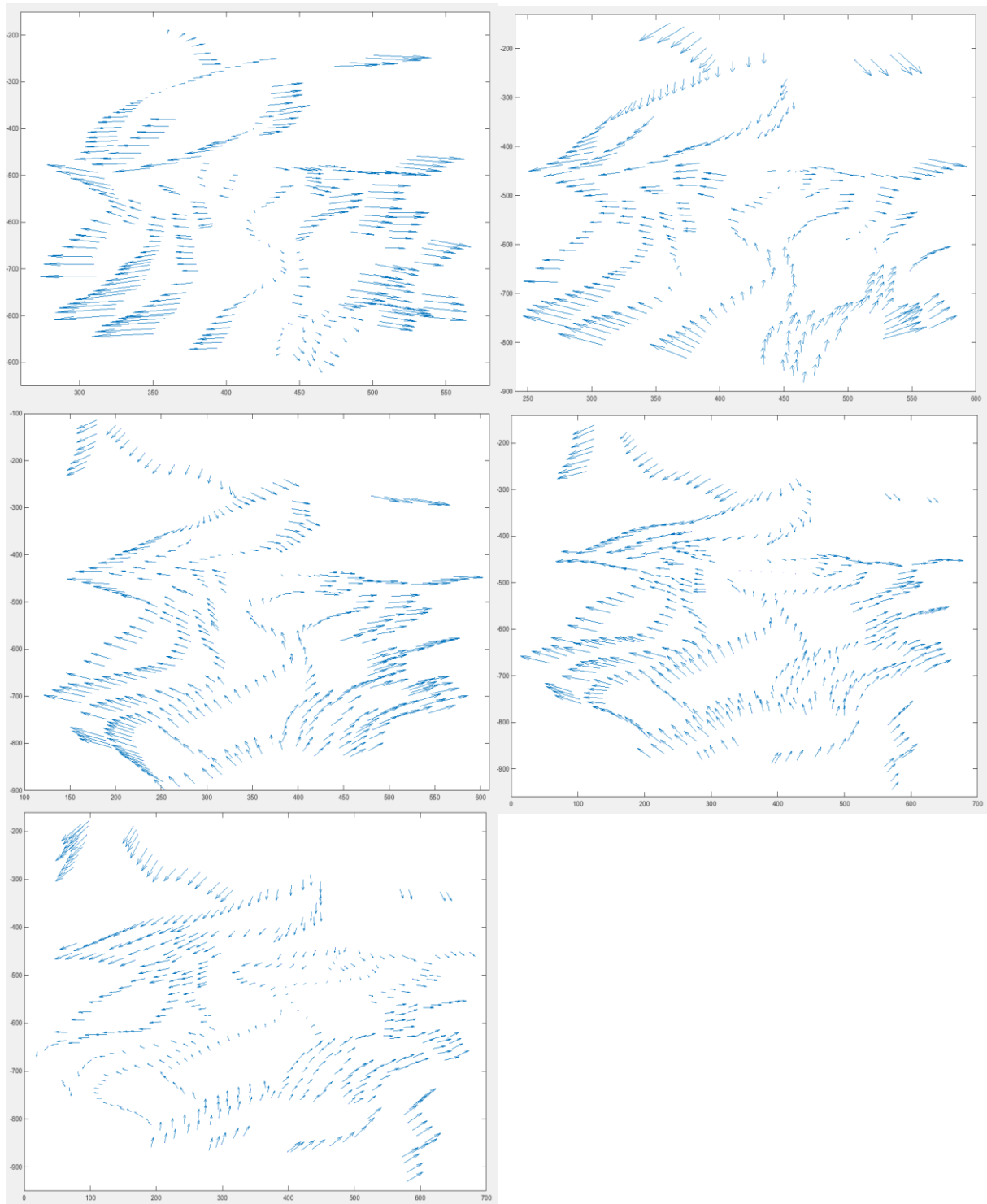
Figure 4.18 – A series of images showing the movement of lamellae between images. Here represented as arrows. This corresponds to figures 4.9, 4.17 and 4.19. It has 5 images instead of 6 as it displays the difference between two images. Increasing strains from 0% 19%, 43%, 103%, 129%, 175% and 209%.
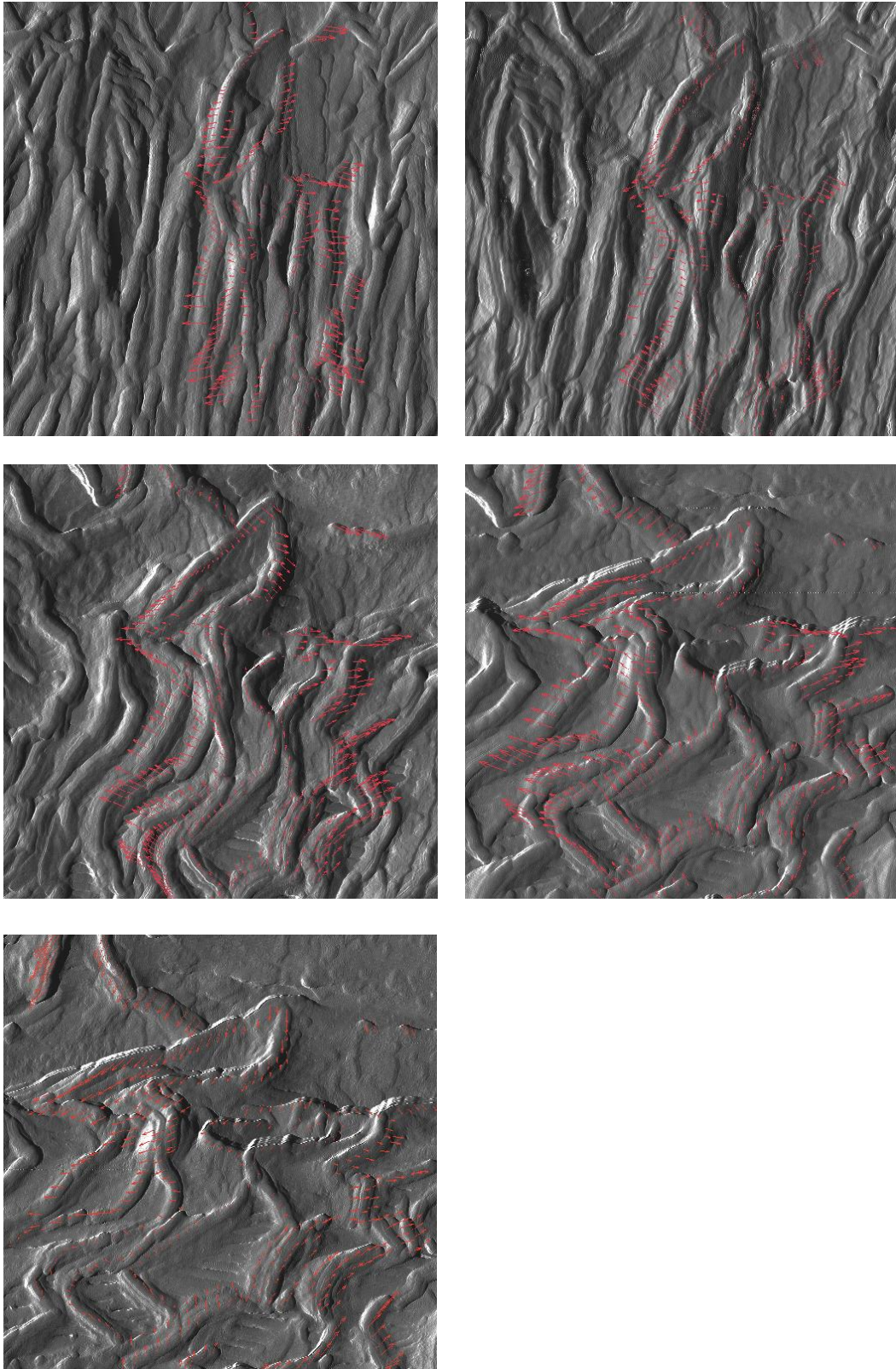
Figure 4.19 – Series of 1.5 images overlaid with arrows showing the movement of the lamellae between successive images. The base images are seen in figure 4.9 and the arrows are from figure 4.18. Increasing strains from 0% 19%, 43%, 103%, 129%, 175% and 209%.

These images allow us to more easily see trends not clearly visible in the base images. This allows the visualization of large scale collective movements of lamellae, such as shear; as well as the movement of individual lamella relative to their neighbours. Generally the lamellae move away from the centre in the stretch direction and towards the centre perpendicular, with magnitudes which are larger further from the centre, this is as expected from Poisson contraction. Arrow size shows the movement relative to the centre, not relative to its neighbours region, so it is useful to compare arrow size to its neighbours.

Collective motions of lamellae are generally easier to see. These movements are generally driven be void and craze opening, leading to significant kinking and bending of lamella. The kinking occurs not just in lamellae neighbouring the crack but in lamellae 100s of nm away. Here we see the dislocation propagating through the film.

Other than when driven by craze formation, lamellae are seen to move in concert with neighbouring lamellae. Often there is movement but not strain as they do not move relative to neighbouring lamellae. This can give rise to possible shear at regions where direction of movement clashes. Between successive images the areas observed to undergo significant deformation are not always the same, often an area is seen to stretch, and later stay relatively static whilst a neighbouring region stretches. This is a demonstration of localised strain hardening. Lamellae breakup can also be seen, a clear example is in the top left where the lamellae rotate to align with the stretch direction and breakup leaving an area unrecognisable to its undeformed state, this fitting procedure helps in tracking these movements.

4.7.2: Corrected sets

The lamellae movement seen above has a potential issue in that the apparent movement has a bias, with it showing lamellae movement relative to the centre of

the imaging area. This gives the impression that areas at the edge undergo more strain which is not the case. It was thus decided to correct these to show the movement of lamellae relative to their local areas rather than the image centre.
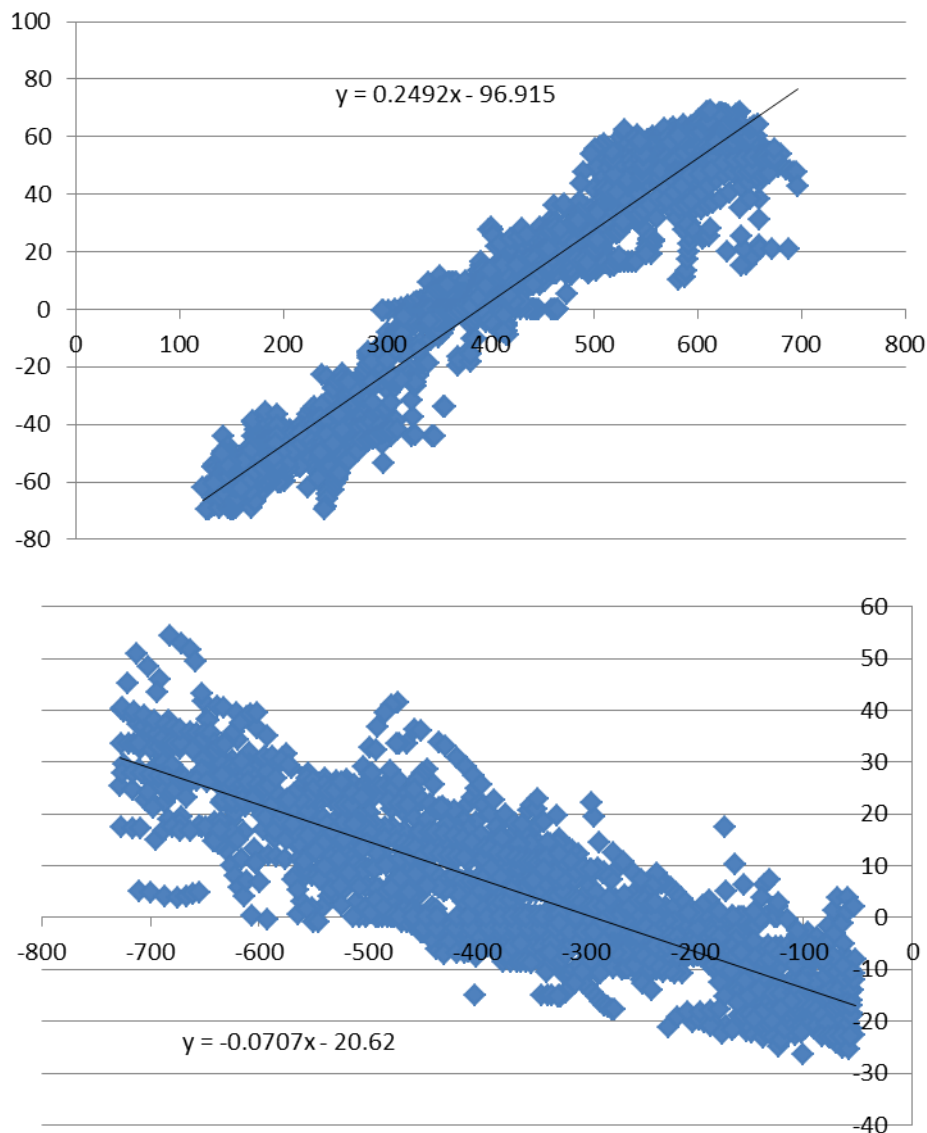
Figure 4.20 –Graphs of lamellae movement in x (top) and y (bottom) based on their position. Between the 1ˢᵗ and 2ⁿᵈ images in a set. These graphs show the expected Poisson's contraction, expanding in x and contracting in y. They were used to create corrected images by subtracting this average movement for every point to give a corrected movement.

To this end Excel was used to calculate the expected average movement for each point in x and y. For each direction, the original position was plotted against movement with a linear fit of this data, giving the expected movement based on

position. This was then subtracted for each point from the measured movement to give a value of how each point deviates from the average movements. This corrected movement has the advantage of making it much easier to see individual lamellae movements, but has the disadvantage of being harder to understand what the images show.
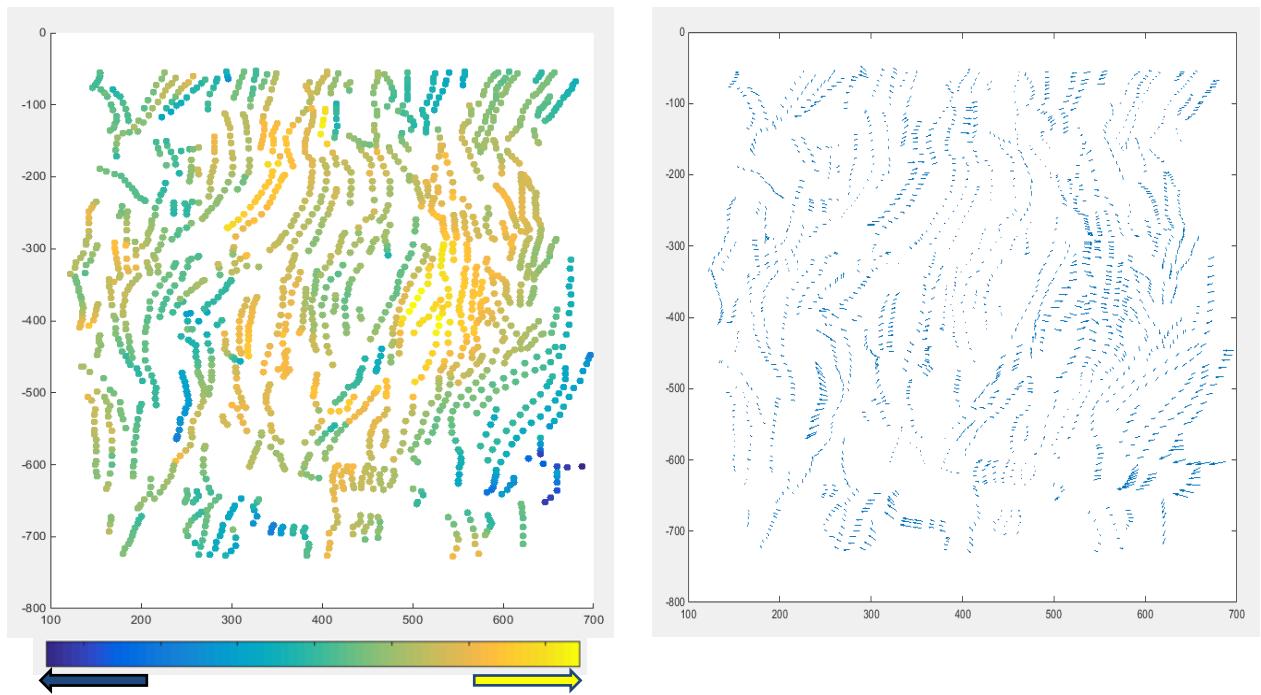
Figure 4.21 - Corrected movement of lamellae between two successive images in a set. Corresponds to figure 4.16. The small scale motion of lamellae is now much more apparent. With the previously stated movement of the horizontal line in the lower right being clear.
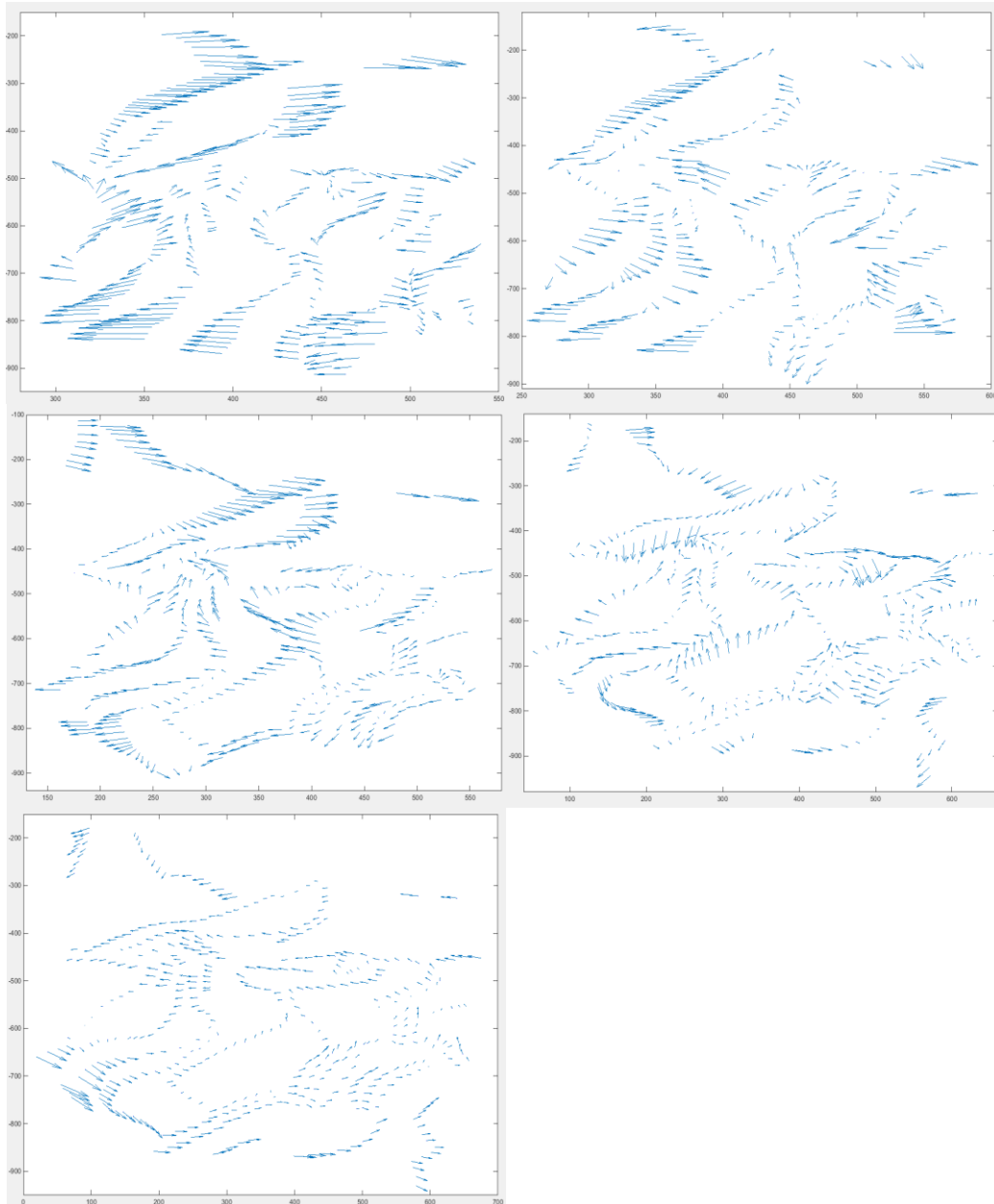
Figure 4.22 - A series of images showing the corrected movement of lamellae between images. Directly corresponds to figure 4.18. Also corresponds to figures 4.9, 4.17 and 4.19. Banding and individual movements are now much clearer as they are not hidden by general movement. Increasing strains from 0% 19%, 43%, 103%, 129%, 175% and 209%.

These corrected sets more easily highlight small scale movements of lamellae. The regions which move relative to the average movement usually do so due to the effect of a nearby craze, and so we see that most lamella reorganisation is driven by crazes. It also shows shear motions that would be otherwise hidden, which is clearest in the first image where the top half goes to the right as the bottom half goes left.

4.8: Discussion

4.8.1: Predictions of where deformation processes occur

It is important to understand why certain areas undergo a large amount of deformation and fracture whilst neighbouring regions remain relatively undeformed. Is it possible to predict which areas will deform most and how they will deform, based on their initial conditions? How close are these predictions?

It can be observed that the branch points of branched lamellae undergo the least deformation. This is likely due to the branch acting to pin the lamellae in position next to each other. Crazes by contrast are formed away from branch points, and are preceded by nanovoids. Craze growth is often curtailed geometrically by branch points, with a branch point forming a 'corner' of a craze.

Whilst a branch point pins the lamella in position, on the opposite side to a branch point, there is sometimes a pinning effect with no visible branch point. This may be due to an unseen branch in lamellae below the surface.

Prediction of deformation is thus possible but limited. It is often possible when looking at the undeformed sample images to pick out some areas which will go on to form crazes, from areas where there is large lamella spacing in areas with lamella perpendicular to the stretch direction.

The process of rotation and kinking are generally driven by crazes, with lamellae acting to maintain alignment with their neighbours, and so their prediction is based on nanovoids and crazes. The fracture of lamellae into blocky elements will then occur, once lamellae are aligned with the stretch direction as it is the only mechanism left.

4.8.2: Comparison to snapshot picture

It is useful to compare the behaviour seen here to what is seen in previous studies, either methods which probe the bulk such as SAXS, or microscopy: such as AFM, SEM, or TEM, which have been used to take snapshots rather than series of images. There are many processes of deformation and fracture which were seen in previous studies. They have all been observed, including: Separation of lamellae due to elongation of amorphous tie-chains, nanovoiding which leads to craze formation, rotation of lamellae leading to buckling to form chevrons, fine crystal slip as seen by tilting and coarse crystal slip which leads to fragmentation of lamellae into blocky elements.

An important difference with this method is the heterogeneity seen at these length scales, where some areas see significant deformation whilst areas 100s of nm away will experience very little. Another related difference is that the processes do not occur in a strict order, with each step following another. For example lamellae often rotate without their connecting tie chains having yet elongated. Also in some cases fragmentation to blocky chains will occur without having fully aligned with the stretch direction.

This raises questions about how lamellae scale properties relates to macroscale properties if there is such variance. In particular the yield point, which would appear to be at odds with observations of yielding occurring at varying times throughout the sample. The likely answer is that over long enough length scales, on the order of 10s of μm these heterogeneities will average out, and macroscale properties can be meaningful.

To compare what we have observed to the process described in the chapter 2 in figure 2.5, the generally accepted deformation process in a semi-crystalline polymer. The process is largely the same:

At the start the sample is undeformed, with crystalline lamellae separated by small amorphous regions.

Increasing lamellae separation is the first processes to occur; this does not only occur at the start but continues throughout the process. At the same time lamellae start to undergo rotation to align with the stretch direction, some of this is tilting due to fine crystal slip. This rotation largely occur in stacks. There is also the formation of nanovoids. These processes occur at the same time in different parts of the material.

Later the rotation leads to lamellae kinking and buckling form chevrons and the nanovoids grow to form crazes. As these processes continue to occur, there is the start of the breakup of lamellae into blocky elements, which is fragmentation, amongst those largely aligned with the stretch direction. This process then comes to dominate with the more and more lamellae breaking up and the surface becoming increasingly fibrillated, with the chains in the polymer aligned with the stretch direction.

The overall process is similar to that described in chapter 2, with the significant difference being that the steps do not occur in a strict order, with many different processes seen to occur at once.

4.9: Conclusions and future work

A method was developed for observing deformation of polymers in situ, on the lamellae scale, and was applied to HDPE. Sets of images have been taken allowing the observation of processes as they occur. The following were seen: separation of lamellae, tilting and rotation of lamellae, alignment with the stretch

direction and breakup into blocky elements. Also significant nanovoiding and craze formation and growth were seen. These all agree with previous studies.

The ability to follow processes gives us information not seen before, on how and where these processes occur. Lamellae movement is seen to be almost entirely driven by crazes, their opening and growth, otherwise they tend to act in concert with their neighbours.

Prediction of deformation is possible but limited. Branch points of branched lamellae are seen to undergo the least deformation, which is assumed to be due to the branch acting to pin the lamellae in position next to each other. Crazes are formed away from branch points and their growth is often curtailed geometrically by branch points, with a branch point forming a 'corner' of a craze. On the opposite side to a branch point, there is sometimes a pinning effect with no visible branch point. This might be due to an unseen branch in lamellae below the surface. Crazes are not seen to all form at once, some new crazes are seen to form later, long after initial crazes.

Sets of images were fitted with mesh of points to help understand the processes. In the future it would be useful to improve this process. An automated fitting process would be both quicker and potentially lead to more accurate and consistent results. This would allow the fitting of larger scale images to understand how the heterogeneity of deformation changes on larger scales. The resolution would need to be increased for this to work.

In conclusion, AFM can be used to observe deformation and fracture of polyethylene in situ on a nm scale. The processes seen in previous literature are followed here, allowing a better understanding of how they occur to be formed.

Chapter 5 – Stretching Polypropylene

5.1: Introduction

Polypropylene is the world's second most widely produced synthetic polymer [138]. It has many uses including films for food covering, clothing and construction, and thus understanding its mechanical properties is important.

Polypropylene is a semi-crystalline polymer, but it forms films with different properties to polyethylene, in particular it is more brittle. This difference in macroscale properties is rooted in different microscale properties which are investigated here.

There have been a number of previous studies of polypropylene's behaviour when stretched under tension. SAXS [144][145][81] has been used to study the processes over time, however this only provides information on changes in structure averaged over the whole sample.

 Imaging techniques including AFM [146][84] and EM [147] have also been used; however they only provide snapshots rather than seeing how an area changes with increasing strain. In this chapter the same area is imaged in successive images, this allows us to watch processes as they occur to better understand them.

Initially the polypropylene used was 100 μm films from Goodfellow. The surface was found to be coated with something, and so was unsuitable for our purposes. New films were produced from pellets, using a hot press, the pellets used were isotactic polypropylene, M_w=190000 and M_n=50000. Film thickness varied between films from 60 to 100 μm, with thickness within an individual film varying by approximately 10 μm. The experiment was performed in ambient conditions at approximately 20 °C, above the glass transition temperature.

5.1.1: Strain measurement

Methods for measuring strain are previously described in chapter 3. The three types of strain described are: macro strain which is measured from the dials of the stretching rig and the initial measurement of the neck, optical strain which is

measured from two points on the sample using the AFM optics, and AFM strain which is measured from two points on AFM images of the sample.
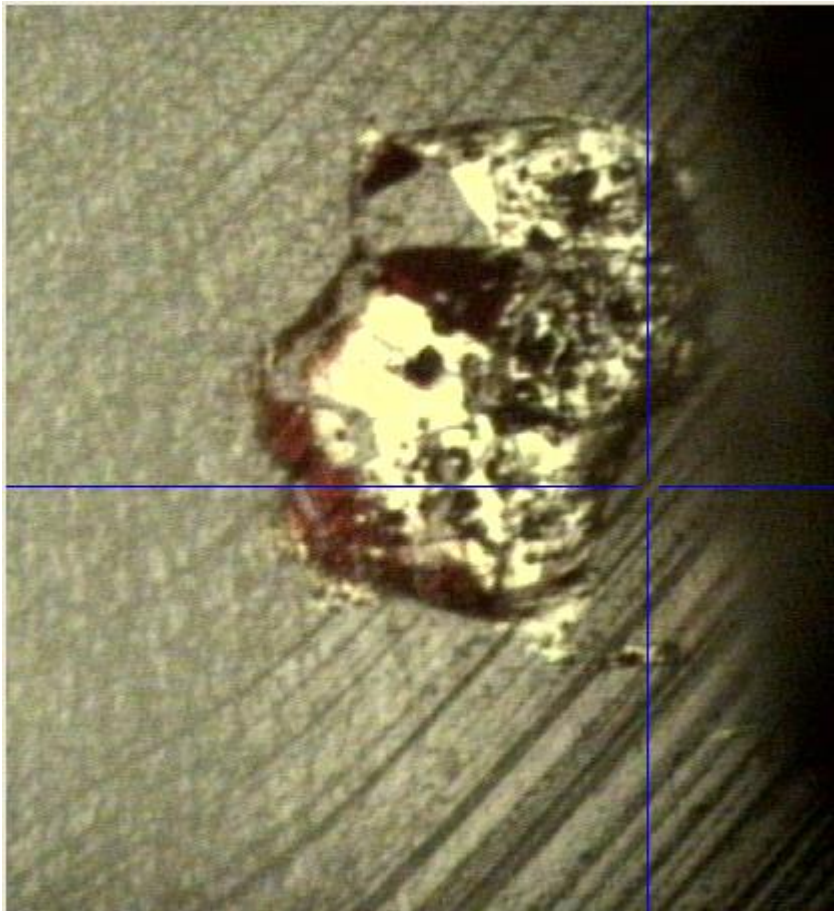
Figure 5.1 – Optical image of polypropylene film and ink dot after being stretched using the AFM optics. The film is stretched horizontally in this image. The diagonal lines are from the mould used in casting. They help to show the highly localised nature of strain in the sample: on the right the film is unstretched and the lines are at the original angle, on the left of the image the film is significantly stretched and the lines are at a new angle and are faded. There is a fairly sharp transition between the areas.

As before, the highly localised nature of the strain poses problems to these methods. This is significantly more pronounced here than for polyethylene. The macro strain has essentially no relation to the strain on the lamella scale and is thus not useful. The optical strain also bears little relation as the strain varies completely within a few μm.

AFM strain is thus the only way left to measure strain. It too has many challenges due to the highly localised nature of the strain. Here how the strain is measured will have a large effect on its value. If the two points measured are in the same crystalline region of the film the strain will be close to zero despite a great deal of the strain to the sample overall. Conversely if the strain is measured across an

opening craze then the measured strain will be very high, regardless of the macroscopic strain. Instead a useful method is to measure across both with the recognisable features furthest apart.

A second difficulty is the differences in strain within an image in the direction perpendicular to the stretch, this presents a problem in finding a single strain value for an image. The solution chosen is to take multiple strain values for each image on different positions vertically and then average them to give the final value. It is also useful to record the range of strains seen within a single image.

5.2: Experimental

The basics of the experiment are similar to that used for polyethylene which is described in Chapter 3. There are a number of important differences in both sample behaviour and experimental procedure compared to Chapter 4. A significant difference is that creep is now a significantly larger issue. After stretching for PE creep will largely go away after 30 mins, here by contrast it takes approximately 3 hours and is still somewhat noticeable. Samples often had to be left overnight to settle, as well as being time consuming this also had the problem of the strains changing as it settled, and sometimes the film would snap overnight.

Also at high strains the problem of creep is worse, with the samples never truly settling and instead continuously creeping until the film snapped. This is mitigated somewhat by always scanning in the same direction and thus the artefacts due to creep are roughly the same between images allowing the relative changes between images to be seen.

1024 lines per image was chosen to give both a good resolution to see details whilst allowing for larger scans to help understand the processes. The higher resolution is needed due to the smaller scale of the features compared to polyethylene. As a consequence of this scan times were 1024 seconds. Higher numbers of lines were not chosen as this would lead to even longer scan times, which would cause major problems with drift and creep, as well as practicality.

Several sets of images have been taken for the polypropylene film. Generally for each set the images were taken of the same place, which allows us to follow the

processes of deformation and fracture at the nm scale. Images were taken at 8, 4 and 2 μm zooming in on the investigated area each time.

In initial stretches undertaken on these samples the area under investigation was seen to not stretch at all, whilst nearby areas stretched significantly, this can be seen in figure 5.1. This problem is due to the highly localised nature of the strain for the sample. There was a need to localise the strain to the imaged area. This was achieved by using a narrower, sharper neck, which involved cutting the sample strips thinner and using a smaller hole punch for the neck. Also, the breakup of the ink dot was watched when stretching the sample to see the strain, and stretching was stopped after an appropriate stretch was observed.

5.3: Initial structure of polypropylene films

The initial structure of the polypropylene film can be seen in figures 5.2 and 5.3. It chiefly consists of small crystallites approximately 10 nm in diameter. These crystallites neighbour each other forming crystalline regions, within these areas exist a number of incipient crazes, as well as a number of point defects, dislocations and voids.
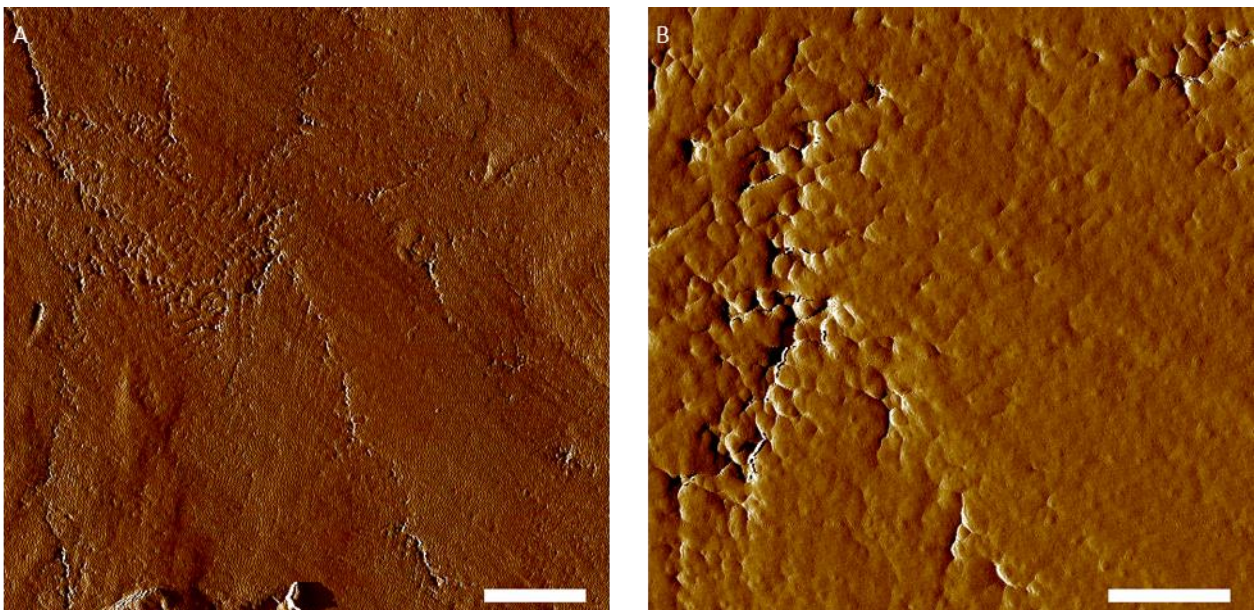
Figure 5.2 - Amplitude image of unstretched polypropylene film. The feature at the bottom centre of A is the end of the fiducial mark. Scale bars 1.25 µm (A) and 400 nm (B). Z scales 490 and 220 mV.

Figure 5.2 shows two images of undeformed polypropylene, with a larger 6 µm and a smaller 2 µm image. At this stage, with the film undeformed there is very little if any fibrillation seen. The incipient crazes are seen throughout the sample and appear to form large structures, though these structures have large numbers of holes in them, they do not have a clear preferred direction. The incipient crazes are likely the boundaries an imperfect spherulite structure. They may be formed by the stresses applied due to cooling.

The samples have some large scale diagonal features; this is due to the aluminium foil used in the hot press to create the films and should have limited effect on the processes seen.

Figure 5.3 shows a zoomed in image of figure 5.2, it has better resolution which allows us to see the crystallites and other features more clearly. The crystallites are of similar but varying size, with the biggest a few times the size of the smallest. They appear randomly packed with large number of defects. In the incipient craze are a few crystallites detached from their neighbours. The height allows us to see that the crazes are lower, and thus thinner than the crystalline regions. These images are similar to some films seen in previous studies [84].
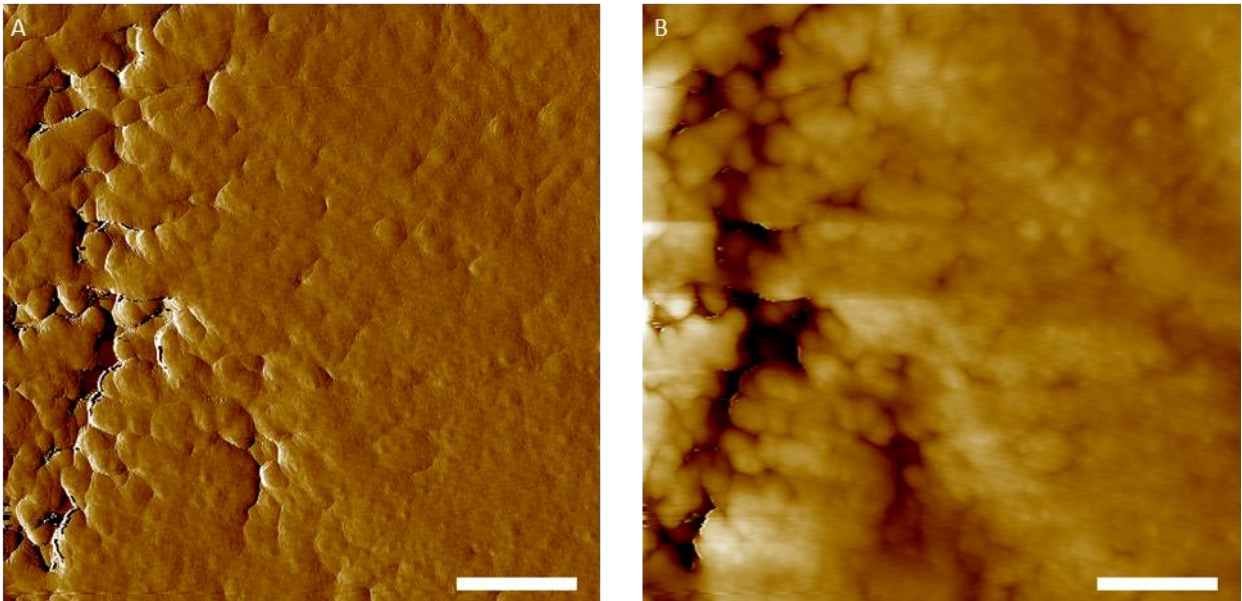
Figure 5.3 – Zoom in on figure 5.2. Amplitude (A) and height (B) images of undeformed polypropylene. The images show the individual crystallites and incipient crazes running throughout. Scale bars 200 nm. Z scales 200 mV and 70 nm.

5.4: Polypropylene deformation

When subjected to a horizontal uniaxial strain the film undergoes deformation and fracture. Due to the highly localised nature of the strain, some areas often undergo little to no strain whilst areas μms away undergo significant strain. The strain is nearly entirely contained in crazes, with very little, if any, deformation and reorganisation seen. The crazes are found to generally occur perpendicular to the stretch direction, with the crazes that grow largest all occurring perpendicular to the stretch direction.

In the crystalline regions, away from crazes, there was little to no change. Differences in these regions between successive images were found to be approximately 1% and thus within the margin of error.

There are a number of other features which have been seen before in deformation of polypropylene films which were not seen here. These include deformation banding and wedge formation.

An example of one of these images is seen in figure 5.4, with a large craze, roughly vertically aligned running through the centre of the image. Across the craze are a number of fibrils, which run perpendicular to the craze edges, these are approximately 5 nm wide and are not uniformly spaced. Within the craze are a number of individual crystallites which appear to have broken off from the sides, these appear as the small circular objects.

The height shows the craze and its fibrils clearest, the amplitude shows the crystallites within the crazes well and usually has the best resolution and dynamic range, and the phase is best to see the crystallites that make up the crystalline regions.

In the lower part of the craze the fibrils are larger and more widely spaced, indicating higher strain. Up from the centre of the craze there are two different branches, which is very common, and is due to the craze following the easiest path to minimise strain mismatches.

Strain mismatches occur when part of a crystalline region is pulled one way by a craze opening, and another part of the same crystalline region is not, or is pulled in a different direction, causing strain within the crystalline region which may lead to a new craze opening.

Outside of the craze the crystalline region seems completely undeformed.
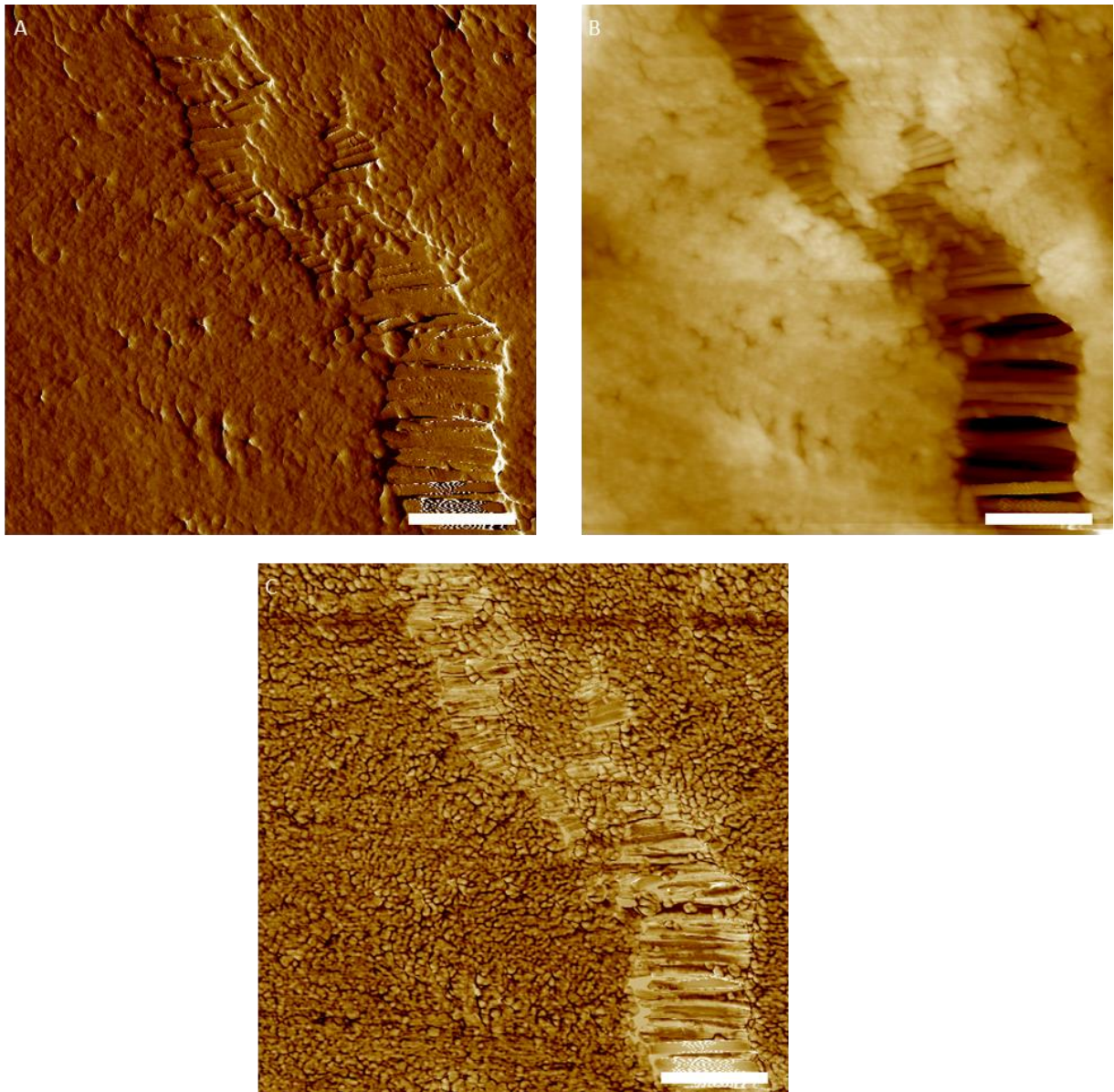
Figure 5.4 – Amplitude (A), height (B) and phase (C) images of a craze occurring in stretched polypropylene, In the crystalline areas either side of the craze the film seems undeformed. Scale bars 400 nm. Z scales 250 mV, 120 nm and 60 °.

5.4.1: Sets of images of polypropylene deformation

Single images of stretched polypropylene can only tell us so much; to better understand what is going on it is important to have a series of images at the same point. Figures 5.5 and 5.6, shows such a series of images, which allows us to watch a craze opening up.

We see the features previously described. Between A and B the craze is seen to get wider and to propagate. The craze is much wider at the bottom, showing the highly localised nature of strain. This can be seen in the large difference in strain values taken from near the top and bottom of the craze, for C they are 38% and 106%. In comparing images it seems the crystallites in crazes match with those previously attached, indicating that they are moved and not created by the strain. Between B and C the crystalline area to the left of the blue dot is seen to break off into the craze.

When looking between A and B it is interesting to see where the crazes occur, in some places it follows the previous incipient craze or other defect, but not always. It might be that it generally starts at a defect and propagates from there. The craze does not include the defect near the blue dot, but instead takes a path to the left.

In order to better understand it is useful to look at digitally zoomed in images, which is possible as the originals are 1024 x 1024; an example is given in figure 5.7 which shows the top part of the craze. Using these images it is now clear that the crystallites in the craze were originally from the sides. We can also see that the crystalline regions are undeformed, a movement of less than 1% between images was measured using Imagej, which is within the error.

It also allows us to see the propagation of the craze vertically. In A there is a large triangular incipient craze and up and to the left of that a small defect marked with a blue dot. By B the craze follows the left side of the triangular defect and has a thin crack to the defect. By C the craze has propagated up past that defect and

further upwards to the right in a different direction. Comparing B and C there is no obvious reason it chose that path rather than another, though obviously it needs to propagate vertically to minimise strain imbalances. The other sides of the triangular incipient craze as well as other defects remain undeformed at this stage, there is little stress on them as it is taken by the craze.
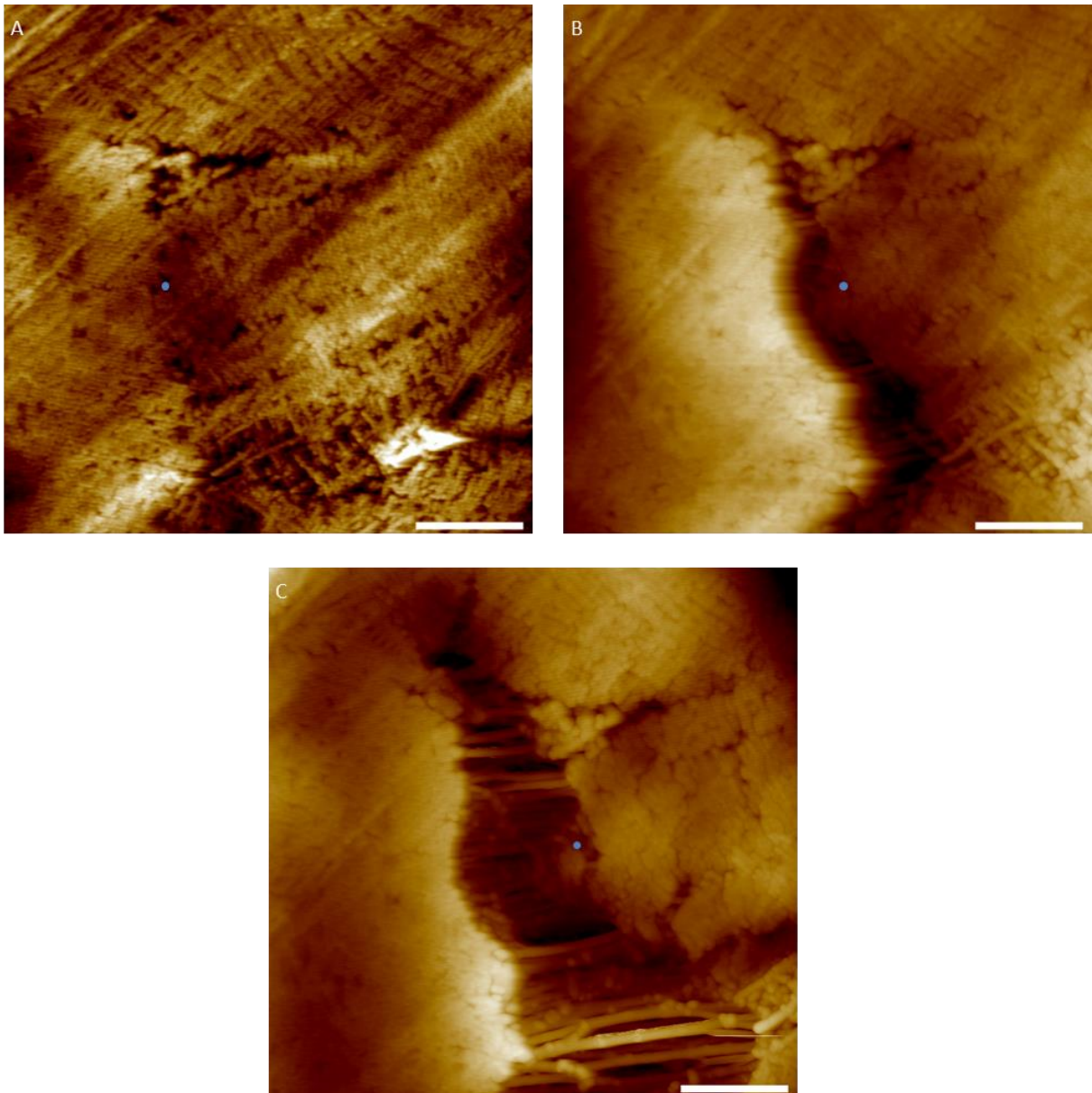
Figure 5.5 – Set of 3 height images corresponds to figure 5.6. Near top of craze strains of 0%, 15% and 38%, near bottom strains of 0%, 42 and 106%. B shows significant shadowing in the craze due to poor tracking of the surface due to the craze. Blue dot in same place in all three images. Scale bar 300 nm. Z scales 50, 140 and 200 nm.
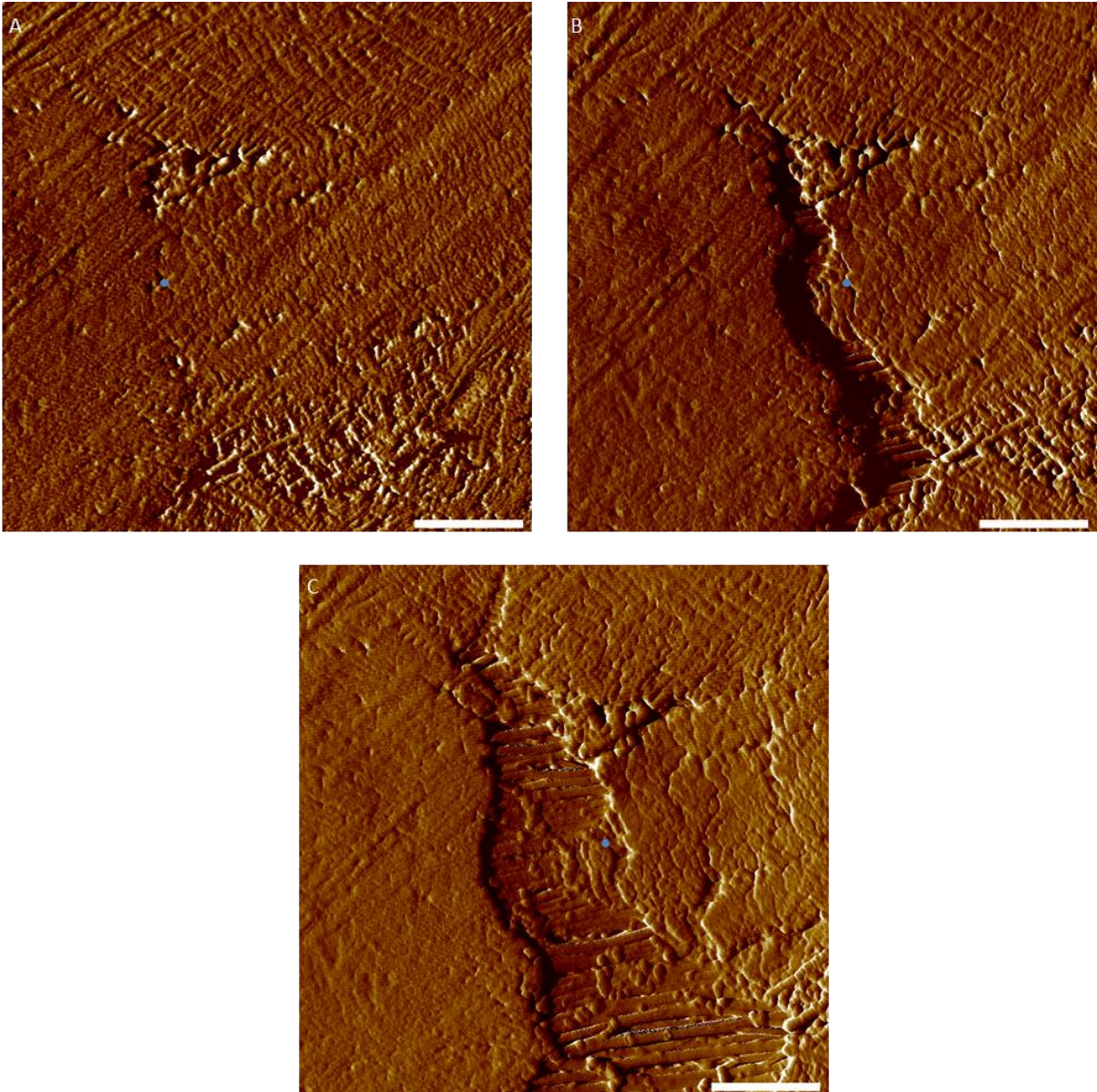
Figure 5.6 –Set of 3 amplitude images, corresponding to figure 5.5. Near top of craze strains of 0%, 15% and 38%, near bottom strains of 0%, 42 and 106%. B shows significant shadowing in the craze due to poor tracking of the surface due to the craze. Blue dot in same place in all images. Scale bar 300 nm. Z scales 230, 240 and 420 mV.
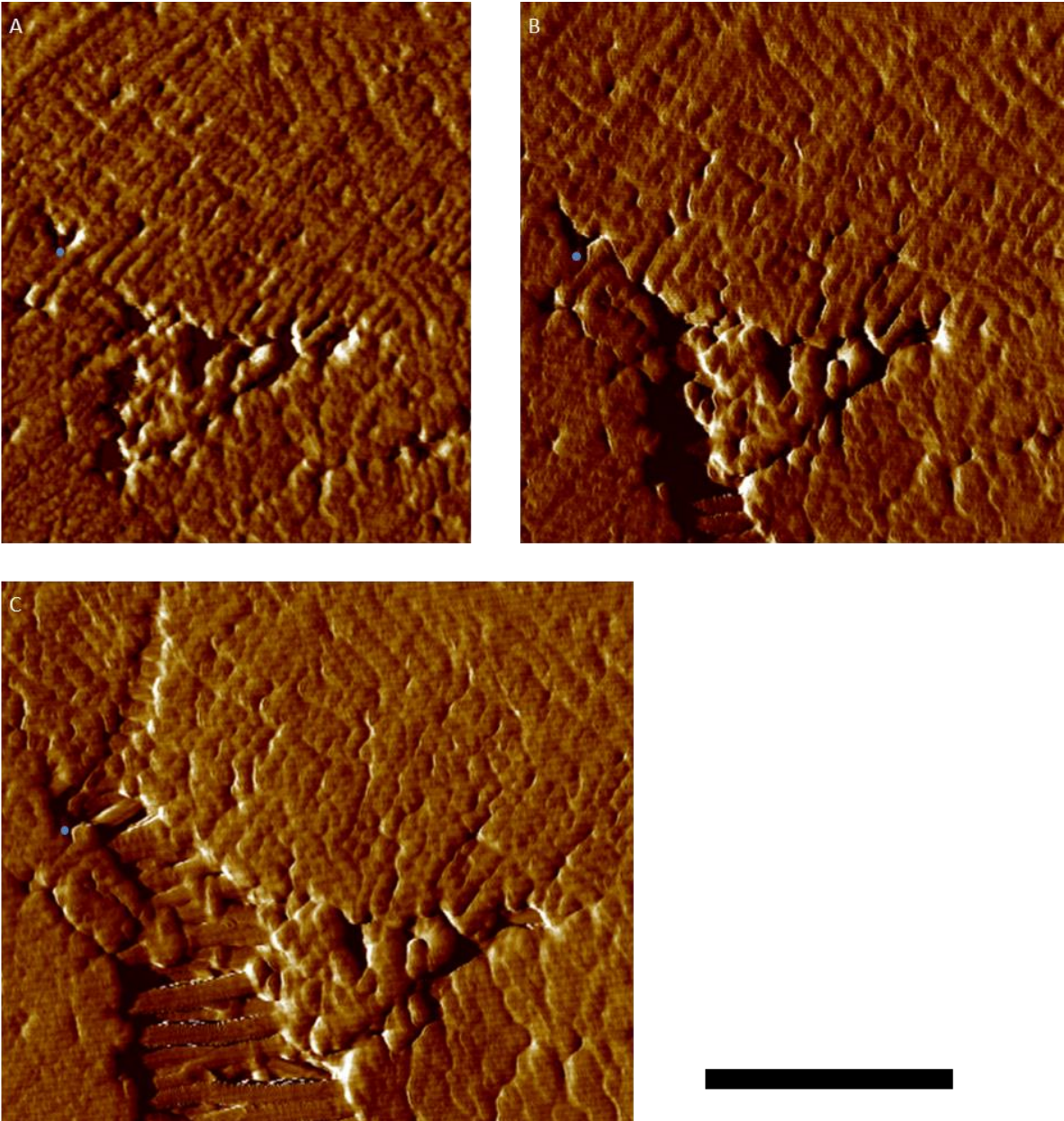
Figure 5.7 – Blown up sections of figure 5.6. Set of Amplitude images with strains of approximately 0%, 15% and 38%. Some shadowing in the craze in B due to poor tracking. Shows the vertical propagation of a craze. Scale bar 300 nm. Z scales 230, 240 and 420 mV.

To understand what is going on it can be useful to look at the bigger picture. Another set of images is in figure 5.8, which are larger scale 4 μm images (smaller scale images of this set are in figures 5.9-5.12).

In the images there are a number of different crazes forming throughout the imaging area. In A there is a main diagonal incipient craze, labelled with a blue dot and a smaller diagonal craze below it labelled with a green dot. In B many new crazes have formed, two of which are centred on the original incipient crazes. There is a significant craze in the top left which appears somewhat of a branch of the main diagonal from near the blue dot, but curves to align vertically. There are also small crazes on the left of the image which are roughly vertically aligned. By C there are some new crazes and the existing crazes have grown. However they have not grown uniformly, with the newer crazes growing significantly more than the original incipient crazes.

This kind of behaviour can be seen many times in different images, where between successive images neighbouring crazes are seen to stretch at different times, with one staying relatively static whilst and the other stretches and vice-versa.

Also of interest is the craze perpendicular to both of the original diagonal crazes between the blue and green dots, this is a secondary craze and can be seen much clearer in figure 5.12 further down. The formation of secondary crazes perpendicular to major crazes is seen to occur frequently. These are formed after the major crazes form and occur due to perpendicular strains caused by mismatches in the primary crazes. Primary crazes are usually perpendicular to the stretch direction, but it was diagonal here due to the original incipient crazes.
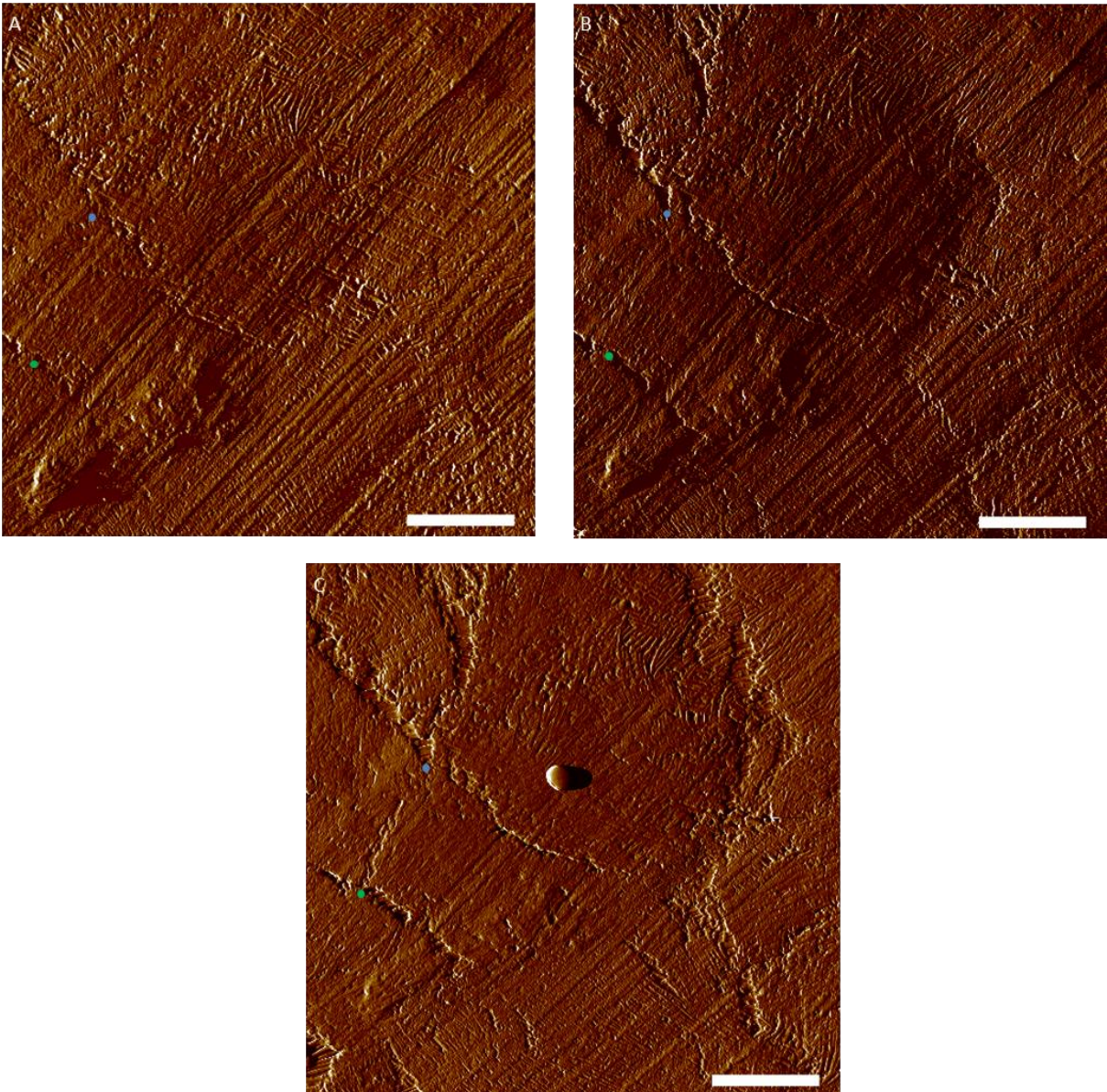
Figure 5.8 –Set of three amplitude images. Strains of 0%, 14% and 21% near the top of the image, and 0%, 9% and 10% near the bottom. The images show large number of crazes opening. The appearance of the round object in C is a contamination spot. Scale bars 800 nm. Z scales 360, 360, 540 mV.

Figures 5.9 and 5.10 are a set of 2 µm images taken of the area between the diagonal crazes in figure 5.8 in height and amplitude. Figures 5.11 and 5.12 are digitally zoomed in regions of figure 5.9. The blue and green dots are in the same place in all images. Figures 5.9 and 5.10 shows the same features descried before.
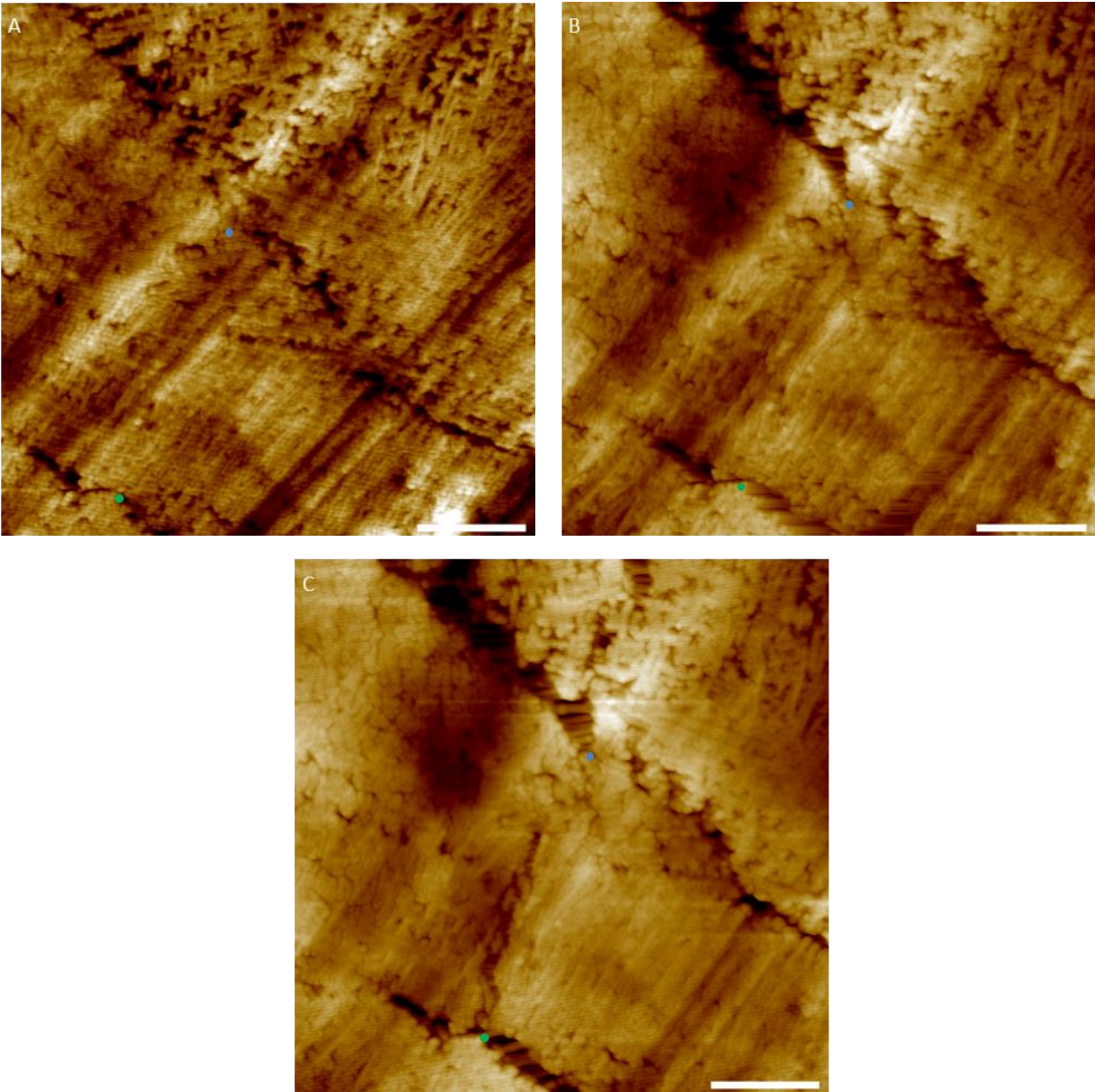
Figure 5.9 - Set of three height images zoomed in on the blue and green dots in figure 5.8, which are in the same place here. Strains of approximately 0%, 12% and 16%. Corresponds to figure 5.10. Scale bars 400 nm. Z scales 40, 60 and 90 nm.
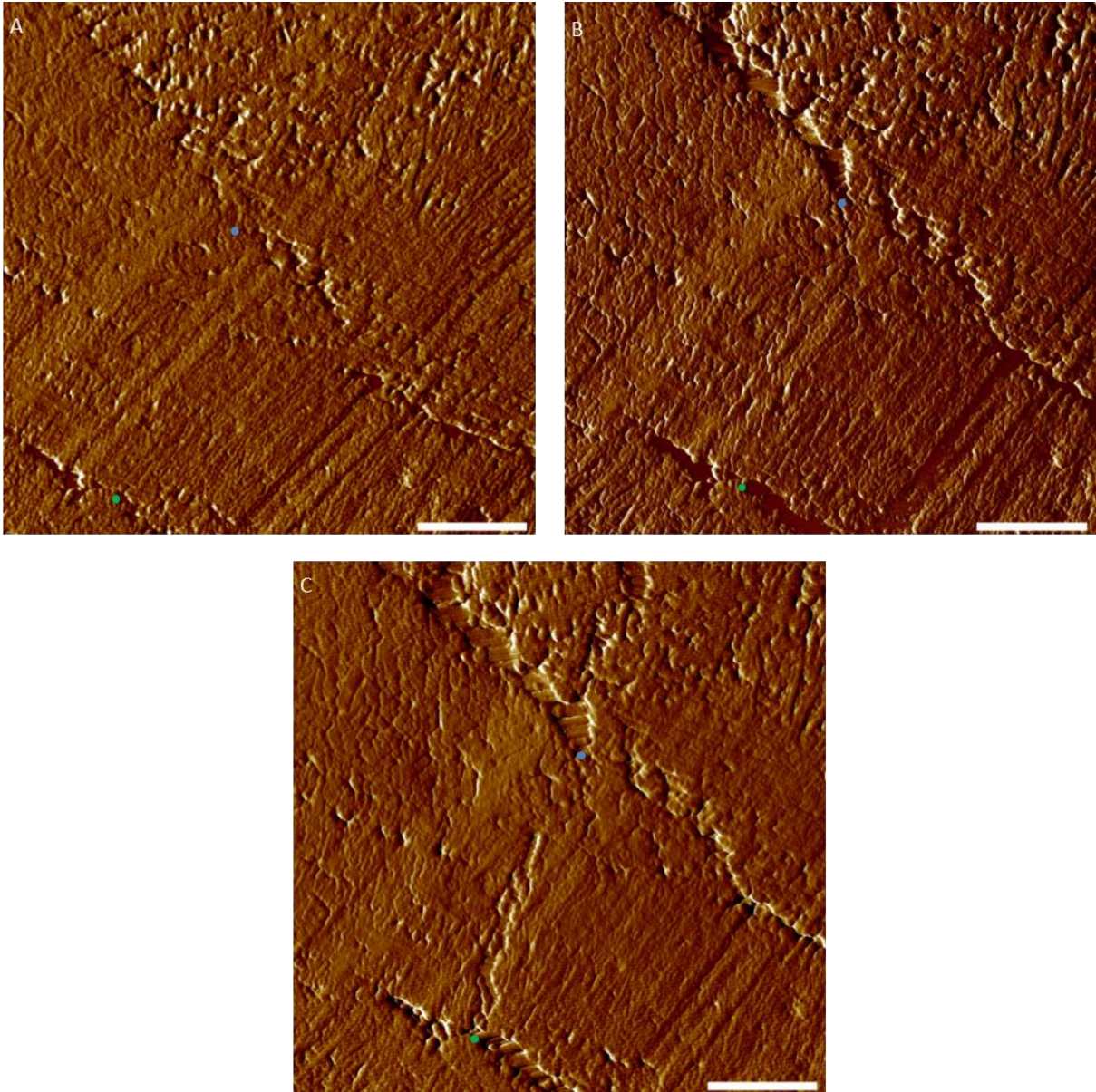
Figure 5.10 – Set of three amplitude images zoomed in on the blue and green dots in figure 5.8, which are in the same place here. Strains of approximately 0%, 12% and 16%. Corresponds to figure 5.9. Blown up sections are shown in figures 5.11 and 5.12. Scale bars 400 nm. Z scales 360, 360 and 540 mV.

Figure 5.11 is digitally zoomed in on the blue dot, in the top half of the main diagonal craze in figure 5.10. In the images you see the craze opening up, directly over the position of the original incipient craze. The craze propagates to fill in some of the gaps present in the first image but still leaves sections further down not complete.

Also in this set is the formation of another craze in the centre top, which at this scale is perpendicular to the primary craze and is thus a secondary craze. By C it is formed, in B there are a number of defects on its path, whereas in A there is nothing to indicate a craze would open up here. Looking at figure 5.8, it is clear the craze started further and then propagated down here to intersect with the diagonal craze.
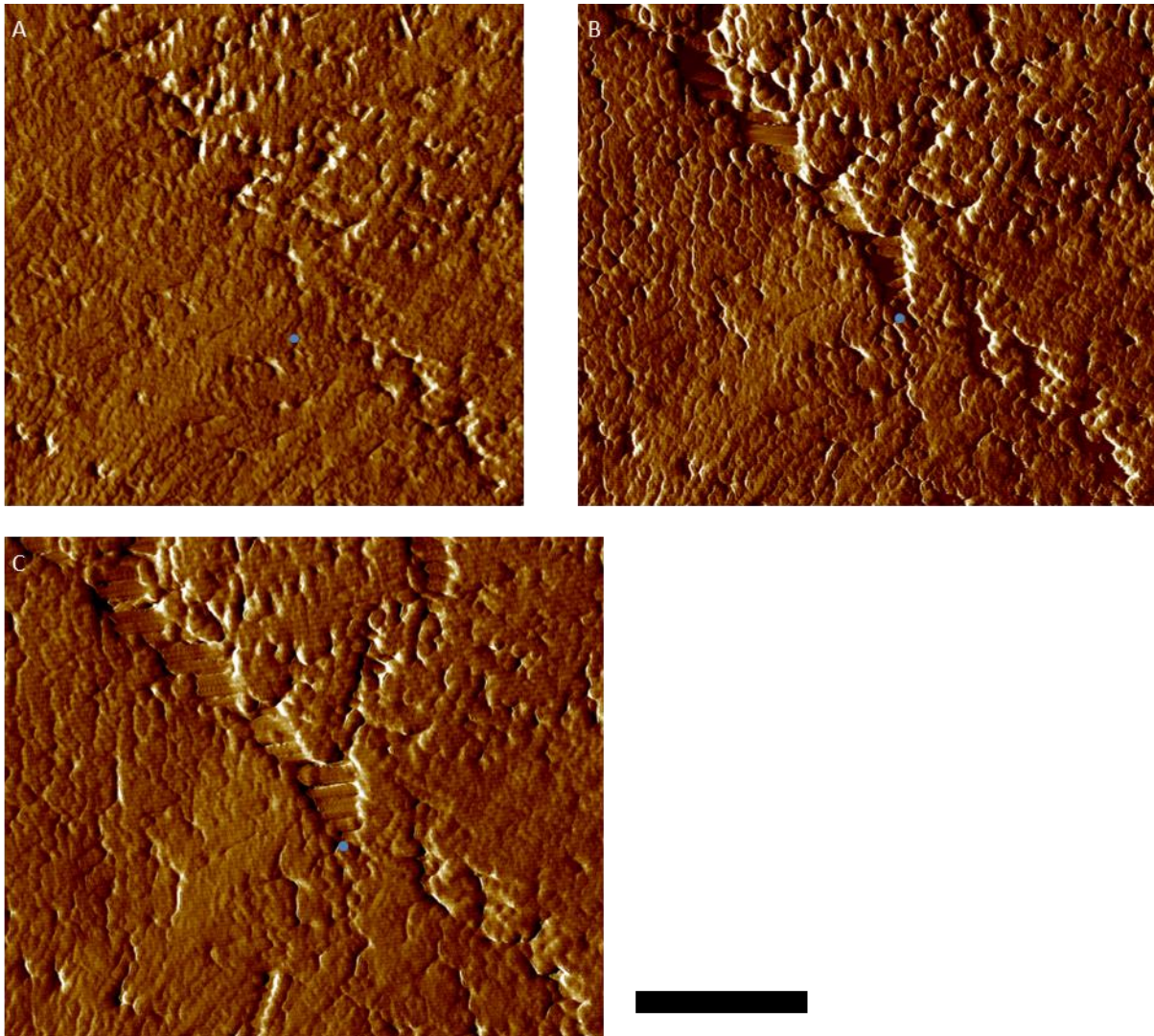
Figure 5.11 – Blown up section of figure 5.10. Shows opening of the diagonal craze and the creation of a new craze perpendicular to it. Strains of approximately 0%, 12% and 16%. Scale bar 400 nm. Z scales 360, 360 and 540 mV.

Figure 5.12 digitally zooms in on the centre of figure 5.10 where a secondary craze forms between the two diagonal crazes, between the blue and green dots. Unlike the previous secondary craze this cannot be formed by propagation from

another craze out of shot. The craze is formed by C, by B there a few defects formed on its path though they are not obviously different to other defects in the sample, in A there is no clear indication that a craze could form and what route it would take. It does not seem possible to predict the crazes formation and route from the early images. Indeed it seems to avoid a more obvious route, the dark line it cuts across, the start and end of which are labelled with arrows in A and C. Thus we cannot always see what is the lowest energy path for the system to take, though the general need for a secondary craze could be predicted from the mismatch of strains of the primary crazes.

The existence of two early secondary crazes here might be due to diagonal nature of the primary crazes inducing more strain mismatch than normal.
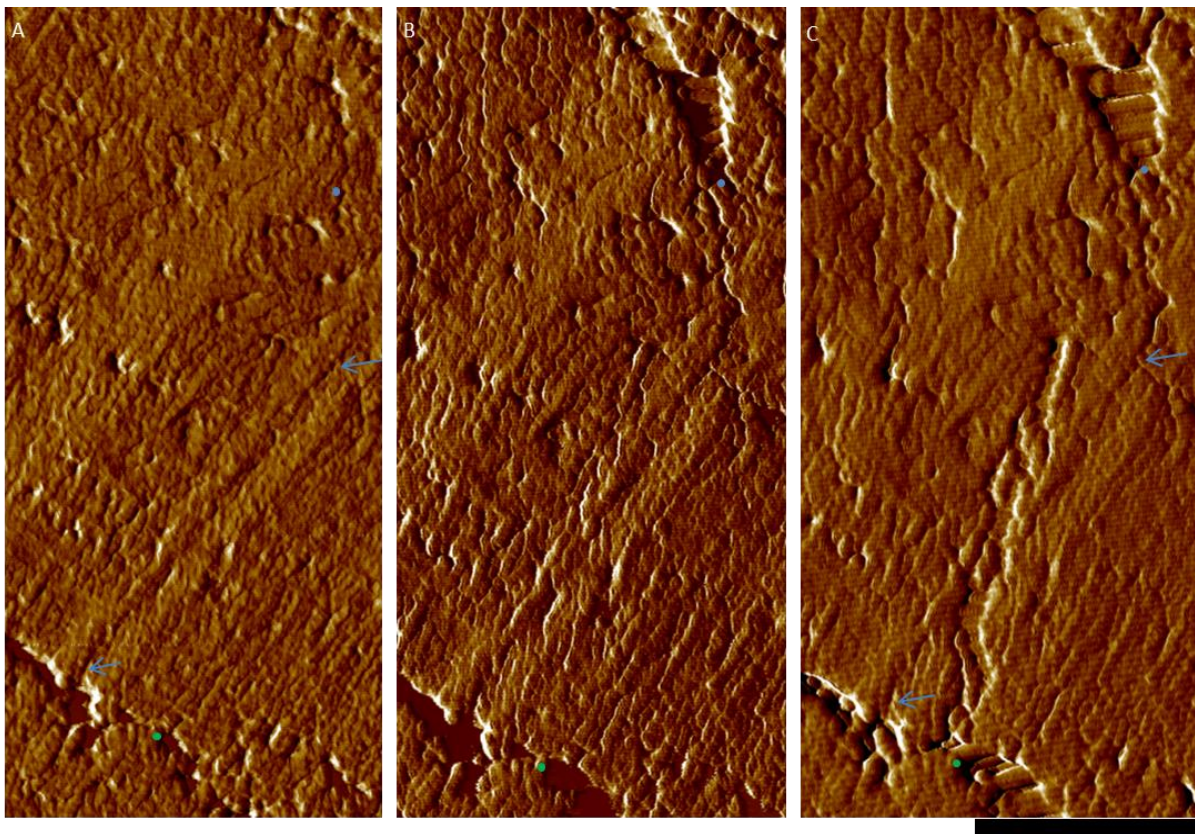
Figure 5.12 – Blown up section of figure 5.10. Strains of approximately 0%, 12% and 16%. C shows the appearance of a secondary craze, which is roughly perpendicular to the primary crazes. In the A and B areas at the craze in the bottom the tip does not track the surface leading to the dark areas seen. Scale bar 400 nm. Z scales 360, 360 and 540 mV.

5.4.2: Polypropylene film behaviour at higher strains

It is useful to investigate the behaviour of the system at higher strains; however it can be difficult to do so due to the highly inhomogeneous nature of the

strain. All previous sets snapped before the imaging area had undergone large strain, due to much higher strain elsewhere in the film.

In order to do this, during a set of images a nearby area that had undergone significant strain was also imaged. Figures 5.13 and 5.14 are a set of two 4 μm images going from medium to large strain in height and amplitude. It is dominated by the central region of the craze which undergoes significant strain with long widely spaced fibrils. This is a large strain which must be equalised by the areas around it leading to large amounts of new crazes and breakup of the crystalline areas.

Various new crazes are seen, including in the top left and the bottom central craze in the second image which are investigated in zoomed in pictures of figures 5.15 (blue) and 5.16 (green).

There is significant breakup of the edges of crystalline regions to individual crystals within fibrillated regions, though the bulk of these regions remain undeformed. Also seen is rotation of features in the bottom right, caused by the expansion of neighbouring cracks.
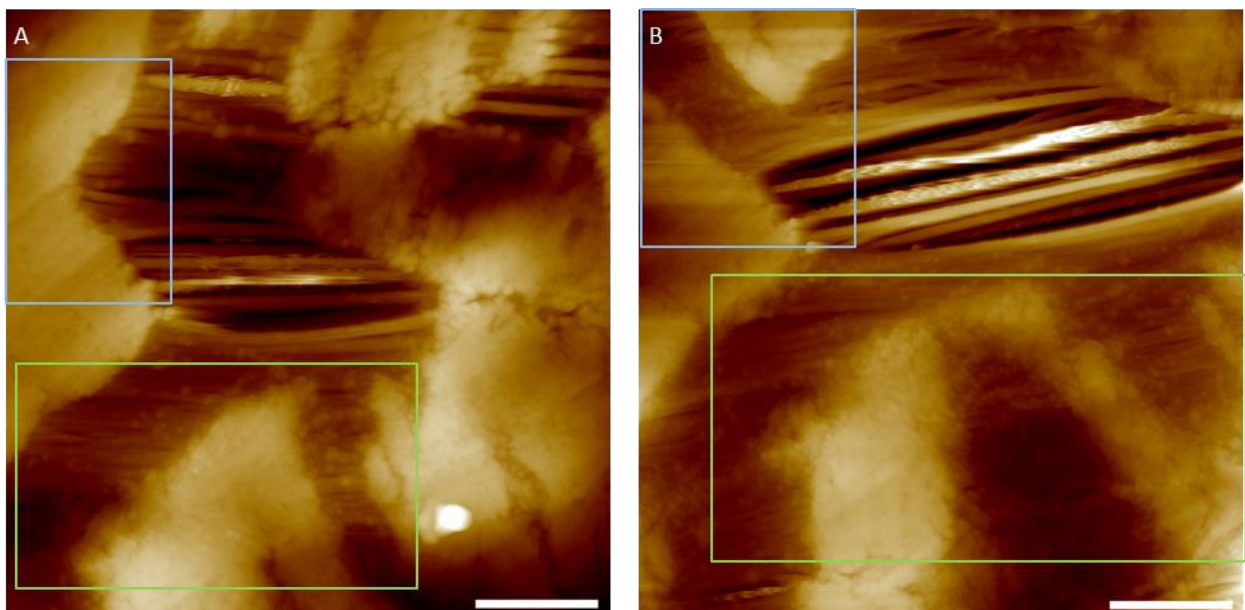
Figure 5.13 - Set of height images. Approximate strains of 227% and 425% near the top and 199% and 353% near the bottom. Corresponds to figure 5.14. The large craze in the middle produces lots of strain in the features around it. This area was chosen to investigate after the

Figure 5.14 – Set of amplitude images. Approximate strains of 227% and 425% near the top and 199% and 353% near the bottom. Corresponds to figure 5.13. The large craze in the middle produces lots of strain in the features around it. This area was chosen to investigate after the first stretch and was approximately 5 μm away from the investigated area which only showed small strain. Rectangles show blown up regions, these are shown in figure 5.15 (blue) and figure 5.16 (green). Scale bars 800 nm. Z scales 550 and 370 mV.

Figure 5.15 is a digitally zoomed in section of the top left of figure 5.14 (blue rectangle). In it are the formation of some crazes not previously present, the large craze from the top right corner which forms a branch from the main craze at the blue dot and the small craze at the top, at the green dot. In comparing A and B there is no clear way to tell why the crazes took that path, with them forming on paths largely free of defects. From larger scale images it seems these cracks both propogated off screen.

There are a large number of crystallites in the craze here which can be matched to crystallites in the crystalline region before. Next to the large dominant craze there has been no break off of crystallites.
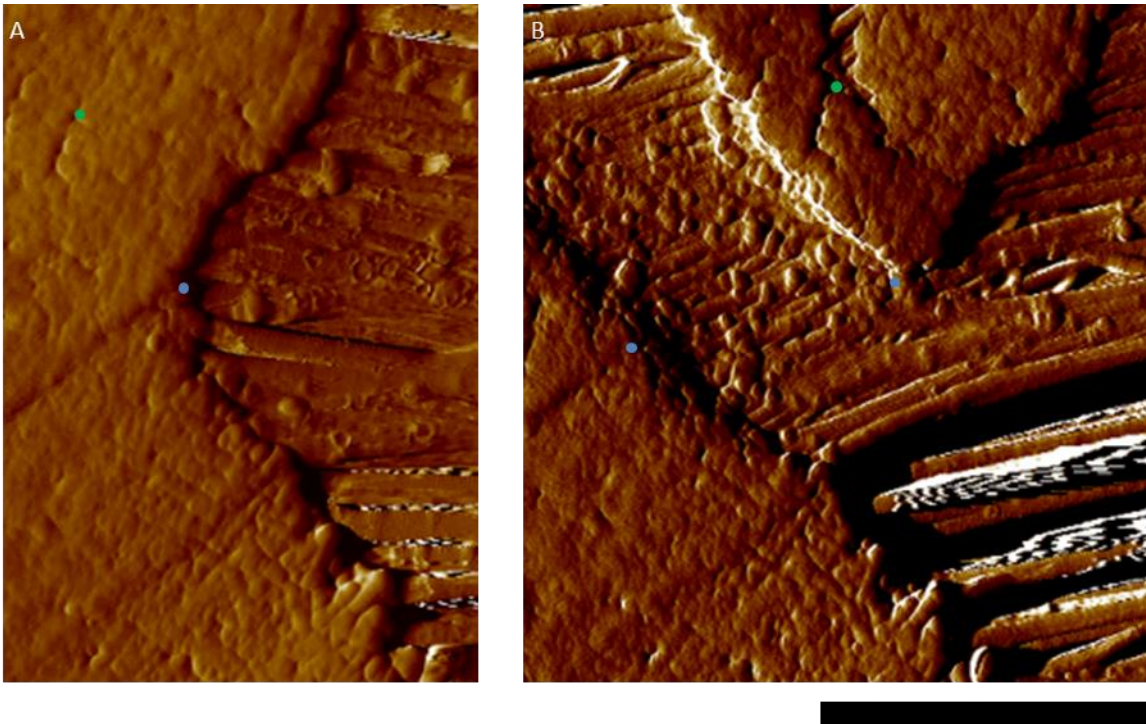
Figure 5.15 – Digitally zoomed in section of figure 5.14. Approximate strains of 227% and 425%. Shows the opening of two crazes in potentially unexpected places. The dots show same place on both images, in B there are two blue dots to show the previously neighbouring areas that have moved apart due to the craze. Scale bar 800 nm. Z scales 550 and 370 mV.
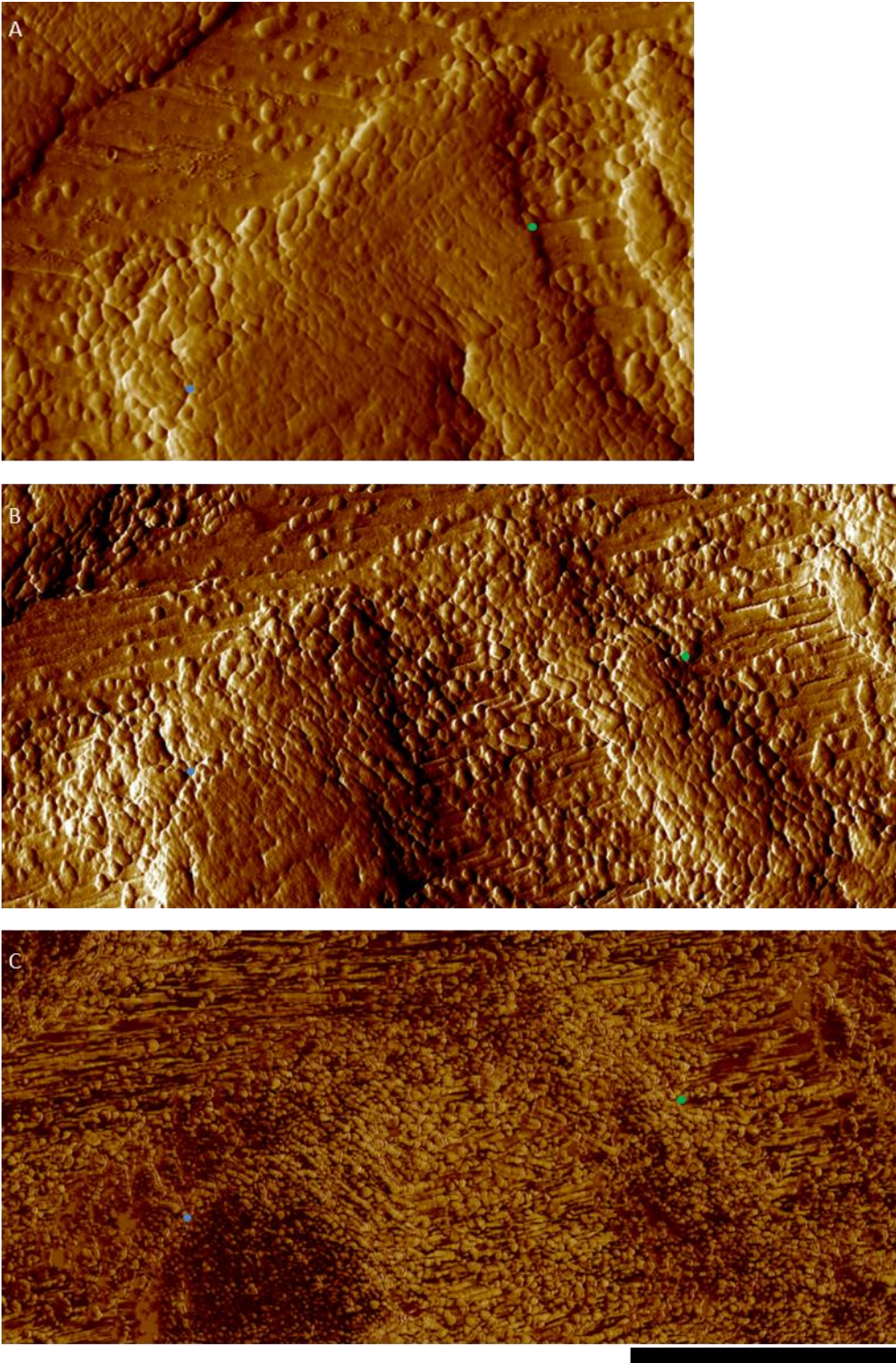
Figure 5.16 – Digitally zoomed in section of figure 5.14. A and B are amplitude images corresponding to A and B of figure 5.14, C is the phase image corresponding to B. Approximate strains of 199% and 353%. The images show the emergence of a craze and the breakup of the edge of a crystalline area. In the phase the fibrils are light and most of the crystalline regions are dark; some crystalline regions, however, are the same colour as the fibrils, these are the ones which are somewhat broken up, with the phase showing the loss of structure. Scale bar 800 nm. Z scales 550 and 370 mV and 80 °.

Figure 5.16 is a digitally zoomed in up area of the bottom of figure 5.14 (green rectangle), which is below the dominant craze. It exhibits significant strain, which is taken up by enlargement of the crazes and some break up of the crystalline regions at its edges.

Of most interest is the break up of crytstalline regions, the middle craze here has a very large numbers of individual crystallites within it, and in surrounding areas large amounts of the crystalite regions appear to be breaking up, both into smaller pieces and to individual crystallites. There remains, however, core crystalline regions where no breakup occurs.

The phase image is shown in C. By comparing B and C we can see that there is a phase contrast between the cyrstalline regions and the fibrils. The crystalline regions which are starting to break up, however, have a phase close to that of the fibrils, even if the surface is nearly all crystalline. This shows the break down of the structure.

It is useful to see what we can predict based on initial conditions. About how and where crazes will form and how they will expand. Crazes were often seen to follow the path of incipient crazes and other defects before propagating onwards. This was not always the case, with many crazes occurring in the middle of crystalline regions with no clear prior indication. These were often, but not always, caused by propagation from a craze outside the imaged area. In the cases where it wasn't, the craze was needed there to balance mismatched strains despite a potentially unfavourable area. Mismatched strains perpendicular to primary crazes give rise to secondary crazes.

Neighbouring parallel crazes are seen to stretch at different times, with one staying relatively static whilst another stretches and vice-versa, which demonstrates localised strain hardening. Overall it can be hard to predict where cracks will form and when based on initial conditions.

5.4.3: Polypropylene film behaviour at extreme strains

The final stages of reorganisation were not seen in these sets as the films snapped before they could be reached. This was due to the highly localised nature of strain in polypropylene, such that areas nearby to the imaged region underwent significantly more strain and snapped. It was not possible beforehand to pick exactly which area this would be. Instead in order to investigate the behaviour of polypropylene at very high strain the most strained areas were simply imaged by themselves. Optically these areas are seen to exhibit stress whitening which is due to the micron scale voids. An example optical image can be seen in figure 5.17, there is a significant difference when compared to figure 5.1.
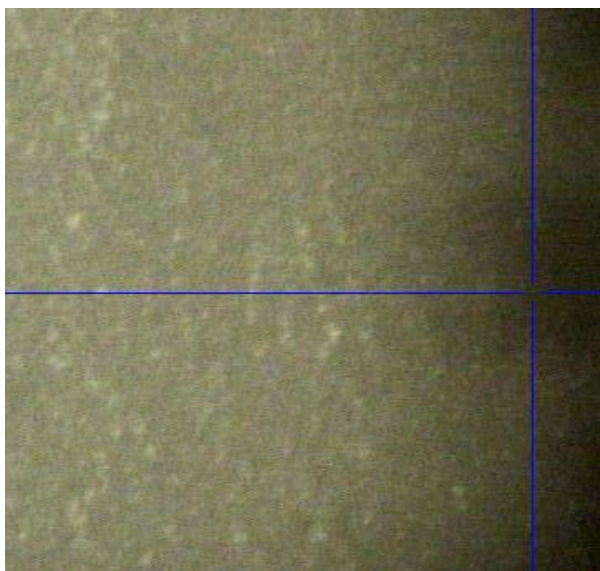
Figure 5.17 – An optical image of the polypropylene film in a highly stretched state. The previous lines have disappeared, the film is lighter due to stress whitening caused by the presence of micron scale voids and crazes. There are some larger scale voids and crazes, visible here as white areas. Approximately 100 μm to the right of this image the sample appears completely unstretched.

A large scale example AFM image is shown in figure 5.18. The film is now in an extremely fibrillated state, with over 90% of the surface covered by fibrils. Spaced within the fibrils are the crystallites which are now separated from each other. They do not appear to have changed size. There still exist significant crystalline regions which appear unchanged from their initial state. These regions are approximately

500 nm in size and are roughly aligned vertically; this is caused by large primary crazes, which were later separated by secondary crazes.

Another major feature is the existence of large cracks which are orientated with the stretch direction and are long and thin, occurring between fibrils. The largest example is seen on the middle left of figure 5.18, but there are many throughout the image. These cracks take up a large amount of the strain and give rise to the stress whitening seen optically.
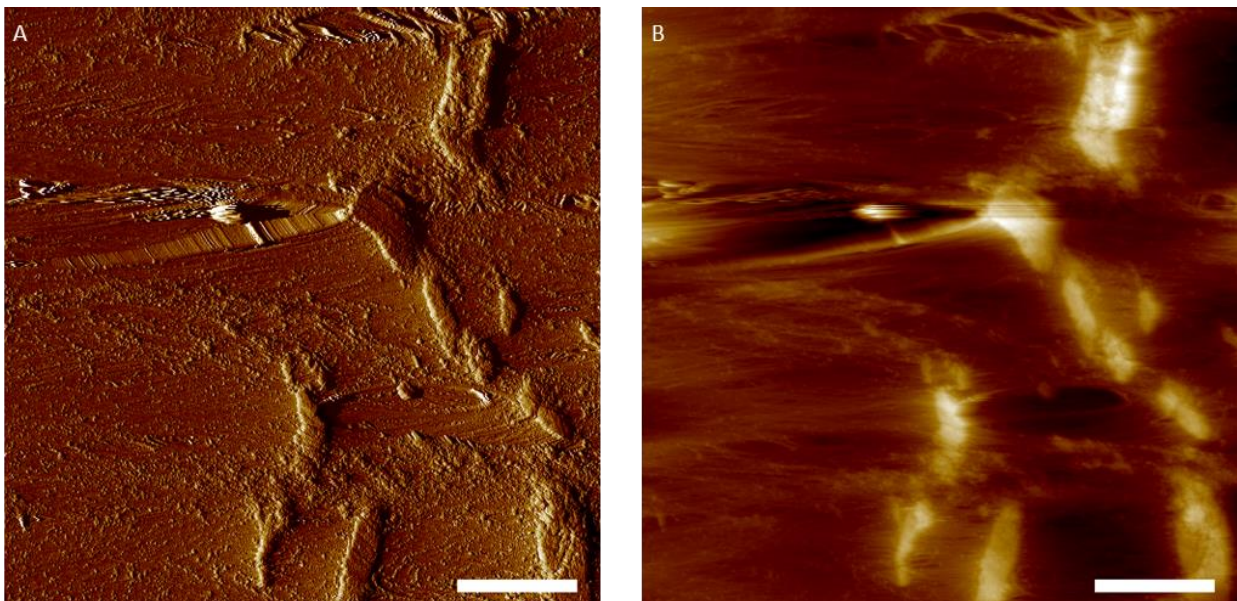
Figure 5.18 –Amplitude (A) and height (B) images of highly stretched polypropylene. The majority of the film is now fibrillated with small crystalline regions remaining. A number of large voids parallel to the stretch direction are now present. Scale bars 2 μm. Z scales 820 mV and 500 nm.

A more zoomed in and thus higher resolution example can be seen in figure 5.19. From the crystalline region in the top left it is clear that, within the region the polymer is undeformed still, and the film will snap long before all of these regions are deformed. The regions have both the same crystallite size and crystallite density as undeformed polypropylene.

On the bottom right is a crystallite region which has broken up somewhat into individual crystallites as has been seen at lower strain. It is unclear if this is currently

in the process of breaking apart to a highly fibrillated state or is largely stable in its present state.

Generally these images are a logical continuation of what is seen at earlier strains, with significantly increased fibrillation, the breakup of the large crystalline regions, and the growth of cracks parallel to the stretch direction. An unexpected feature is the structure seen on the centre right of figure 5.19, where the fibrils are not aligned with the stretch direction. These appear to form geometric shapes, and we refer to them as geometric crazes.
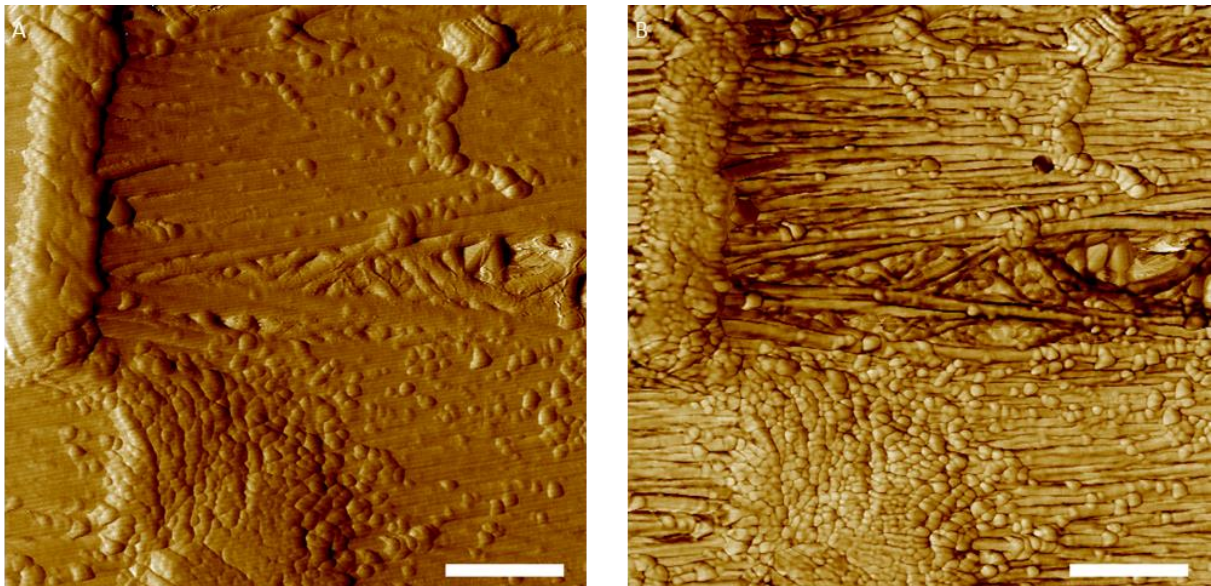
Figure 5.19 –Amplitude (A) and phase (B) images of highly stretched polypropylene. Most of the surface is fibrillated with individual crystallites within, there remain crystalline regions, the top retains its structure, whereas the bottom has broken apart. On the right in the centre of the image are fibrils that are not parallel to the stretch direction, but instead form geometric shapes. Scale bars 800 nm. Z scales 620 mv and 40 °.

5.5: Geometric crazes

Geometric crazes were seen very frequently in all samples at high strain. Examples are shown here in figures (5.19-5.21), they do not appear to have been

seen before elsewhere, though similar feature were seen in Chapter 6, for polyethylene near crack edges.

These features consist of regions of the craze where the fibrils are not aligned parallel to their neighbouring fibrils, the bulk of which are aligned perpendicular to the crazes' edges. Instead short sections of fibril are arranged in geometric patterns at angles to each other and the main parallel fibrils. These features are found to form between parallel fibrils in lens shaped formations with thicknesses a few times that of the fibrils themselves and lengths of up to a few μm. There tends to be a large number of these geometric crazes in the same region.

There is a phase difference with neighbouring fibrils as can be seen in figure 5.19 above, indicating they have different physical properties. They are assumed to be formed by a combination of localised strains occurring in multiple directions. These stresses perpendicular to the stretch direction occur due a mismatch in stresses caused by the opening of the crazes. With the crazes not always occurring perpendicular to the stretch direction and varying in width within the craze.
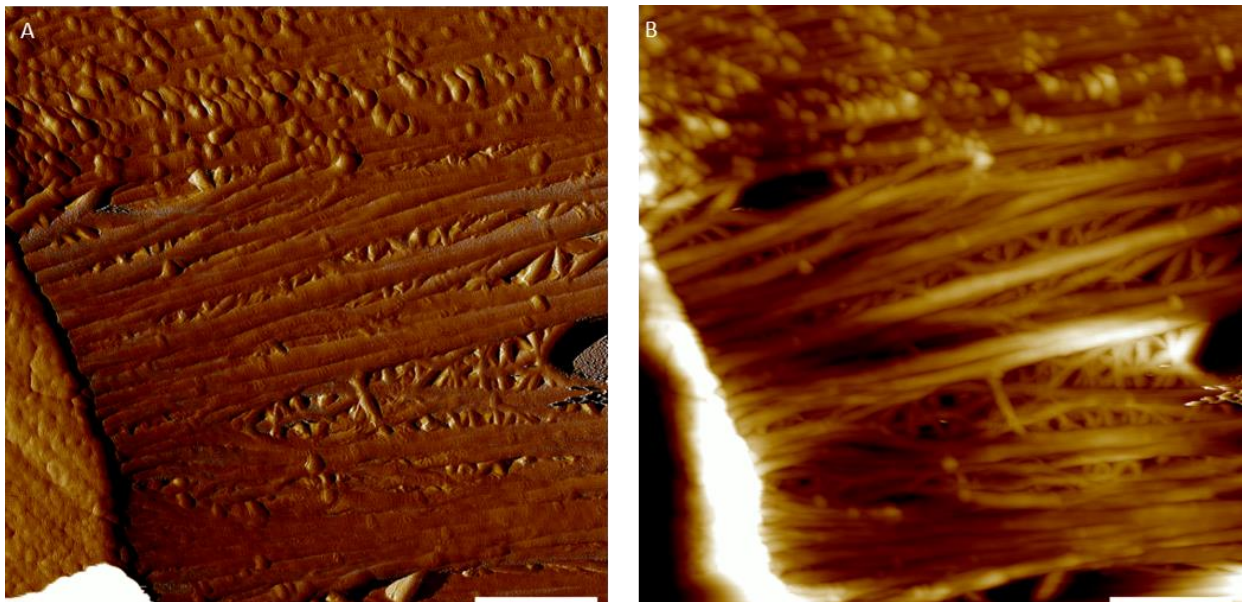
Figure 5.20 –Amplitude (A) and height (B) images showing numerous examples of geometric crazes with fibrils at different angles to the stretch direction. The feature in the bottom left is an imaging artefact. In the centre right one of the geometric crazes becomes a void

indicating that they could act as precursors to large scale void formation. Scale bars 800 nm. Z scales 200 mV and 180 nm.

Figure 5.20 is an example of an image with a large number of these features. It can be seen that they do not simply form in lens shaped regions, but can have more complex structures.

At the top of the image is an area where there are a large number of crystallites but no geometric crazes, whereas below there are few crystallites near to the geometric crazes. This is an observation that is generally repeated, perhaps large numbers of crystallites act to hinder their formation.

The height image allows us to see that the geometric crazes do not differ in height significantly to neighbouring fibrils, although they generally appear slightly lower. Present within the region with geometric crazes is a number of voids, in particular the one on the middle right edge which continues on as a voids a few μm in size. This would seem to indicate that these features can later lead to void formation.

Figure 5.21 gives another example of an image with geometric crazes, there are not as many as in figure 5.20 but there are still several present, this smaller density of the features is perhaps more typical. These share the same characteristics discussed before.
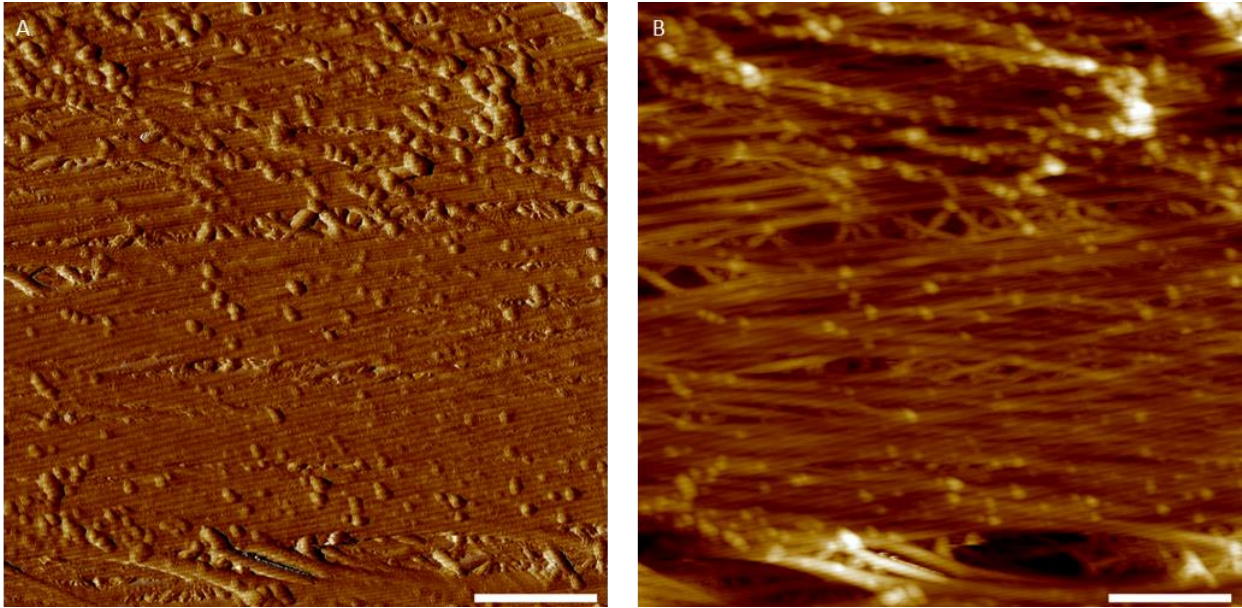
Figure 5.21 – Amplitude (A) and height (B) images showing examples of geometric crazes. There is noise present as small diagonal lines. Scale bars 800 nm. Z scales 170 mV and 70 nm.

5.5.1: Angular distribution of geometric craze fibrils

In order to understand these crazes it is useful to understand how they are arranged geometrically, as looking at the images it is possible to pick out many apparent shapes. To get a clearer picture the angular distribution of these fibrils in the geometric crazes was measured. Two different measurements were taken: fibril angle relative to both their nearest neighbours at each join, to see if any geometric shapes dominate; and also measuring their angle relative to the stretch axis. These values were measured by opening the images in Imagej and manually measuring the angles with the angle tool and the straight line tool.
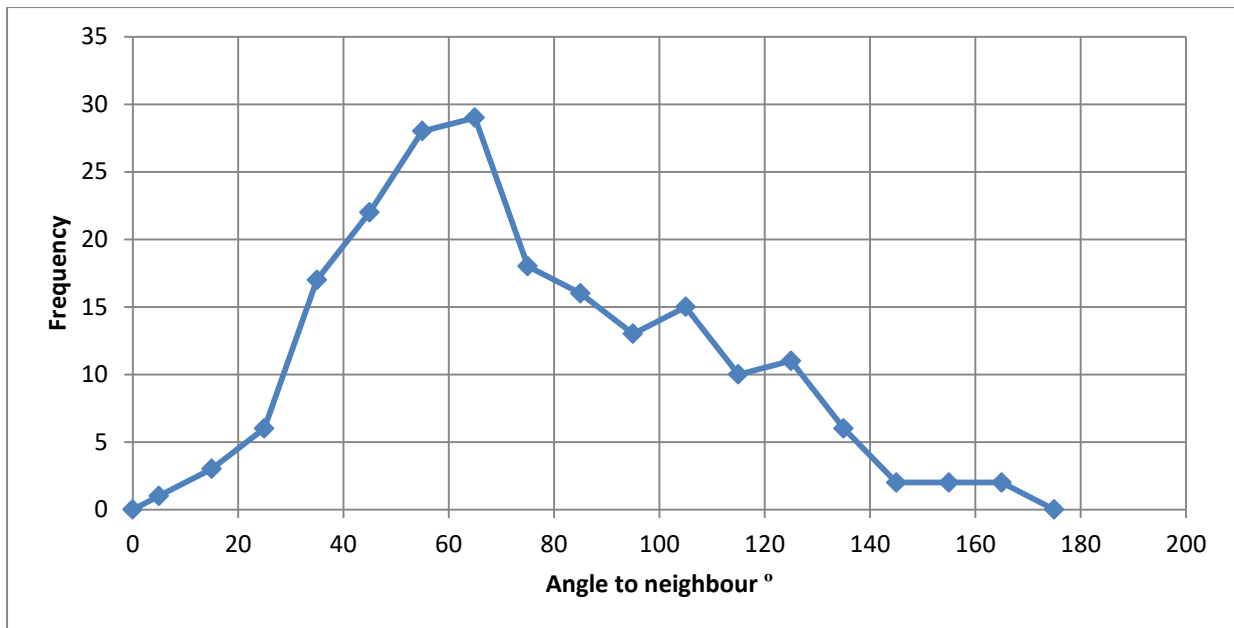
Figure 5.22 – Chart of frequency versus angle to neighbouring fibril for geometric crazes. There is a broad peak around 60 °.

Figure 5.22 shows the angle of the fibrils to its neighbours at each join. This shows a fairly broad peak at 60 °. There does not appear to be any significant peaks at other geometric angles such as 45 ° or 90 °, although examples of this can be seen in images. It is likely they are just cherry picking by the brain.

Figure 5.23 shows the angle of the fibrils to the stretch direction, this is similar to figure 5.22, with broad peaks at 60 ° and 120 °, which are both 60 ° to the horizontal, this angle is not in agreement with values for the shear banding angle, or any angles in the monoclinic unit cell indicating that is not the cause here.

An explanation for why 60 ° is the peak angle here is simply due the dominance of triangles in the structure of geometric crazes, with them being the simplest and strongest shape. If we assume that they are formed by a combination of localised strains occurring in multiple directions due to craze openings, then it seems they tend to move due to strain until they reach a point where they are supported enough to stop moving, which tends to be about 60 °.
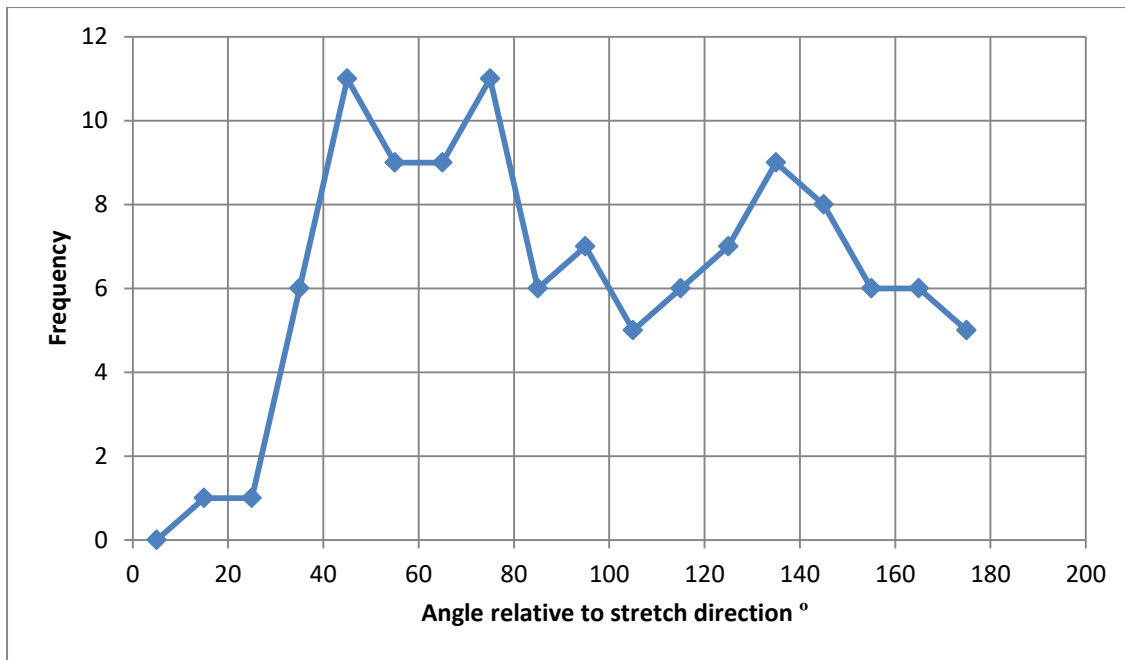
Figure 5.23 – Chart of frequency versus angle to stretch direction for geometric crazes. There are two broad peaks around 60 ° and 120 °.

5.7 Summary

To compare what we have observed to the process described in the chapter 2 it is useful to set out the sequence of the processes we have seen. The process has a number of differences. An example is shown in figure 5.24.

At the start, in A the sample is undeformed, it appears to be a kind of spherulite structure with individual crystallites separated by thin amorphous regions, and incipient crazes.

When the sample is stretched, in B there is no apparent increase in separation between neighbouring crystallites, and there was virtually no deformation seen in the crystallites themselves or crystalline regions up to high strains.

Instead the strain is taken up almost entirely by crazes. These sometimes were associated with the original incipient crazes, and sometimes formed in entirely new

places. These primary crazes are initially, long thin and aligned perpendicular to the stretch direction.

As the sample is stretched more, strain is seen to be extremely heterogeneous. Within a craze, there may be a significant difference in craze width, and nearby crazes can by of very different sizes. Often an area is seen to undergo strain and then stop whilst a nearby area undergoes strain in what appears to be localised strain hardening. In C the craze is seen to continue to grow and individual crystallites begin break off into the fibrils in crazes.

New crazes appear are seen to form later, rather than just at the start as is seen in D and E. In D a secondary craze has formed, secondary crazes form perpendicular to primary crazes to relieve strains caused by the primary crazes. In E a new primary craze has formed whilst the original craze hasn't. Within the crazes nanovoids are seen to form.

As the strain increases further the crazes continue to grow and the surface is increasing the fibrillated. Geometric crazes are seen in regions of the crazes. Individual crystallites continue to break off the crystalline regions, and there is now large scale breakup of some areas of crystalline regions into individual crystallites. Throughout this the crystallites themselves appear to have undergone little to no change.

At extremely high strains the surface is largely fibrillated, as is shown in F, though there are still a number of crystalline regions which remain undeformed. There is also large scale cavitation seen, with voids parallel with the stretch direction.
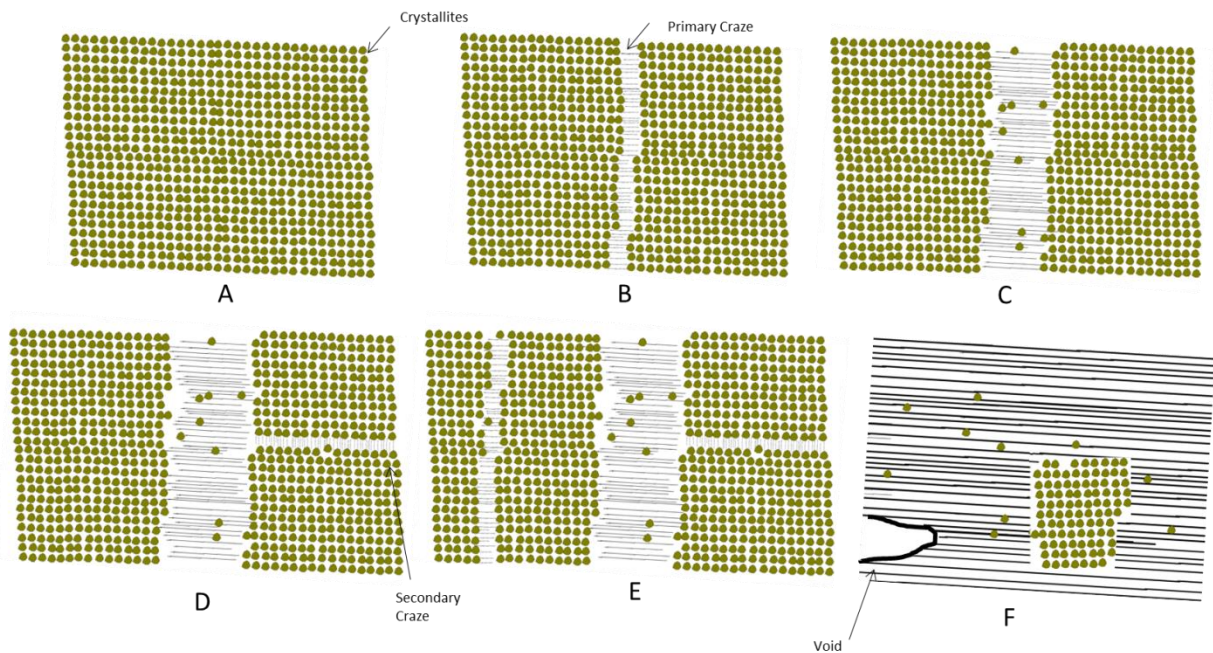
Figure 5.24 –An example of the processes seen for polypropylene with increasing strain. A – Undeformed, individual crystallites with amorphous regions between them. B – A primary craze opens. C – The craze grows and individual crystallites break off into the craze. D – Primary craze continues to grow and secondary craze appears. E – A new craze opens, whilst the old one don't undergo significant strain. F – Extreme strain leading to a highly fibrillated state. Some crystalline regions remain. Voids appear.

5.8 Conclusions and future work

The method developed in chapter 3 for observing deformation of polymers in situ, on the nanometre scale, was applied to polypropylene. Using this we have seen the processes as they occur, these largely agreed with previous studies, but important new insights were gained.

Strain was found to be almost entirely localised to crazes. Crystalline regions were found exhibit virtually no deformation, until individual crystallites broke off into the craze. At very high strains larger areas broke up into individual crystallites, these areas were seen to have a phase difference to undeformed crystalline regions, showing their changing material properties as they begin to break up.

The crystal blocks within the crazes can be traced back to the individual crystallites that form the crystalline regions, without appearing to shrink or undergo deformation. Thus it appears they act passively to the processes going on around them, which in contrast to the behaviour of lamellae in polyethylene.

The crazes, and in particular the largest primary crazes, were found to largely occur perpendicular to the stretch direction. Secondary crazes perpendicular to the primary crazes, were seen, these are formed due to mismatches in strains perpendicular to the stretch direction caused by the primary crazes opening.

The rate of individual craze growth was seen to vary between neighbouring crazes. They are seen to stretch at different times, with one staying relatively static whilst another stretches and vice-versa, which demonstrates localised strain hardening.

There are other processes which are seen in other studies which are not seen here including deformation banding and wedge formation; these are larger scale processes.

By watching the same areas over time we can begin to understand why the crazes form and grow where they do. The primary and secondary crazes are formed due to the overall strain, and perpendicular strains caused by mismatches respectively, however where they will occur is not clear. Some crazes seem to nucleate at defects and incipient crazes before propagating onwards, however this is often not the case. Many of the crazes we see here have propagated from outside the imaging area, which is sometimes visible in larger images.

Some crazes, however, clearly start in the imaging area without any defects, in fact crazes often choose routes next to but avoiding a defect, even if a nearby defect might seem to offer a more obvious route. This may be due to defects below the surface of the sample which we cannot see, or it may simply be that defects are not that important in choosing the best route to minimise strain.

To better understand this in the future it would be useful to repeat this data with larger scan sizes whilst still keeping the same resolution. This would increase the problem of drift and so to mitigate this higher scan speeds could be used, perhaps making use of techniques such as torsional tapping and torsional resonance AFM. It would also be useful to take more images in each set to better follow the processes. Applying a fitting procedure to follow the movement of the crystallites on the surface would also be useful.

A feature not seen in any previous studies is the existence of 'geometric crazes', these are areas within fibrillated regions where the fibrils are not aligned parallel to neighbouring fibrils, short sections of fibril are arranged in apparent geometric patterns at angles to each other and the main parallel fibrils. Similar features are seen in by crack edges in polyethylene in chapter 6.

They are assumed to be formed by a combination of localised strains occurring in multiple directions. These stresses perpendicular to the stretch direction occur due a mismatch in stresses caused by the opening of the crazes. In the future it would be useful to observe the formation of geometric crazes. This would require being able to follow the same area at high strains, and would require stretching the sample then choosing the area that was stretching the most to follow.

Angular analysis, showed the peak of their angles, both to themselves and to the stretch direction to be 60°, which is assumed be due the strongest structures tending to form, and doesn't seem to bear any relation to the shear banding angle or the unit cell.

Chapter 6 – In situ Observation of Fracture in Polyethylene Films

6.1: Introduction

How a polymer reacts to strain depends on its surroundings. Cracks and holes in a polymer will change how it deforms and fractures, by causing changes in the stress around the feature, thus creating complex local stress fields with forces of both extension and shear present

Cracks are a key problem for the structure of materials, not just in thin films as studied here but for a large range of fields including construction. Cracks can be very dangerous, as through fatigue they can lead to failure of the material. It is thus important to understand their effects on the microstructure of a material to understand its macroscopic properties.

In this chapter polyethylene film is used with cracks initiated in the sides and then stretched. Polyethylene is a simple, well characterised model system to see how in situ AFM can add to our understanding of these processes

Previous studies have been undertaken to study the behaviour of polyethylene and other semi-crystalline polymers near a crack. These include SAXS [68][74] however these only provide information on changes in structure averaged over a large area of the sample. Also imaging techniques including AFM [88] and EM [148][149] however they provide snapshots rather than seeing how an area evolves with increasing strain, or follow the same area at low resolution.

6.2: Experimental details

This experiment uses the same setup as seen in chapters 4 and 5. The same polyethylene film as chapter 4 is used, cut into dog bone shapes and attached to the

stretching stage. The key difference is that a crack is cut into film. Two cracks were cut into the film on either side of the neck to increase the number of samples to investigate. The cracks were initially approximately 100 μm in length and 1 μm wide. With a total neck width of approximately 1 cm, the cracks were judged to be too far apart to influence one another.

Cracks were cut with either a scalpel or a razor blade. Original a single crack was made in the centre of the neck by cutting from above, however this was found to produce scratches in the sample at the crack tips, damaging the area that was to be investigated. Instead cracks were cut from the sides of the neck, edge on, which led to a clean cut, as can be seen in figure 6.1.
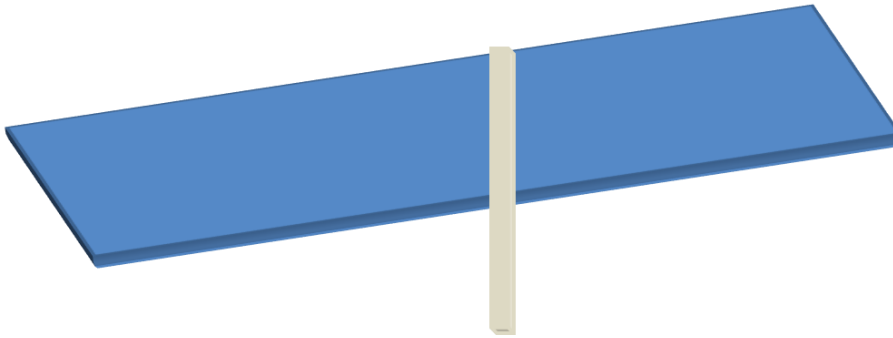
Figure 6.1– Schematic of the razor (grey) cutting the film (blue) from the side, edge on.

After this the samples were stretched and left to settle for approximately 30 minutes before imaging. The stretches were much smaller in macro strain than for simple stretched polyethylene as the strain was concentrated by the crack tip. Stretching causes both the crack to widen and to propagate forwards, however its propagation was much smaller than the widening. An example can be seen in figure 6.2.

Leaving the crack to settle caused it to widen slightly, and if left overnight it would widen more, indicating that the crack was always moving rather than settling, which is as expected [5].
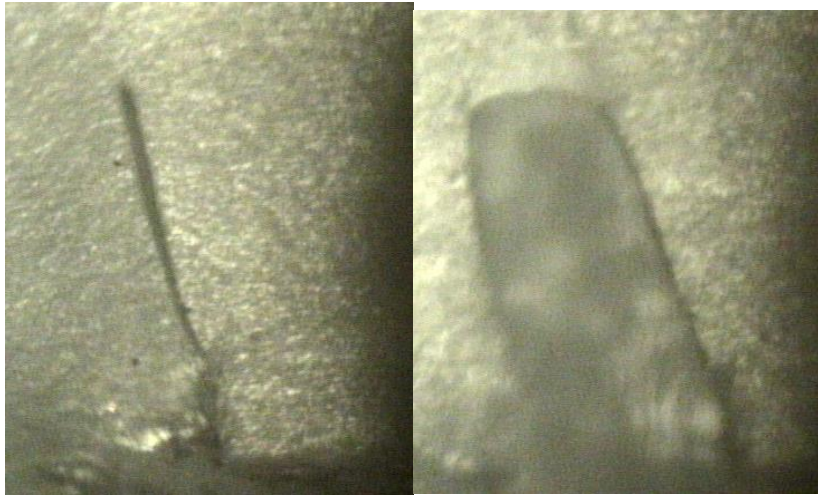
Figure 6.2 - Optical images of a crack taken before (left) and after (right) stretching. Note that there is little propagation of the crack and it has assumed a rounded rectangular shape.

6.2.1: Strain measurements

It is important to measure the strain. Methods for measuring this are largely as described in chapter 3. The three types of strain described there are: macro strain which is measured from the dials of the stretching rig and the initial measurement of the neck, optical strain which is measured from 2 points on the sample using the AFM optics, and AFM strain which is measured from 2 furthest measurable points on AFM images of the sample.

The material in this chapter is polyethylene, the same as in chapter 4, however the crack acts to localise the strain leading to some unique challenges in measuring the strain.

The macro strain has virtually no relation to the strain near the crack and so is not useful. The optical strain can be measured either from the breakup of an ink-dot or the width of the crack. The ink-dot was found to be superfluous for both strain measurement and finding the same area and so was not used for later experiments. This strain is a useful measure, but has little relation to the strain on the lamella scale

which is highly localised by the crack tip and varies greatly within a few μm. AFM strain measurements were thus used.

The strain values could only be calculated in sets of images where the same area was imaged as it stretched. In single images or sets approaching a crack edge this could not be achieved. It is possible to estimate the strain by comparing the images to those that are part of sets, however this was found to be highly subjective and so is not shown here.

6.3: Single AFM images of polyethylene near the edge of a crack

To start with individual images were taken in various places near the crack. The degree of deformation was found to vary greatly with distance from the edge. Figure 6.3 shows an image taken a significant distance from the crack edge, approximately 100 μm. At this distance there is no deformation seen, the area here is similar to the bulk of the neck, in that it is essentially undeformed polyethylene which matches with the images seen in chapter 4. How the deformation varies with distance from the edge can be better seen later on in section 6.5.

The sample consists of crystalline lamellae and small amorphous regions between them, the lamellae appear as bright lines and the amorphous regions as thin dark areas between them. Here the lamellae are largely edge on and thus appear as sharp lines; initially they are generally aligned perpendicular to the stretch direction with some deviation. At this stage there is no fragmentation of lamellae, nanovoiding or fibrillation present and the lamellae are largely straight.
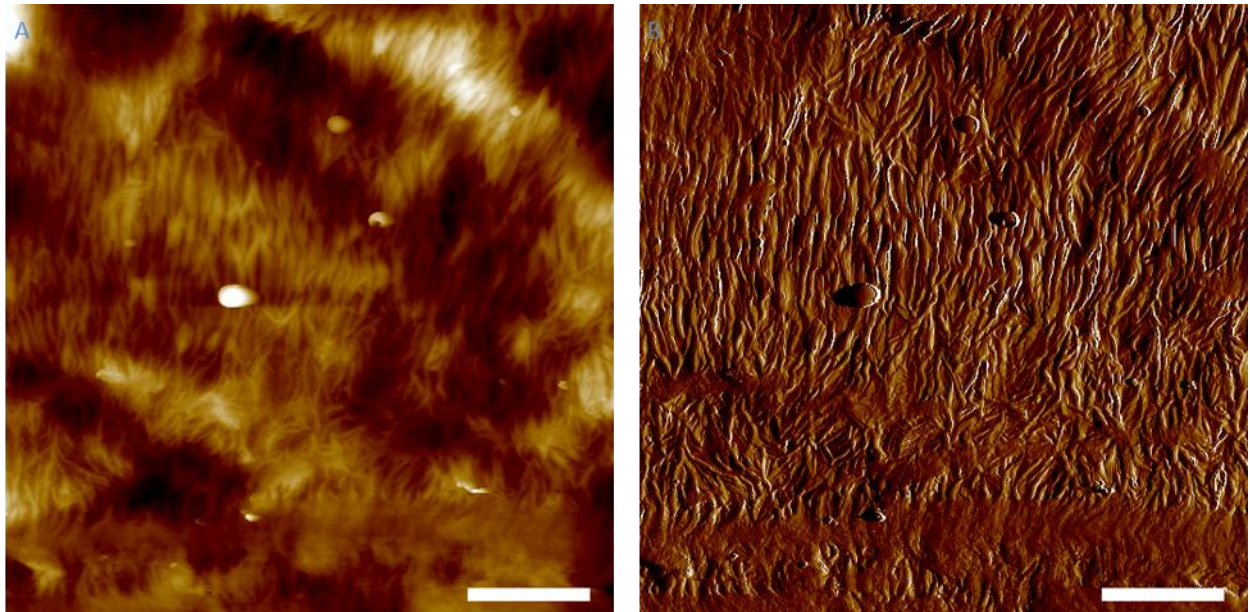
Figure 6.3 – Height (A) and amplitude (B) images taken approximately 100 µm from the crack tip. This area shows no visible deformation, demonstrating the small scale effect of the crack tip's presence. Scale bar 800 nm. Z scales 270 nm and 840 mV.

Figure 6.4 was taken nearer to the crack tip, approximately 8 µm away. Here significant deformation can be seen. The lamellae have separated from their neighbours; they have undergone significant tilting and rotation to align with the both overall stretch direction and the edge of the crack tip. There are some small voids and crazes, as well as some fragmentation of lamella into smaller blocky elements with fibrils formed between them.

The bottom of the image is closer to the crack edge, which leads to a general increase in deformation. This is visible on this length scale, with the lamellae more aligned with the crack edge; this transition, however, is not very uniform.
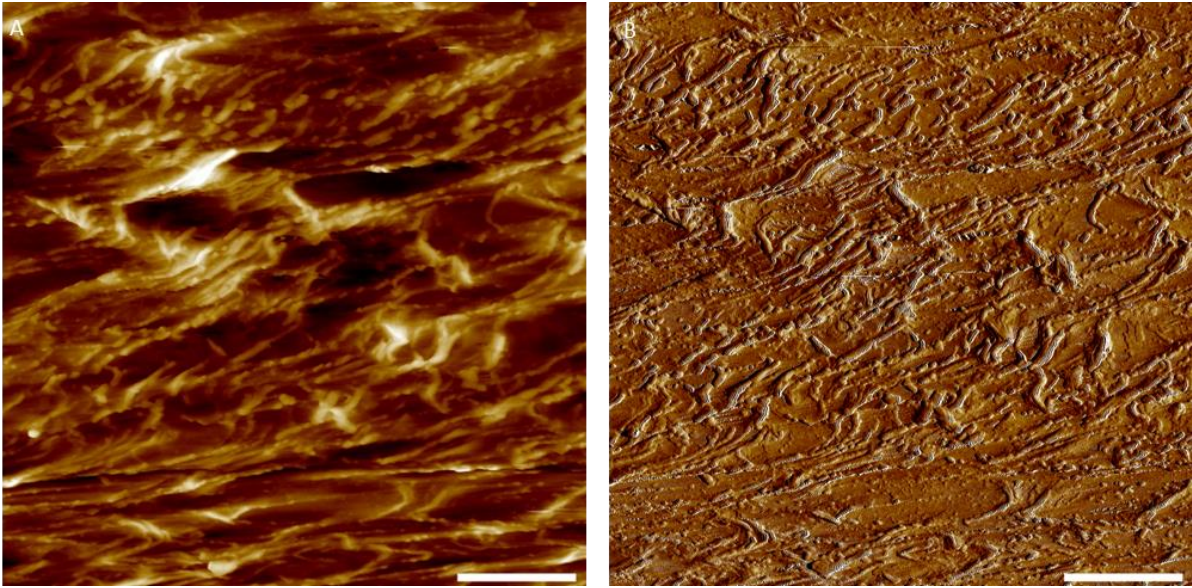
Figure 6.4 – Height (A) and amplitude (B) images taken approximately 8 μm from the crack tip. Scale bar 800 nm. Z scales 200 nm and 700 mV.
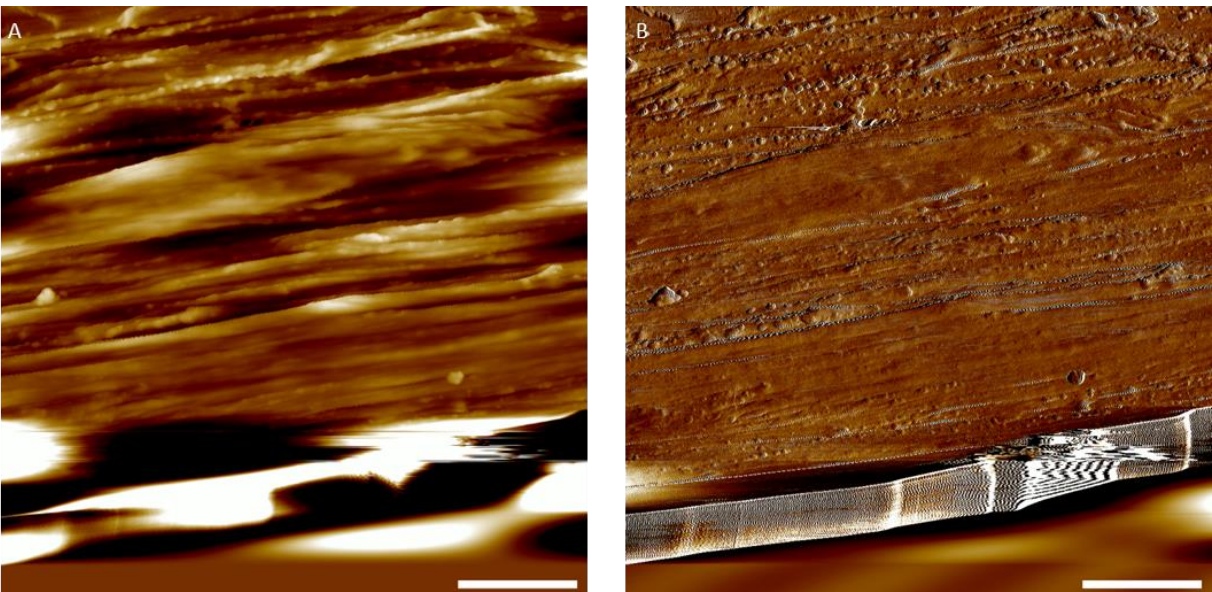
Figure 6.5 - Height (A) and amplitude (B) images showing the edge of the crack tip at the bottom of the image. Scale bar 800 nm. Z scales 200 nm and 500 mV.

Figure 6.5 was taken at the edge of the crack tip, which is visible at the bottom of the image where the AFM cannot track the surface any more. The film has now transitioned into a new state which is almost completely fibrillated with a large number of blocky elements, which have formed from the lamellae. The fibrils are highly ordered and are well aligned with the crack edge.

The film near the crack edge has a lot of similarities to the end stage deformation of stretched polyethylene as seen in chapter 4; the key difference is that here the fibrils are more closely spaced, with a lack of voids present. This is likely due to the confining effect of the crack edge, as well as any effects due to shear.

Figure 6.6 was taken near the left side of the tip of the crack, approximately 10 µm from the edge. The image is of low quality with a large number of lines and a failure to track the surface on the left side of the image. This is because there is significant difficulty in taking images near the sides of the crack as the film is not well supported and so is prone to be moved by the AFM. A change in scan direction to 90° was tried, but didn't help imaging. Another example of an image from the side of the crack tip can be seen in figure 6.11 later on.

Nevertheless, the images allow us to see what occurs at the sides of the crack tip, the left side of the image is further from the edge, here the lamellae are aligned roughly horizontally and are relatively undeformed. On the right side the lamellae are aligned roughly vertically, with the crack tip. They have begun to break up into blocky elements and the area is highly ordered. There appears to be a faster transition from undeformed to highly aligned, than in areas in line with the crack tip.

The fact that the lamellae are aligned with the crack edge shows that the strain caused by the crack edge is much greater than the overall strain. It also shows that the film is deformed parallel to the edge, rather than simply pulled apart. This is in agreement with the literature [68].
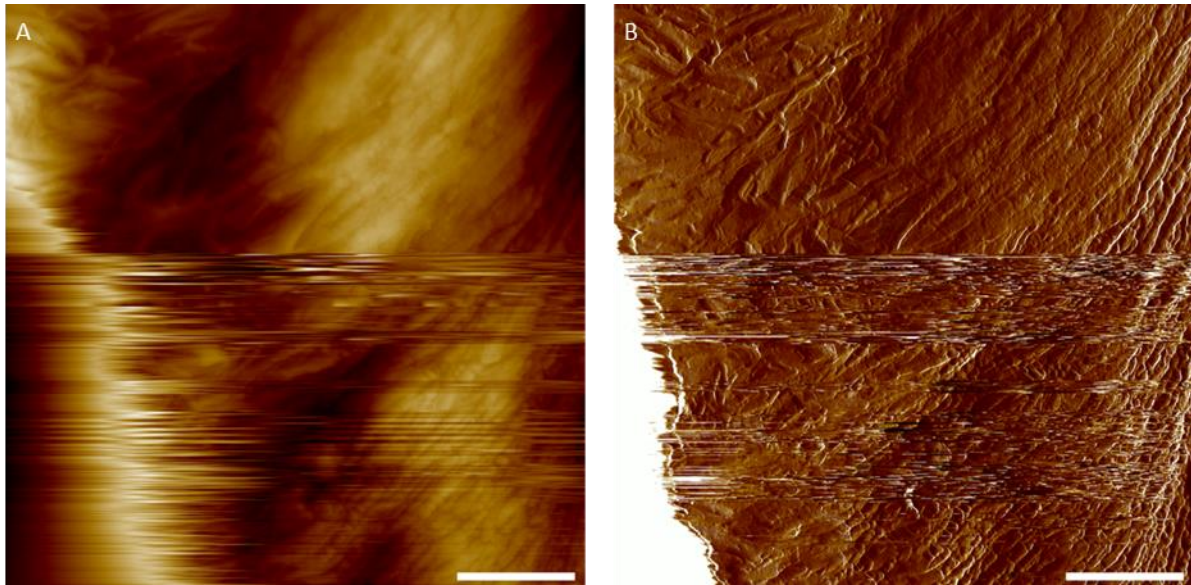
Figure 6.6 - Height (A) and amplitude (B) images taken 10 μm from the left side of the crack tip. Scale bar 800 nm. Z scales 650 nm and 800 mV.

Taken together these images give us an idea of the strain map around a crack tip. The strain is largely parallel to the crack edge and decreases with distance. In areas in line with the crack the deformation continues much further out. This implies a flow of material towards the tip.

6.3.1: Well defined white areas at the end of cracks with high uniform deformation

When looking at the cracks optically there is usually a white area at the end of the crack tip. This is optical whitening, indicating that this area is highly deformed and there are roughly micron length features scattering the light. In many cases there is a large well defined white area within which there is a sustained high deformation that appears relatively uniform, these are approximately 100 μm in size. This can be seen optically in figure 6.7, comparing it to figure 6.2 we can see that the white area is clearer, larger and its edges are better defined.

It is not clear what triggers the formation of this structure. It was thought that it might be formed when the crack is cut with a blunter object due to greater

multiaxial forces, however testing with a sharper razor and a blunter scalpel both led to the formation of both types of regions.

Figure 6.7 –Optical image of a crack with a white area at the crack tip. The white area is much larger and clearer than in figure 6.1.

Figure 6.8 is a 10 μm image taken in the centre of a white area. It shows the structure with the lamella have completely broken up into widely spaced blocky elements and a completely fibrillated surface. This is similar to the structure at the crack edge though less closely packed.

There is also some larger scale structures of less deformed material with lamellae still intact, this is clearest as the white band in the bottom of the height image which is higher than the surrounding highly deformed material.

Over the scale of the image it is relatively uniform, with no clear difference in deformation between the top and bottom of the image. This remains similar throughout the entire white area.
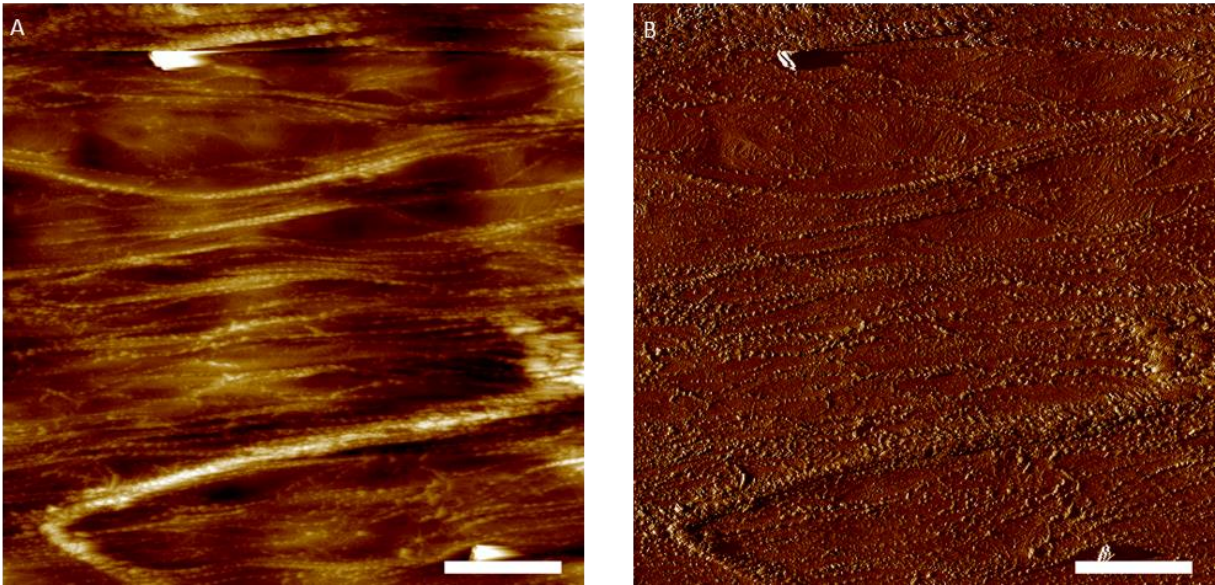
Figure 6.8 – Height (A) and amplitude (B) images taken within the white area. Scale bar 2 µm. Z scales 210 nm ad 710 mV.

A 4 µm image is seen in figure 6.9 which is from a different sample; this allows us to see more details of these areas. The surface is almost entirely fibrillated, with the blocky elements, which are the remains of the lamellae, within them. The features are generally aligned with the stretch direction and crack edge.

Different regions within the image have different characteristics. In the bottom half and top left the fibrils are tightly packed and well-ordered and there is little space between blocky elements.

Most of the top half of the image has a different structure, with the main long fibrils parallel to the stretch direction with significant separation from each other, and with widely spaced blocky elements.

Between the main fibrils are regions where the fibrils are not aligned parallel to their neighbouring fibrils, instead short sections of fibril are arranged in geometric patterns at angles to each other and the main parallel fibrils. We refer to these formations as geometric crazes, this is the same name we use to refer to similar features in Chapter 5 in very highly stretched polypropylene. They do not appear to

have been seen elsewhere before. Geometric crazes do not only occur in these highly defined white areas, but can be found in other highly stretched areas.
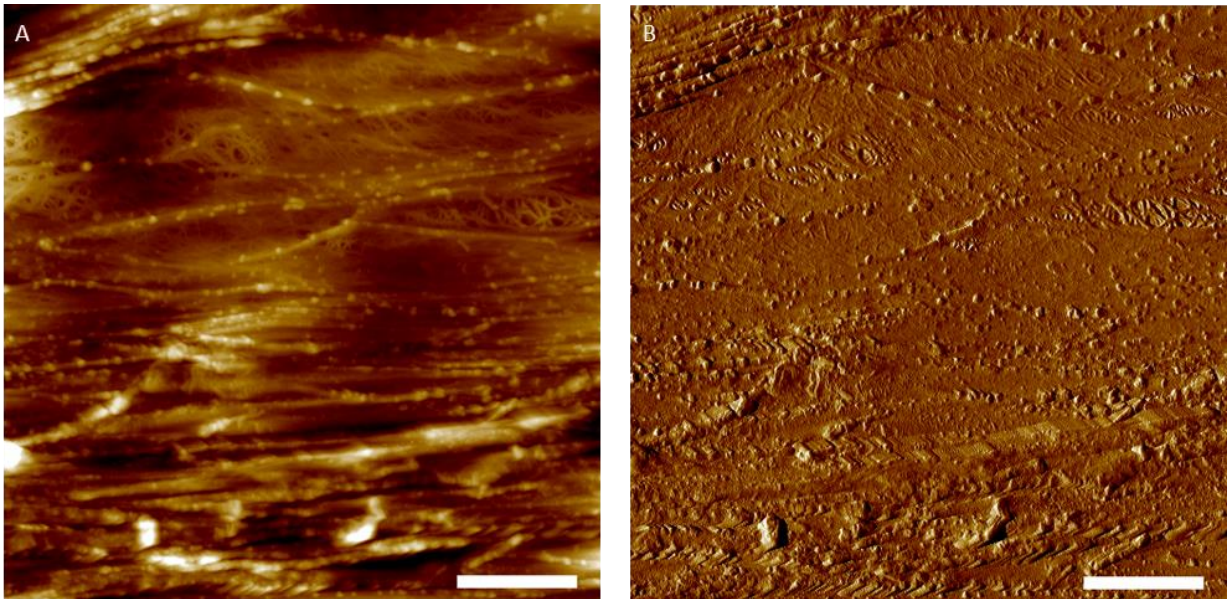
Figure 6.9 - Height (A) and amplitude (B) images taken within the white area. Scale bar 800 nm. Z scales 100 nm and 400 mV.

6.4: Geometric Crazes

Geometric crazes were found to occur very frequently in most samples at high local strain. There are many examples shown throughout the chapter, in figures (6.9-6.11, 6.14-6.18 and 6.22-6.23)

Figure 6.10 is a zoom in on a region in the top left of figure 6.9, an area dominated by geometric crazes. This is a pattern that is seen often, there tends to be a large number of these geometric crazes in the same region and large regions without any, indicating that local conditions lead to their formation.

The features are seen to form between widely spaced main fibrils in large formations of varying size and shape. The regions are longer in the direction of strain and can range up to half a μm in width and a few μm in length.

The individual fibrils are approximately 20 nm in length and a thickness of a couple of nm, they are usually significantly thinner than the main fibrils. The fibrils are arranged so that they are connected to nearby fibrils at points, and the angles of the fibrils relative to each other appear in many instances to be forming fairly regular shapes.

There are no blocky elements within the geometric crazes, they exist only on the main fibrils, which are widely spaced near geometric crazes indicating that the local strain is higher.
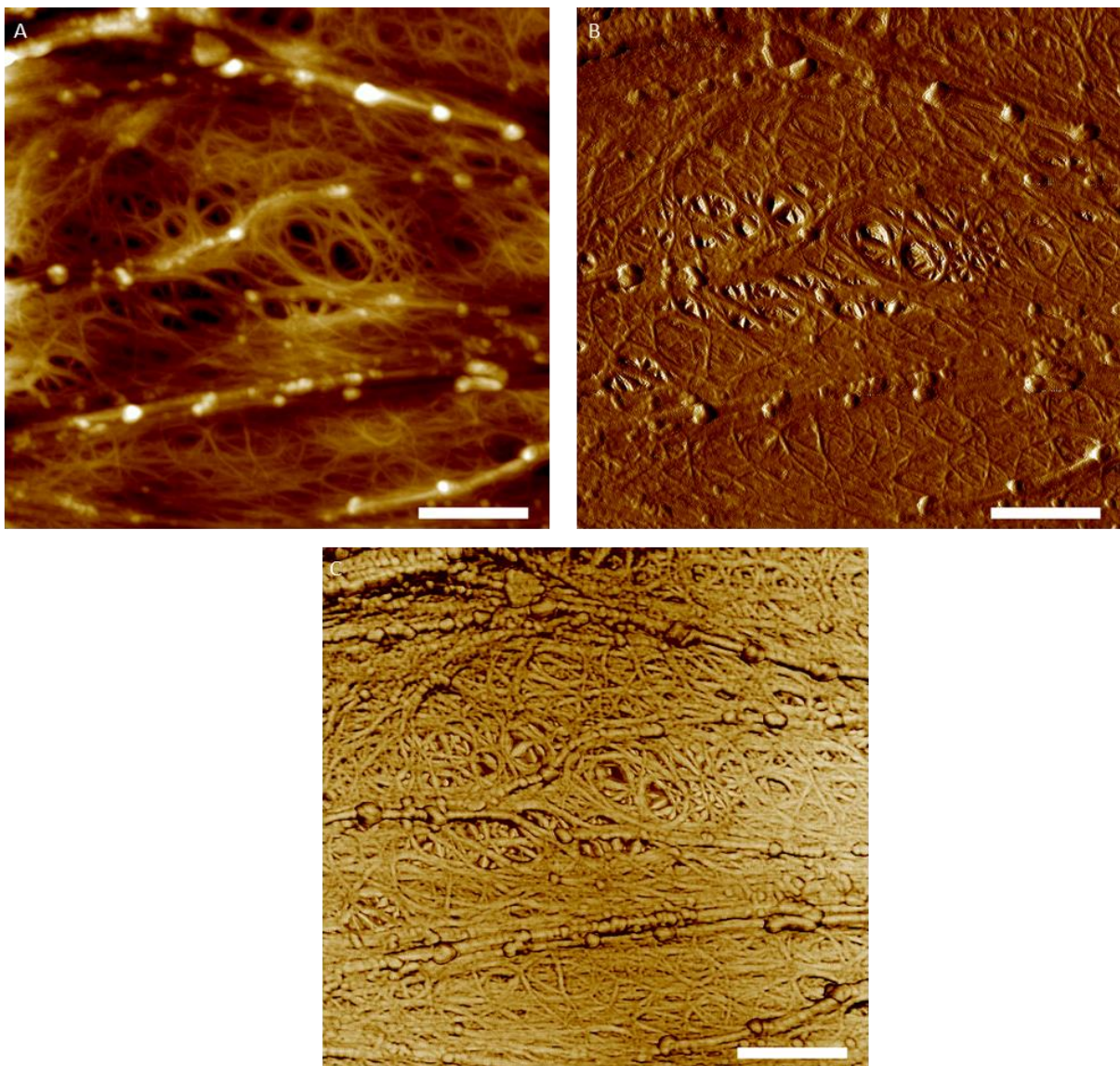
Figure 6.10 - Height (A), amplitude (B) and phase (C) images centred on a region of geometric crazes. Scale bar 300 nm. Z scales 40 nm, 160 mV and 70°.

Figure 6.11 shows an example of geometric crazes occurring in an area of the sample to the side of the crack tip, where the main fibrils are aligned vertically. They once again occur between the main fibrils and occur at a range of angles. Their presence here shows that geometric crazes don't only occur in line with the crack tip, with the conditions also occurring here.

The geometric crazes here are simpler and they exist as long thin areas between fibrils, however this may just be coincidence as it is the only image of geometric crazes at the side of the crack tip.
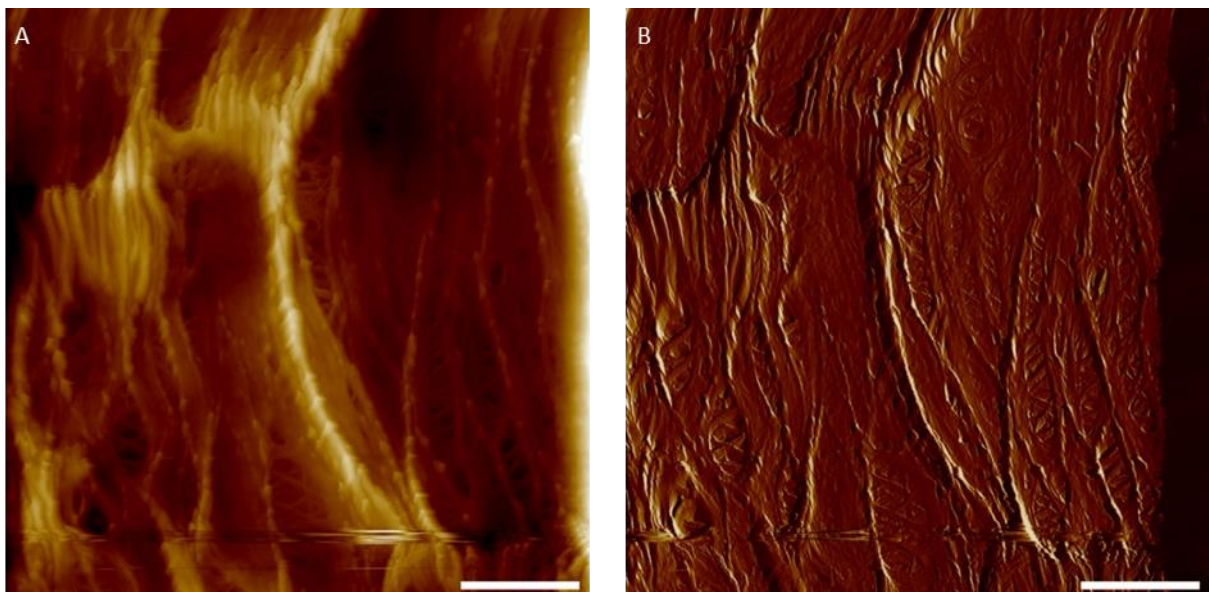
Figure 6.11 - Height (A) and amplitude (B) images taken on the left side of a crack tip. Some geometric crazes are seen here. Scale bar 300 nm. Z scales 530 nm, 1600 mV.

6.4.1: Angular analysis of the geometric crazes

To help understand these crazes it is useful to analyse them geometrically. Looking at the image such as figure 6.10 it is possible to pick out many apparent shapes, but to see what, if any, shapes dominate an angular distribution of the fibrils was undertaken.

The process was the same as in chapter 5, with Imagej used to manually measure angles on areas of geometric crazes within images, the values for a number of images were collected and the data for all of them are shown on the graphs here. Once again two different measurements were taken, one for the angle of a fibril relative to the stretch axis and one for the angles between joins.

Figure 6.12 shows the angle of the fibrils to its neighbours at each join. This shows the main peak at 40° and a secondary peak at 80° with other possible peaks at further multiples. This pattern was seen in all images investigated.
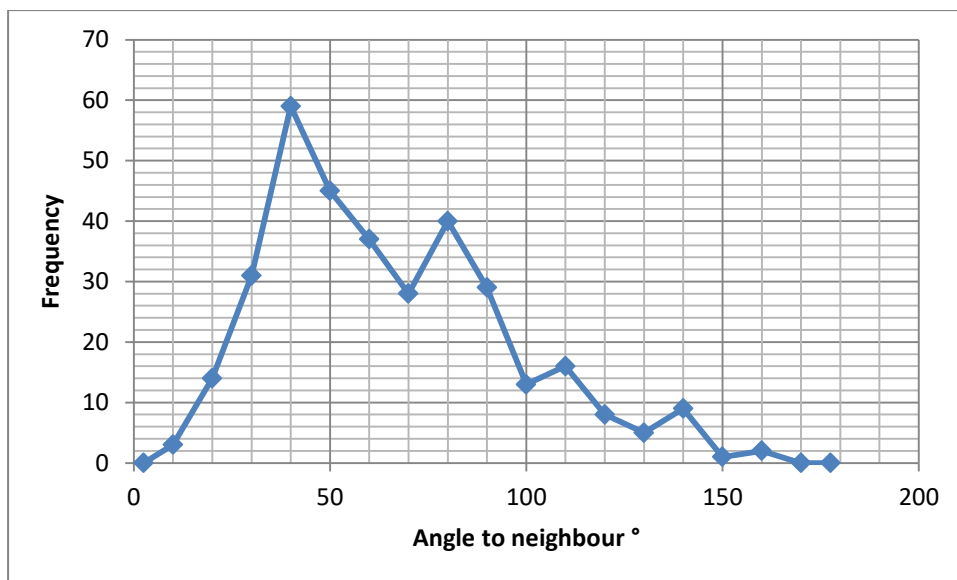
Figure 6.12 - Chart of frequency versus angle to neighbouring fibril for geometric crazes. There are large peaks at 40° and 80°.

Figure 6.13 shows the angle of the fibrils to the stretch direction, it shows five peaks roughly evenly spaced. $180^{\circ}/5 = 36^{\circ}$ and so these values are consistent with figure 6.12, which had a primary peak at 40°. This angle is somewhat similar but not in agreement with values for the shear banding angle indicating that is not the cause here.

There was some variance in individual images, all had five visible peaks. In some images the peaks were equal in size where in others the first peak was

significantly larger than the others. This variance shows a dependence on the local conditions.

These results are very different to those seen for the geometric crazes in polypropylene in chapter 5, where there were broad peaks around 60 ° and 120 °. As to why the principle peak here is 40 ° instead of 60 ° we don't know, other than the different material properties lead to different outcome. The angles do not seem to agree with the shear banding angle or any angles in the monoclinic unit cell or orthorhombic unit cell.
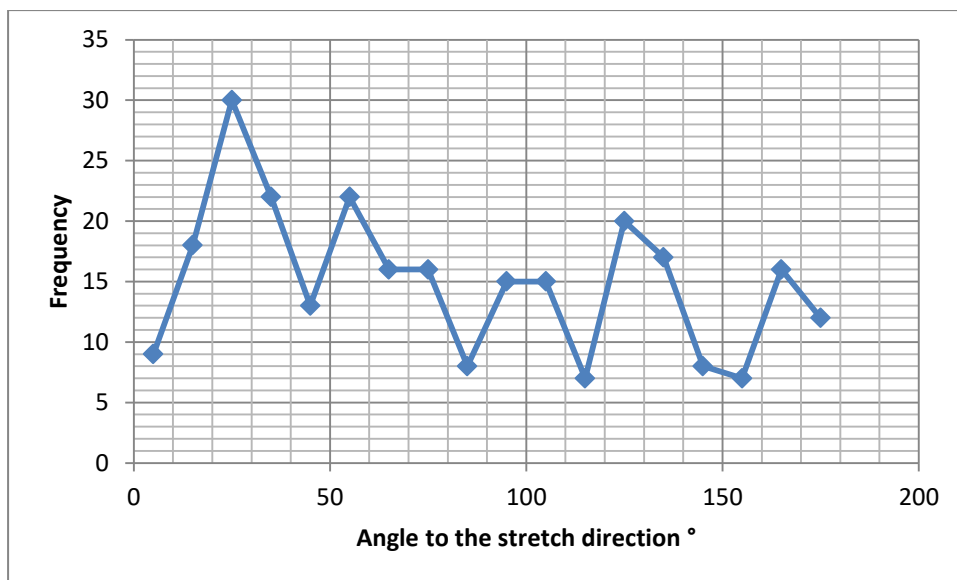
Figure 6.13 - Chart of frequency versus angle to stretch direction for geometric crazes. There are five peaks roughly evenly spaced.

6.5: Sets of neighbouring images approaching a crack edge

To get a better picture of how the deformation varies depending on position relative to the crack, sets of images were taken of neighbouring areas. This was achieved by imaging an area then offsetting to what should be the area bordering it and taking a new image. This process was repeated to form lines of images showing

how the sample changed with distance to the crack. As an open loop scanner was used there was usually significant overlap between neighbouring images.

Figures 6.14 and 6.15 show a set of images, in both height and amplitude, which head towards the edge of a crack without a defined white area. The images have been overlaid to form one continuous image. From top to bottom there is a significant change in deformation.

At the top, in the first couple of images, the sample exhibits some deformation but it is not that substantial despite only being approximately 20 μm from the crack edge. The lamellae here show more spacing and alignment to the stretch direction than in undeformed areas, many lamellae are buckled to form chevrons. A number of small voids and crazes are present.

Further down the deformation increases, with the lamellae becoming significantly more aligned with the crack edge, because of this there are significantly fewer buckled lamellae as the sample becomes more ordered. The small voids and crazes disappear to be replaced by larger fibrillated areas. After aligning with the crack edge lamellae start to break up into individual blocky elements.

At the bottom of the set near the crack the system is highly ordered, with the surface completely fibrillated, the fibrils all align with the crack edge and are closely packed. Blocky elements are highly spread out along the fibrils. Some geometric crazes can be seen in these regions.

This set is useful as it shows the scale over which these changes in deformation occur. It also shows that there is not a uniform progression of deformation; some areas can seem more deformed than the areas below them, such as the top of the section on the right compared to the area directly below.

The images also show the scale of the drift of the system. This can be seen from the position of the images relative to each other, as subsequent images are

137

slightly to the side of the previous image. Each image took 1024 seconds, 17.1 minutes, during which there is a drift of approximately 200 nm, which is approximately 10 nm/min.

Figure 6.14 – Set of overlapping amplitude images heading towards the crack edge on a crack without a defined white area. Each individual image is 4 µm, scale bar 800 nm. Z scale 500 mv. (Left) set in full, (centre and right) set split in two to see it at a larger scale. Same set as in figure 6.15.
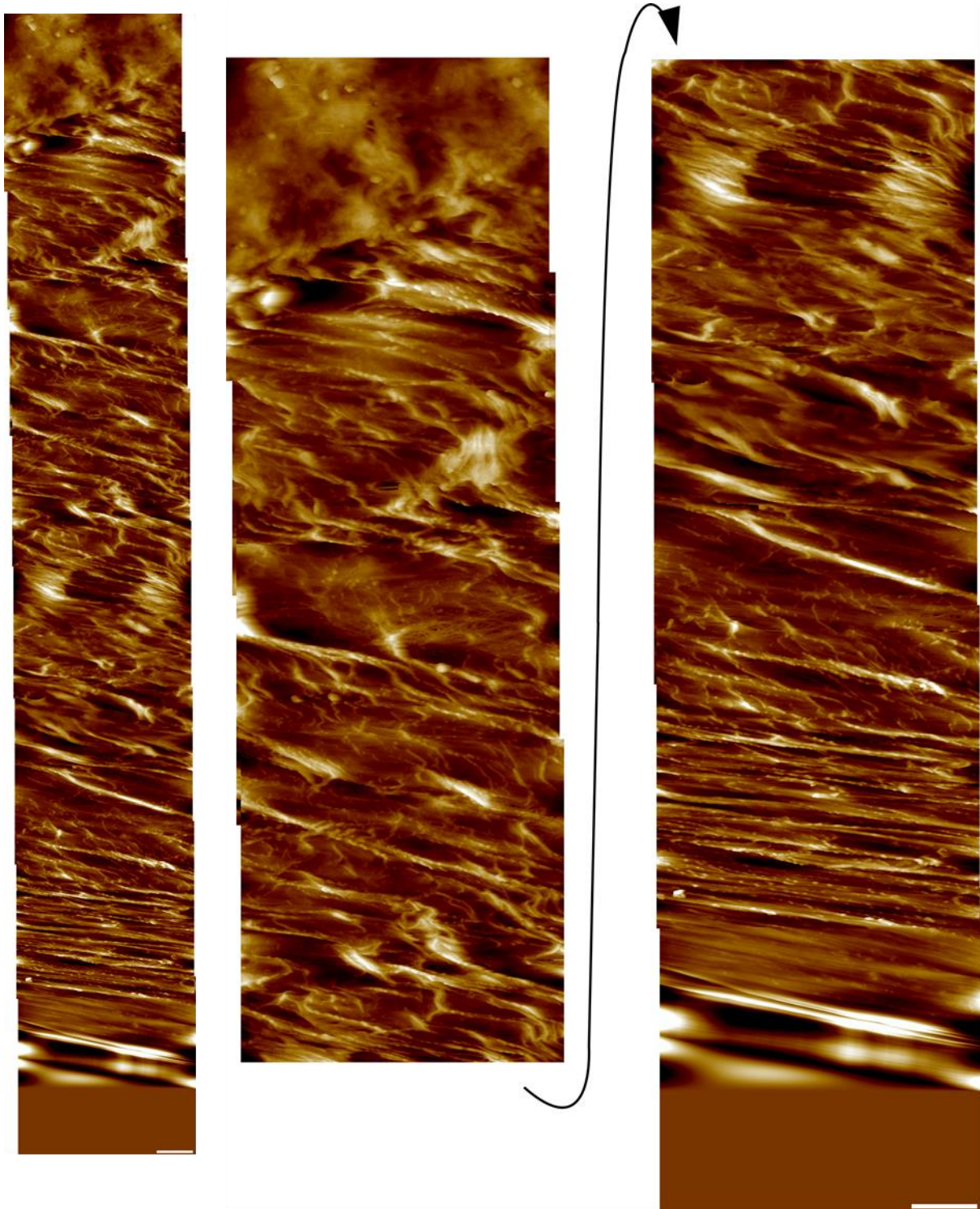
Figure 6.15 - Set of overlapping height images heading towards the crack edge on a crack without a defined white area. Each individual image is 4 µm, Scale bars 800 nm. Z scale 200 nm. (Left) set in full, (centre and right) set split in two to see it at a larger scale. Same set as in figure 6.14.

Figures 6.16, 6.17 and 6.18 are two sets both taken on the same sample. Figure 6.16 show the height and amplitude channels for a set of images moving from next to the defined white area to within it, in line with the crack, figure 6.17 shows a blown up version of the amplitude channel. Figure 6.18 is a set further down, from the white area to the crack edge.

At the top of figures 6.16 and 6.17 the set starts similarly to figures 6.14 and 6.15, with the sample showing moderate deformation. The deformation appears smaller here as it is further from the edge to the white area than they are to the crack.

Further down the deformation increases, largely as seen before, with an increase in alignment of the lamellae and a close packing of them, after which they begin to break up into blocky elements. The change in deformation with distance is similar to in figures 6.14 and 6.15 indicating there are similar mechanisms at work.

Towards the bottom of the set there is a cross over into the well-defined white area. From the optical image it is not possible to tell when this occurs. However in figure 6.17 in the middle of the right section there is a sharp black line which seems to provide the edge, this is also visible in the height where the AFM tracking goes bad, possibly because of a drop in height.

After the edge there is a clear change in the structure. It now matches that of previously seen white areas, which have a highly fibrillated state with blocky elements and the fibrils less closely packed than at craze edges. On the left side here there is also a less deformed band where the surface resembles the surface above the edge, this has been noted before in figure 6.8. Further down geometric crazes are seen, otherwise the structure does not appear to change significantly going further into the white area.
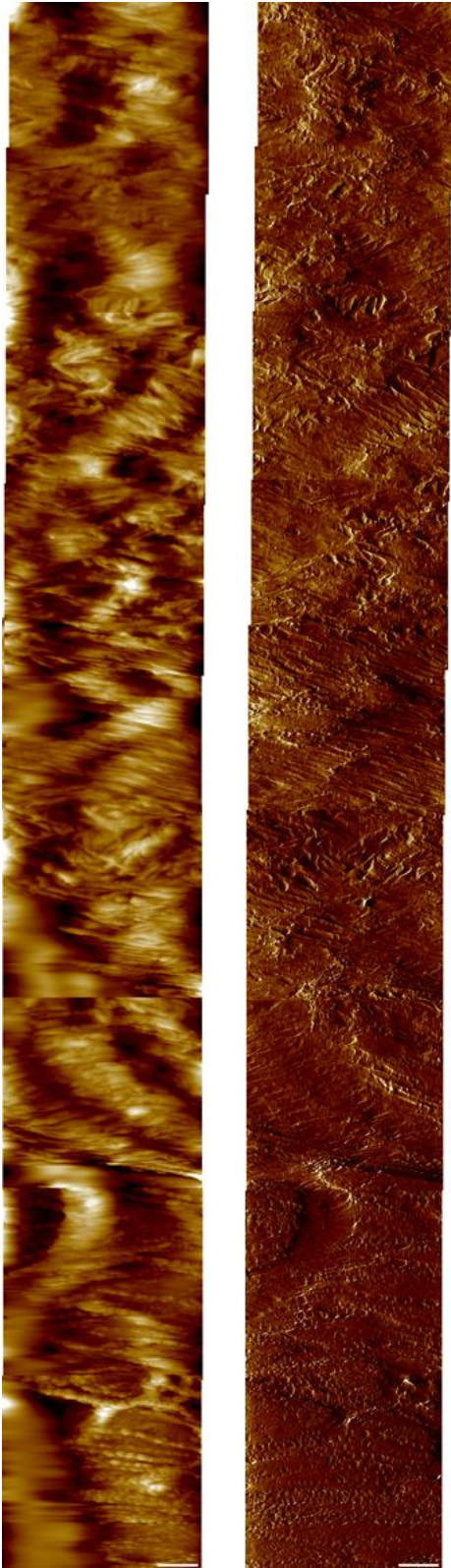
Figure 6.16 - Set of height (left) and amplitude (right) images on a crack with a well-defined white area, heading towards and over edge of the white area. Enlarged amplitude set in figure 6.17. The height shows poor tracking on the left of some images as retrace was saved rather than the trace. Each individual image is 4 μm, scale bar is 800 nm. Z scales 550 nm and 800 mV.
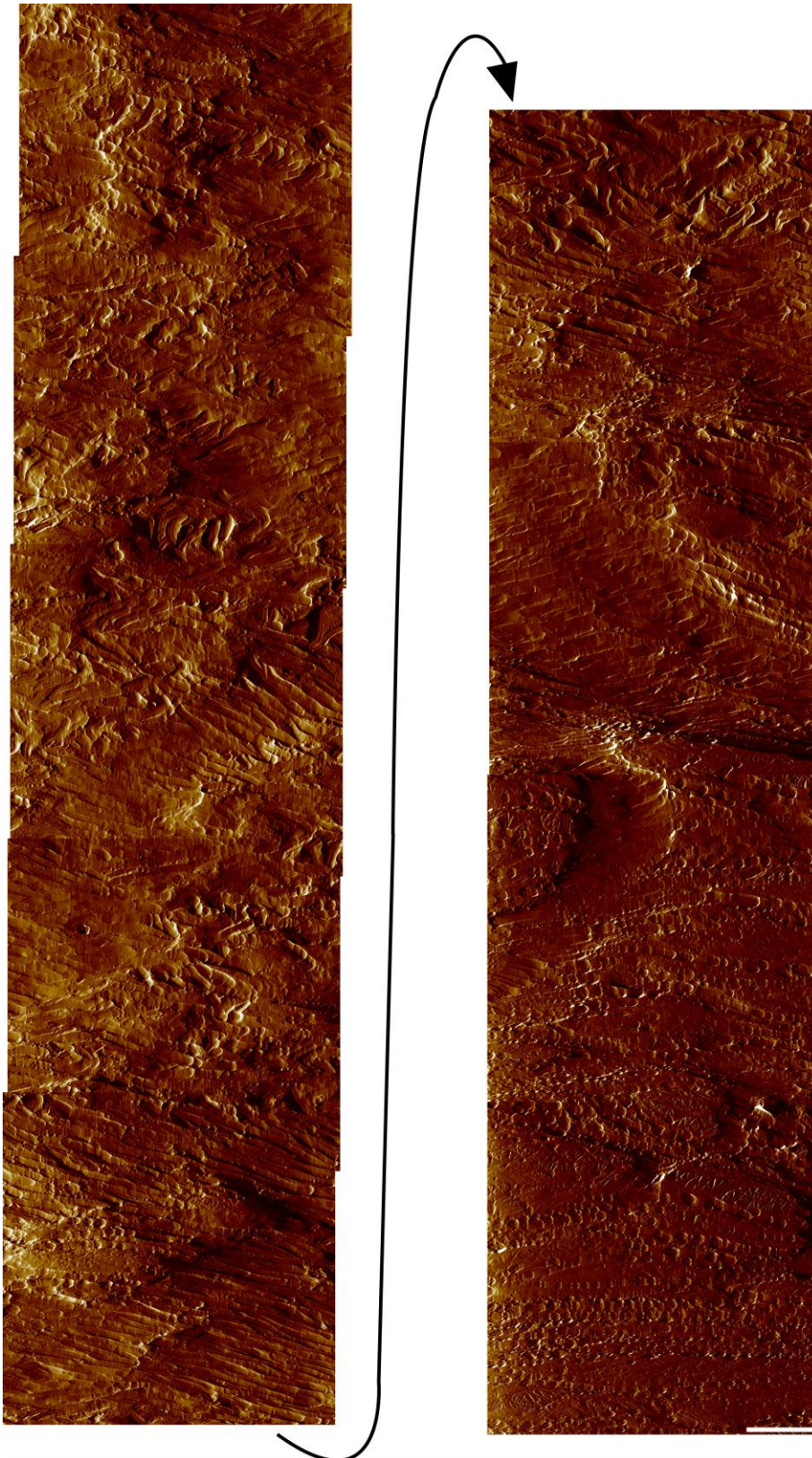
Figure 6.17 - Set of amplitude images on a crack with a well-defined white area, heading towards and over edge of the white area. Set split in two to see it at a larger scale. Each individual image is 4 μm, scale bar is 800 nm. Same set as in figure 6.16. Z scale 800 mV.

Figure 6.18 is a set of images heading from within the defined white area to the crack edge. For most of the set the structure is very similar to that seen in other images on white areas, with highly aligned fibrils, blocky elements and geometric crazes. This set starts approximately 100 µm below figure 6.17, yet the structure hasn't changed. This shows that throughout the white area there is a relatively uniform level of deformation and that this is the case even at both larger and smaller length scales.

Near the crack edge there are some changes in the structure, with the blocky elements appearing smaller and the fibrils less widely spaced. There are also larger structures associated with the crack edge.

Horizontal sets were attempted, approaching the crack edge from the side. These, however, suffered significant imaging problems close to the edge as previously discussed and so are not presented.
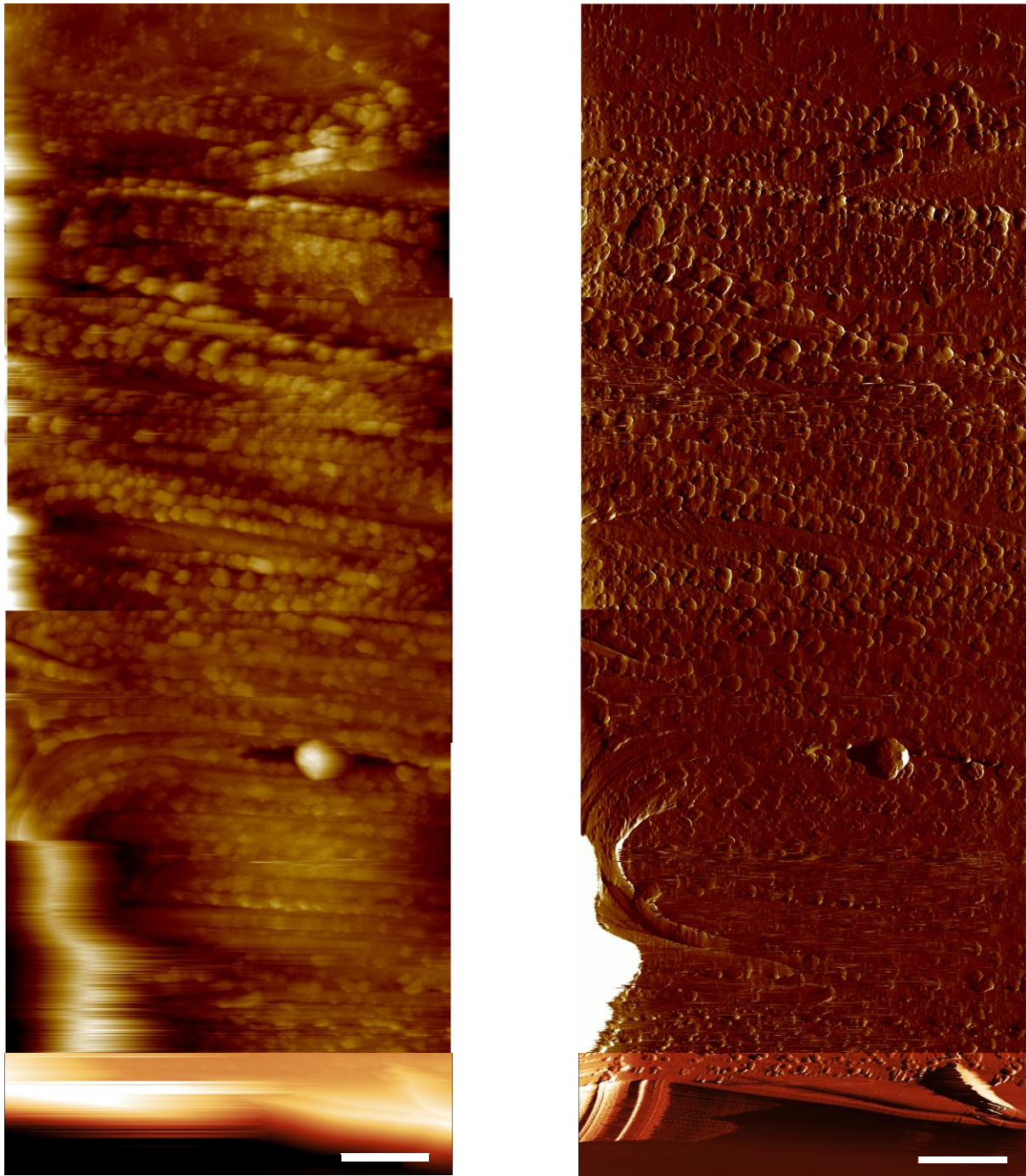
Figure 6.18 - Sets of height (left) and amplitude (right) images on a crack with a well-defined white area, heading from the white area towards the crack edge. Last image in the set could not be opened in Nanoscope was plotted with Gwyddion instead. Each individual image is 4 µm, scale bar is 800 nm. Z scales 400 nm and 900 mV.

6.6: Sets taken in the same area as the film is stretched

To understand what is going on it is important to take sets of images at the same place so we can watch the processes as they occur. This was achieved using the same technique seen in chapters 4 and 5. A suitable area was found, then a fiducial mark was made by the scratching the surface with an AFM tip. The tip was replaced and the investigated area was imaged, the sample was then stretched and left to settle. The same area was found using the fiducial mark and imaged again, this process was repeated until the area was so deformed the fiducial mark could not be found and recognised.

Originally an ink-dot was used as a larger scale fiducial mark as in chapters 4 and 5, however the crack tip was found to serve this function more accurately and more easily and so the ink-dot was no long used.

Sets of images of several sizes were taken zooming in on the investigated area, at sizes of 10, 5, 2.5 and 1.5 µm. These images were all taken with a pixel density of 512.

As the sample is stretched the crack both widens and propagates forward slightly. This is a potential problem when imaging in the same spot as the imaging area could be pulled apart between images. The extent of propagation could not be seen in the optical images, it was seen to be fairly small and was assumed to be on the order of 10s of µm. This was later seen to be false as seen in figure 6.20 where the propagation is seen to be significantly smaller.

Nevertheless, to help combat this, the early sets were situated 10s of µms away from the crack edge and small strains were used. An example of this is seen in figure 6.19, the investigated area was initially approximately 50 µm away from the crack edge.

The same processes seen in simple stretched polyethylene in chapter 4 are also seen here. Lamellae are seen to separate, increasing their long period, which is due to elongation of amorphous tie chains. They tilt and rotate, which is caused by fine crystal slip, to align with the stretch direction, which is horizontal. They largely align with neighbouring lamellae, rotating in stacks. This also leads to buckling to form chevrons. Nanovoids are seen which lead to craze formation and growth, in particular the large central craze. There is also the start of fragmentation into blocky elements.
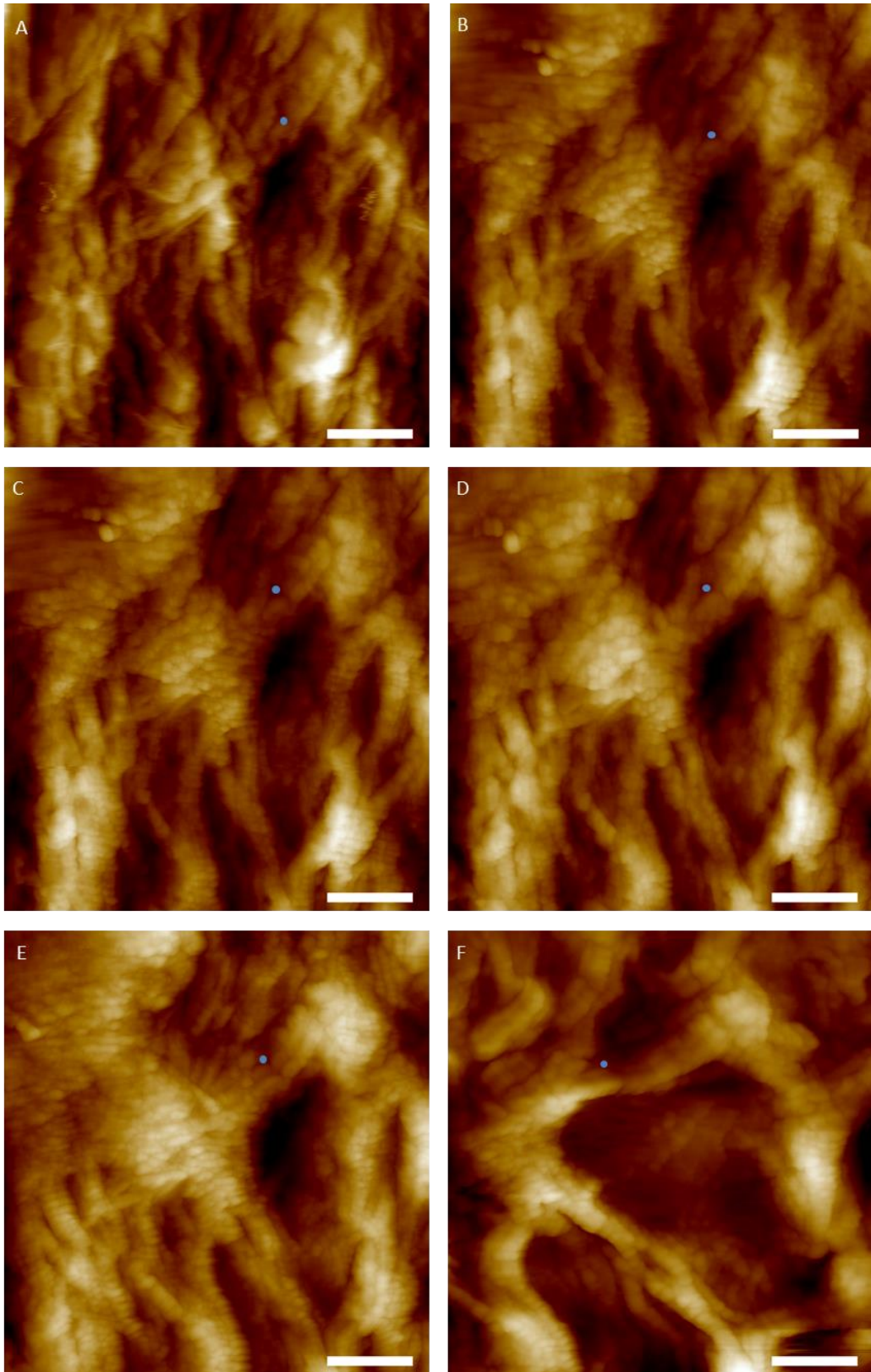
Figure 6.19 –Series of height images of polyethylene deformation near a crack tip. Tip artefact produces the blocky texture seen. Strains of 0, 3, 6, 12, 23 and 125%. Scale bars are 300 nm. Z scales 200, 100, 100, 100, 100 and 150 nm.

A key difference to what is seen with stretched polyethylene is the large scale rotation seen in the images over the entire image, this is due to shear. This occurs as the crack tip causes a complex local strain field consisting of both biaxial stretch and shear forces. Not present in this set is late stage deformation which is seen in images above, this includes the transition to a close packed highly fibrillated structure and the formation of geometric crazes within it.

In order to see the late stage deformation processes images were taken closer to the crack edge, figures 6.20-6.25 are all from the same experiment.

As seen in figure 6.20, the area was initially approximately 15 µm from the crack edge, and at the 4th image it was approximately 12 µm away, showing very little propagation. This allowed higher strains to be seen.
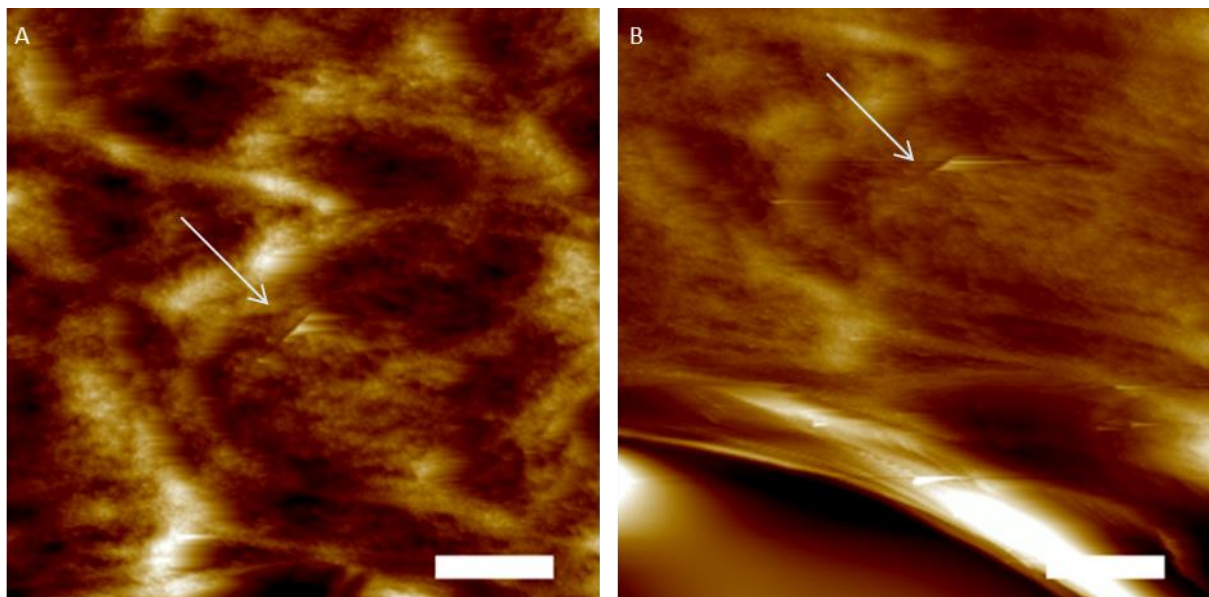
Figure 6.20 – Height images showing the distance to the crack edge of the investigated region at the start (A) and by the 4th image in the set (B). The investigated region was directly below the fiducial mark (highlighted). At the bottom of each image is the crack edge. Strains at investigated region of 0 and 51%. Scale bar is 8 µm. Z range 1100 and 3500 nm.

Figure 6.21 shows the set of 10 µm images taken. At the centre top of each image is the end of the fiducial mark, however due to the nature of the deformation the other areas of the image are not constant, with the investigated area shown in figure 6.24, which is to the right of Y, having moved off image by the D. The fiducial

mark, labelled W, acts as the fixed point to these images relative to which the rest of the image moves.

At the top of the image the features present in A are still there in the last images albeit with significant deformation seen, including lamellae separation and rotation and the formation of a number of crazes and voids.

Within the images the group of lamellae labelled X moves a little closer to the fiducial mark but largely keeps its place. It undergoes large deformation, with the bottom of the feature moving to the left.

The group labelled Y starts on the left of the image slightly below the halfway point. Throughout the set it moves up and to the right, ending to the right of X. Larger deformation can be seen with the lamellae all rotating to align with the stretch axis.

The group labelled Z starts in the bottom right of the image, it moves up and to the right, ending on the right side of the image, to the right of the other features. The area undergoes even more deformation with the lamellae highly aligned with the stretch axis and spread out.

Below these features in E and F are new areas which have appeared from off image to the left and below, this region is almost completely aligned and well-ordered and will be near to the crack edge. The area is also seen to move up and to the right between images.

The movement of these individual areas show us how deformation takes place for the overall image. There is an overall movement of the features of up and to the right, with a much larger movement horizontally than vertically. The investigated area is presumably slightly to the right of the centre of the crack tip, if it were on the left the features would presumably move to the left.

Movement is larger close to the crack, which will fade away to no movement in the undeformed areas a long way from the edge. This leads to an overall apparent tilting movement which is shear banding. Deformation is seen to occur at all points in this image but is much larger closer to the crack edge as expected.
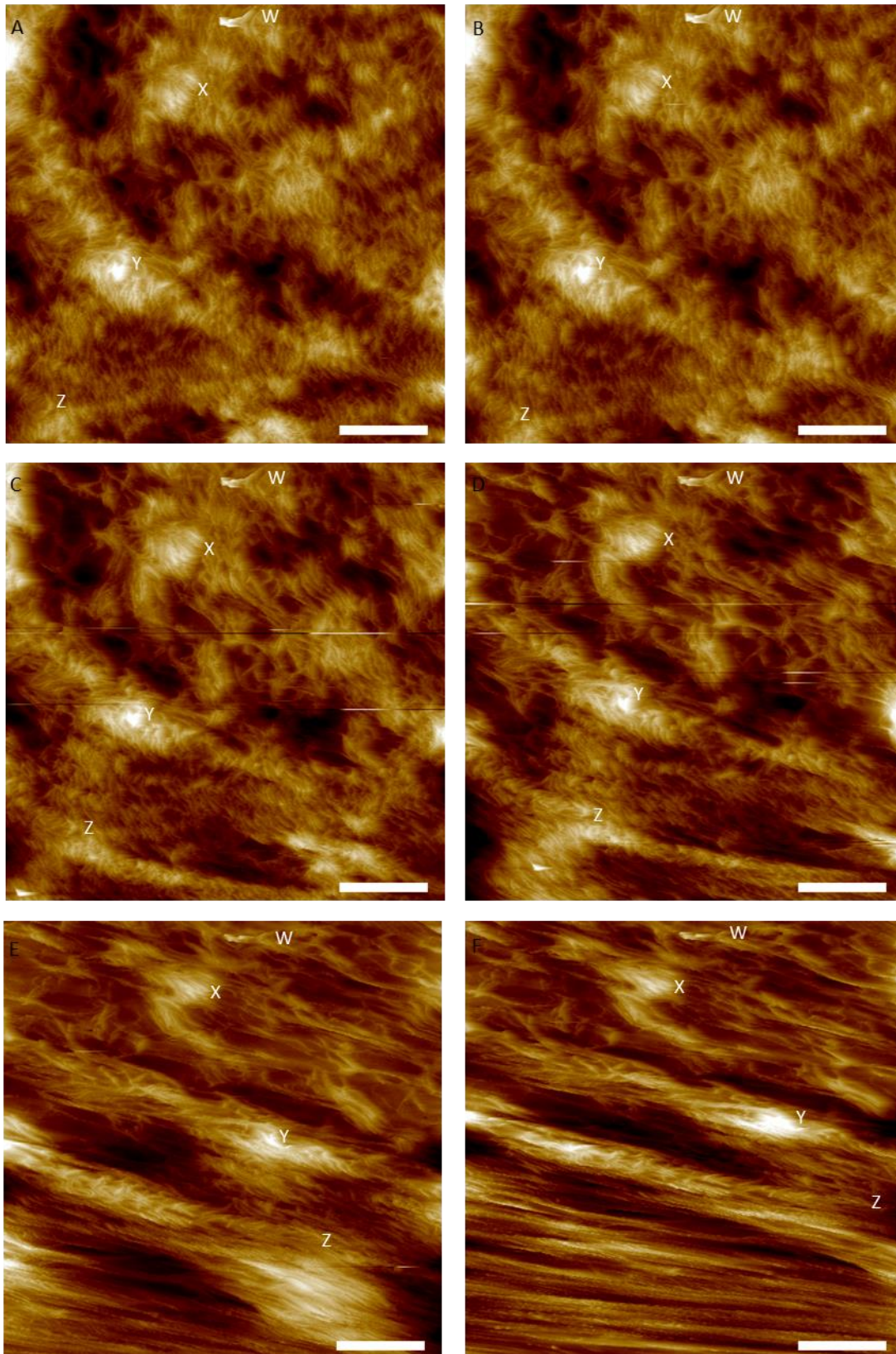
Figure 6.21 –Series of height images, taken close to the crack edge. Same area as figures 6.22 and 6.24. Strains of 0%, 4%, 18%, 51%, 71% and 98%. Scale bar is 2 μm. Z scales 450 nm.

Figure 6.22 is the set of 2.5 μm images, it has a higher resolution than figure 6.21, allowing us to see the details of the deformation processes more easily, though not as well as figure 6.24. The deformation processes seen in figure 6.19 are seen here. We can watch individual lamellae separate from their neighbours, undergo rotation and buckling and begin to break up into blocky elements. We also see significant shear with the bottom of the image moving significantly more to the right than the top.

Of unique interest are the features in the top right corner of the images where we can see geometric crazes forming and growing. These are clearly present in the later images of the set. In order to better understand what is happening the relevant areas from figure 6.22 were digitally zoomed in, the amplitude channel was used as it made the geometric crazes easier to see. These are displayed in figure 6.23.

As the set continues the deformation changes the imaging area, firstly it gets wider to try to keep the same features in view; secondly some features are lost off the edge of the image.

There are three main areas in these images where geometric crazes are formed: on the top left which is to the left a patch of vertically aligned lamellae above the blue dot; and on the top right, which is to the right of that patch. The final area ends in the bottom left of the image but starts at the bottom in the centre, to the right of a right angle of lamellae.

In A, in the top left and right areas there are some small voids and simple crazes which will lead to geometric crazes; in the bottom area however there are no voids and no clear indication that this area will form them. By B the original voids and crazes have grown slightly, and there is a new void on the right of the top right area.

By C there has been significant changes, the previous voids have now all grown to form simple crazes, some of these are normal and some are geometric. In the bottom area some voids and crazes have formed. By D the top crazes grow

without getting any more complex, at the bottom they have grown with the creation of a larger geometric craze. By E the crazes have grown even more, at the centre top of the image nearby crazes have merged to form a single, more complicated structure

This set shows geometric crazes forming from earlier voids and simple crazes, they occur both from the merging of nearby crazes and from growth of a single craze. These voids and crazes are seen to form at different times and different deformation levels, with the bottom one forming later despite being in a more deformed region. We cannot predict beforehand where these will form. It is assumed that geometric crazes are formed by a combination of localised strains occurring in multiple directions.
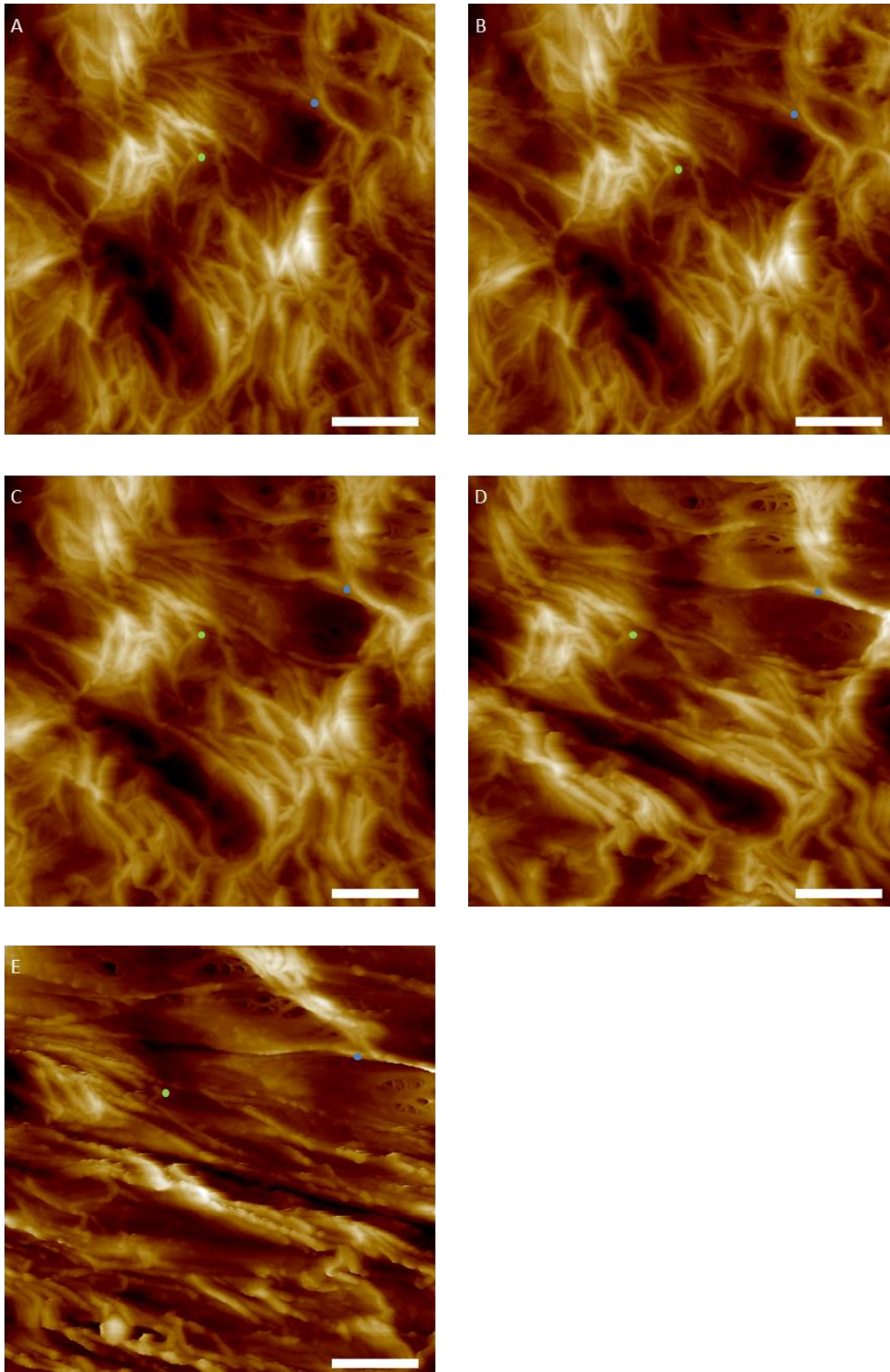
Figure 6.22 - Series of 2.5 μm height images, taken close to the crack edge. Same area as figures 6.21 and 6.24. Strains of 0%, 4%, 18%, 51% and 71%. Scale bar is 800 nm. Z scales 220 nm.
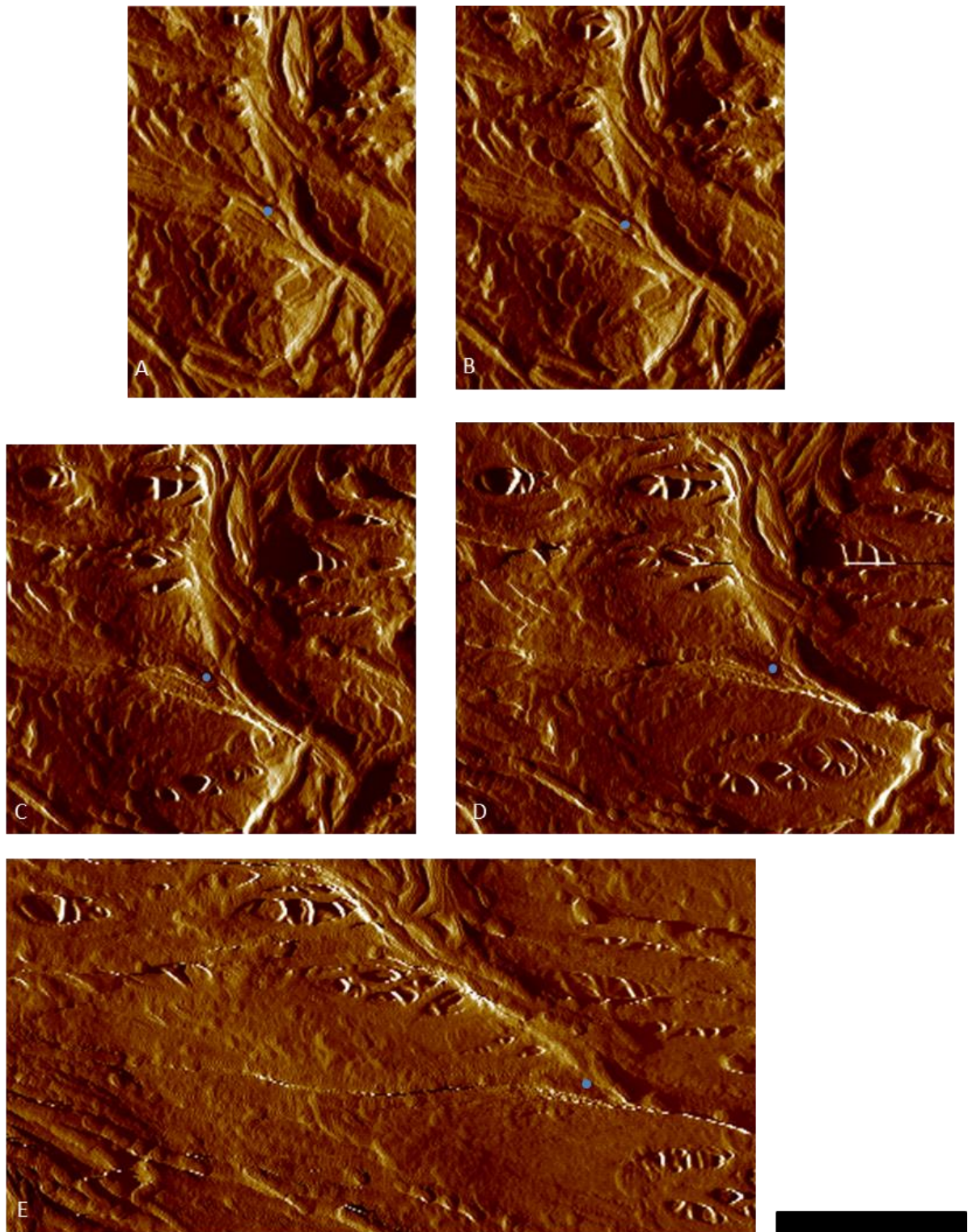
Figure 6.23 –Digitally zoomed in sections from the 2.5 μm set of amplitude images which correspond to figure 6.22. Blue dots in same place. All images same scale. Images don't show exactly the same region due to movement of features between images. Strains of 0%, 4%, 18%, 51% and 71%. Scale bar is 800 nm. Z scales 400 mV.

Figures 6.24 and 6.25 shows the set of images for 1.5 µm, it is higher resolution than figure 6.22 and so allows more study of the deformation process. Geometric crazes are not seen in most of these images.

The same processes seen before are also present here. At the start the area is already slightly deformed by its proximity to the crack edge, with a number of crazes present, in particular the large one in the bottom right, and many lamellae showing some buckling. These crazes are roughly 100s of nm in size, perpendicular to the stretch direction and of roughly ellipsoidal shape

As the crack widens we see further deformation with the lamella starting to align heavily with the crack edge. Neighbouring lamellae tend to align with each other rotating in stacks. Once they are largely aligned with the stretch direction they begin to slip against their neighbours.

Initially the crazes are seen to widen however later they appear to rotate with the neighbouring lamella, eventually becoming long in the horizontal direction but thin in the vertical direction as they are squeezed by the relatively closely spaced lamellae. The fibrils within a craze are already roughly aligned with the stretch direction and do not rotate.

At the later stages the lamellae that are aligned begin to breakup into blocky elements, caused by coarse chain slip. Shear is once again seen with the bottom of the image moving significantly more to the right than the top.
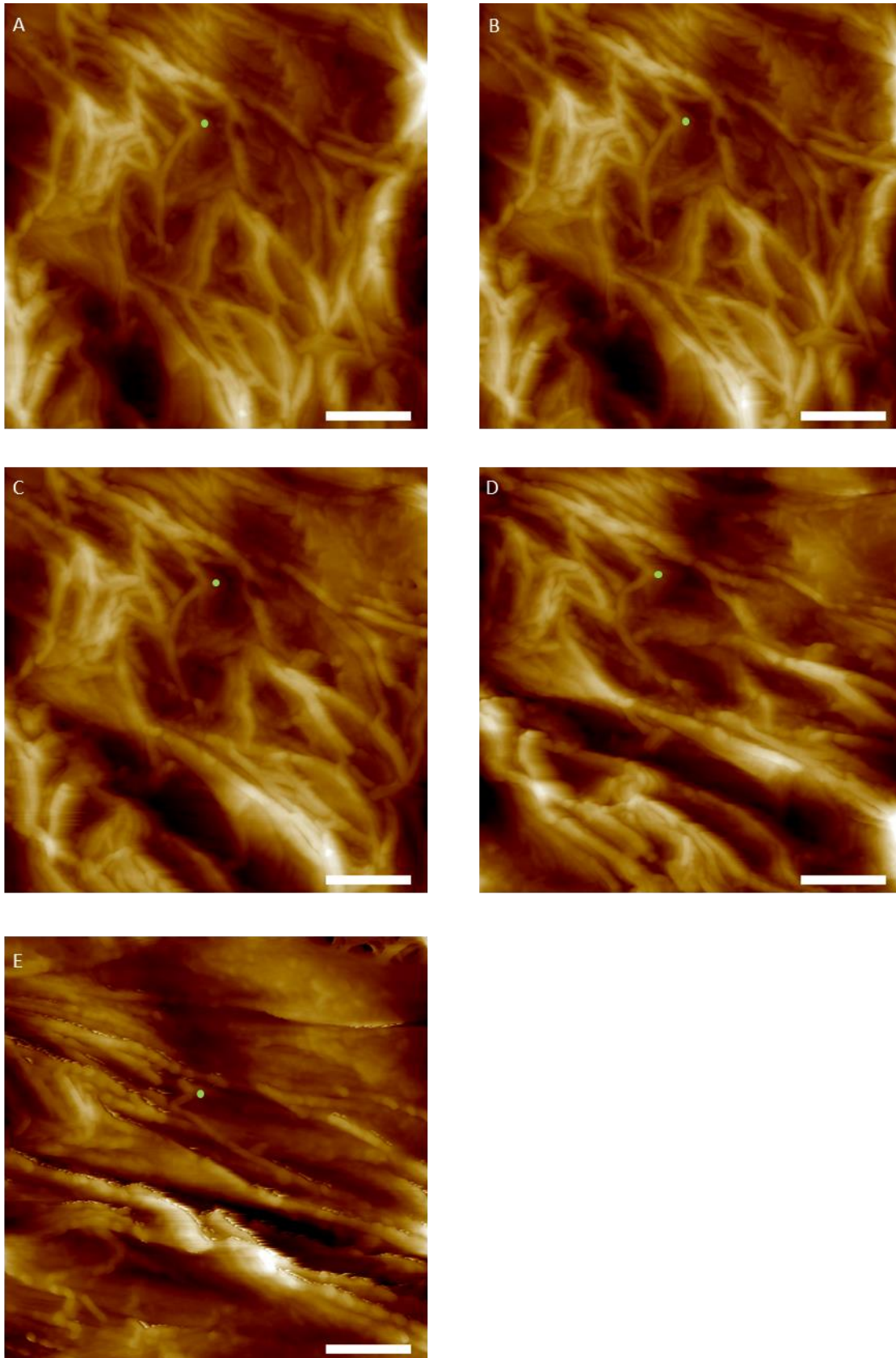
Figure 6.24 - Series of height images, taken close to the crack edge. Corresponds to figure 6.25. Same area as figures 6.21 and 6.22. A damaged tip in the last image produces a poor quality image. Strains of 0%, 4%, 18%, 51% and 71%. Scale bar is 300 nm. Z scale 160 nm.
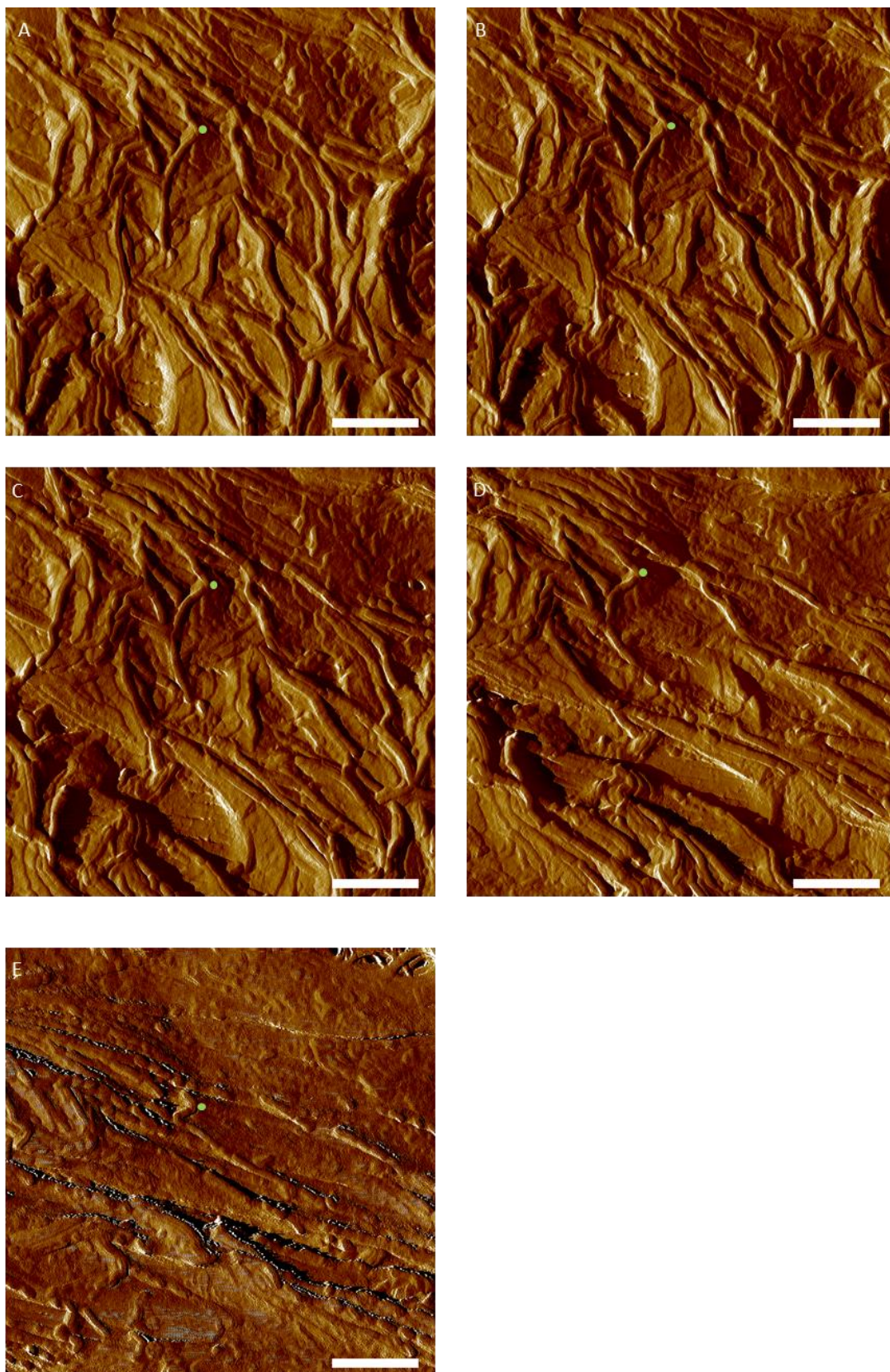
Figure 6.25 - Series of amplitude images, taken close to the crack edge. Corresponds to figure 6.24. A damaged tip in the last image produces a poor quality image. Same area as figures 6.21 and 6.22. Strains of 0%, 4%, 18%, 51% and 71%. Scale bar is 300 nm. Z scale 240 mV.

6.6.1: Mapping lamellae movement between images using a mesh of points

To extract more information from the images, the 1.5 μm set from figure 6.24 was fitted with a mesh of points which allows the movement of lamellae and other features throughout successive stretches to be followed and mapped. The process is the same as described in chapter 4.

Figures 6.26 and 6.27 both show the same set of data in two different ways using the scatter and quiver functions respectively. The two methods have different strengths, with scatter best for seeing large scale movements and quiver best for small scale deviations. In figure 6.28 the arrows were overlaid on the images in order to see movement better. The arrow size shows the movement relative to the centre of the image, not relative to its neighbouring region, so it is useful to compare arrow size to its neighbours.

Most interesting is the overall movement of the lamellae, generally the top of the image moves left whilst the bottom moves right which is a clear depiction of shear. This is in contrast to stretched polyethylene which is seen in chapter 4. There the region stretches so that the lamellae move away from the centre in the stretch direction and towards the centre perpendicular to it, with magnitudes which are larger further from the centre, and the horizontal movement being much larger than the vertical.

There is both tensile strain and shear seen here, which is seen to be strongest in the earlier images. In the first image, at the top the left areas moves to the left whilst the right is relatively stationary, and at the bottom the right areas move right whilst the far left moves left. This is in agreement with a superposition of tensile strain and shear. The change of strain between images decreases with increased deformation, so in the final image the effect is less visible.

We can also see smaller scales variations, which are often due to craze growth and rearrangement. This is clearest in the movements of the separate group in the bottom left, which is due to the craze opening to its right. The individual movement of lamellae here is much more complex than would be seen by averaging techniques describing the overall effect.
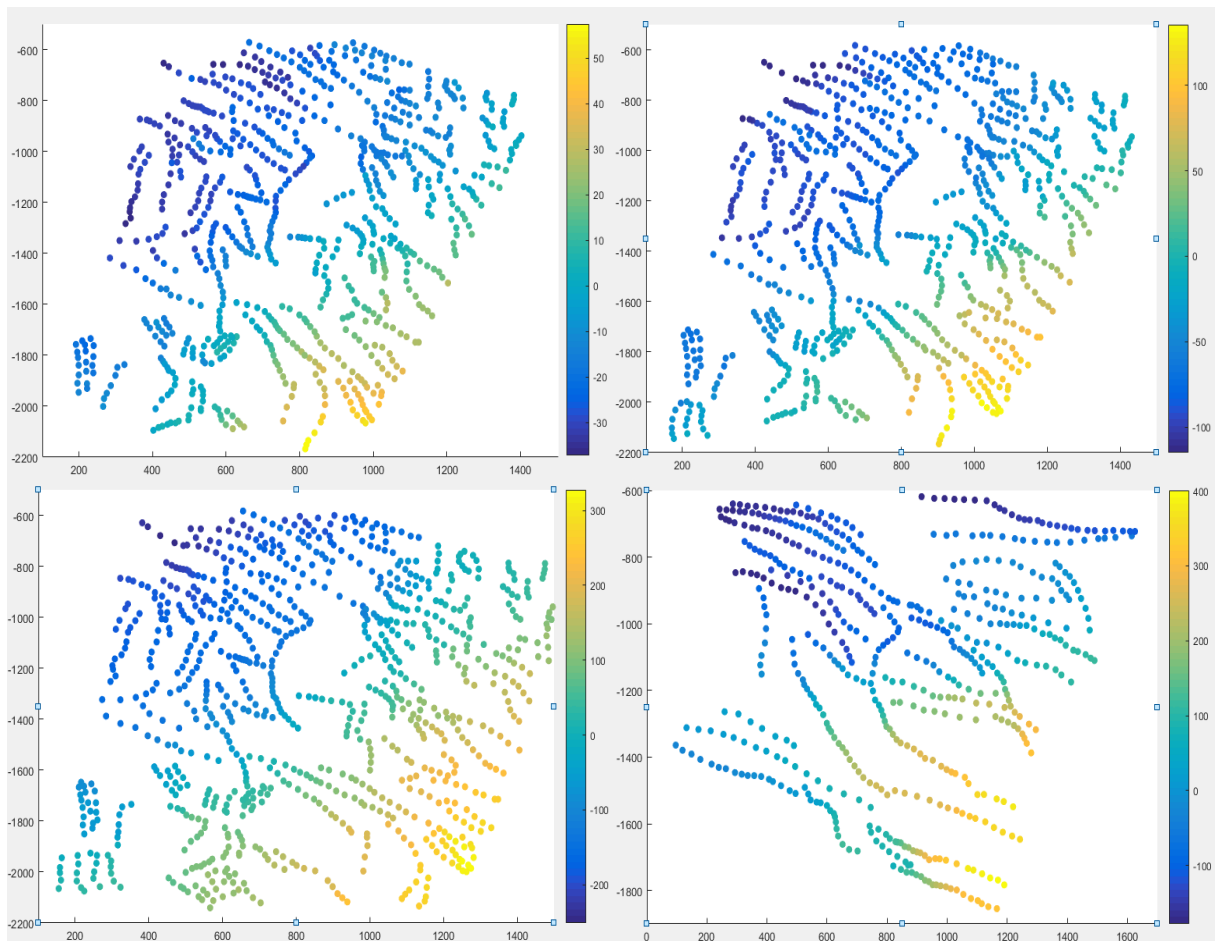
Figure 6.26 - A series of images showing the movement of lamellae between images in line with the stretch direction. This corresponds to figure 6.27. Here represented as coloured circles. Yellow circles move to the right and blue moves to the left. It has 4 images instead of 5 as it displays the difference between two images.
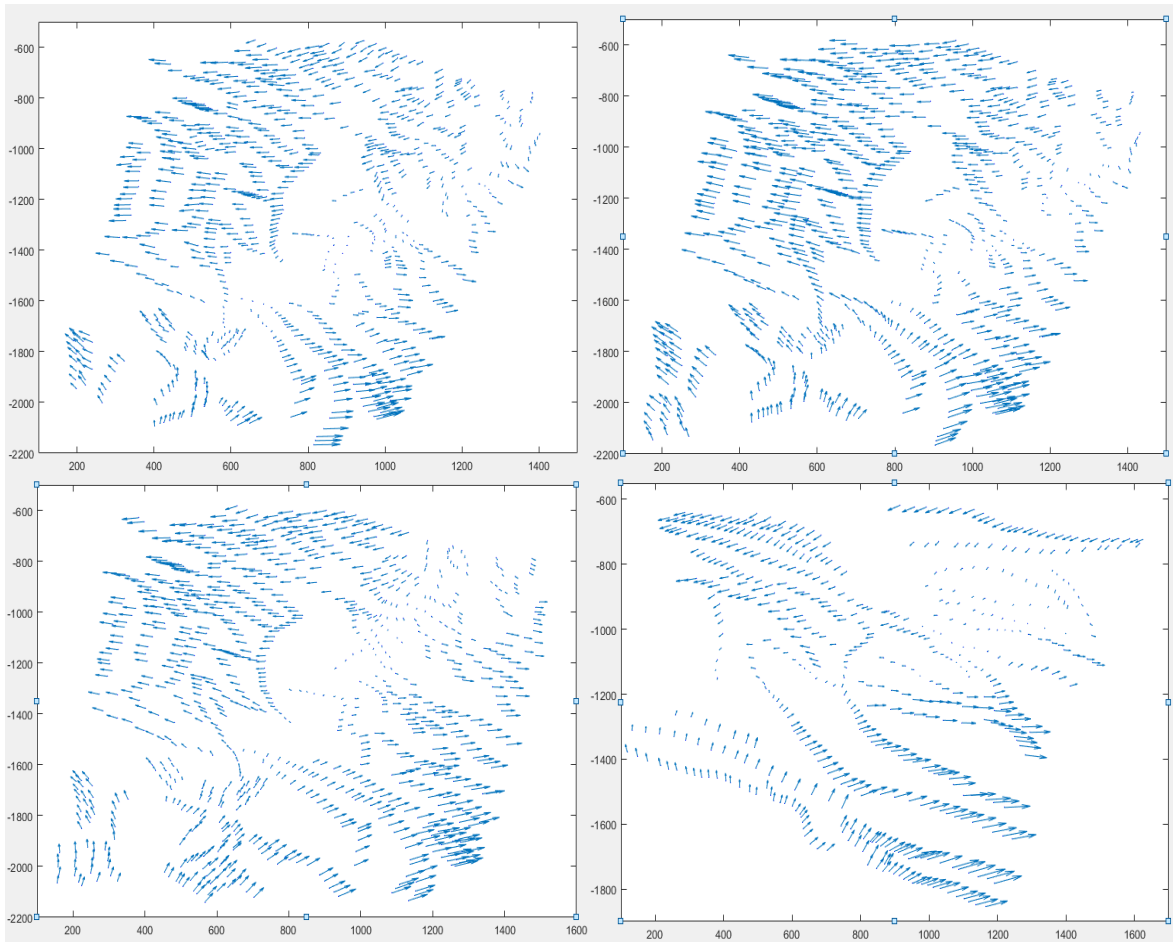
Figure 6.27 - A series of images showing the movement of lamellae between images. Here represented as arrows. This corresponds to figure 6.26. The size of the arrows represents the magnitude of its movement. It has 5 images instead of 4 as it displays the difference between two images.
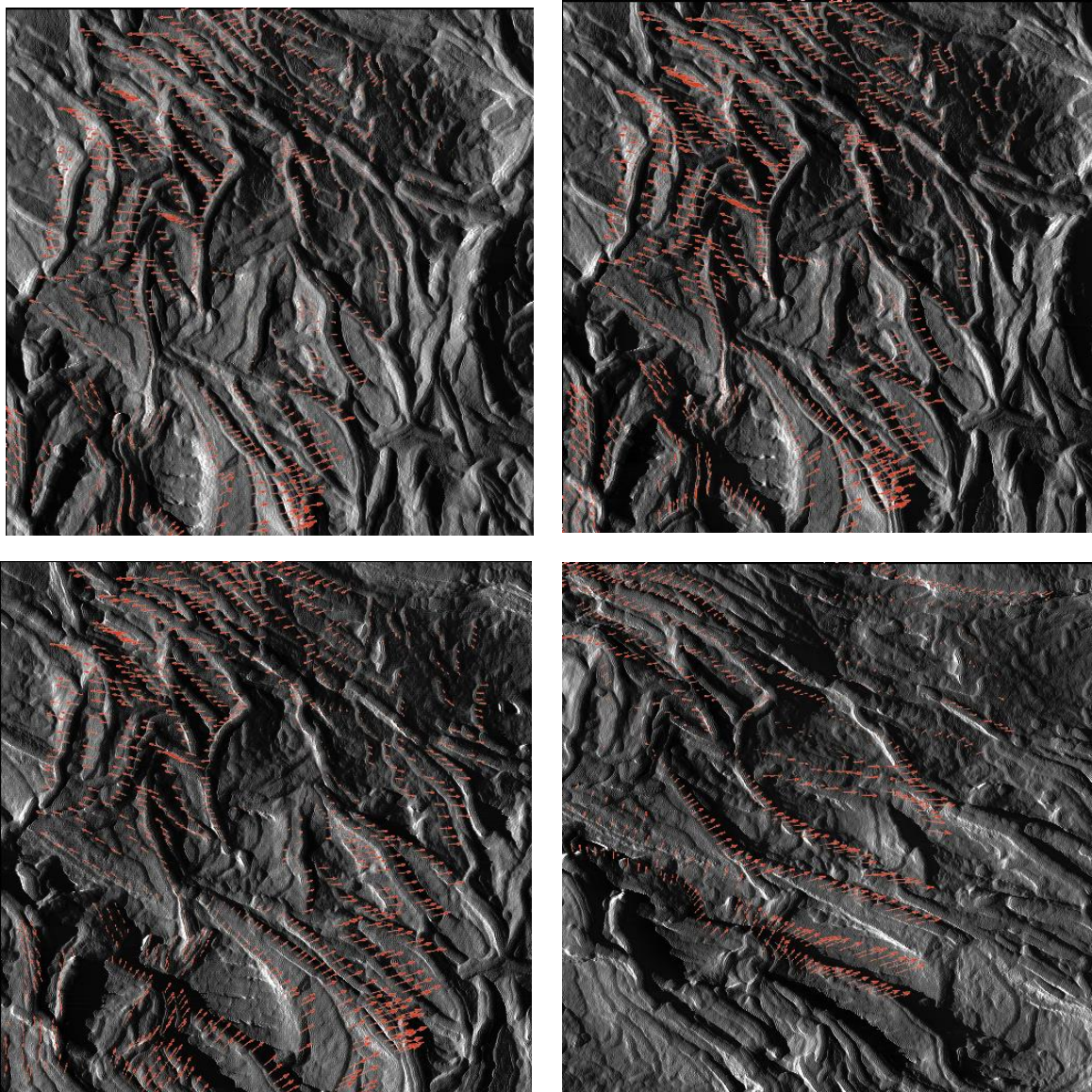
Figure 6.28 - Series of 1.5 μm images overlaid with arrows showing the movement of the lamellae between successive images. The base images are seen in Figure 6.24 and the arrows are from figure 6.27.

6.8: Conclusions and future work

The previously developed method was applied to study the effect of crack edges on polyethylene deformation and fracture. Previous studies used methods such as SAXS which only collect information averaged over a large area; or fairly low resolution snapshots with microscopy techniques such as AFM. The unique aspect of

this work is that it was possible to take nanometre scale images near a crack edge, both mapping spatially and watching the same area evolve with increasing strain.

A distribution of both strain and thus stress, which varied with both magnitude and orientation, was seen around the crack tip. This was found to largely agree with previous studies, with the stress aligned with the crack edge and decreasing with distance over the scale of 10s of μms. This kind of distribution implies a flow of material towards the tip.

A key exception to this was the existence of large (~100 μm) areas of uniformly high deformation which appeared at the end of the crack tip and had somewhat sharp boundaries to the rest of the film. This is likely caused by multiaxial strain.

The deformation processes occurring are similar to those seen in chapter 4 for stretched polyethylene including the existence of crazes, a difference being the large scale shear seen throughout. Also within a couple of μms of the crack edge, the surface was completely fibrillated, with closely packed fibrils aligned with the edge, there are no voids here, they appear to have been closed up by the shear forces from the edge.

In highly stretched regions 'geometric crazes' have been seen, these are areas within fibrillated regions where the fibrils are not aligned parallel to neighbouring fibrils, instead short sections of fibril are arranged in apparent geometric patterns at angles to each other and the main parallel fibrils. These features have not been seen in previous studies, they would not be visible in spectroscopy methods or in low resolution microscopy. It is assumed that they are formed by a combination of localised strains occurring in multiple directions caused by the crack tip.

The geometric crazes are similar to features seen for polypropylene in chapter 5. Here they are generally larger and more complex, and so have a difference in most common angles between fibrils. It is not clear why exactly these differences occur,

obviously they stem from the difference in material properties, with polypropylene being more brittle and thus they perhaps have less room to grow.

In the future it is important to investigate further how these geometric crazes form and grow and so more sets close to the crack edge could be taken. In particular it is important to capture high resolution sets of images and so these at larger scales would be used. These images would be fitted with meshes of points to help understand the process. An automated fitting procedure would help here, both to increases accuracy and consistency and to allow the fitting of larger scale images. These procedures would also be useful in understanding the development of the defined uniform high deformation area by watching how it forms.

Chapter 7 – Preliminary study of the application of Torsional Resonance AFM to polymer structures

7.1: Introduction

This chapter explores some of the uses of Torsional Resonance mode (TR) AFM. TR is a dynamic AFM mode similar to tapping mode, except instead of being oscillated flexurally the cantilever is oscillated torsionally about its long axis, causing the tip to oscillate parallel to the surface with a small dither motion.

Two different TR cantilever holders were used here. A custom built holder using an 'oppositely poled piezos' setup and a commercial holder which used a 'two piezos two signal' method.

TR has a number of potential advantages compared to tapping mode including higher sensitivity and stability, and a large phase contrast. These advantages can be useful for imaging, force curves and measuring surface properties. It also has the potential to sense in-plane forces and allows us to learn about the environment above the surface of the sample.

The original aim of the work in this chapter was to use TR to investigate molecular water structure on surfaces, its variations with the local hydrophilicity of the surface, and how this would affect imaging with AFM. However the focus shifted to exploring TR sensitivity to in plane forces on scales below a nanometre and using this to measure molecular orientation of chains within lamellae in polyethylene, however the measurement of orientation was not clear.

The original aim builds on previous work by Nic Mullin [116][127][150], who used both TR and torsional tapping (TT). His interest was in using them for high resolution imaging; this was only achieved on hydrophobic surfaces. It was thought this might be due to a difference in molecular water structure, with less orientation allowing better imaging.

To study this TR force curves have been taken, allowing a study of molecular scale water layering on surfaces with differing chemistries, both hydrophobic and hydrophilic. A number of samples have been studied including patterned self-assembled monolayers (SAMs) which have well controlled surface chemistry, as well as simpler surfaces of mica, silicon and highly oriented pyrolytic graphite (HOPG). Later TR is used to measure molecular orientation by differences in phase when the chains are aligned with the dither direction.

7.2: Experimental

In this project two AFMs with different methods of operation have been used, both of which operated in ambient conditions. The first of which used a Bruker Multimode AFM, it made use of Nanoscope software 5 with a NanoScope 3a controller and could not operate in TR mode natively and so was modified to operate in TR mode. It used a rectangular silicon nitride Bruker TESPA cantilever with a flexural spring constant of approximately 40 N/m.

The AFM was set up as shown in figure 7.1 in an 'oppositely poled piezos' setup. The system is driven by the sinusoidal tapping mode signal from the Bruker Multimode, and converted to a torsional action via a custom built holder. The holder contains two oppositely poled piezoelectric actuators with a stiff glass rocker between them, when receiving the same signal one will expand whilst the other contracts thus creating a 180° phase shift between opposite ends of the stiff bridge, which causes torsional motion of the cantilever. The tip was bonded to the glass rocker using a UV curing epoxy resin (Norland NOA81); which had two advantages over superglue, it allowed more time for accurate tip placement and it eliminated tip contamination due to outgassing.
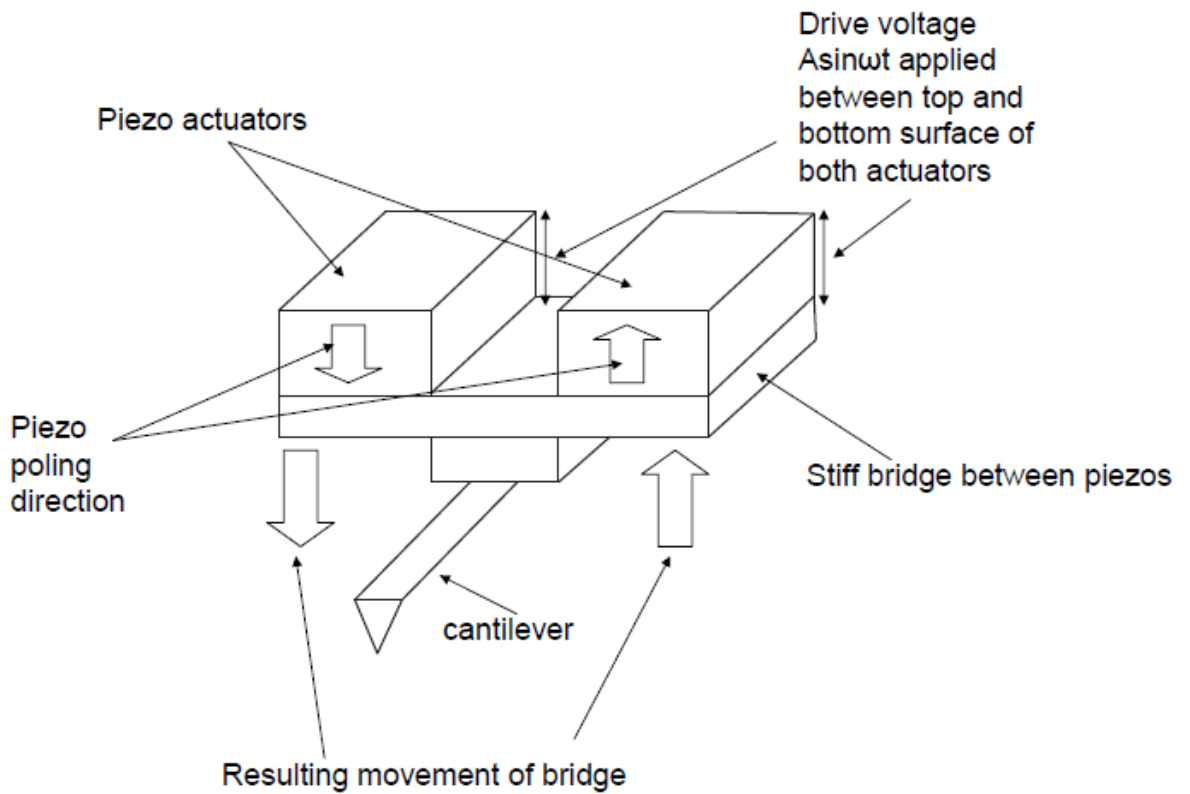
Figure 7.1 – A schematic diagram of the 'oppositely poled piezo' method used to produce torsional oscillation. Reproduced from [116].

The optical beam bounce allows measurements of both flexural and lateral deflection of the cantilever. However the controller only allows access to the flexural signal. To operate in TR mode the torsional deflection must be collected. It is possible to collect this by modifying the flexural signal.
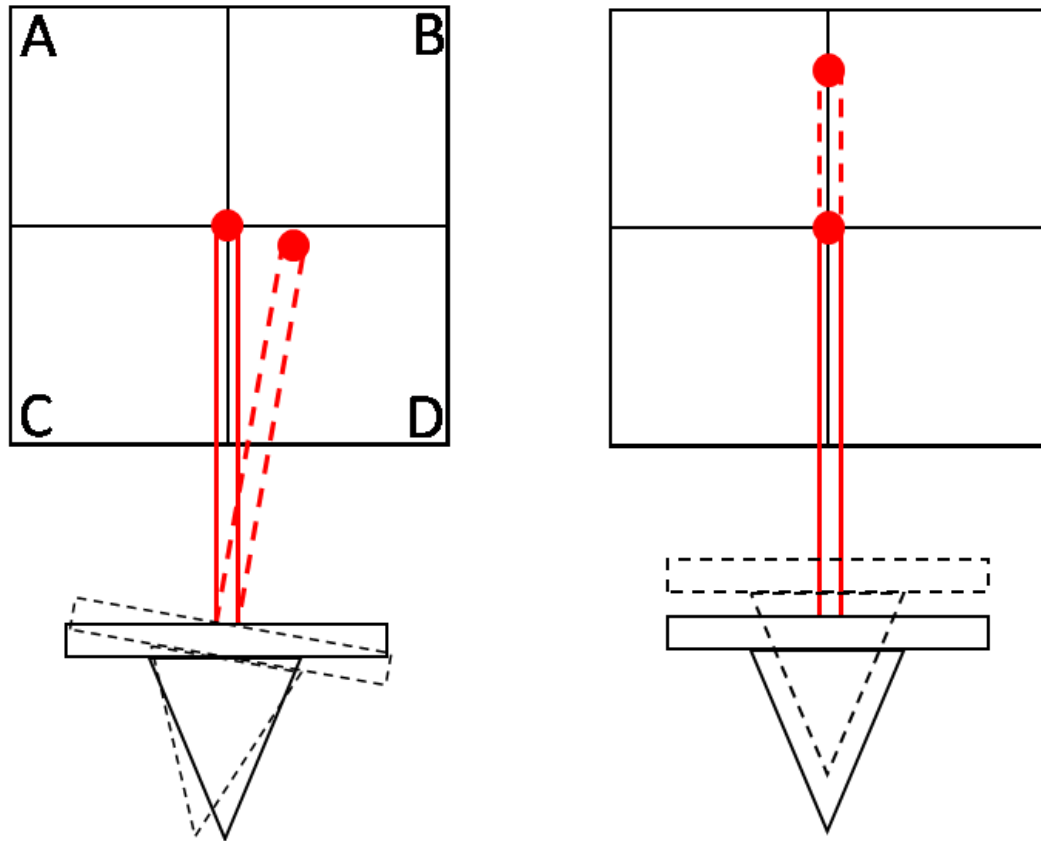
Figure 7.2 – A diagram of the movement of laser spots on a four split photodiode in response to torsional (left) and flexural (right) AFM tip deflections.

The photodiode is split into four sections as seen in figure 7.2, for each section the amount of light falling onto them is proportional to the current created; these currents are then converted to voltages; and from these values the normalized flexural and torsional deflection, in volts, are given respectively by:

$$\Delta V_{flex} = \frac{(V_a + V_b) - (V_c + V_d)}{V_a + V_b + V_c + V_d}$$

(7.2)

and

$$\Delta V_{tors} = \frac{(V_a + V_c) - (V_b + V_d)}{V_a + V_b + V_c + V_d}$$

(7.3)

where V denotes a voltage and the subscript denotes the corresponding photodiode section.

By comparing equations 2 and 3 it can be easily seen that interchanging V_c and V_b converts one equation to the other. Thus a connector cable was used to interchange these two signals between the optical head and the microscope base. This caused the microscope's detection and feedback electronics to act upon the torsional deflection in the same way as they would the flexural signal.

Later another AFM was used, a Bruker Dimension ICON. This had the advantage that TR mode can be performed natively, without the use of a custom holder or patch cable. This is possible because it comes with a pre-built holder which is a split piezo, it has two piezoelectric actuators which are poled the same way. Separate drive signals approximately 180° out of phase are sent to the actuators causing them to expand and retract out of phase, creating torsional excitation of the cantilever as is seen in figure 7.3.

In a perfect world the two actuators would be identical and thus they could be driven by signals of the same amplitude with a 180° phase difference. In reality the actuators are likely to be of slightly different sizes, positions and may be bonded differently; all of this should be accounted for in order to determine the optimal drive signals.
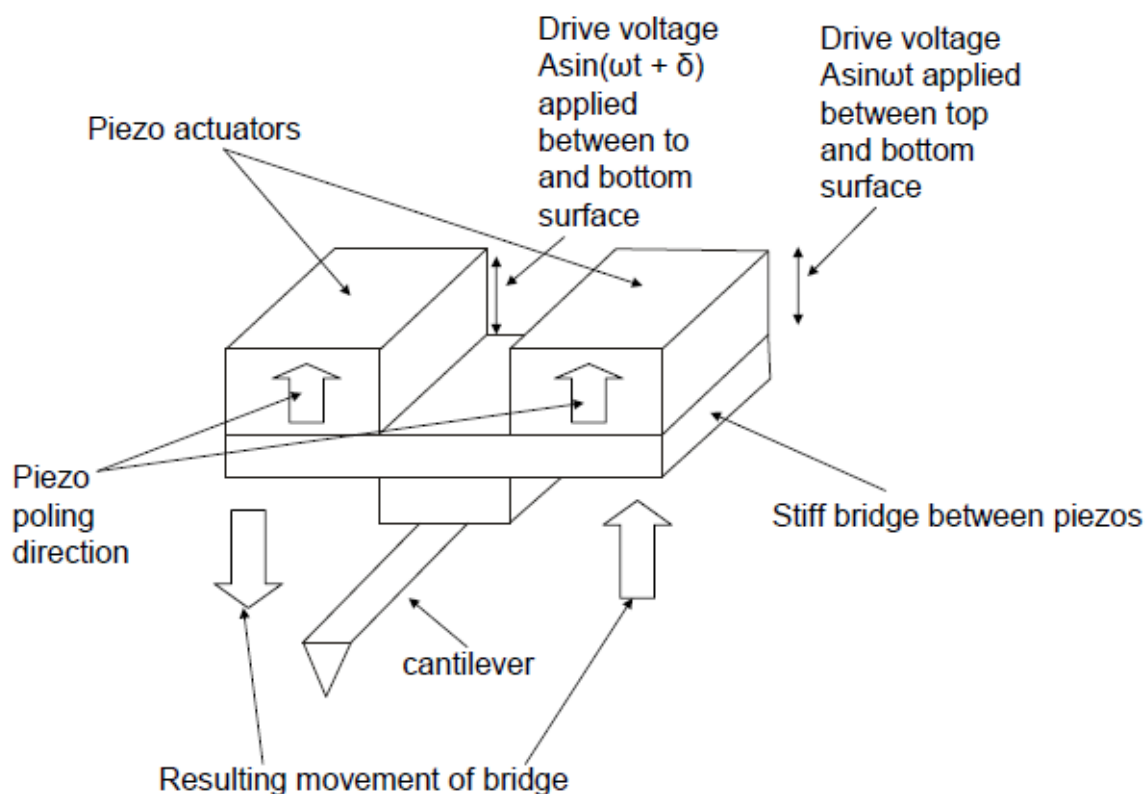
Figure 7.3 – A schematic diagram of the 'two piezos two signal' method to produce torsional oscillation. Reproduced from [116].

This is achieved using a feature in the software known as TR balance, here a balance mode control unit is used to adjust the amplitudes of the two drive signals in order to maximise the torsional response at a given drive power. The balance tune runs on a scale of 0 – 10 V, with 5 V being where both drives receive the same drive signal; and 0 and 10 is where only 1 actuator is in operation. Typically TR balance chooses values close to 0 or 10 V.

7.2.1: Self-assembled monolayers

Patterned self-assembled monolayers (SAMs) are useful samples for imaging as they can easily produce surfaces with differing chemistry and reasonably sharp interfaces between them. A SAM is a monolayer assembly of molecules which forms spontaneously, via self-assembly on a substrate. Individual molecules consist of three

parts: a head group which binds to the surface, a long tail which drives self-assembly by Van der Waals interactions with neighbouring molecules and a functional group which determines the surface properties of the monolayer.

The SAMs used here are alkane thiols, which consist of: a thiol head group which will bond to a gold substrate, long alkane chains and different functional groups. Three different functional groups are used here; one of which is hydrophobically terminated octadecanethiol (ODT), and two which are hydrophilically terminated 11-mercaptoundecanoic acid (MUA) and, 11-mercapto-1-undecanol (MUD).

Production of the samples begins by fabricating the substrates. They are created by piranha cleaning a silicon wafer onto which a 10 nm layer of chromium is thermally evaporated followed by a 150 nm layer of gold. 1mM solutions for each thiol were then created by mixing their respective powders with degassed ethanol, next the substrates were immersed for 24 hours in the ODT solution forming a single monolayer and finally they were cut into individual samples using a diamond tipped scribe.

The samples were then patterned using photolithography as seen in figure 7.4. They were covered in a 200 mesh mask weighed down by a quartz plate and exposed with a 244 nm laser at 100 mW for 25 minutes. In exposed regions this causes the sulphur-gold bond to change, by photooxidising the more strongly bound alkylthiolate adsorbate complexes to create weakly bound sulfonates, these may now be easily displaced by solution and replaced by adsorption of the second SAM molecules.

The samples were each then placed in one of the hydrophilic SAM solutions and left for an hour for monolayers to form before being transferred to ethanol. Note that the second SAMs are given significantly less time to form than the first, thus reducing the quality of the monolayer; if left for longer they would begin to

displace the ODT monolayer.
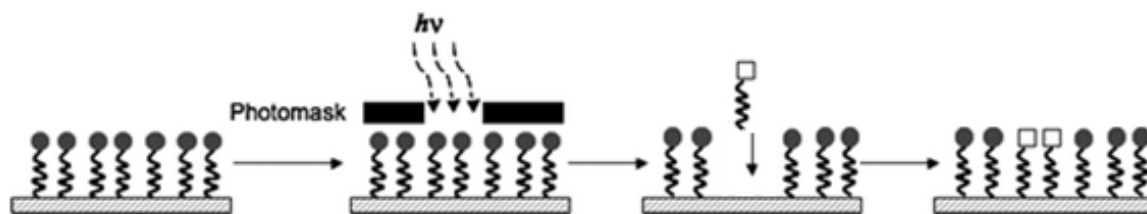
Figure 7.4 - Diagram of photolithographic patterning of SAMs, in exposed areas the thiol-gold bond is broken allowing them to be displaced by molecules which form a second SAM.

7.3: Imaging SAMs with TR

The samples were each imaged using the Multimode in TR mode; the procedure is similar to that which is commonly used for TM. The cantilever was tuned to just below resonance frequency, on the steepest part of the peak, the phase was set to zero and a free amplitude of 1 – 1.5 V was used, which corresponds to a tip amplitude of 2-3 nm.

The tip was engaged, with a setpoint of approximately 70% of the free amplitude to allow for stable imaging; higher setpoints, like those used in TM mode lead to feedback instability and poor surface tracking, as this corresponds to a steep drop in the force curve, as shown in figure 7.6. The optimal feedback gains were found to be similar to TM, roughly 0.5 for integral gain and 1 for proportional gain. Thermal drift is present, and so before taking data the cantilever is realigned and then left for 5 minutes to stabilise; the process is repeated until the drift is small, a voltage shift of 10 mV per minute.

For each of the samples, the images showed roughly similar features, as seen in figure 7.5: There is a strong phase contrast between the hydrophobic and hydrophilic areas, which is assumed to be due to differences in capillary forces, in addition contrast difference changes between samples in line with the polarity of the hydrophilic group.

Additionally there is a faint but discernible contrast difference visible in the height channel which corresponds to a shift in amplitude. There should be no measurable height difference between the thiols, and so to test this the samples were imaged in contact mode, with no height difference detected. The change is thus assumed to be due a change in the amplitude oscillation as a function of distance from the surface due to surface properties. In [116] it was shown that an increase in dissipative tip-sample interaction forces led to a reduction in amplitude, and thus the amplitude difference seen could be due to differing strengths of tip-sample forces between the surfaces, possibly due to differences in capillary forces.
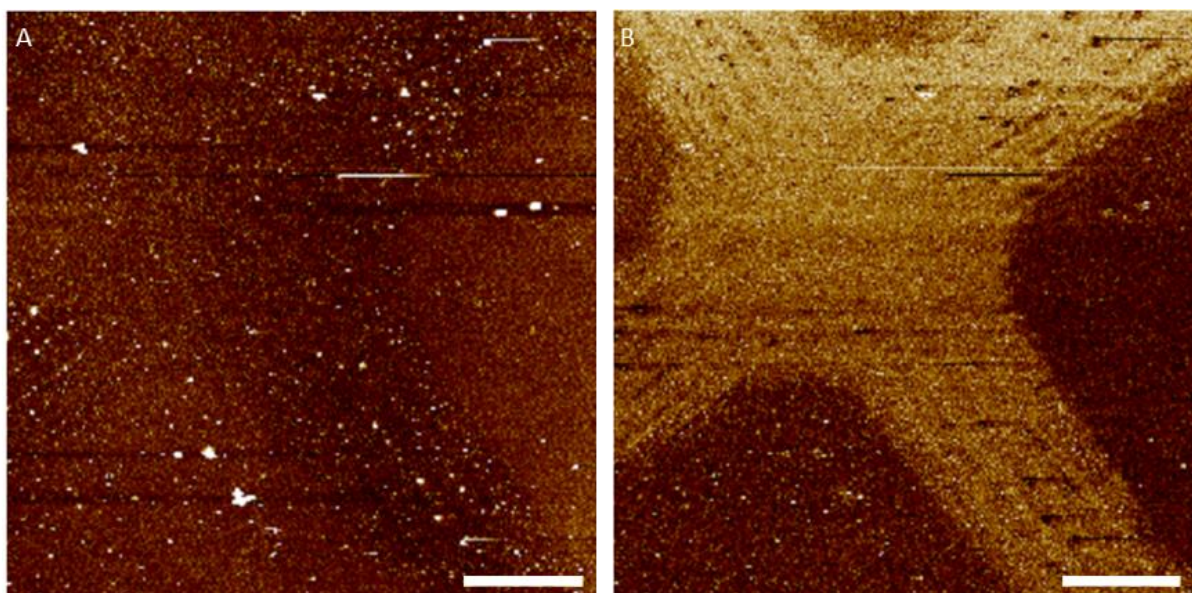
Figure 7.5 - TR height (A) and phase (B) images, taken on a grid pattern of MUA and ODT SAMs; which show a large phase contrast and a small but discernable difference in amplitude. Scale bars 4 μm. Z scales 12.5 nm and 38 °.

7.4: TR Force curves

TR can also be used to take force curves, it has many possibly advantages here including better sensitivity and stability. To take these force curves the AFM was first set up to image in TR mode and the region of interest found and located in the centre of the image, after which force mode was entered. The force curve was triggered using the amplitude; when a certain amplitude limit was reached, which corresponds to the tip pressing into the sample surface, the tip will stop and retract.

The amplitude must be set precisely, if too low the tip will press hard into the sample, damaging both sample and tip, if too high the tip will stop and retract before reaching the surface and thus the region of interest in the force curve may not be seen. Over time drift may affect the amplitude and so a relative trigger is used to minimise this.

The parameters are set in order to optimise the force curves. A ramp size of 100 nm was used, this is a compromise between increased speed and resolution and being long enough to ensure complete pull off from the surface. The number of samples per force curve was set to 4096 to increase resolution, higher numbers of samples would not be useful due to high noise levels, and thus they would provide no more information and would only act to increase measurement times and thus drift.

A typical TR Force curve is shown in figure 7.6, the top graph shows the torsional oscillation amplitude and the bottom the flexural deflection signal which were collected simultaneously, the blue is the extension and the red is the retraction.

At the start of the curve the tip is a long distance from the sample, the cantilever oscillates at its free amplitude and experiences no flexural deflection. This continues as the tip approaches the surface until there is a large steep drop in amplitude and a corresponding drop in cantilever deflection; the cantilever is bent

towards the surface as there is a large adhesive force which is due to the formation of a water meniscus.

As the tip extends further there is a shallower amplitude decay, and a shallow upturn in deflection which is due to interactions within the water meniscus. This is believed to be due to both the resonant frequency shifting gradually upwards due to the increasing lateral stiffness; and the reduction in quality factor due to increasing lateral viscosity [116].

Finally there is often a second drop in amplitude which corresponds to a snap to the surface and the cantilever pivoting around the tip. There is a corresponding rise in deflection which corresponds to the cantilever deflecting upwards as it pushes into the sample surface. The cantilever then retracts which is seen in red, this shows a large hysteresis due to adhesion forces, primarily the water meniscus after which there is a sharp jump caused by the breaking of the water neck.
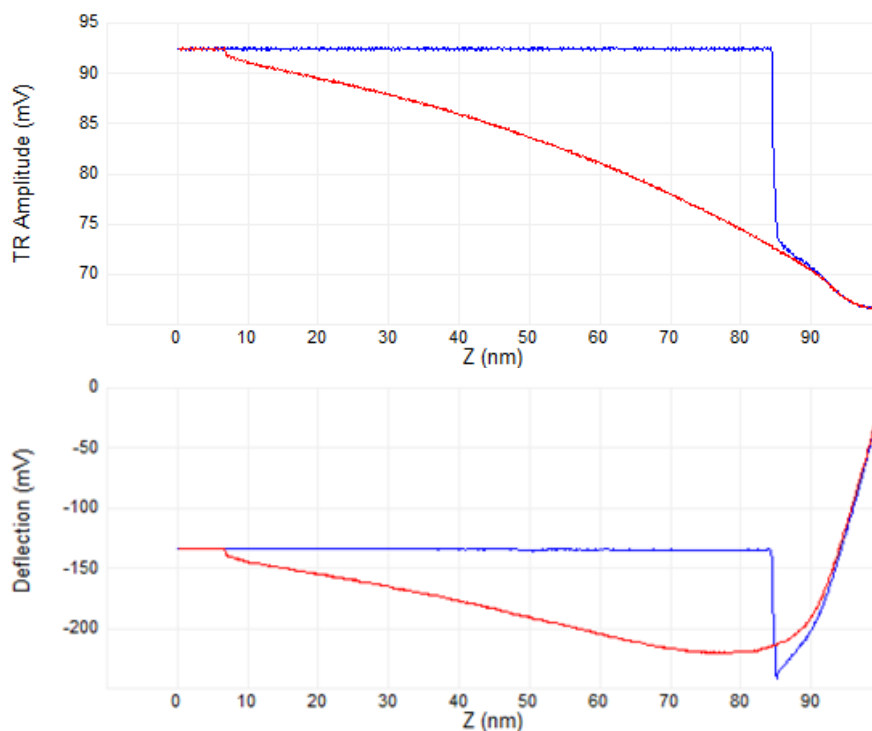
Figure 7.6 - A TR force curve taken over silicon, showing the torsional amplitude (top), and flexural deflection (bottom).
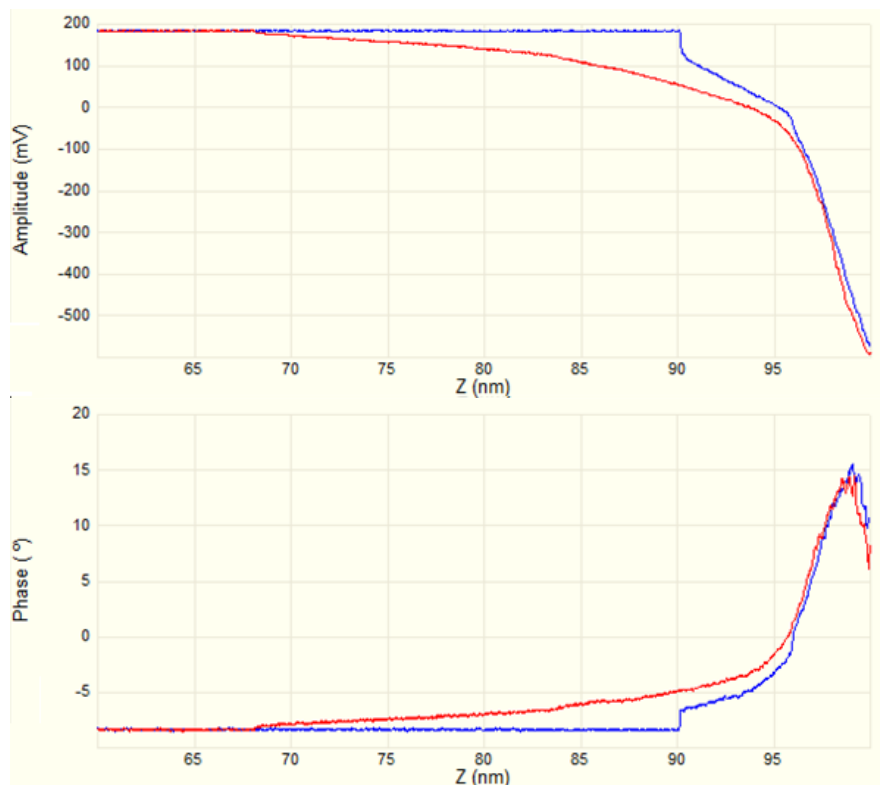
Figure 7.7 – A TR force curve taken over silicon showing the torsional amplitude (top) and phase (bottom).

It is also possible to acquire the torsional phase force curve, this is shown in Figure 7.7. Away from the surface the phase remains constant, there is then a sharp rise corresponding to those seen in the amplitude and deflection signals which is due to the formation of a water meniscus. After this the phase continues to increase more slowly as tip-surface interactions act to damp the oscillation. Finally there is a sharp turning point as the tip begins to push into the sample surface. That this is due to pushing into the surface can be seen by comparing it to a corresponding deflection force curve.

When the cantilever is pinned to the surface it will vibrate at a different frequency, the first clamped mode of the cantilever is much higher than the free torsional mode [151], so the phase being monitored approaches zero. It is useful to acquire the force curves for both the phase and amplitude as they can be used to reconstruct the tip-sample force.

7.5: Surface induced molecular water layering

An interesting potential use of TR force curves is to study how water is molecularly structured around different surfaces, and the role this may play in biological systems. In ambient conditions water naturally adsorbs to the majority of surfaces, and thus mediates interaction between neighbouring surfaces and molecules.

Water at interfaces exhibits different properties to those seen in bulk. Water is known to exhibit surface induced layering at liquid-solid interfaces, the intermolecular interactions within the water are affected by the surface properties, which can lead to layering, as seen in figure 7.8.
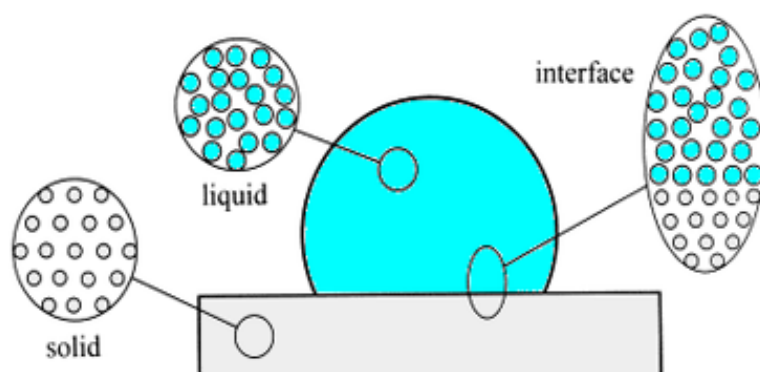
Figure 7.8 – Diagram of a water droplet on a solid surface. In bulk liquid the water molecules have no long range ordering; whereas at the solid-liquid interface they exhibit layering due to interactions with the solid. Adapted from [152].

The structure and extent of the layering is thought to be determined by interactions with the solid surface and are thus dependent on the different chemical properties of the surface [153]. The effects of the surface decay with distance from the sample and so the structure is found to exist for only a few layers. The first layer is quite highly structured and it is this layer that is generally of most interest as it is thought to determine the interfacial properties [154].

Understanding these interactions is crucial to many different fields throughout biology and materials sciences; most importantly understanding the behaviour of the

water shells surrounding biochemical molecules like proteins and DNA, and also other fields including understanding cell membrane water transport and creating biosensors [155]. The existence of surface induced water layering has been known about since 1983 where surface force apparatus (SFA) was used to measure its effect [156].

In ambient conditions, as an AFM tip approaches a surface it interacts with the adsorbed water, pushing successive layers of water out of the way, and technological developments have allowed SPM techniques to be used to investigate this structure. Shear force microscopy (ShFM) was used by Antognozzi to demonstrate the presence of ordered layers of water between the ShFM tip and a mica surface [157]. More recently significant advances have been made by Fukma and Asakawa, using a highly sensitive custom built AFM operating in FM-TM, with a vertical oscillation amplitude of 0.1–0.3 nm, roughly 10 times the sensitivity available with current commercial AFMs [158].

Torsional resonance atomic force microscopy (TR AFM) offers a way to directly probe this water structure, it holds several advantages compared to previous techniques: its dynamics inherently lead to higher sensitivity which is needed to detect the very low forces involved. The tip remains in the attractive region of the surface potential throughout and the tip's motion is insensitive to normal surface forces, these lead to high stability. It also has lower oscillation amplitudes, needed due to the small size of the water layers so as to not disturb them. Which is possible due to its increased sensitivity and stability relative to other AFM modes.

The region where water structure is found is after formation of the water meniscus and before the snap to contact, which occurs partway up the slope in the amplitude signal. The flexural deflection is not sensitive enough to detect the structure and so only the amplitude and phase channels are used.

The previous force curves were not sensitive enough to see the oscillatory features which are indicative of water layering; and so care was taken to achieve a high degree of sensitivity. The microscope was left to stabilise for 30 min to reduce thermal drift; the ramp size was reduced to approximately 30 nm to increase resolution and a clean area of the sample was chosen to reduce contamination. Force curves were taken over the all three SAMs with no clear difference between the hydrophobic and hydrophilic SAMs.

Hydration layering has been seen in many force curves, on both extension and retraction, as can be seen in figures 7.9 and 7.10. These curves show oscillatory features with a period of approximately 2.7 Å, which is in agreement with the hydrodynamic radius of water [156]and with values from previous studies [157], [159]. These oscillatory features are seen in the expected region of the force curve between the formation of the water meniscus and snap to contact and there is thus strong evidence for water layering. Most commonly three peaks were seen, with higher numbers of peaks not found, although additional small peaks would be very difficult to pick out over the noise.
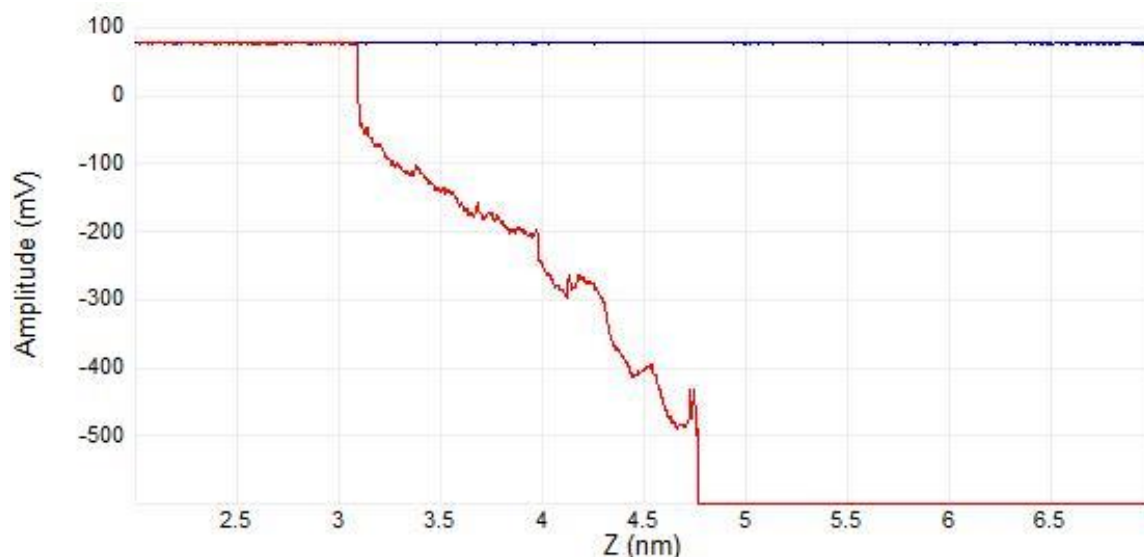
Figure 7.9 – A small section of a TR Amplitude retraction curve (red) taken over an ODT monolayer in ambient conditions. The step-like features are clearly visible in the lower part of the curve; the average separation of peaks is 2.8 Å, the hydrodynamic radius of water. Small peaks are also visible on the upper part of the curve which may due to hydration layers on the cantilever tip.

Oscillatory features are seen in both amplitude and phase curves, as can be seen in figure 7.10, they occur in the same place on both curves. The peaks in the phase signal are larger and more distinct than in the amplitude, with the small peaks clearer suggesting that phase signal may show more sensitivity. However the noise peaks are also much larger in the phase signal and it is the size of the peaks relative to the noise that is important, here the phase signal seems worse than the amplitude.
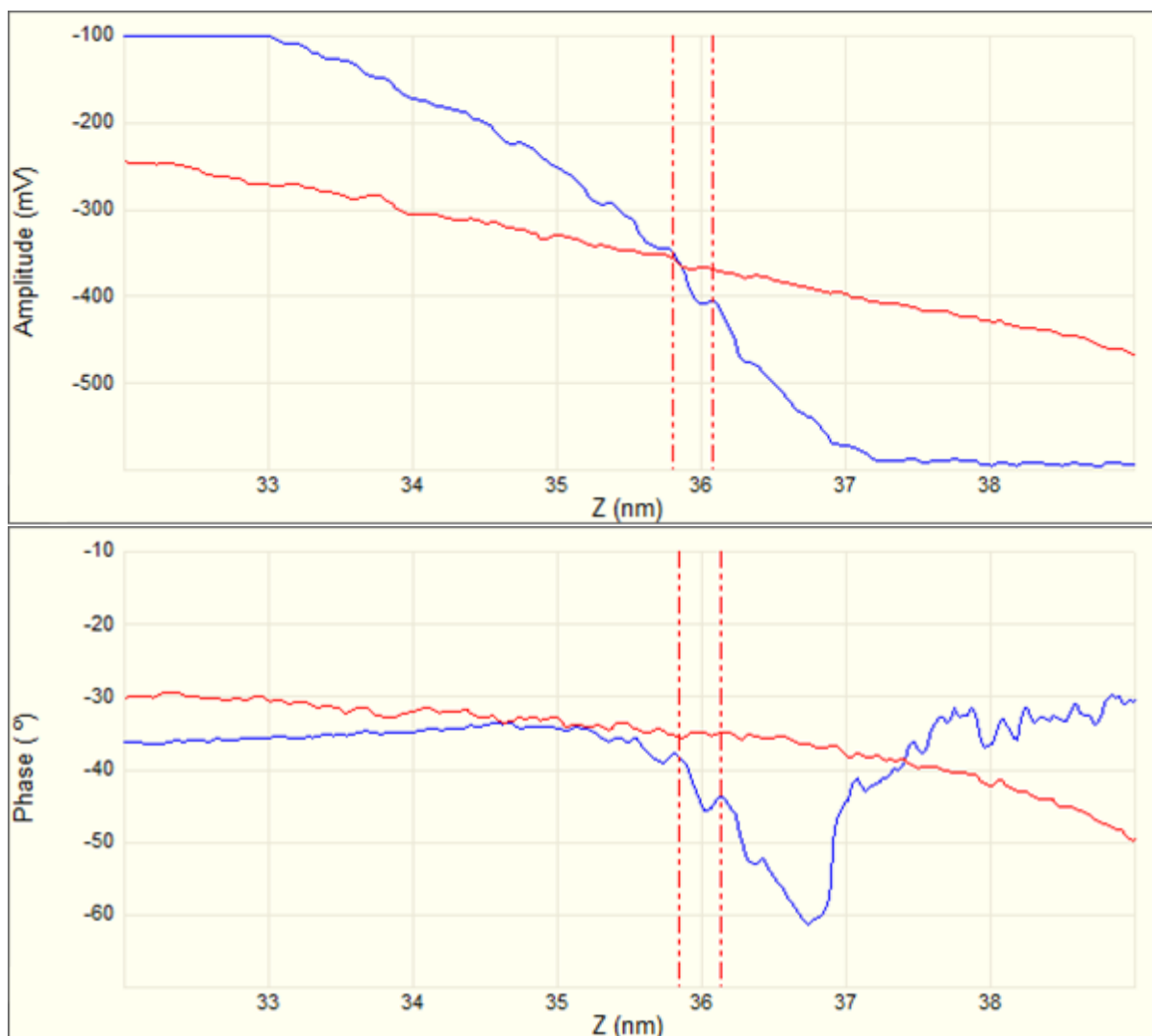
Figure 7.10 - Amplitude (top) and phase (bottom) curves taken in TR mode over ODT, on both these oscillatory features are seen with peaks occurring in the same place with spacing of 2.9 Å.

In order to more easily visualise the oscillatory features it can be useful to isolate them. This is done by fitting a line to represent the amplitude curve without any oscillatory features or noise and then taking this away from the data. This process is seen in figure 7.11, here the oscillatory features are much clearer in the graph and they can be compared directly to the noise. The features consist of the 3 peaks at the end which have spacings of 2.9 Å, to the left of that are lots of other peaks are due the noise. By comparing the oscillatory features to the noise differences can be distinguished: they are much larger and clearer, they have the expected spacing, and occur in the expected region of the force curve.
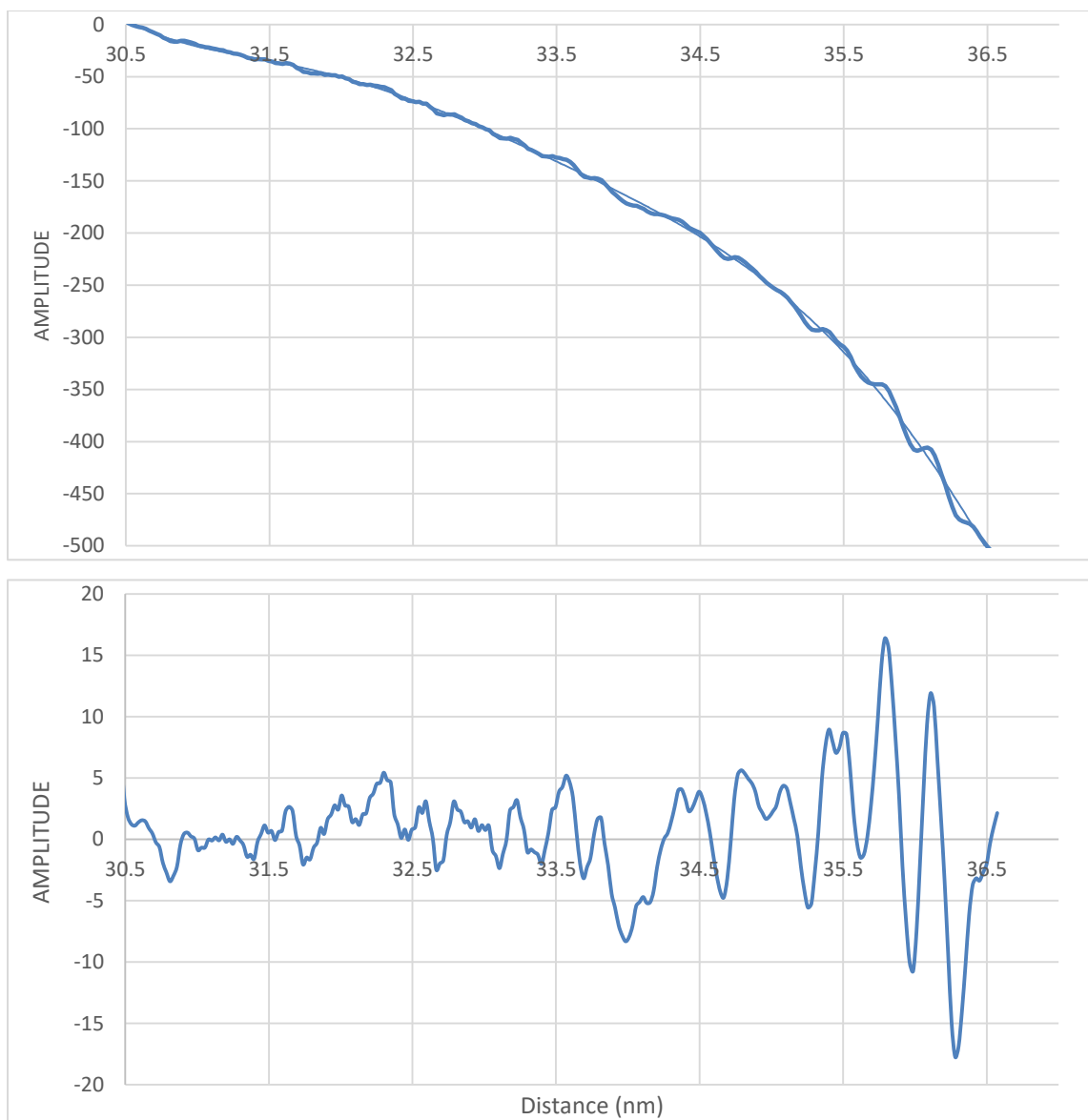
Figure 7.11 – Deviations (bottom) from the amplitude curve (top) which can be seen by fitting a line and taking it away. This makes the oscillatory feature much clearer. Compared to the other deviations the oscillatory features are larger and much more clearly defined.

The above results were all collected with the Multimode, and it was expected that the ICON might have greater sensitivity. This was however not the case with no clear features seen at all over a number of experiments. A possible explanation may be the presence of cross talk between the neighbouring piezoelectric actuators in the new commercial holder. They may be close enough for a signal to pass between them with could induce some flexural motion in the cantilever thus making detection of water layers impossible. Another explanation may be that the asymmetric tip oscillation supplied by the holder acts to disturb the water layers.

7.5.1: Differences in molecular water layering on hydrophobic and hydrophilic surfaces

No clear difference in the force curves was seen between the hydrophilic and hydrophobic SAMs. It was thought that this may be due to contamination and surface defects, and so some simpler surfaces were used, these were silicon, mica and highly oriented pyrolytic graphite (HOPG) samples. Silicon and mica are both hydrophilic and HOPG is hydrophobic. Silicon wafers were cut with a diamond tipped scribe and cleaned with acetone and isopropyl alcohol (IPA); mica and HOPG were both freshly cleaved using adhesive tape.

A number of force curves were taken on each of the three surfaces. In approximately 1 in 5 curves features which appeared to correspond to molecular water layering were seen; this ratio was the same for all surfaces. For each curve the number of peaks and the spacing between peaks were recorded and the average for each surface was measured.

Surface	Peaks spacing (nm)	No. peaks per curve
HOPG	0.280 ± 0.035	2.26
Mica	0.292 ± 0.044	2.44
Silicon	0.290 ± 0.042	2.37

Table 7.2 – Average peak spacing and number of peaks for the oscillatory features on different surfaces.
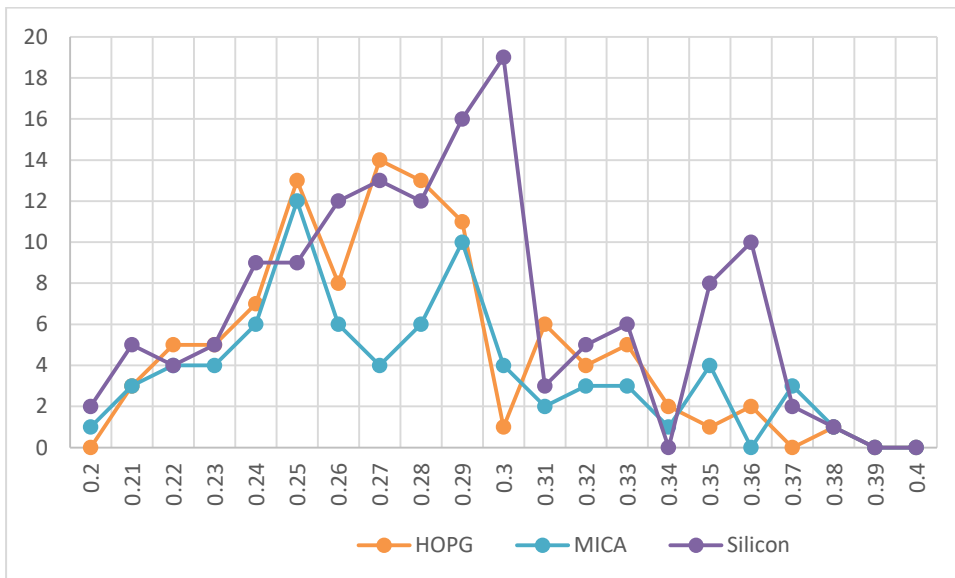
Figure 7.12 – Histograms showing range of spacing of oscillatory features for Silicon, Mica and HOPG. The jumpy nature is in part due to a resolution mismatch.

Table 7.1 shows the average peak spacing and number of peaks for the oscillatory features on the three surfaces and figure 7.12 shows a histogram of the recorded peak spacing.

All three surfaces have average spacings consistent with the hydrodynamic radius of water, and are thus indicative of molecular water layering. There was no difference found in number of peaks between samples. The histogram shows that there is a wide variation in individual peak spacings. However the two hydrophilic surfaces mica and silicon have very similar average spacings, with a slightly smaller spacing seen for the hydrophobic surface HOPG. The difference between these is greater than the margin of error, however the difference is only slightly more than two standard deviations and so these differences are not conclusive.

7.6: Measuring chain orientation in polyethylene lamellae

TR AFM was used to attempt to measure chain orientation within lamellae and how that might change as the film was subjected to tensile strain. Within lamellae are individual polymer chains, in undeformed polyethylene these chains are aligned perpendicular to the lamellae [21]. When the polymer is stretched the lamellae are deformed and eventual fractured, during which the orientation of the chains within the lamellae will change, but it was not clear from the data presented in chapter 4 when or to what extent this transformation occurs.

In TR the tip stays close to the surface throughout its oscillation, it oscillates with a small dither perpendicular to the cantilever, with an amplitude less than 1 nm. The orientation of objects on the surface at a length scale similar to the oscillation could affect its amplitude and phase. TR of polyethylene shows a strong phase contrast and so it is thought that it might be possible to use this to see chain orientation. Techniques such as SAXS can be used to measure average chain orientation for a sample, but this method would be the first to provide a local measure of orientation.

Care must be taken in that differences in phase can be dependent on many variables, including how much the features align with the scan direction.

The custom built stretching rack was designed to fit under the Dimension and was much too large for the ICON and Multimode. Thus In order to image stretched polymer films in TR, and in particular the same areas which had been imaged with the Dimension, it is necessary to use a technique to transfer the film. A custom built frame was developed for this purpose.

The frame can be seen in figure 7.13, it consists of a thin metal washer. The film is on the stretching rack, under tension. Superglue is then used to stick the frame to the film from above, with the centre of the neck in the middle of the washer, well away from any contaminating glue. The film is the cut either side of the

frame to separate it from the stage, the film within it remains in tension. A metal puck is then adhered to the film from below for support. The frame is thin enough that the film towards its centre can be imaged without the cantilever or its holder hitting the frame.

Figure 7.13 – A frame consisting of a metal washer which is used to keep the film under tension when transferring to another microscope. The white paper seen here was only used in this test.

A number of images of polyethylene were taken, an example is seen in figure 7.14 which shows it undeformed. It can be seen that this provides a good image similar to what is seen in TM and contact mode, clearly showing the lamellae. The phase is interesting showing a high contrast. It is not seen here but TR can be more prone to issues tracking the surface than TM.
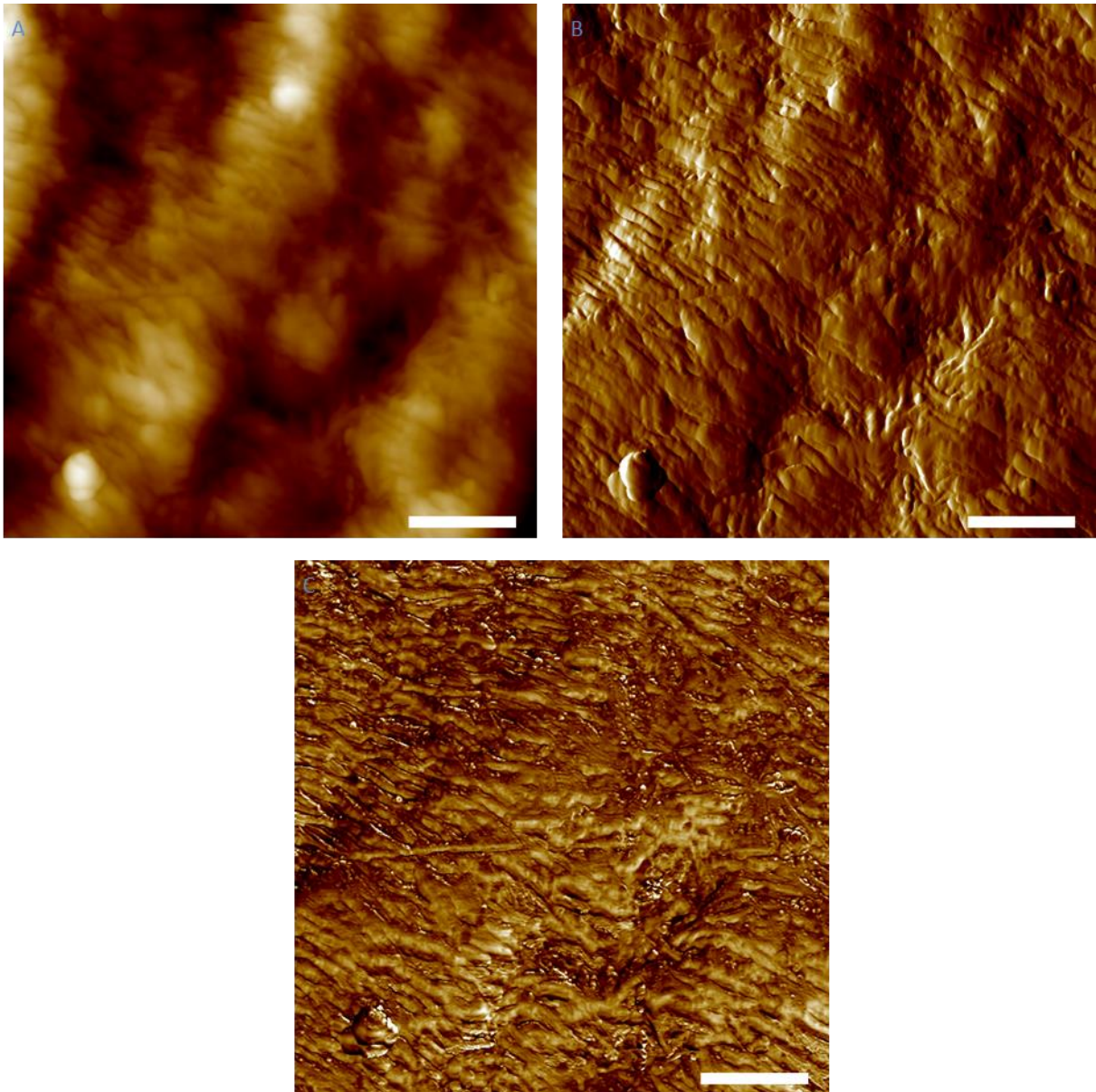
Figure 7.14 –TR height (A), amplitude (B) and phase (C) images of unstretched polyethylene. Scale bars 1 μm.

To measure a change in chain orientation, we must first be sure of measuring the chain orientation; this was done on unstretched polyethylene where the chains will be aligned perpendicular to the lamellae. The sample here was simply attached to a metal puck with super glue.

To do this TR mode was used to image areas of the film where there are lamellae which are both in line with, and at 90 ° to, the slow scan direction, and thus the dither direction. This would give the largest contrast difference between the

lamellae. 1 µm images are chosen to give high resolution, an example is shown in figure 7.15 in A, here there is a clear apparent contrast difference between vertical and horizontal lamellae. This is true for a number of different images.

To check if the observed contrast difference is due to the dither direction or the scan direction images were taken of the same area at scanning angles of both 0 ° and 90 °. At 0 ° the scan and dither direction are aligned, and at 90 ° they are perpendicular to each other. An example is shown in both A and B in figure 7.15, in B where the scan direction has been rotated the large contrast difference is not visible, indicating it was due to scan direction.
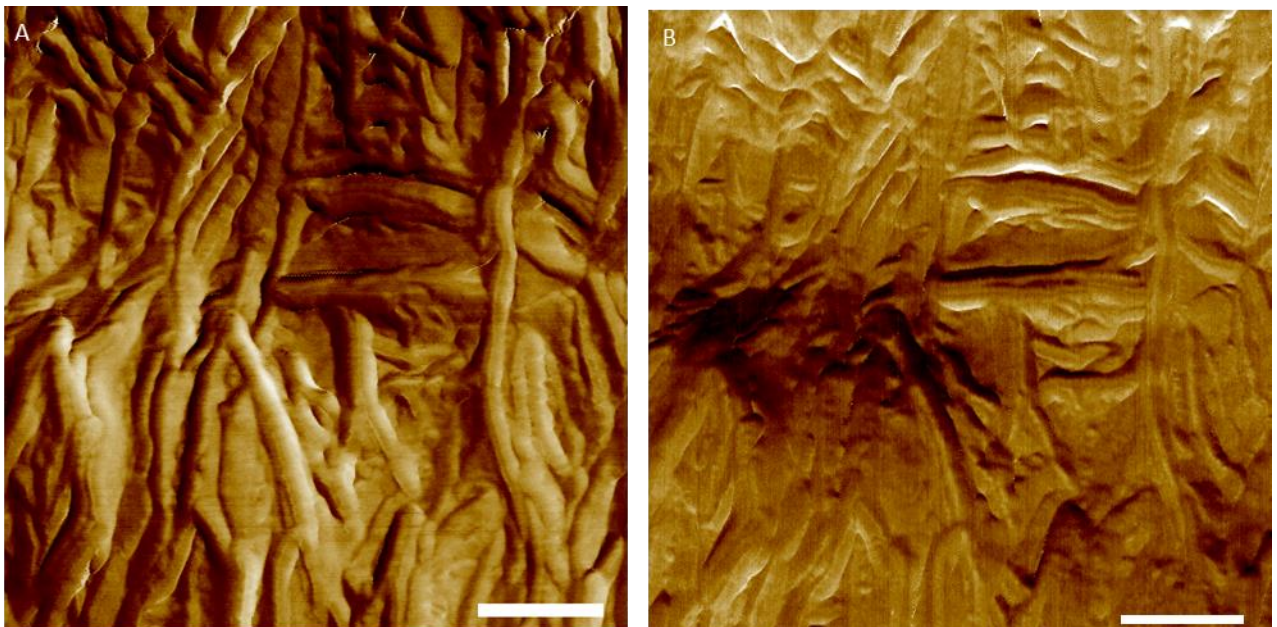
Figure 7.15 – Two TR phase image of the same area taken at 0° (A) and 90° (B). Scale bars 200 nm. Z scales 50°.

It is important to numerically measure the difference in brightness. This was done using Imagej, where the average brightness of each lamella in an image was measured and the average values for those aligned with and perpendicular to the dither direction taken. This was repeated for the corresponding 90 ° image and the values were compared.

The values can be seen in table 7.2. For the first image there is a large difference between lamellae aligned with the dither direction and those perpendicular to it. When the scan axis is rotated however the lamellae in both directions have similar brightness, with those perpendicular to the dither direction being slightly brighter.

These results show that the difference in brightness is due more to the alignment of the lamellae with the scan direction than the alignment of the chains with the TR dither direction, and thus it is difficult to use this method to measure chain orientation.

Scan Angle	Alignment of lamellae	Brightness
0°	Aligned with dither direction / Aligned with fast scan direction	1.38
	Perpendicular to dither direction / Perpendicular to fast scan direction	0.48
90°	Aligned with dither direction/ Perpendicular to fast scan direction	1.09
	Perpendicular to dither direction / Aligned with fast scan direction	1.21

Table 7.3 –How brightness varies with lamellae alignment with both the fast scan direction and the TR dither direction, for two different areas. Brightness in arbitrary units.

There would appear to be some effect due to alignment with TR dither direction, with the difference in brightness in the 90° image much smaller than for 0°.

This indicates that a combination of both effects is in play, with the effect from alignment with the fast scan direction being larger.

It could thus be possible to measure a change in chain orientation from the difference in brightness values for aligned and perpendicular lamellae at both 0° and 90° scan angles. This was however judged to be a not clear enough potential measurement, which would have a large error, and it seems this experiment does not have the necessary sensitivity.

A number of things were tried to increase the sensitivity. The machine was left overnight to settle. A range of different amplitudes and set points were used, with different relative setpoint used. However better results could not be obtained.

7.7: Conclusions and future work

In this chapter a number of uses of TR AFM were investigated, using both a custom built holder and a commercial holder. TR was shown to have promise for imaging, with a high phase contrast and the possibility for high speeds.

The existence of surface induced molecular water layering was shown, with oscillatory features with spacings consistent with the hydrodynamic radius of water. This was observed on a range of surfaces, including both hydrophobic and hydrophilic surfaces. A difference in average peak spacing based on the hydrophobicity of the surface was seen, however this difference was not substantially larger than the margin of error given the high variability of the force curves, and so more work would be needed to be sure of this difference.

Overall the oscillatory features were not observed consistently on force curves, with the features only clearly occurring in a small percentage of curves. In

order for this work to move forward it is important to understand why this occurs and to improve their consistency and to more clearly distinguish them from the noise.

There are several possible explanations for this; it could be that hydration layers do naturally occur rarely, though this is highly unlikely as they were found to be common in previous studies [160]. It could also be that they are rare here due to contamination of the surface and the tip, though this is unlikely as curves were similar over a range of surfaces.

A more likely explanation is that the layers exist but are not seen; they may be disturbed by the motion of the tip, or they may be either not measured at all or smaller than the background noise. Detecting the water layers requires a high degree of sensitivity which may not have been always achieved.

The commercial holder from the ICON was seen as a way to solve this, with potentially higher sensitivity, however this was not the case with no clear features seen at all over a number of experiments. A possible explanation may be the presence of cross talk between the neighbouring piezoelectric actuators in the new commercial holder. They may be close enough for a signal to pass between them with could induce some flexural motion in the cantilever thus making detection of water layers impossible. Another explanation may be that the asymmetric tip oscillation supplied by the holder acts to disturb the water layers.

There are a number of ways to potentially improve measurements using the current AFM. Increased humidity may improve the occurrence of water layering. Also decreasing the noise more, would make the signal clearer. A hood, a Bruker MMAHC-212, was used for this purpose with no apparent improvement. Alternately the AFM used may not have enough sensitivity and another could be used.

In the longer term, there are many new avenues to explore, including surfaces functionalised with proteins and the effect on water layering of cryoprotectant molecules, which are known to disrupt hydrogen bonding.

TR was also used to attempt to measure chain orientation in polyethylene lamellae by a change in the phase based on if they are aligned or not with the dither direction. A large difference was seen between neighbouring perpendicular lamellae across a number of images, however this was seen to be more due to alignment with the scan direction than the dither. Once this effect was factored out, there was a small effect due to alignment with dither direction but this was not considered large enough to proceed as there would be a large error involved.

The experiment does not appear to have the necessary sensitivity. The steps to improve it are largely the same as for water layering, with lower noise and perhaps a difference instrument.

Once the sensitivity has improved, the technique could then be used to measure how the orientation of the chains within lamellae change with deformation. TR could be used in conjunction with the images in the other chapters to build a better understanding of the effect of chain orientation on lamellae rotation and breakup.

Chapter 8 – Conclusions and further work

In the work presented here, atomic force microscopy has been used to investigate the deformation and fracture of semi-crystalline polymers, in situ, at the lamellae scale. This chapter will summarise the key findings and comment upon the perspectives for the use and future development of these techniques. Each area of research addressed in this work is discussed below in its own subsection.

In chapter 4, HDPE was stretched and imaged in situ, sets of images in the same place were taken allowing the observation of processes as they occur. The processes seen agree with the results of previous studies, the following were seen: separation of lamellae, tilting and rotation of lamellae, alignment with the stretch direction and breakup into blocky elements. Also significant nanovoiding and craze formation and growth were seen.

By following processes, information on where the processes start and how they progress was gathered, this has not been seen before. Other than a small change in lamellae separation, lamellae movement appears to be almost entirely driven by crazes, their opening and growth, otherwise they tend to act in concert with their neighbours. Branch points of branched lamellae were seen to undergo the least deformation, this is assumed to be due to the branch acting to pin the lamellae in position next to each other.

Crazes form away from branch points and their growth is often curtailed geometrically by branch points, with a branch point forming a 'corner' of a craze. On the opposite side to a branch point, there is sometimes a pinning effect with no visible branch point. This might be due to an unseen branch in lamellae below the surface. Crazes are not seen to all form at once, some new crazes are seen to form later, long after initial crazes.

Meshes of points were fitted to sets of images to help understand the processes. In the future it would be useful to improve this process. An automated

fitting process would be both quicker and potentially lead to more accurate and consistent results. This would allow the fitting of larger scale images to understand how the heterogeneity of deformation changes on larger scales. The resolution would need to be increased for this to work.

Isotactic polypropylene was stretched, and its deformation and fracture was observed in situ, on the nanometre scale. The processes were largely seen to proceed as seen in previous studies, though with some key differences.

Strain was found to be almost entirely localised to crazes. Crystalline regions were found to exhibit virtually no deformation, until individual crystallites broke off into the craze. At very high strains larger areas broke up into individual crystallites, these areas were seen to have a phase difference to undeformed crystalline regions, showing their changing material properties as they begin to break up.

The crystal blocks within the crazes can be traced back to the individual crystallites that form the crystalline regions, without appearing to shrink or undergo deformation. Thus it appears they act passively to the processes going on around them, which is in contrast to the behaviour of lamellae in polyethylene.

The crazes, and in particular the largest primary crazes, were found to largely occur perpendicular to the stretch direction. Secondary crazes perpendicular to the primary crazes, were seen, these are formed due to mismatches in strains perpendicular to the stretch direction caused by the primary crazes opening.

The rate of individual craze growth was seen to vary between neighbouring crazes. They are seen to stretch at different times, with one staying relatively static whilst another stretches and vice-versa, which demonstrates localised strain hardening.

There are other processes which are seen in other studies which are not seen here including deformation banding and wedge formation; these are larger scale processes.

By watching the same areas over time we can begin to understand why the crazes form and grow where they do. The primary and secondary crazes are formed due to the overall strain, and perpendicular strains caused by mismatches respectively, however where they will occur is not clear. Some crazes seem to nucleate at defects and incipient crazes before propagating onwards, however this is often not the case. Many of the crazes we see here have propagated from outside the imaging area, which is sometimes visible in larger images.

Some crazes, however, clearly start in the imaging area without any defects, in fact crazes often choose routes next to but avoiding a defect, even if a nearby defect might seem to offer a more obvious route. This may be due to defects below the surface of the sample which we cannot see, or it may simply be that defects are not that important in choosing the best route to minimise strain.

To better understand this in the future it would be useful to repeat this data with larger scan sizes whilst still keeping the same resolution. This would increase the problem of drift and so to mitigate this higher scan speeds could be used, perhaps making use of techniques such as torsional tapping and torsional resonance AFM. It would also be useful to take more images in each set to better follow the processes. Applying a fitting procedure to follow the movement of the crystallites on the surface would also be useful.

A feature not seen in any previous studies is the existence of 'geometric crazes', these are areas within fibrillated regions where the fibrils are not aligned parallel to neighbouring fibrils, short sections of fibril are arranged in apparent geometric patterns at angles to each other and the main parallel fibrils. Similar features are seen in by crack edges in polyethylene in chapter 6. They are assumed

to be formed by a combination of localised strains occurring in multiple directions. These stresses perpendicular to the stretch direction occur due a mismatch in stresses caused by the opening of the crazes. In the future it would be useful to observe the formation of geometric crazes. This would require being able to follow the same area at high strains, and would require stretching the sample then choosing the area that was stretching the most to follow. Angular analysis, showed the peak of their angles, both to themselves and to the stretch direction to be 60°, which is assumed be due the strongest structures tending to form, and doesn't seem to bear any relation to the shear banding angle or the unit cell.

The effect of crack edges on polyethylene deformation and fracture was studied. Both mapping spatially and watching the same area evolve with increasing strain. A distribution of both strain and thus stress, which varied with both magnitude and orientation, was seen around the crack tip. This was found to largely agree with previous studies, with the stress aligned with the crack edge and decreasing with distance over the scale of 10s of μms. This kind of distribution implies a flow of material towards the tip. A key exception to this was the existence of large (~100 μm) areas of uniformly high deformation which appeared at the end of the crack tip and had somewhat sharp boundaries to the rest of the film. This is likely caused by multiaxial strain.

The deformation processes occurring are similar to those seen in simple extension for stretched including the existence of crazes, a difference being the large scale shear seen throughout. Also within a couple of μms of the crack edge, the surface was completely fibrillated, with closely packed fibrils aligned with the edge, there are no voids here, they appear to have been closed up by the shear forces from the edge.

In highly stretched regions 'geometric crazes' have been seen, these are once again areas within fibrillated regions where short sections of fibril are arranged in apparent geometric patterns at angles to each other and the main parallel fibrils.

These features have not been seen in previous studies, they would not be visible in spectroscopy methods or in low resolution microscopy. It is assumed that they are formed by a combination of localised strains occurring in multiple directions caused by the crack tip. The geometric crazes are similar to features seen for polypropylene in chapter 5. Here they are generally larger and more complex, and so have a difference in most common angles between fibrils.

In the future it is important to investigate further how these geometric crazes form and grow and so more sets close to the crack edge could be taken. In particular it is important to capture high resolution sets of images and so these at larger scales would be used. These images would be fitted with meshes of points to help understand the process. An automated fitting procedure would help here, both to increases accuracy and consistency and to allow the fitting of larger scale images. These procedures would also be useful in understanding the development of the defined uniform high deformation area by watching how it forms.

The polyethylene and polypropylene samples used here can be seen to have very different behaviour under tension. For polyethylene there are large amounts of both deformation and fracture seen, for polyethylene however there is almost no deformation of the individual crystallites. This would seem to indicate that in the HDPE used the crystals are relatively weak compared to the amorphous region, and must contain a significant number of defects; whereas in the isotactic polypropylene the crystals must be strong with few defects. Polypropylene is generally a more brittle material than polyethylene, but this will depend greatly on factors such as the branching and molecular weight of the materials.

In both chapter 5 with stretched polypropylene and chapter 6 with polyethylene near a crack edge geometric crazes have been seen. The similarities between the two is that that they both consist of regions within fibrillated regions where short sections of fibril are arranged in apparent geometric patterns at angles

to each other and the main parallel fibrils. Both the fibrils and the regions are of somewhat similar size, and occur between the main fibrils.

The differences are that the polyethylene geometric crazes are seen to be larger and more complex, with those in polypropylene only occur in thin lens shaped regions. There is also a difference in the most common angle of the fibrils, it is approximately 60 ° for polypropylene and 36 ° for polyethylene, with no clear significance seen to these angles.

In both cases these features occur at extremely high strains, and where there appears to be some multiaxial strain, caused by the crack tip for polyethylene and the mismatch in strain due to craze opening in polypropylene. So these are seen as the likely causes of these features.

It is not clear what exactly causes the differences seen between the materials, although clearly they will stem from the difference in material properties, with polypropylene being more brittle and thus they perhaps have less room to grow.

Overall it seems that AFM is useful for studying these phenomena, as it has allowed them to be studied in situ at the lamellae scale. It could be used to give higher resolution images to allow chains to be seen, or to extract material properties from the sample.

AFM does have its drawbacks here, it only sees surface processes and is limited to thin films, and so it cannot see the large scale cavitation that may occur in the bulk. It also cannot see and branch points and defects which may occur below the surface of the film and may be affecting how the deformation and fracture proceed. AFM is also a slow imaging technique, which both makes it slow to take data, and leads to problems of creep and drift effecting images. In the future faster scanning modes could have used here to mitigate some of this.

A number of uses of TR AFM were investigated. TR was shown to have promise for imaging, with a high phase contrast and the possibility for high speeds.

The existence of surface induced molecular water layering was shown, with oscillatory features with spacings consistent with the hydrodynamic radius of water. This was observed on a range of surfaces, including both hydrophobic and hydrophilic surfaces. A difference in average peak spacing based on the hydrophobicity of the surface was seen, however this difference was not substantially larger than the margin of error given the high variability of the force curves, and so more work would be needed to be sure of this difference.

Overall the oscillatory features were not observed consistently on force curves, with the features only clearly occurring in a small percentage of curves. In order for this work to move forward it is important to understand why this occurs and to improve their consistency and to more clearly distinguish them from the noise. It is likely that the layers exist but are not seen; they may be disturbed by the motion of the tip, or they may be either not measured at all or smaller than the background noise. Detecting the water layers requires a high degree of sensitivity which may not have been always achieved.

There are a number of ways to potentially improve measurements using the current AFM. Increased humidity may improve the occurrence of water layering. Also decreasing the noise more, would make the signal clearer. In the longer term, there are many new avenues to explore, including surfaces functionalised with proteins and the effect on water layering of cryoprotectant molecules, which are known to disrupt hydrogen bonding.

TR was also used to attempt to measure chain orientation in polyethylene lamellae by a change in the phase based on if they are aligned or not with the dither direction. A large difference was seen between neighbouring perpendicular lamellae across a number of images, however this was seen to be more due to alignment with

the scan direction than the dither. Once this effect was factored out, there was a small effect due to alignment with dither direction but this was not considered large enough to proceed as there would be a large error involved.

The experiment does not appear to have the necessary sensitivity. The steps to improve this would include lower noise and perhaps a difference instrument. Once the sensitivity has improved, the technique could then be used to measure how the orientation of the chains within lamellae change with deformation. TR could be used in conjunction with the images in the other chapters to build a better understanding of the effect of chain orientation on lamellae rotation and breakup.

There are many possible avenues for the future of this project, these include: Using different samples to explore the effects of branch content on how the processes occur. LDPE, has significantly more branching than HDPE, and because of this has greater flexibility and lower strength. The effect of different molecular weights can also be seen, with UHMWPE having very high strength. Sets could also be taken at different temperatures or strain rates, with the use of a specialised stage, to see their effects. Different semi-crystalline polymers such as polyethylene terephthalate (PET) or polytetrafluoroethylene (PTFE) could also be investigated.

A strain gauge could be integrated into the stage, in order to measure stress-strain curves to compare with what is seen in the images.

It would be useful to use Micro focus X-ray techniques, these have spot sizes of less than 10 µm, allowing measurements to be taken on the scale of some of the images shown here. These results could be compared with the images seen here. This is particularly important around crack tips, where strain varies significantly with position.

Small-angle electron scattering (SAES) could be used to examine the structure of the fibrils. Also photoelasticity measurements could be taken using the birefringence of the material to measure changes in local deformation.

Molecular scale AFM imaging could also be undertaken, such as that undertaken by Mullin and Savage [161][162] using TT AFM. This could allow the imaging of the chains within lamellae and how they change during deformation.

Bibliography

[1]   R. J. Young and C. I. Chung, "Introduction to Polymers," *J. Eng. Mater. Technol.*, vol. 104, no. 4, p. 297, 1982.

[2]   W. B. Jensen, "The Origin of the Polymer Concept," *J. Chem. Educ.*, vol. 85, no. 5, p. 624, 2008.

[3]   L. H. Baekeland, "Original papers: The synthesis, constitution, and uses of bakelite," *Ind. Eng. Chem.*, vol. 1, no. 3, pp. 149–161, 1909.

[4]   H. Staudinger, "Über Polymerisation," *Berichte der Dtsch. Chem. Gesellschaft (A B Ser.*, vol. 53, no. 6, pp. 1073–1085, 1920.

[5]   R. J. Fleming, "An introduction to polymer physics," *Physicist*, vol. 40, no. 1. p. 26, 2003.

[6]   M. Rubinstein and R. H. Colby, "Polymer Physics," *Oxford Univ. Press New York*, 2003.

[7]   J. Rösler, H. Harders, and M. Bäker, Mechanical behaviour of engineering materials: Metals, ceramics, polymers, and composites. 2007.

[8]   A. Peterlin, "Folded chain model of highly drawn polyethylene," *Polym. Eng. Sci.*, vol. 9, no. 3, pp. 172–181, 1969.

[9]   H. D. Keith and F. J. Padden, "Deformation mechanics in crystalline polymers," *J. Polym. Sci.*, vol. 41, no. 138, pp. 525–528, 1959.

[10]   H. D. Keith, F. J. Padden, and R. G. Vadimsky, "Intercystalline links - Critical Evaluation," *J. Appl. Phys.*, vol. 42, no. 12, p. 4585, 1971.

[11]   A. Keller, "A note on single crystals in polymers: Evidence for a folded chain configuration," *Philos. Mag.*, vol. 2, no. 21, pp. 1171–1175, 1957.

[12]   A. Keller and A. O'Connor, "Study of single crystals and their associations in polymers," *Discuss. Faraday Soc.*, vol. 25, p. 114, 1958.

[13]   D. H. Reneker and P. H. Geil, "Morphology of polymer single crystals," *J. Appl. Phys.*, vol. 31, no. 11, pp. 1916–1925, 1960.

[14]   S. Allen and L. Thomson, *The structure of materials*. John Wiley & Sons, 1999.

[15]   D. Mi, C. Xia, M. Jin, F. Wang, K. Shen, and J. Zhang, "Quantification of the effect of Shish-Kebab structure on the mechanical properties of polypropylene samples by controlling shear layer thickness," *Macromolecules*, vol. 49, no. 12, pp. 4571–4578, 2016.

[16]   Y. Zhao, G. Matsuba, and H. Ito, "Shear-induced crystallization and rheological behavior of syndiotactic polystyrene," *J. Mater. Res.*, vol. 27, no. 10, pp. 1372–1378, 2012.

[17]   P. I. Vincent, "The necking and cold-drawing of rigid plastics," *Polymer (Guildf).*, vol. 1, pp. 7–19, 1960.

[18]   C. G'Sell, J. M. Hiver, A. Dahoun, and A. Souahi, "Video-controlled tensile testing of polymers and metals beyond the necking point," *J. Mater. Sci.*, vol. 27, no. 18, pp. 5031–5039, 1992.

[19]   A. M. Vinogradov and S. Schumacher, "Cyclic creep of polymers and polymer-matrix composites," *Mech. Compos. Mater.*, vol. 37, no. 1, pp. 29–34, 2001.

[20]   E. M. Arruda, M. C. Boyce, and R. Jayachandran, "Effects of strain rate, temperature and thermomechanical coupling on the finite strain deformation of glassy polymers," *Mech. Mater.*, vol. 19, no. 2–3, pp. 193–212, 1995.

[21]   P. B. Bowden, R. J. Young, and M. Science, "Deformation mechanisms in crystalline polymers," *J. Mater. Sci.*, vol. 9, no. 12, pp. 2034–2051, 1974.

[22]   L. Lin and a. S. Argon, "Structure and plastic deformation of polyethylene," *J. Mater. Sci.*, vol. 29, no. 2, pp. 294–323, 1994.

[23]   A. Galeski, Strength and toughness of crystalline polymer systems, vol. 28, no. 12. 2003.

[24]   R. G. Quynn and H. Brody, "Elastic 'Hard' Fibers. I.," *J. Macromol. Sci. Part B*, vol. 5, no. 4, pp. 721–738, 1971.

[25]   W. E. Kaufman and J. M. Schultz, "Lamellar and interlamellar structure in melt-crystallized polyethylene - Part 3 Effects of small deformation," *J. Mater. Sci.*, vol. 8, no. 1, pp. 41–46, 1973.

[26]   G. E. Attenburrow and D. C. Bassett, "Compliances and failure modes of oriented chain-extended polyethylene," *J. Mater. Sci.*, vol. 14, no. 11, pp. 2679–2687, 1979.

[27]   W. L. Wu, V. F. Holland, and W. B. Black, "Kink bands by compression of ultra-drawn linear polyethylene," *Journal of Materials Science*, vol. 14, no. 1. pp. 250–252, 1979.

[28]   G. W. Groves and P. B. Hirsch, "Interlamellar slip in polyethylene," *Journal of Materials Science*, vol. 4, no. 10. pp. 929–932, 1969.

[29]   T. Tagawa, "Piled-lamellae structure in polyethylene film and its deformation," *J. Polym. Sci. Part B Polym. Phys.*, vol. 18, no. 5, 1980.

[30]   F. Auriemma, G. Alfonso, and C. De Rosa, Polymer Crystallization 1: From Chain Microstructure to Processing. Springer, 2017.

[31]   D. M. Shinozaki and G. W. Groves, "The plastic deformation of oriented polypropylene and polyethylene: deformation mechanisms," *J. Mater. Sci.*, vol. 8, no. 7, pp. 1012–1022, 1973.

[32]   T. Hinton, J. G. Rider, and L. A. Simpson, "Chain and fibrillar slip in oriented polyethylene," *J. Mater. Sci.*, vol. 9, no. 8, pp. 1331–1336, 1974.

[33]   S. G. Burnay and G. W. Groves, "Deformation mechanisms in oriented high density polyethylene," *J. Mater. Sci.*, vol. 13, no. 3, pp. 639–646, 1978.

[34]   R. Hiss, S. Hobeika, C. Lynn, and G. Strobl, "Network stretching, slip processes, and fragmentation of crystallites during uniaxial drawing of polyethylene and related copolymers. A comparative study," *Macromolecules*, vol. 32, no. 13, pp. 4390–4403, 1999.

[35]   B. Na, Q. Zhang, Q. Fu, Y. Men, K. Hong, and G. Strobl, "Viscous-force-dominated tensile deformation behavior of oriented polyethylene," *Macromolecules*, vol. 39, no. 7, pp. 2584–2591, 2006.

[36]   A. Peterlin, "Molecular model of drawing polyethylene and polypropylene," *J. Mater. Sci.*, vol. 6, no. 6, pp. 490–508, 1971.

[37]   A. Peterlin, "Plastic deformation of polymers with fibrous structure," *Colloid Polym. Sci. Kolloid Zeitschrift Zeitschrift für Polym.*, vol. 253, no. 10, pp. 809–823, 1975.

[38]   J. M. Schultz, *Polymer Material Science*. Englewood Cliffs, NJ: Prentice Hall, 1974.

[39]   R. O. Ebewele, "Polymer Science and Technology," *Polym. Sci. Technol.*, p. 483, 2000.

[40]   M. Bevis and E. B. Crellin, "The geometry of twinning and phase transformations in crystalline polyethylene," *Polymer (Guildf).*, vol. 12, no. 11, pp. 666–684, 1971.

[41]   P. Allan, E. B. Crellin, and M. Bevis, "Stress-induced twinning and phase transformations in polyethylene single crystals," *Philos. Mag.*, vol. 27, no. 1, pp. 127–145, 1973.

[42]   A. Cowking, J. G. Rider, I. L. Hay, and A. Keller, "A study on the orientation effects in polyethylene in the light of crystalline texture - Part 3 On the effect of applied stress on the molecular and textural orientation," *J. Mater. Sci.*, vol. 3, no. 6, pp. 646–654, 1968.

[43]   H. Kiho, A. Peterlin, and P. H. Geil, "Polymer deformation. VI. Twinning and phase transformation of polyethylene single crystals as a function of stretching direction," *J. Appl. Phys.*, vol. 35, no. 5, pp. 1599–1605, 1964.

[44]   A. Keller and D. P. Pope, "Identification of structural processes in deformation of oriented polyethylene," *J. Mater. Sci.*, vol. 6, no. 6, pp. 453–478, 1971.

[45]   R. E. Cohen, Z. Bartczak, and A. S. Argon, "Evolution of the Crystalline Texture of High-Density Polyethylene during Uniaxial Compression," *Macromolecules*, vol. 25, no. 18, pp. 4692–4704, 1992.

[46]   A. Galeski, Z. Bartczak, A. S. Argon, and R. E. Cohen, "Morphological Alterations during Texture-Producing Plastic Plane Strain Compression of High-Density Polyethylene," *Macromolecules*, vol. 25, no. 21, pp. 5705–5718, 1992.

[47]   A. Blaise, C. Baravian, S. André, J. Dillet, L. J. Michot, and R. Mokso, "Investigation of the mesostructure of a mechanically deformed HDPE by synchrotron microtomography," *Macromolecules*, vol. 43, no. 19, pp. 8143–8152, 2010.

[48]   C. Thomas, R. Seguela, F. Detrez, V. Miri, and C. Vanmansart, "Plastic deformation of spherulitic semi-crystalline polymers: An in situ AFM study of polybutene under tensile drawing," *Polymer (Guildf).*, vol. 50, no. 15, pp. 3714–3723, 2009.

[49]   A. Rozanski, A. Galeski, and M. Debowska, "Initiation of cavitation of polypropylene during tensile drawing," *Macromolecules*, vol. 44, no. 1, pp. 20–28, 2011.

[50]   A. Pawlak, A. Galeski, and A. Rozanski, "Cavitation during deformation of semicrystalline polymers," *Prog. Polym. Sci.*, vol. 39, no. 5, pp. 921–958, 2013.

[51]   F. Addiego *et al.*, "Cavitation in unfilled and Nano-CaCO3 filled HDPE subjected to tensile test: Revelation, localization, and quantification," *Polymer Engineering and Science*, vol. 50, no. 2. pp. 278–289, 2010.

[52]   A. Pawlak and A. Gałeski, "Cavitation during tensile drawing of semicrystalline polymers," *Polimery/Polymers*, vol. 56, no. 9, pp. 627–636, 2011.

[53]   D. . Hughes, A. Mahendrasingam, W. . Oatway, E. . Heeley, C. Martin, and W. Fuller, "A simultaneous SAXS/WAXS and stress-strain study of polyethylene deformation at high strain rates," *Polymer (Guildf).*, vol. 38, no. 26, pp. 6427–6430, 1997.

[54]   A. Pawlak, "Cavitation during tensile deformation of high-density polyethylene," *Polymer (Guildf).*, vol. 48, no. 5, pp. 1397–1409, 2007.

[55]   B. Na and R. Lv, "Effect of cavitation on the plastic deformation and failure of isotactic polypropylene," *J. Appl. Polym. Sci.*, vol. 105, no. 6, pp. 3274–3279, 2007.

[56]   M. F. Butler, A. M. Donald, and A. J. Ryan, "Time resolved simultaneous small- and wide-angle X-ray scattering during polyethylene deformation—II. Cold drawing of linear polyethylene," *Polymer (Guildf).*, vol. 39, no. 1, pp. 39–52, 1998.

[57]   M. Yamaguchi and K.-H. Nitta, "Optical and acoustical investigation for plastic deformation of isotactic polypropylene/ethylene-1-hexene copolymer blends," *Polym. Eng. Sci.*, vol. 39, no. 5, pp. 833–840, 1999.

[58]   X. Zhang *et al.*, "Deformation-mediated superstructures and cavitation of poly (l-lactide): In-situ small-angle X-ray scattering study," *Polymer (Guildf).*, vol. 53, no. 2, pp. 648–656, 2012.

[59]   S. Humbert, O. Lame, J. M. Chenal, C. Rochas, and G. Vigier, "New insight on initiation of cavitation in semicrystalline polymers: In-situ SAXS measurements," *Macromolecules*, vol. 43, no. 17, pp. 7212–7221, 2010.

[60]   M. F. Butler, A. M. Donald, and A. J. Ryan, "Time resolved simultaneous small- and wide-angle X-ray scattering during polyethylene deformation—I. Cold drawing of copolymer," *Polymer (Guildf).*, vol. 39, no. 1, pp. 39–52, 1998.

[61]   A. Pawlak and A. Galeski, "Cavitation during tensile deformation of polypropylene," *Macromolecules*, vol. 41, no. 8, pp. 2839–2851, 2008.

[62]   F. Chu, T. Yamaoka, H. Ide, and Y. Kimura, "Microvoid formation process during the plastic deformation of alpha-form polypropylene," *Polymer (Guildf).*, vol. 35, no. 16, pp. 3442–3448, 1994.

[63]   Y. Liu, C. H. L. Kennard, R. W. Truss, and N. J. Calos, "Characterization of stress-whitening of tensile yielded isotactic polypropylene," *Polymer (Guildf).*, vol. 38, no. 11, pp. 2797–2805, 1997.

[64]   H. E. H. Meijer and L. E. Govaert, "Mechanical performance of polymer systems: The relation between structure and properties," *Prog. Polym. Sci.*, vol. 30, no. 8–9, pp. 915–938, 2005.

[65]   E. Rosenberg, N. Brusselle-Dupend, and T. Epsztein, "A mesoscale quantification method of cavitation in semicrystalline polymers using X-ray microtomography," *Mater. Sci. Eng. A*, vol. 528, no. 21, pp. 6535–6544, 2011.

[66]   N. Brusselle-Dupend, E. Rosenberg, and J. Adrien, "Characterization of cavitation development while tensile testing PVF2 using 3D X-ray microtomography," *Mater. Sci. Eng. A*, vol. 530, no. 1, pp. 36–50, 2011.

[67]   L. Laiarinandrasana, J. Besson, M. Lafarge, and G. Hochstetter, "Temperature dependent mechanical behaviour of PVDF: Experiments and numerical modelling," *Int. J. Plast.*, vol. 25, no. 7, pp. 1301–1324, 2009.

[68]   Y. J. Tang *et al.*, "Mapping the damaged zone around the crack tip in high density polyethylene with synchrotron microfocus small angle X-ray scattering technique," *Chinese J. Polym. Sci. (English Ed.*, vol. 28, no. 2, pp. 165–170, 2010.

[69]   S. Rudraraju, A. Van der Ven, and K. Garikipati, "Three-dimensional isogeometric solutions to general boundary value problems of Toupin's gradient elasticity theory at finite strains," *Comput. Methods Appl. Mech. Eng.*, vol. 278, pp. 705–728, 2014.

[70]   D. P. Pope and A. Keller, "Deformation of oriented polyethylene — additional effects observed at high temperatures," *J. Mater. Sci.*, vol. 12, no. 6, pp. 1105–1108, 1977.

[71]   R. Arridge, "Assumption of homogenous elasticity in theories of lamellar texture of polymers," *J. Mater. Sci.*, vol. 9, no. 1, 1974.

[72] Y. Tang *et al.*, "Uniaxial deformation of overstretched polyethylene: In-situ synchrotron small angle X-ray scattering study," *Polymer (Guildf).*, vol. 48, no. 17, pp. 5125–5132, 2007.

[73] X. Li, Y. Mao, H. Ma, F. Zuo, B. S. Hsiao, and B. Chu, "An in-situ X-ray scattering study during uniaxial stretching of ionic liquid/ultra-high molecular weight polyethylene blends," *Polymer (Guildf).*, vol. 52, no. 20, pp. 4610–4618, 2011.

[74] N. E. Zafeiropoulos *et al.*, "Microfocus X-ray scattering scanning microscopy for polymer applications," *Macromol. Rapid Commun.*, vol. 26, no. 19, pp. 1547–1551, 2005.

[75] A. Agar, F. Frank, and A. Keller, "Crystallinity effects in the electron microscopy of polethylene," *Philos. Mag.*, vol. 4, no. 37, pp. 32–55, 1959.

[76] D. C. Bassett, "On moire patterns in the electron microscopy of polymer crystals," *Philos. Mag.*, vol. 10, no. 106, pp. 595–615, 1964.

[77] M. Williams, "Mechanical properties of crystalline polymers interpreted in terms of dislocations," *Ann. N. Y. Acad. Sci.*, vol. 155, no. A2, 1969.

[78] L. Jarecki and D. J. Meier, "Ultra-high modulus polyethylene. 1 Effect of drawing temperature," *Polymer (Guildf).*, vol. 20, no. 9, pp. 1078–1082, 1979.

[79] Z. Bartczak, "Texture evolution in large strain simple shear deformation of high density polyethylene," *Polymer (Guildf).*, vol. 35, no. 16, pp. 3427–3441, 1994.

[80] P. Miller, D. J. Buckley, and E. J. Kramer, "Microstructure and origin of cross-tie fibrils in crazes," *J. Mater. Sci.*, vol. 26, no. 16, pp. 4445–4454, 1991.

[81] A. Rozanski and A. Galeski, "Crystalline Lamellae Fragmentation during Drawing of Polypropylene," 2015.

[82]   U. L. T. Süss and N. W. J. Dual, "Novel Method for Analyzing Crack Growth in Polymeric Microtensile Specimens by In Situ Atomic Force Microscopy," pp. 463–472, 2010.

[83]   A. Dasari, S. J. Duncan, and R. D. K. Misra, "Microstructural aspects of tensile deformation of high density polyethylene," *Mater. Sci. Technol. Feb ProQuest Sci. Journals pg*, vol. 19, no. 2, 2003.

[84]   S. Hild and E. Physics, "A Nanoscopic View of Structure and Deformation of Hard Elastic Polypropylene with Scanning Force Microscopy," pp. 1953–1959, 1996.

[85]   a. Dasari and R. D. K. Misra, "Microscopic aspects of surface deformation and fracture of high density polyethylene," *Mater. Sci. Eng. A*, vol. 367, no. 1–2, pp. 248–260, 2004.

[86]   A. Dasari, J. Rohrmann, R. D. K. Misra, A. Dasari, J. Rohrmann, and R. D. K. Misra, "Atomic force microscopy characterisation of scratch deformation in long and short chain isotactic polypropylenes and ethylene-propylene copolymers Atomic force microscopy characterisation of scratch deformation in long and short chain isotactic polypropyl," vol. 836, no. June 2016, 2013.

[87]   F. Detrez, S. Cantournet, and R. Seguela, "Plasticity/damage coupling in semi-crystalline polymers prior to yielding: Micromechanisms and damage law identification," *Polymer (Guildf).*, vol. 52, no. 9, pp. 1998–2008, 2011.

[88]   U. Lang, T. Süss, N. Wojtas, and J. Dual, "Novel method for analyzing crack growth in polymeric microtensile specimens by in situ atomic force microscopy," *Exp. Mech.*, vol. 50, no. 4, pp. 463–472, 2010.

[89]   M. C. Roggemann and J. G. Williams, "Use of an atomic force microscope to measure surface deformations in polymeric systems," *J. Adhes. Sci. Technol.*, vol. 4243, no. August, 2016.

[90]   J. Zhong and D. He, "Combination of Universal Mechanical Testing Machine with Atomic Force Microscope for Materials Research," *Sci. Rep.*, vol. 5, no. August, p. 12998, 2015.

[91]   A. Y. Yarysheva, E. G. Rukhlya, L. M. Yarysheva, D. V. Bagrov, A. L. Volynskii, and N. F. Bakeev, "The structural evolution of high-density polyethylene during crazing in liquid medium," *Eur. Polym. J.*, vol. 66, pp. 458–469, 2015.

[92]   J. S. Higgins, "Recent Developments in Polymer Applications of Small-Angle Neutron , X-ray and Light Seattering," *J. Appl. Crystallogr.*, vol. 11, pp. 346–375, 1978.

[93]   L. H. Sperling, "Characterization of polymer conformation and morphology through small-angle neutron scattering—A literature review," *Polym. Eng. Sci.*, vol. 24, no. 1, pp. 1–21, 1984.

[94]   C. Baravian, S. André, N. Renault, N. Moumini, and C. Cunat, "Optical techniques for in situ dynamical investigation of plastic damage," in *Rheologica Acta*, 2008, vol. 47, no. 5–6, pp. 555–564.

[95]   A. Blaise, C. Baravian, J. Dillet, L. J. Michot, and S. Andre, "Characterization of the mesostructure of HDPE under 'In situ' uniaxial tensile test by incoherent polarized steady-light transport," *J. Polym. Sci. Part B Polym. Phys.*, vol. 50, no. 5, pp. 328–337, 2012.

[96]   S. N. Zhurkov and V. E. Korsukov, "Atomic mechanism of fracture of solid polymers," *J. Polym. Sci. Polym. Phys. Ed.*, vol. 12, no. 2, pp. 385–398, 1974.

[97]   S. Sakurai *et al.*, "Ultra small-angle X-ray scattering studies on structural changes in micrometers upon uniaxial stretching of segmented polyurethaneureas," *Polymer (Guildf).*, vol. 50, no. 6, pp. 1566–1576, 2009.

[98]   L. Laiarinandrasana, T. F. Morgeneyer, H. Proudhon, and C. Regrain, "Damage of semicrystalline polyamide 6 assessed by 3D X-ray tomography: From microstructural evolution to constitutive modeling," *J. Polym. Sci. Part B Polym. Phys.*, vol. 48, no. 13, pp. 1516–1525, 2010.

[99]   T. F. Morgeneyer *et al.*, "Nanovoid morphology and distribution in deformed HDPE studied by magnified synchrotron radiation holotomography," *Polymer (Guildf).*, vol. 55, no. 25, pp. 6439–6443, 2014.

[100]   A. Galeski, L. Koenczoel, E. Piorkowska, and E. Baer, "Acoustic emission during polymer crystallization," *Nature*, vol. 325, no. 6099, pp. 40–41, 1987.

[101]   A. Galeski, E. Piorkowska, L. Koenczoel, and E. Baer, "Acoustic emission during crystallization of polymers," *J. Polym. Sci. Part B Polym. Phys.*, vol. 28, no. 7, pp. 1171–1186, 1990.

[102]   C. G'Sell, J. M. Hiver, and A. Dahoun, "Experimental characterization of deformation damage in solid polymers under tension, and its interrelation with necking," *Int. J. Solids Struct.*, vol. 39, no. 13–14, pp. 3857–3872, 2002.

[103]   L. C. Cessna, "Dilatometric studies of polymers undergoing high and low rate tensile deformation," *Polym. Eng. Sci.*, vol. 14, no. 10, pp. 696–701, 1974.

[104]   A. Pawlak, A. Rozanski, and A. Galeski, "Thermovision studies of plastic deformation and cavitation in polypropylene," *Mech. Mater.*, vol. 67, pp. 104–118, 2013.

[105]   A. Pawlak and A. Galeski, "Plastic deformation of crystalline polymers: The role of cavitation and crystal plasticity," *Macromolecules*, vol. 38, no. 23, pp. 9688–9697, 2005.

[106] D. J. Bacon and K. Tharmalingam, "Computer simulation of polyethylene crystals - Part 3 The core structure of dislocations," *J. Mater. Sci.*, vol. 18, no. 3, pp. 884–893, 1983.

[107] S. Lee and G. C. Rutledge, "Plastic deformation of semicrystalline polyethylene by molecular simulation," *Macromolecules*, vol. 44, no. 8, pp. 3096–3108, 2011.

[108] S. Jabbari-farouji, J. Rottler, O. Lame, A. Makke, M. Perez, and J. Barrat, "Correlation of structure and mechanical response in solid-like polymers," *J. Phys. Condens. Matter*, vol. 194131, p. 194131, 2015.

[109] G. H. Michler and F. J. Baltá Calleja, Nano- and Micromechanics of Polymers Structure Modification and Improvement of Properties, no. 3. 2012.

[110] J. Karger-Kocsis and S. Fakirov, "Nano- and Micromechanics of Polymer Blends and Composites," in *Nano- and Micromechanics of Polymer Blends and Composites*, 2009, pp. i–xxi.

[111] E. Hecht, *Optics*. Addison-Wesley Longman, Incorporated, 2002.

[112] R. Erni, M. D. Rossell, C. Kisielowski, and U. Dahmen, "Atomic-resolution imaging with a sub-50-pm electron probe," *Phys. Rev. Lett.*, vol. 102, no. 9, 2009.

[113] R. Egerton, Physical principles of electron microscopy : An introduction to TEM, SEM, and AEM. New York: Springer, 2005.

[114] G. Binnig, H. Rohrer, C. Gerber, and E. Weibel, "Surface Studies by Scanning Tunneling Microscopy," *Phys. Rev. Lett.*, vol. 49, pp. 57–61, 1982.

[115] G. K. Bennig, "Atomic force microscope and method for imaging surfaces with atomic resolution." Google Patents, 1988.

[116]   N. Mullin, "Dynamic Imaging Methods for Scanning Probe Microscopy Submitted for the degree of Doctor of Philosophy . Nicholas William Mullin Department of Physics and Astronomy University of Sheffield September 2009," University of Sheffield, 2009.

[117]   Z. L. W. Weilie Zhou, Scanning microscopy for nanotechnology : techniques and applications / edited by Weilie Zhou and Zhong Lin Wang. New York : Springer, 2007.

[118]   F. J. Rubio-Sierra, W. M. Heckl, and R. W. Stark, "Nanomanipulation by atomic force microscopy," *Adv. Eng. Mater.*, vol. 7, no. 4, pp. 193–196, 2005.

[119]   H. J. Butt, B. Cappella, and M. Kappl, "Force measurements with the atomic force microscope: Technique, interpretation and applications," *Surf. Sci. Rep.*, vol. 59, no. 1–6, pp. 1–152, 2005.

[120]   P. Eaton and P. West, *Atomic Force Microscopy*. Oxford, 2010.

[121]   T. Kawagishi, A. Kato, Y. Hoshi, and H. Kawakatsu, "Mapping of lateral vibration of the tip in atomic force microscopy at the torsional resonance of the cantilever.," *Ultramicroscopy*, vol. 91, no. 1–4, pp. 37–48, May 2002.

[122]   C. Su, "Torsional Resonance Probe-Based Instrument And Method," 2005.

[123]   M. Reinstadtler, T. Kasai, U. Rabe, B. Bhushan, and W. Arnold, "Imaging and measurement of elasticity and friction using the TRmode," *J. Phys. D-Applied Phys.*, vol. 38, no. 18, pp. R269–R282, 2005.

[124]   Y. Martin, C. C. Williams, and H. K. Wickramasinghe, "ATOMIC FORCE MICROSCOPE FORCE MAPPING AND PROFILING ON A SUB 100-A SCALE," *J. Appl. Phys.*, vol. 61, no. 10, pp. 4723–4729, 1987.

[125]   Y. X. Song and B. Bhushan, "Dynamic analysis of torsional resonance mode of atomic force microscopy and its application to in-plane surface property extraction," *Microsyst. Technol. Nanosyst. Storage Process. Syst.*, vol. 12, no. 3, pp. 219–230, 2006.

[126]   C.-W. Yang and I.-S. Hwang, "Soft-contact imaging in liquid with frequency-modulation torsion resonance mode atomic force microscopy.," *Nanotechnology*, vol. 21, no. 6, p. 65710, Feb. 2010.

[127]   N. Mullin and J. Hobbs, "Torsional resonance atomic force microscopy in water," *Appl. Phys. Lett.*, vol. 92, no. 5, 2008.

[128]   F. Cajori, A History of Physics in its Elementary Branches. Macmillan, 1899.

[129]   H. Thoms, "Wilhelm Conrad Röntgen and the Early History of the Roentgen Rays," *Yale J. Biol. Med.*, vol. 6, no. 4, p. 482, 1934.

[130]   M. Von Laue, "Concerning the detection of X-ray interferences," *Nobel Lect.*, pp. 347–355, 1915.

[131]   W. Bragg, "The diffraction of short electromagnetic waves by a crystal," *Proc. Camb. Philol. Soc.*, vol. 17, pp. 43–57, 1913.

[132]   A. Guinier, "La diffraction des rayons X aux tres petits angles: applications a l'etude de phenomenes ultramicroscopiques," *Annales de physique*, vol. 12. pp. 161–237, 1939.

[133]   A. Guinier and G. Fournet, *Small-Angle Scattering of X-rays*. New York: Jonh Wiley and Sons, 1955.

[134]   S. J. Richardson *et al.*, "Watching mesoporous metal films grow during templated electrodeposition with in situ SAXS," *Nanoscale*, vol. 9, no. 29, pp. 10227–10232, 2017.

[135] C. Neylon, "Small angle neutron and X-ray scattering in structural biology: Recent examples from the literature," *European Biophysics Journal*, vol. 37, no. 5. pp. 531–541, 2008.

[136] O. Glatter and O. Kratky, *Small Angle X-ray Scattering*. Academic Press, 1982.

[137] H. Schnablegger and Y. Singh, "The SAXS guide: getting acquainted with the principles," *Ant. Paar*, p. 124, 2013.

[138] O. Pringer and A. Baner, Plastic Packaging: Interactions with Food and Pharmaceuticals. Wiley, 2008.

[139] M. F. Butler, A. M. Donald, and A. J. Ryan, "Time resolved simultaneous small- and wide-angle X-ray scattering during polyethylene deformation—II. Cold drawing of linear polyethylene," *Polymer (Guildf).*, vol. 39, no. 1, pp. 39–52, 1998.

[140] L. Fu *et al.*, "Stretching temperature and direction dependency of uniaxial deformation mechanism in overstretched polyethylene," *J. Polym. Sci. Part B Polym. Phys.*, vol. 52, no. 10, pp. 716–726, 2014.

[141] P. B. McDaniel, J. M. Deitzel, and J. W. Gillespie, "Structural hierarchy and surface morphology of highly drawn ultra high molecular weight polyethylene fibers studied by atomic force microscopy and wide angle X-ray diffraction," *Polym. (United Kingdom)*, vol. 69, 2015.

[142] D. V. Bagrov, A. Y. Yarysheva, E. G. Rukhlya, L. M. Yarysheva, A. L. Volynskii, and N. F. Bakeev, "Atomic force microscopic study of the structure of high-density polyethylene deformed in liquid medium by crazing mechanism," *J. Microsc.*, vol. 253, no. 2, pp. 151–160, 2014.

[143]   A. Krajenta, A. Rozanski, and R. Idczak, "Morphology and properties alterations in cavitating and non-cavitating high density polyethylene," *Polymer (Guildf).*, vol. 103, pp. 353–364, 2016.

[144]   F. Zuo *et al.*, "The role of interlamellar chain entanglement in deformation-induced structure changes during uniaxial stretching of isotactic polypropylene," *Polymer (Guildf).*, vol. 48, no. 23, pp. 6867–6880, 2007.

[145]   G. Machado *et al.*, "Morphological and crystalline studies of isotactic polypropylene plastically deformed and evaluated by small-angle X-ray scattering , scanning electron microscopy and X-ray diffraction," *Eur. Polym. J.*, vol. 45, no. 3, pp. 700–713, 2009.

[146]   K. Uchida, K. Mita, O. Matsuoka, T. Isaki, K. Kimura, and H. Onishi, "The structure of uniaxially stretched isotactic polypropylene sheets: Imaging with frequency-modulation atomic force microscopy," *Polym. (United Kingdom)*, vol. 82, pp. 349–355, 2016.

[147]   A. Dasari, J. Rohrmann, and R. D. K. Misra, "Microstructural evolution during tensile deformation of polypropylenes," *Mater. Sci. Eng. A*, vol. 351, no. 1–2, pp. 200–213, 2003.

[148]   G. H. Michler and R. Godehardt, "Deformation mechanisms of semi-crystalline polymers on the submicron scale," *Cryst. Res. Technol.*, vol. 35, no. 6, pp. 863–875, 2000.

[149]   V. A. Online *et al.*, "RSC Advances growth of high-density polyethylene," pp. 28191–28202, 2015.

[150]   N. Mullin, C. Vasilev, J. D. Tucker, C. N. Hunter, C. H. M. Weber, and J. K. Hobbs, "'torsional tapping' atomic force microscopy using T-shaped cantilevers," *Appl. Phys. Lett.*, vol. 94, no. 17, 2009.

[151]   M. Reinstaedtler, U. Rabe, V. Scherer, J. a. Turner, and W. Arnold, "Imaging of flexural and torsional resonance modes of atomic force microscopy cantilevers using optical interferometry," *Surf. Sci.*, vol. 532–535, pp. 1152–1158, Jun. 2003.

[152]   J. F. van der Veen, "Melting and freezing at surfaces," *Surf. Sci.*, vol. 433–435, no. 0, pp. 1–11, 1999.

[153]   T. Uchihashi, M. Higgins, Y. Nakayama, J. E. Sader, and S. P. Jarvis, "Quantitative measurement of solvation shells using frequency modulated atomic force microscopy," *Nanotechnology*, vol. 16, no. 3, pp. S49–S53, 2005.

[154]   A. Verdaguer, G. M. Sacha, H. Bluhm, and M. Salmeron, "Molecular structure of water at interfaces: Wetting at the nanometer scale," *Chem. Rev.*, vol. 106, no. 4, pp. 1478–1510, 2006.

[155]   K. Jinesh and J. Frenken, "Capillary Condensation in Atomic Scale Friction: How Water Acts like a Glue," *Phys. Rev. Lett.*, vol. 96, no. 16, p. 166103, Apr. 2006.

[156]   J. N. Israelachvili and R. M. Pashley, "MOLECULAR LAYERING OF WATER AT SURFACES AND ORIGIN OF REPULSIVE HYDRATION FORCES," *Nature*, vol. 306, no. 5940, pp. 249–250, 1983.

[157]   M. Antognozzi, a. D. L. Humphris, and M. J. Miles, "Observation of molecular layering in a confined water film and study of the layers viscoelastic properties," *Appl. Phys. Lett.*, vol. 78, no. 3, p. 300, 2001.

[158]   H. Asakawa, S. Yoshioka, K. Nishimura, and T. Fukuma, "Spatial Distribution of Lipid Headgroups and Water Molecules at Membrane/Water Interfaces Visualized by Three-Dimensional Scanning Force Microscopy," *ACS Nano*, vol. 6, no. 10, pp. 9013–9020, 2012.

[159]   T. Fukuma, M. J. Higgins, and S. P. Jarvis, "Direct imaging of individual intrinsic hydration layers on lipid bilayers at Angstrom resolution," *Biophys. J.*, vol. 92, no. 10, pp. 3603–3609, 2007.

[160]   E. T. Herruzo, H. Asakawa, T. Fukuma, and R. Garcia, "Three-dimensional quantitative force maps in liquid with 10 piconewton, angstrom and sub-minute resolutions.," *Nanoscale*, vol. 5, no. 7, pp. 2678–85, Apr. 2013.

[161]   N. Mullin and J. K. Hobbs, "Direct imaging of polyethylene films at single-chain resolution with torsional tapping atomic force microscopy," *Phys. Rev. Lett.*, vol. 107, no. 19, 2011.

[162]   R. C. Savage, N. Mullin, and J. K. Hobbs, "Molecular Conformation at the Crystal-Amorphous Interface in Polyethylene," *Macromolecules*, vol. 48, no. 17, pp. 6160–6165, 2015.